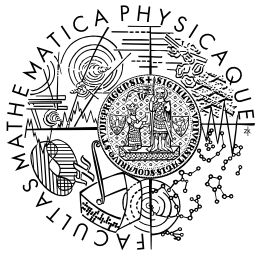

FACULTY
OF MATHEMATICS
AND PHYSICS
Charles University

DOCTORAL THESIS

Michaela Walterová

Orbital and internal dynamics of terrestrial planets

Department of Geophysics

Supervisor of the doctoral thesis: RNDr. Marie Běhounková, Ph.D.
Study programme: Physics of the Earth and Planets
Study branch: Physics

Prague 2020

I declare that I carried out this doctoral thesis independently, and only with the cited sources, literature and other professional sources. It has not been used to obtain another or the same degree.

I understand that my work relates to the rights and obligations under the Act No. 121/2000 Sb., the Copyright Act, as amended, in particular the fact that the Charles University has the right to conclude a license agreement on the use of this work as a school work pursuant to Section 60 subsection 1 of the Copyright Act.

In ..... date ....

Author's signature

In the first place, I would like to express my endless gratitude to dr. Marie Běhounková for her guidance over the past years. Marie spent hours proofreading my manuscripts, abstracts, and presentations, inspired me with many helpful suggestions and was always here to assist me with the formalities of the doctoral studies. Her kindness and support helped me to overcome the moments when the finalisation of this thesis seemed impossible. Likewise, I would like to thank prof. Ondřej Čadek for his support during difficult times and for his trust in my abilities.

My relationship with exoplanets has not always been simple and on the journey leading to the results presented in this work, I was several times brought to a dead end. It was only thanks to the support from the following people that I actually persevered to the end: Julie N. N. and Tomáš P. inspired me with their enthusiasm and love for planetary science. Pavel N. and Jan L. as well as my dear office mates Celeste B., Vojtěch P., Kateřina P. S., Ľubica V., and Jakub P. (in the order of appearance) showed me that I am not alone, discouraged me from leaving Academia, and shared with me many illuminating thoughts. *Sodales carissimi et doctissimi* from the Department's Latin circle helped me not to become overwhelmed by scientific work. Over the span of the last years, I have greatly appreciated the pleasant and friendly environment at the Department and I would like to thank all my colleagues for the enlightening lectures and discussions as well as for the joyful moments spent together at the hiking trips. Namely, I thank doc. Hana Čížková for her advice and help with formalities, dr. Ladislav Hanyk for taking care of the Department's hardware and software, prof. Jiří Zahradník for his kind words and insights, doc. Oldřich Novotný for his suggestions and interest in my work, and doc. Ctirad Matyska for lectures that helped me to understand some of the concepts used in this thesis.

Last but not least, I am grateful to my friends and family, in particular to my husband Filip, for support and tolerance. I also sincerely thank dr. Ana-Catalina Plesa for her patience.

On a more professional note, related directly to the content of this work, I would like to thank prof. Ondřej Čadek for providing me with his numerical model *Andy*, that was used extensively in Chapter 7 and served as a benchmark for the semi–analytical models presented in Chapters 3 to 6. I would also like to thank doc. Jakub Velímský, who shared with me his module calculating the ratio of two factorials by prime factorisation (and thus saved me from integer overflows). Part of the results included in the thesis (Chapters 3, 4, 7, and Appendices A, D) is based on two published papers. Regarding the paper published in 2017, I thank the anonymous editors of *Celestial Mechanics and Dynamical Astronomy* for the coordination of the review process. I am also grateful to the two anonymous reviewers for their constructive comments and recommendations, which have been helpful in improving the paper and, consequently, the corresponding chapter of the present work. Regarding the paper published in 2020, I am thankful to prof. Brian Jackson, the scientific editor of *The Astrophysical Journal*, for the coordination. I would also like to thank dr. Michael Efroimsky for his comments on the manuscript and for his kind suggestions, that I truly appreciate.

The research received funding from the following grants and projects:

Czech Science Foundation Project Nos. 14-04145S and 19-10809S

Charles University project GA UK No. 338214

Charles University Grant SVV 260447/2017 and 115-09/260581

The Ministry of Education, Youth and Sports, the Large Infrastructures for Research, Experimental Development and Innovations project "e-Infrastructure CZ – LM2018140".

Title: Orbital and internal dynamics of terrestrial planets

Author: Michaela Walterová

Department: Department of Geophysics

Supervisor: RNDr. Marie Běhounková, Ph.D., Department of Geophysics

Abstract: Close–in exoplanets are subjected to intense tidal interaction with the host star and their secular evolution is strongly affected by the resulting tidal dissipation. The tidal dissipation not only provides an additional heat source for the planet's internal dynamics but it also contributes to the evolution of the planet's spin rate and orbital elements. At the same time, the tidal dissipation itself is also determined by the planet's thermal state and by the spin–orbital parameters. The evolutions of the orbit and of the interior are, therefore, intrinsically linked. In this work, we combine analytical and numerical techniques to gain insight into the interconnection between the internal properties and the orbital evolution, with special focus on the role of tides. After a general study of parametric dependencies of the tidal heating and tidal locking, we present a semi–analytical model assessing the coupled tidally–induced thermal–orbital evolution in systems consisting of a host star and one or two planets. Specifically, we study the thermal–orbital evolution in three systems inspired by existing low–mass exoplanets and in a model system with ongoing Kozai–Lidov oscillations. Two additional studies illustrate the derivation of planet—planet tidal potential and the analysis of tidal phenomena in viscoelastic bodies in a numerical approach.

Keywords: tidal evolution, thermal evolution, terrestrial exoplanets

Název práce: Orbitální a vnitřní dynamika terestrických planet

Autor: Michaela Walterová

Katedra: Katedra geofyziky

Vedoucí disertační práce: RNDr. Marie Běhounková, Ph.D., Katedra geofyziky

Abstrakt: Planety nacházející se v těsné blízkosti své mateřské hvězdy jsou významně ovlivňovány slapovou interakcí. Slapové zatěžování a z něj vyplývající disipace mechanické energie přispívají jak k vnitřní dynamice těchto těles, tak k vývoji jejich oběžné dráhy a rychlosti rotace. Slapová disipace ovšem na parametrech oběžné dráhy a podobě planetárního nitra také sama závisí a její studium tedy nelze oddělit od studia tepelného vývoje planety. V této práci se zabýváme analytickým a numerickým modelováním vzájemné vazby mezi vývojem nitra a oběžné dráhy terestrických exoplanet, se zvláštním důrazem na roli slapů. Vedle obecné studie parametrických závislostí slapového zahřívání a stability spin-orbitálních resonancí se v práci věnujeme spřaženému modelu, s jehož pomocí lze studovat vzájemnou vazbu mezi tepelným vývojem a vývojem oběžné dráhy v soustavách s jednou či dvěma planetami. Vyvinutý model aplikujeme jednak na studium tří jednoplanetárních soustav inspirovaných skutečnými terestrickými exoplanetami, jednak na studium modelové soustavy s probíhajícími Kozaiovými-Lidovovými oscilacemi. Ve dvou dodatečných studiích odvozujeme vzájemný slapový potenciál buzený mezi dvěma planetami v soustavě a představujeme též numerický model, s jehož pomocí lze studovat slapové jevy v diferencovaných planetách řízených viskoelastickou reologií.

Klíčová slova: slapový vývoj, termální vývoj, terestrické exoplanety

Contents

Introduction

From the peculiar rotation of planet Mercury to the unexpected geological activity of Pluto, the tidal interaction has played an essential role in shaping the present–day face of the Solar System. Tides affect the spin rate of planetary bodies, contribute to their thermal budget and internal stress fields, sculpt their orbits, and—in worlds endowed with an ocean—cause periodic redistribution of the water masses. For an observer standing on the Earth, the most prominent results of tidal interaction are, indeed, the daily cycle of high tides and low tides—and the synchronous rotation of the Moon.

That both phenomena are inherently linked by the force of gravity was first explained by Sir Isaac Newton in *Philosophiæ Naturalis Principia Mathematica* (1687). Newton was aware of the tidal force's weakness; therefore, he specifically discussed the tidal effects (caused by the Moon and by the Sun) in fluid components of the Earth, where even a weak force results in observable motions. Likewise, concerning the figure of the Moon, Newton proposed that were the lunar material made of fluid, the tides raised by the Earth would transform its shape to a prolate spheroid and the Moon would be driven to a synchronous rotation[1]: the only stable spin state it can possibly acquire (*"In alio enim situ corpus lunare quiescere non potest, sed ad hunc situm oscillando semper redibit."*). The effect of tides on the spin state of celestial bodies is and was—even in Newton's times—observable not only in the case of the Moon but also in the case of other large satellites in the Solar System. Starting with the discovery of synchronous rotation of Saturn's moon Iapetus by Giovanni Domenico Cassini (in 1671), the equality of the orbital and the rotational period has been empirically confirmed among all major moons of Jupiter, Saturn, Uranus, and Neptune. A dynamically–evolved double–synchronised rotation state, in which both the "planet" and the satellite keep the same face towards each other, was found about forty years ago in the Pluto–Charon system (Christy and Harrington, 1978).

Although inevitable for the Moon and the other natural satellites, the synchronous rotation is not the only possible spin state of tidally–evolved bodies. As revealed by the radio observations of Pettengill and Dyce (1965) and analysed in an extensive literature (Peale and Gold, 1965; Goldreich and Peale, 1966; Correia and Laskar, 2009; Noyelles et al., 2014), the innermost planet Mercury rotates 1.5–times faster than is the mean angular velocity of its revolution around the Sun (the *mean motion*), and it is thus trapped in a 3:2 spin–orbit resonance. This super–synchronous resonant rotation can be attributed to a relatively high eccentricity of Mercury's orbit and to large variations in the tidal torque over the course of an orbital period. While unexpected by the observers at the time of the discovery, the higher–order resonances of celestial bodies on eccentric orbits are

[1] According to Newton's reasoning, since the synchronous rotation has already been acquired, the Moon must have had a prolate shape from earlier times. The synchronisation of lunar rotation was also studied by Kant, Laplace, Helmholtz, and by Darwin.

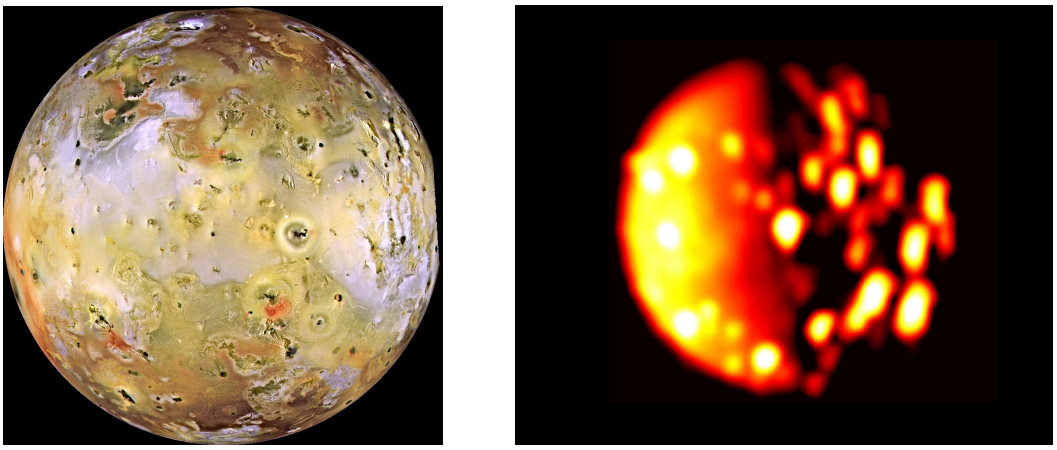

(a) Composite image from Galileo (b) IR image from Juno

Figure 1: Jupiter's moon Io as an example of strongly tidally heated body. Panel (a), a composition of images taken in different filters, depicts the moon's surface, marked by ongoing volcanic activity. Panel (b) unveils the thermal radiation of the moon, with multiple active hot spots.
Source of image (a): NASA/JPL/University of Arizona
Source of image (b): NASA/JPL-Caltech/SwRI/ASI/INAF/JIRAM

predicted by the tidal theory (e.g., Peale and Gold, 1965; Goldreich, 1966; Correia and Laskar, 2009; Makarov, 2012; Correia et al., 2014; Ferraz-Mello, 2015); at extreme orbital eccentricities, the synchronous rotation may even become unstable (see, e.g., Figue 5 of Ferraz-Mello, 2015).

Tidally–loaded celestial bodies, if rotating nonsynchronously, possessing nonzero axial tilt or orbiting on eccentric trajectories, are also subjected to periodic variations in the tidal force and in the interior stress field. The resulting tidal friction in materials of imperfect elasticity (be it solid or liquid) is not only the original cause of the above–mentioned synchronisation or resonant locking, but also a driving mechanism for the orbital evolution. Nonelastic tidal deformation is accompanied by the dissipation of mechanical energy, and a celestial body, drained slowly of its *vis viva*, descends to a lower orbit, in a closer vicinity of its host. Since the total angular momentum in the system has to be conserved, the migration to a lower orbit should also be followed by a decrease in the orbital eccentricity and by a gradual diminishing of the energy dissipation. Nevertheless, the presence of other effects in the systems of natural satellites—or in the pairs of a planet and a satellite—may give rise to a different outcome. First, the exchange of angular momentum and energy between a rapidly rotating planet and a close–in moon above the corotation radius[2] may lead to the orbit's expansion. This mechanism is observed in the Earth–Moon system, where it might have played an important role in past orbital evolution (e.g., Ćuk and Stewart, 2012; Wisdom and Tian, 2015; Ward et al., 2020). Similarly, the tidally–driven orbit expansion presumably

[2]The corotation radius is the radial distance from the planet's centre, at which the satellite's mean motion equals the planet's spin rate.

contributes to the orbital dynamics in the satellite systems of giant planets, where it is, however, also complemented by another mechanism (e.g., Goldreich, 1965; Dermott et al., 1988; Neveu and Rhoden, 2019).

An intriguing feature of the Solar System (and also of other planetary systems in the Universe), is the affinity of its members for commensurabilities (e.g., Peale, 1976; Murray and Dermott, 1999). In addition to the spin–orbit resonances, in which the rotational frequency equals an integer multiple of half the mean motion, the moons and planets (and asteroids) are often found in orbit–orbit resonances, the most notable being the Laplace resonance between the Jovian satellites Io, Europa, and Ganymede. Systems of satellites with commensurate orbital periods are able to maintain nonzero orbital eccentricities despite the tidal dissipation, and their dynamics are thus greatly enhanced by the dissipated mechanical energy. A particularly extreme case of a tidally–heated body in the Solar System is the moon Io (Figure 1). Orbiting at only five Jupiter radii above the surface of its enormous host planet, Io experiences surface heat flux that is approximately $25,000$ times higher than the average surface heat flux at the Earth (e.g., Peale et al., 1979; Segatz et al., 1988; Veeder et al., 1994; Steinke et al., 2020). In icy moons, tidal heating can provide the energy needed for the maintenance of subsurface water oceans (e.g., Cassen et al., 1979; Sotin et al., 2009; Hussmann et al., 2010) and the related tidal stresses in the ice shells can be the process behind their surface tectonic features (e.g., Matsuyama and Nimmo, 2008; Rhoden et al., 2012).

This brief overview of tidal effects shaping the interiors, orbits, and rotation states of the Solar System bodies shows us the way to the range of phenomena that can be acting in other, potentially very different planetary systems. Given the present count of more than 4,000 confirmed exoplanets[3], the methods originally developed for the study of Solar System bodies can now be also applied to the large statistical set of these distant, often highly exotic worlds. While the present–day orbital eccentricities of the Solar System planets and satellites are relatively small, with the highest value, $e = 0.2$, exhibited by Mercury, the range of eccentricities found in exoplanetary systems spans from 0 up to ~ 1 (e.g., Tamuz et al., 2008; Blunt et al., 2019; Udry et al., 2019). In contrast to the Solar System, the most eccentric orbits are being inhabited by giant gaseous planets, with masses of few to several Jupiters. Such violent worlds, dragged by tides in the pericentre and freezing in the apocentre, are hardly comparable to the quiescent giants of our own, loaded by a flock of small icy satellites.

Nevertheless, the primary focus of the present work is the class of *terrestrial exoplanets*. Although usually not orbiting on the extreme trajectories described above, terrestrial exoplanets can also be subjected to exotic environments, very unlike those encountered in the Solar System. Since the most successful detection techniques used in exoplanetary science are based on indirect measurements and, therefore, are most sensitive to close–in exoplanets around low–mass stars, the statistical set of extrasolar worlds contains many examples of planets orbiting

[3]As of December 11, 2020, the *NASA Exoplanet Archive* lists 4,307 confirmed extrasolar planets, with 716 records having a radius smaller than 1.5 Earth radii ($R_\oplus$).

in the closest vicinity of their hosts. As can be expected, based on the theory developed originally for the Moon, such exoplanets undergo strong tidal loading and energy dissipation and their rotation is most probably synchronised. The orbital eccentricities of close–in terrestrial exoplanets are typically lower than for the orbits of extrasolar gas giants (Van Eylen and Albrecht, 2015; Van Eylen et al., 2019). However, although the orbital eccentricities tend to be lower, they are not always zero, and they may allow for a prolonged tidal activity. Some of the close–in worlds are found in tightly–packed multi–planetary systems, in which they may undergo the same (or similar) type of resonant eccentricity forcing as present in the systems of Jovian or Saturnian satellites. The orbital dynamics might even drive a system to a long resonant chain, as is the case with TRAPPIST–1 (Luger et al., 2017), Kepler–80 (Shallue and Vanderburg, 2018) or HD 158259 (Hara et al., 2020). Even in single–planetary systems, the orbital eccentricities can be driven to nonzero values either by tidal interaction of the planet with a rapidly rotating host star (Bolmont and Mathis, 2016; Boué and Efroimsky, 2019) or they can be maintained on nonzero values, acquired earlier, by processes acting in the planetary interior and diminishing the tidal response (e.g., Henning et al., 2009; Shoji and Kurita, 2014; Makarov, 2015; Makarov et al., 2018). This last type of processes, namely the thermal evolution of planetary interior with partial melting, will also be considered in the tidal model introduced in the main part of the present work.

In this thesis, we discuss several topics related to solid–body tides and to their cooperation with other phenomena. The work is divided into seven chapters and three thematically distinct parts and is organised as follows:

- The first part covers the theoretical and empirical background of the topic. In Chapter 1, we overview the basic concepts of celestial mechanics and provide evolution equations that will be used in the rest of the work. Special attention is given to two possible sources of orbital evolution: the tidal interaction and the third–body perturbation, both described by the formalism of the Darwin–Kaula theory. Chapter 2, on the other hand, deals with the interior properties of terrestrial worlds. After a discussion of the detection and characterisation techniques used in exoplanetary science, we explore the sources of macroscopic deformation in the Earth, along with the possibilities of their theoretical description. We also introduce the empirically–motivated models used in modern tidal theories and briefly outline the energy balance in the interior of terrestrial planets.

- The second part presents a semi–analytical model of coupled thermal–orbital evolution of tidally–loaded terrestrial exoplanets. Beginning with Chapter 3, which illustrates the parametric dependencies of quantities relevant to our study (namely, the tidal torque, the stability of super–synchronous spin–orbit resonances, and the tidal dissipation), the exposition continues with Chapter 4, in which we discuss the semi–analytical method itself[4]. The

[4]Chapters 3 and 4 are adapted from a published paper (Walterová and Běhounková, 2020).

chapter introduces a standard 1d parameterised model of mantle convection, the inclusion of an emergent magma ocean to the tidal model, and the numerical scheme used. After this practically–oriented introduction, we apply the model to three low–mass exoplanets with potentially nonzero orbital eccentricity (Proxima Centauri b, GJ 625 b, and GJ 411 b) and observe the long–term evolution of their orbital elements, spin rate, and thermal state. In Chapter 5, the model from the previous chapters is further extended by including a third–body perturbation in the form of a highly–inclined outer perturber.

- The third part consists of two independent studies that are approaching the tidal interaction from different perspectives. Chapter 6 shows a variation on the harmonic expansion of the tidal potential (Kaula, 1961), applied to the case of tides raised by a planet on another planet in the system. Finally, in Chapter 7, we provide a numerical treatment of the tidal loading, calculated in the time domain and presenting an alternative to the semi–analytical model considered in the second part of the present thesis[5].

The seven chapters summarised above are supplemented by four appendices, which outline the normal mode theory and the calculation of the tidal heating, provide details of the numerical scheme used in the last chapter, and list the partial derivatives used in the semi–analytical model of the central chapters. The main outcomes of our studies are then given in Conclusion.

[5]Chapter 7 is almost identical to Walterová and Běhounková (2017).

1. Secular orbital evolution

In this chapter, we are going to introduce two mechanisms governing the orbital evolution of close–in exoplanets in multi–planetary systems: the tidal interaction and the third–body perturbation. The tidal interaction with the host star results in secular shrinking of the orbit and gradual decay of the orbital eccentricity. On the other hand, the gravitational interaction with other planet(s) in the system may contribute to secular maintenance of large orbital eccentricities, potentially leading to prolonged periods of increased tidal activity. After two sections introducing the set of Keplerian elements and the standard perturbation theory, we dive directly into the waters of Darwin–Kaula theory, which provides a comprehensive and intuitive description of the two mechanisms in question. Then, we present a set of auxiliary orbital elements and, finally, we briefly discuss the evolution of planetary rotation.

1.1 Orbital elements

Let us assume a simple model system consisting of two point masses. The first point mass, m_*, will be denoted as a star (or "the primary"), while the second point mass, m_1, will symbolise a planet (or "the secondary"). If we put the two masses in an otherwise empty Euclidean space and prescribe their initial positions and velocity vectors, they will start moving under the mutual attraction described by Newton's law of universal gravitation

$$F = \mathcal{G}\frac{m_* m_1}{r^2} \,, \tag{1.1}$$

where F is the force magnitude, $\mathcal{G}$ is Newton's gravitational constant, and r denotes the mutual distance between the two point masses. Regarding the evolution of the model system with known initial conditions, we may ask the following questions: What are the trajectories of the two masses? How can we express the position vectors and the instantaneous velocities at an arbitrary time? The presented task, known as *the two–body problem*, is the simplest integrable problem of celestial mechanics and its solution is thoroughly explained in the first chapters of every introductory textbook on the topic (Brouwer and Clemence, 1961; Kovalevsky, 1967; Murray and Dermott, 1999).

Here, we limit ourselves to a simple statement that the motion of the common barycentre of the system is uniform and linear and, in barycentric coordinates, the two point masses follow trajectories described by conic sections. Depending on the total energy $\mathcal{E}$ of the system, the trajectories are either elliptical ($\mathcal{E} < 0$), parabolical ($\mathcal{E} = 0$) or hyperbolical ($\mathcal{E} > 0$). When finding the solution to the two–body problem, it is also conventional to substitute the two point masses by the total mass $\mathcal{M} = m_* + m_1$, concentrated in the barycentre, and by a virtual particle with the reduced mass $\mu = m_* m_1/(m_* + m_1)$, which orbits around $\mathcal{M}$. This substitution reduces the two–body problem to a one–body problem. Nevertheless,

if the host star is considerably more massive than the planet ($m_1 \ll m_*$), it approximately holds that

$$\mathcal{M} \approx m_* \qquad \text{and} \qquad \mu \approx m_1 \ .$$

Throughout this work, we assume that the condition $m_1 \ll m_*$ is always satisfied[1]. Specifically, the positions of the planets are always referred to the position of the host star (i.e., we express the equations of motion in *asterocentric coordinates*).

Keplerian elements According to Kepler's first law of planetary motion, a planet moves around its host star on an elliptical orbit, having the star in one of its foci. The trajectory of a planet on elliptical orbit can be characterised by six constants, the *orbital elements*, that enable the prediction of the planet's position at an arbitrary time. Figure 1.1 depicts the introduction of Keplerian elements $\{a, e, i, \omega, \Omega, t_0\}$, a set of constants with immediate geometrical meaning. While the semi–major axis a and the eccentricity e define the shape of the ellipse, the angular variables, Ω, ω and i, anchor the orbit in space with respect to the inertial reference frame XYZ. The longitude of the ascending node Ω is measured in the reference plane, from the reference direction X to the nodal line. The argument of periapsis ω is measured in the orbital plane, from the nodal line to the periapsis π, in which the planet gets closest to the host star. Finally, the inclination i marks the angle between the reference plane and the orbital plane. To initialise the planet's position in the orbit, the five introduced elements need to be complemented by a sixth element, which can be either the time of periapsis passage t_0 or, alternatively, the mean anomaly at epoch, marked as σ. In this work, we prefer the second option. The mean anomaly M, a linear function of time defined as the angle delimited by the periapsis, the position of the host star and the position of a hypothetical body on a circular orbit with the same orbital period T as the studied planet, is then calculated as

$$M = n(t - t_0) = nt + \sigma \ , \tag{1.2}$$

with n being the mean motion,

$$n = \frac{2\pi}{T} = \sqrt{\frac{\mathcal{G}(m_* + m_1)}{a^3}} \ . \tag{1.3}$$

Figure 1.1 also introduces the instantaneous distance r of the planet from the star and the true anomaly v. Both quantities change non-linearly with time and their values depend on the orbital eccentricity. This observation will result in the introduction of Hansen coefficients and the eccentricity functions later in this chapter. On circular orbits, the true anomaly equals the mean anomaly.

[1] In Chapters 3 to 5, we always consider $m_1/m_* \sim 10^{-5}$.

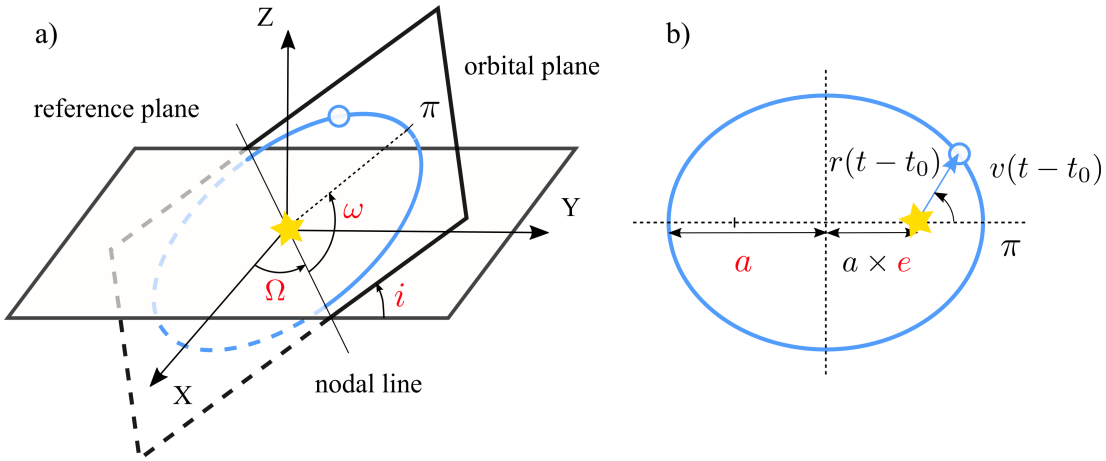

Figure 1.1: Introduction of the Keplerian orbital elements. (a) The orientation of the orbital plane with respect to the inertial reference frame XYZ is determined by the longitude of the ascending node Ω and the inclination i. Additionally, the position of the orbit's periapsis (point π) in the orbital plane is specified by the argument of periapsis ω. (b) The semi–major axis a and the orbital eccentricity e define the size and the shape of the orbit. The planet's actual position at time t, described by the instantaneous distance r and the true anomaly v, requires the time of periapsis passage t_0.

Three names for three angles In the previous paragraph, we mentioned three distinct terms with the significance of angles measured from different directions: the *longitude*, the *argument* and the *anomaly*. Here, we will specify the definition of the three terms. As can be inspected in Figure 1.1, the longitude of the ascending node Ω is measured from the fixed reference direction, the argument of periapsis ω is measured from the nodal line and the mean or true anomaly marks an angle measured from the periapsis in the direction of the planet's movement. In parallel to the longitude of the ascending node, we can also introduce other longitudes, that will be defined with respect to the reference direction. The *longitude of periapsis* is an oblique angle given by

$$\varpi = \Omega + \omega \,, \tag{1.4}$$

the *mean longitude* is defined similarly as

$$\lambda = \Omega + \omega + M \,, \tag{1.5}$$

and the *mean longitude at epoch* as

$$\epsilon = \Omega + \omega + \sigma \,. \tag{1.6}$$

The definition of angles related to a reference direction becomes particularly advantageous in situations where either the nodal line or the periapsis becomes undefined. Therefore, we will use these coordinates for the introduction of nonsingular elements, applicable to zero inclination or zero eccentricity cases

(Section 1.4). The set of Keplerian elements with three longitudes $\{\Omega, \varpi, \epsilon\}$ will also be preferred in the discussion of third–body perturbation.

Other sets of orbital elements Although in the rest of this work, we are going to study the orbital evolution in terms of the Keplerian elements, it should be noted that different problems of celestial mechanics may require the introduction of different, better–suited sets of constants. While the strong suit of the Keplerian elements is their immediate geometrical meaning, they cannot be directly accommodated for problems formulated in the Hamiltonian formalism, since they do not satisfy Hamilton's canonical equations (i.e., they are not canonical). Examples of problems best formulated in the Hamiltonian approach is the derivation of Lagrange planetary equations, the study of the dynamics of resonance or resonance encounters, and algebraic mappings (e.g., Brouwer and Clemence, 1961; Kozai, 1962; Peale, 1969, 1976; Murray and Dermott, 1999; Boué, 2020). The Hamiltonian formulation also facilitates coordinate transformations and—as is important in the context of our work—it has been successfully employed in the rigorous re–derivation of tidal equations (Boué and Efroimsky, 2019).

As an example of the canonical orbital elements, we mention the set of *Delaunay variables* (Murray and Dermott, 1999), which is, in the scope of tidal dynamics, often complemented by *Andoyer variables* for the motion of the rotation axis. The Delaunay variables consist of three generalised coordinates, $\{l = M, g = \omega, h = \Omega\}$ and their conjugate momenta, which correspond to a rescaled total energy of the system, the total angular momentum, and the z–component of the total angular momentum. A similar system of canonical elements, in which the generalised coordinates are represented by the longitudes defined in the previous paragraph, is the set of *Poincaré variables* (Murray and Dermott, 1999).

1.2 Perturbation theory

A point–mass planet orbiting a point–mass star in an idealised, empty space would retain its initial orbital elements forever. The same would also hold for a system consisting of a non–deformable spherical star and a non–deformable spherical planet. However, in all realistic cases found in Nature, the assumptions taken in the simple two–body problem are generally not satisfied. First, the host star as well as the planet are rotating extended bodies. Their shape is distorted due to the rotation, tidal deformation and inherent topography; their gravitational field is further altered by non–homogeneities in the interior and, potentially, by relativistic effects (Rubincam, 1977). These phenomena present one of the possible sources of orbital evolution. Second, the star and the planet are, in reality, never entirely shielded from the influence of other bodies or other material in the environment. Be it the multiplicity of the host star, the presence of other companions in the system, a gas or dust disk, the physical environment always shapes the orbits of the celestial bodies.

The perturbation theory, which forms the basis of the following derivations, assumes that the influence of either of the perturbations is small and that the

trajectory of the studied body can still be described by a Keplerian ellipse[2]. If the force generated by the disturbance is conservative, the gravitational effect of the perturbation can be characterised by the disturbing potential or disturbing function $\mathcal{R}$. The total potential Φ, governing the motion of the body, is then written as

$$\Phi = \Phi_{2\mathrm{B}} + \mathcal{R} \,, \tag{1.7}$$

where $\Phi_{2\mathrm{B}}$ signifies the gravitational potential of the host star as sensed by the planet in the two–body problem,

$$\Phi_{2\mathrm{B}} = \frac{\mathcal{G}m_*}{r} \,. \tag{1.8}$$

As we will see in the following section, the exact form of the disturbing function depends on the nature of the problem. Different perturbations induce different variations in the orbital elements. For a disturbing function expressed in the Keplerian elements, the evolution of the shape and the orientation of the orbit can be described by the set of *Lagrange planetary equations* (e.g., Brouwer and Clemence, 1961; Kovalevsky, 1967):

$$\frac{\mathrm{d}a}{\mathrm{d}t} = \frac{2}{na}\frac{\partial \mathcal{R}}{\partial \sigma} \,, \tag{1.9a}$$

$$\frac{\mathrm{d}e}{\mathrm{d}t} = \frac{1-e^2}{na^2 e}\frac{\partial \mathcal{R}}{\partial \sigma} - \frac{\sqrt{1-e^2}}{na^2 e}\frac{\partial \mathcal{R}}{\partial \omega} \,, \tag{1.9b}$$

$$\frac{\mathrm{d}i}{\mathrm{d}t} = \frac{\cot i}{na^2\sqrt{1-e^2}}\frac{\partial \mathcal{R}}{\partial \omega} - \frac{1}{na^2\sqrt{1-e^2}\sin i}\frac{\partial \mathcal{R}}{\partial \Omega} \,, \tag{1.9c}$$

$$\frac{\mathrm{d}\Omega}{\mathrm{d}t} = \frac{1}{na^2\sqrt{1-e^2}\sin i}\frac{\partial \mathcal{R}}{\partial i} \,, \tag{1.9d}$$

$$\frac{\mathrm{d}\omega}{\mathrm{d}t} = \frac{\sqrt{1-e^2}}{na^2 e}\frac{\partial \mathcal{R}}{\partial e} - \frac{\cot i}{na^2\sqrt{1-e^2}}\frac{\partial \mathcal{R}}{\partial i} \,, \tag{1.9e}$$

$$\frac{\mathrm{d}\sigma}{\mathrm{d}t} = -\frac{2}{na}\frac{\partial \mathcal{R}}{\partial a} - \frac{1-e^2}{na^2 e}\frac{\partial \mathcal{R}}{\partial e} \,. \tag{1.9f}$$

In equations (1.9), we used the set of osculating orbital elements containing ω and σ. However, when inspecting the mutual gravitational perturbation of two or more planets in the system, it might be advantageous to express the angular variables with respect to a fixed reference direction. Therefore, we also present the alternative form of the Lagrange planetary equations, with the argument of periastron (ω) and the mean anomaly at epoch (σ) substituted by the longitude

[2]Specifically, the orbital elements of the trajectory that would be taken by the planet upon vanishing of the perturbation at time t are known as *osculating elements* (e.g., Kovalevsky, 1967).

of periastron (ϖ) and the mean longitude at epoch (ϵ), respectively (Murray and Dermott, 1999):

$$\frac{\mathrm{d}a}{\mathrm{d}t} = \frac{2}{na}\frac{\partial \mathcal{R}}{\partial \epsilon} , \tag{1.10a}$$

$$\frac{\mathrm{d}e}{\mathrm{d}t} = -\frac{\sqrt{1-e^2}}{na^2 e}(1-\sqrt{1-e^2})\frac{\partial \mathcal{R}}{\partial \epsilon} - \frac{\sqrt{1-e^2}}{na^2 e}\frac{\partial \mathcal{R}}{\partial \varpi} , \tag{1.10b}$$

$$\frac{\mathrm{d}i}{\mathrm{d}t} = -\frac{\tan\frac{i}{2}}{na^2\sqrt{1-e^2}}\left(\frac{\partial \mathcal{R}}{\partial \epsilon} + \frac{\partial \mathcal{R}}{\partial \varpi}\right) - \frac{1}{na^2\sqrt{1-e^2}\sin i}\frac{\partial \mathcal{R}}{\partial \Omega} , \tag{1.10c}$$

$$\frac{\mathrm{d}\Omega}{\mathrm{d}t} = \frac{1}{na^2\sqrt{1-e^2}\sin i}\frac{\partial \mathcal{R}}{\partial i} , \tag{1.10d}$$

$$\frac{\mathrm{d}\varpi}{\mathrm{d}t} = \frac{\sqrt{1-e^2}}{na^2 e}\frac{\partial \mathcal{R}}{\partial e} + \frac{\tan\frac{i}{2}}{na^2\sqrt{1-e^2}}\frac{\partial \mathcal{R}}{\partial i} , \tag{1.10e}$$

$$\frac{\mathrm{d}\epsilon}{\mathrm{d}t} = -\frac{2}{na}\frac{\partial \mathcal{R}}{\partial a} - \frac{1-e^2}{na^2 e}(1-\sqrt{1-e^2})\frac{\partial \mathcal{R}}{\partial e} + \frac{\tan\frac{i}{2}}{na^2\sqrt{1-e^2}}\frac{\partial \mathcal{R}}{\partial i} . \tag{1.10f}$$

1.3 Darwin–Kaula expansion

The rest of our journey through the theoretical foundations of the secular orbital evolution focuses on two kinds of periodic perturbations: the third–body perturbation due to a second planet in the system and the tidal perturbation due to the finite dimension of the studied body. A classical approach to the mathematical description of such periodic perturbations to the planet's orbit is presented by the *Darwin–Kaula expansion*. Sir George Howard Darwin, the author of innumerable scientific essays, with topics ranging from the lunar theory to the practical aspects of tidal waves in English channels, was the first one to describe the orbital evolution of a satellite revolving around a tidally deformed planet (Darwin, 1880). In his analysis, he treats the tidal wave as a degree–2 surface spherical harmonic and studies in detail the tidal terms corresponding to the leading frequencies in the Earth–Moon system[3]. To distinguish between the two roles of the satellite—as a tide–raising body and as a body whose orbit is disturbed by the tidal distortion of the planet—he formally introduces two model satellites (moon and Diana) with two sets of orbital elements. The two satellites and their respective sets of elements are identified with each other upon the derivation of the evolution equations. Since no restrictions apply to the character of the satellites, the theory describes the orbital evolution of the Moon as well as the "orbital evolution" of the Sun with respect to the Earth—and vice versa.

A similar approach to the derivation of the tidal disturbing function and the evolution equations was taken by William Mason Kaula. Kaula (1964) (see also

[3]The use of harmonic analysis in the tidal theory was inaugurated by William Thompson (Lord Kelvin), a friend, teacher, and inspirer of George Darwin.

Kaula, 1961) writes the tidal potential, which is raised by the disturbing body, in the form of a spherical harmonic decomposition and derives Fourier series to analyse its changes in time. The derivation is, basically, a chain of binomial expansions, yielding the tidal potential expressible as

$$\Phi = \sum_{lmpq} \mathcal{A}_{lmpq}(a, e, i) \cos \psi_{lmpq}(\lambda, \varpi, \Omega) \, . \tag{1.11}$$

Here, the indices lm correspond to the spherical harmonic decomposition and the indices pq to the expansion into Fourier modes. The frequencies of the individual modes are obtained as linear combinations of the time derivatives $\dot{\lambda}$, $\dot{\varpi}$, $\dot{\Omega}$, and of the Earth's spin rate $\dot{\theta}$. Later, Kaula (1964) revives the "double-satellite" derivation of Darwin (1880) and, after identifying the two satellites with each other, obtains evolution equations for the individual modes of the series introduced in expression (1.11). In a similar manner, he also derives the disturbing function and the evolution equations for a satellite perturbed by another body with the same primary (Kaula, 1962).

The theory of William Kaula became particularly fruitful in the field of space-based geodesy and a large volume of classical literature is based on his pioneering work on this topic. In the scope of planetary science, the Darwin–Kaula expansion is valued mainly for the feasibility of discerning which modes are important for a given analysis and which modes can be neglected. The expansion into Fourier modes also seems advantageous in the case of tides in nonelastic bodies, whose response to external loading is more easily described in the frequency domain than in the time domain. The details of the Darwin–Kaula expansion applied to the two aforementioned problems, namely the third–body perturbation and the motion around a tidally distorted primary, are given in the next two subsections.

1.3.1 Third–body perturbation

Assumptions First, let us focus on the case of two planets (or satellites) orbiting the same primary. Let m_1 symbolise the inner planet and m_2 the outer one. Correspondingly, the subscripts 1 and 2 of all studied quantities will refer to the inner and the outer planet, respectively. Specifically, a_1 and a_2 will symbolise the semi–major axes of the two planets, defined with respect to the host star. Since the problem is to be treated in the scope of the perturbation theory, we assume that the two orbits are non–crossing, thus

$$a_1(1 + e_1) < a_2(1 - e_2) \, . \tag{1.12}$$

Condition (1.12) ensures that the periapsis of the outer planet is still further away from the host star than the apoapsis of the inner planet and that the two planets never collide[4]. To remain in the domain of the perturbation theory, we

[4]The dynamics of planetary systems also enable the existence of collisionless crossing orbits. A famous example of crossing orbits in the Solar System are Neptune and Pluto: their orbital configuration is stable thanks to the 3:2 orbit–orbit resonance (Varadi, 1999). Numerous examples of other stable configurations not fulfilling the condition (1.12) are given in, e.g., Murray and Dermott (1999).

also require that the disturbing function for each of the planets is much smaller than the Newtonian potential due to the primary,

$$\mathcal{R}_1 \ll \frac{\mathcal{G}m_*}{r_1} \qquad \text{and} \qquad \mathcal{R}_2 \ll \frac{\mathcal{G}m_*}{r_2} \,. \tag{1.13}$$

In other words, the trajectories of both planets can be at each time t described by a Keplerian orbit.

Inner planet Under the given conditions, the disturbing function for the inner planet can be written as (Kaula, 1962)

$$\mathcal{R}_1 = \frac{\mathcal{G}m_2}{a_2} \sum_{l=2}^{\infty} \sum_{m=0}^{l} \sum_{p,p'=0}^{l} \sum_{q,q'=-\infty}^{\infty} \kappa_m \frac{(l-m)!}{(l+m)!} \left(\frac{a_1}{a_2}\right)^l \mathcal{F}_{lmp}(i_1) \mathcal{F}_{lmp'}(i_2) \mathcal{H}_{lpq}(e_1) \mathcal{G}_{lp'q'}(e_2) \cos\psi \,, \tag{1.14}$$

with

$$\psi = (l-2p'+q')\lambda_2 - (l-2p+q)\lambda_1 - q'\varpi_2 + q\varpi_1 + (m-l+2p')\Omega_2 - (m-l+2p)\Omega_1 \tag{1.15}$$

and

$$\kappa_m = (2-\delta_{m0}) \,, \qquad \text{where} \qquad \delta_{m0} = \begin{cases} 0 & \text{for } m \neq 0 \,, \\ 1 & \text{for } m = 0 \,. \end{cases} \tag{1.16}$$

Equation (1.14), in parallel to the general expression for the Darwin–Kaula expansion of the tidal potential (1.11), characterises each mode of the disturbing function by six indices. As earlier, the indices pq stand for the Fourier series expansion of the periodic orbit of the inner planet and the indices $p'q'$ denote the same for the outer planet. In equation (1.14), we also see Kaula's functions of inclination $\mathcal{F}_{lmp}(i)$ and the functions of eccentricity $\mathcal{G}_{lpq}(e)$, $\mathcal{H}_{lpq}(e)$ for an inner and an outer perturbation, respectively. These three kinds of functions arise during the derivation of the disturbing function (Kaula, 1961, 1962) and will be further discussed in Subsection 1.3.3. At this point, to estimate the magnitude of each term in the Darwin–Kaula expansion, it might be instructive to mention that (Kaula, 1961; Murray and Dermott, 1999)

$$\mathcal{G}_{lpq}(e) = o\left(e^{|q|}\right) \qquad\qquad \mathcal{H}_{lpq}(e) = o\left(e^{|q|}\right) \tag{1.17}$$

and

$$\mathcal{F}_{lmp}(i) = o\left(\sin^{|m-l+2p|}\frac{i}{2}\right) \,. \tag{1.18}$$

Note that, in general, the disturbing function for the inner planet depends on all orbital parameters of both planetary bodies. We would also point out at the structure of the argument ψ, a linear combination of the angular variables λ_i, ϖ_i, and Ω_i. Interestingly, the sum of the coefficients standing before the individual variables is identically zero. This, so–called *d'Alembert relation* (e.g., Murray and Dermott, 1999), is fulfilled thanks to our choice to describe the orbit by

the longitudes $\{\lambda, \varpi, \Omega\}$ in place of the mean anomaly M and the argument of periapsis ω.

In the above expansion, we neglected the term $l = 0$. This term does not depend on the orbital elements of the inner planet m_1 and, consequently, it does not contribute to the orbital evolution. The second term, $l = 1$, is zero due to our choice of asterocentric coordinates (e.g., Murray and Dermott, 1999). In the barycentric coordinate system, with the semi–major axes a_1 and a_2 defined with respect to the common barycentre, the term $l = 1$ would correspond to the motion of the common barycentre, caused by the orbit of the outer planet m_2.

Outer planet Almost identical to the case of the inner planet, the disturbing function for the outer planet can be written as (Murray and Dermott, 1999)

$$\mathcal{R}_2 = \frac{\mathcal{G}m_1}{a_2} \sum_{l,m,p,p',q,q'} \kappa_m \frac{(l-m)!}{(l+m)!} \left(\frac{a_1}{a_2}\right)^l \mathcal{F}_{lmp}(i_1)\mathcal{F}_{lmp'}(i_2)\mathcal{H}_{lpq}(e_1)\mathcal{G}_{lp'q'}(e_2)\cos\psi + \mathcal{R}_{\rm ac} \tag{1.19}$$

with

$$\mathcal{R}_{\rm ac} = \mathcal{G}m_1 \left[\frac{a_1}{a_2^2}\mathcal{H}_{1pq}(e_1)\mathcal{G}_{1p'q'}(e_2) - \frac{a_2}{a_1^2}\mathcal{G}_{1pq}(e_1)\mathcal{H}_{1p'q'}(e_2)\right] \times \\ \times \sum_{m=0}^{1}\sum_{p,p'=0}^{1}\sum_{q,q'=-\infty}^{\infty} \kappa_m \frac{(1-m)!}{(1+m)!}\mathcal{F}_{1mp}(i_1)\mathcal{F}_{1mp'}(i_2)\cos\psi \tag{1.20}$$

and with the limits of summations in equation (1.19) same as in equation (1.14). Here, the term $l = 0$ is neglected in concordance with convention, although it depends on a_2 and, therefore, contributes to a slow secular variation in the mean longitude ϵ. The additional term $\mathcal{R}_{\rm ac}$, which we denote as the "asterocentric correction", contains the contribution of $l = 1$ and corresponds, again, to our choice of the coordinate system.

Secular evolution The disturbing functions for the inner and the outer planet have the form of a sum of periodic functions with arguments $\psi = \psi_{lmpp'qq'}$. Each term of the Darwin-Kaula expansion thus contributes to the resulting behaviour of the system at a distinct period and with a distinct amplitude. Depending on their characteristic rates of change, we may divide the individual angular elements in ψ into "slow" and "fast" variables. The fast variables, λ_1 and λ_2, characterise the variations of the disturbing function on the scale of one orbital period. The remaining, slow variables, on the other hand, determine the secular evolution of the system under the third–body perturbation. The linear combination of all angular variables in ψ represents the unique configuration of the planetary system at a given time.

To filter out the short–scale variations of the disturbing function, we need to obtain its mean value, averaged over the fast variables. The secular contribution

to the disturbing function is thus obtained as

$$\langle \mathcal{R}_i \rangle^{\mathrm{sec}} = \frac{1}{4\pi^2} \int_0^{2\pi} \int_0^{2\pi} \mathcal{R}_i \, \mathrm{d}\lambda_1 \, \mathrm{d}\lambda_2 = \sum \mathcal{A}_i \cos\psi \, , \tag{1.21}$$

where the right–hand side satisfies

$$(l - 2p + q) = 0 \wedge (l - 2p' + q') = 0 \, ,$$

the summation is performed over all $lmpp'qq'$ modes fulfilling the given condition and the symbol $\mathcal{A}_i = \mathcal{A}_{i,lmpp'qq'}(a_1, a_2, e_1, e_2, i_1, i_2)$ serves as a shorthand for the amplitude of each mode. Any short–scale variations of $\mathcal{A}_i$, i.e., the variations of the semi–major axes, the eccentricities, and the inclinations over one orbital period, were neglected in the averaging. The argument ψ in the secular case depends only on the slow variables, so that

$$\psi^{\mathrm{sec}} = -q'\varpi_2 + q\varpi_1 + (m - l + 2p')\Omega_2 - (m - l + 2p)\Omega_1 \, . \tag{1.22}$$

In addition to the contribution indicated in equation (1.21), the secular evolution of the two–planetary system may also be affected by the presence of *orbit–orbit resonances*. In that case, the secular disturbing function $\langle \mathcal{R}_i \rangle^{\mathrm{sec}}$ would need to be complemented by additional terms arising due to the resonant behaviour.

Orbit–orbit resonances A resonance between the orbits of two planets in a system occurs whenever the ratio of their orbital or orbit precession periods equals a rational number, preferably with small numerator and denominator. By the orbit precession we understand the precession of the pericentre, quantified by $\dot{\varpi}$, or the precession of the nodal line, quantified by $\dot{\Omega}$. The system is said to be in resonance if the time derivative of the argument ψ,

$$\dot{\psi} = (l-2p'+q')(n_2+\dot{\epsilon}_2) - (l-2p+q)(n_1+\dot{\epsilon}_1) - q'\dot{\varpi}_2 + q\dot{\varpi}_1 + (m-l+2p')\dot{\Omega}_2 - (m-l+2p)\dot{\Omega}_1 \, , \tag{1.23}$$

equals or closely approaches zero for some combination of the indices. Then, the corresponding terms in the Darwin–Kaula expansion play the leading role in the disturbing function and in the evolution equations for the system.

Since the orbit precession frequencies are typically lower, compared to the mean motions, the most prominent resonances are the *mean–motion resonances*, approximately satisfying the criterion

$$(l - 2p' + q')n_2 - (l - 2p + q)n_1 \approx 0 \, . \tag{1.24}$$

As n_2 denotes the mean motion of the outer planet and n_1 the mean motion of

the inner planet, the ratio between the prefactors of the two mean motions in (1.24) can be expressed as

$$\frac{l-2p'+q'}{l-2p+q} \approx \frac{k+j}{k} \ , \tag{1.25}$$

where k and j are small integers. Specifically, j is called the *order of resonance* and the arguments ψ fulfilling the relation (1.25) are labelled as the *resonant arguments*. For the sake of illustration, let us write down several resonant arguments corresponding to the $2:1$ mean–motion resonance. Along with them, we also indicate the magnitude of the lowest–order term in the corresponding amplitudes $\mathcal{A}$, given by the indices $lmpp'qq'$:

$$\begin{aligned}
\psi^{\mathrm{res}} &= 2\lambda_2 - \lambda_1 - \varpi_1 \ , & \mathcal{A} &\propto \left(\frac{a_1}{a_2}\right)^2 e_1 \\
\psi^{\mathrm{res}} &= 2\lambda_2 - \lambda_1 - \varpi_2 \ , & \mathcal{A} &\propto \left(\frac{a_1}{a_2}\right)^2 e_2 \\
\psi^{\mathrm{res}} &= 2\lambda_2 - \lambda_1 - \varpi_1 - \Omega_2 + \Omega_1 \ , & \mathcal{A} &\propto \left(\frac{a_1}{a_2}\right)^2 e_1 \sin\frac{i_1}{2} \sin\frac{i_2}{2} \\
\psi^{\mathrm{res}} &= 4\lambda_2 - 2\lambda_1 - 2\varpi_1 \ , & \mathcal{A} &\propto \left(\frac{a_1}{a_2}\right)^4 e_1^2
\end{aligned} \tag{1.26}$$

The four chosen examples offer several observations: 1) The resonant arguments must satisfy the d'Alembert relation; therefore, the frequencies of the resonant terms always contain a contribution from the orbital precession. 2) Generally speaking, lower coefficients in the resonant arguments indicate higher amplitudes of the corresponding terms. However, this conclusion depends on the orbital inclinations and eccentricities. 3) If the resonant argument depends on ϖ but does not depend on Ω, the amplitude of the term is proportional to e (but not to i). This kind of resonances is called the *eccentricity–type resonance*. 4) If the resonant argument also depends on Ω, the amplitude of the term is also proportional to i. Resonances in which the argument consists of the mean longitudes and longitudes of the ascending nodes (not illustrated in this example) are called the *inclination–type resonances*.

A system in the proximity of a mean–motion resonance is characterised by periodic variations in the semi–major axes, the eccentricities, and the inclinations. The variations may be large and in the case of close–in moons (such as the Jovian or Saturnian satellites) or close–in exoplanets (such as TRAPPIST-1) they may lead to alternating periods of increased and decreased tidal heating (e.g., Ojakangas and Stevenson, 1986; Spohn, 1991; Luger et al., 2017). Due to the oscillatory nature of the long-term evolution, the changes in the resonant arguments resemble, in a simplified case[5], the motion of a linear harmonic oscillator. Using the *pendulum*

[5]The illustrative pendulum model is derived specifically for the circular restricted three–body problem, where the outer planet possesses a circular orbit, the inner planet is of negligible mass (and its effect on the outer planet is thus negligible), and both bodies are moving in the reference plane (Murray and Dermott, 1999).

model (e.g., Murray and Dermott, 1999), it can be shown that, depending on the total energy of the system, the angle ψ^{res} either librates about a stable point or it circulates[6]. The stable point is $\psi = 0$ for odd–order resonances and $\psi = \pi$ for even–order resonances (e.g., Winter and Murray, 1997).

In addition to the secular terms and the terms corresponding to orbit–orbit resonances (if present), the study of orbital evolution over the entire age of the system may also require the inclusion of *secular resonances*. The secular resonances involve coupling between orbit precessions of the two bodies. In other words, they consist of resonances between the respective $\dot{\varpi}$ and/or $\dot{\Omega}$. In the Solar System, the secular resonances involving Saturn contribute to the present structure of the asteroid belt (Froeschle and Morbidelli, 1994) and the resonance between the perihelium precessions of Jupiter and Mercury may be responsible for large past excursions of the Mercurian eccentricity (Laskar, 2008). A specific type of a secular resonance, affecting the motion of highly inclined or eccentric asteroids, is the (von Zeipel–)Kozai–Lidov mechanism (von Zeipel, 1910; Lidov, 1962; Kozai, 1962). This topic will be discussed in more detail in Chapter 5. On extremely long timescales, comparable to the age of the system, the secular co–evolution of the planets is also subject to other effects, such as the tidal loading. The description of this phenomenon in the scope of the Darwin–Kaula theory is given in the following subsection.

1.3.2 Tidal loading

The tidal loading and the related tidal phenomena result from the gravitational action on an extended, deformable body. A planet subjected to the gravitational force exerted by the host star, and to the centrifugal force due to its revolution around the host star, deforms under the influence of the differential—tidal—force and assumes the shape of a prolate spheroid. In response to the tidal loading, it forms two tidal bulges. If the planet were perfectly elastic, the symmetry axis of the prolate spheroid would be identical to the line connecting the two bodies. One of the tidal bulges would be raised on the hemisphere facing the host star and the other on the opposite hemisphere.

However, the response of realistic planets is never perfectly elastic. As a consequence of the energy dissipation in the planet's interior, the tidal bulge forms gradually and the resulting symmetry axis of the deformed planet does not necessarily coincide with the direction to the host star. Due to the planet's rotation and its movement around the star on a potentially eccentric orbit, the tidal bulge can get carried away from that direction by a small angle. Several possible definitions of this *tidal lag* will be given in one of the following paragraphs, where we will also see that the character of the tidal deformation offers a unique insight into the structure, composition, and rheological properties of the planet.

The gravitational force acting on the unaligned tidal bulges gives rise to the

[6] In an extreme case, when the total energy of the system equals the critical energy dividing the librational and oscillatory regions in the phase space (the separatrix), the resonant angle undergoes a transitional type of motion with infinite period.

tidal torque, which is then responsible for the evolution of the planet's spin rate. Similarly, the energy dissipation in the planet's interior results in the long–term orbital evolution. The secular changes in the spin rate and in the orbital elements are mutually interconnected due to the dependence of the tidal lag on the frequency of the planet's rotation. Since the tidal torque and the evolution equations depend very steeply on the semi–major axis, the tidal effects are particularly important in the case of close–in moons and planets. The theory unfolded in this subsection is later applied to Chapters 3, 4, and 5.

Orientation of the planet Kaula (1961) expresses the position of the secondary relative to the primary, i.e., using orbital elements defined with respect to the primary's equator and its intersection with the orbital plane. Such an approach is natural to the problem of geometric utilisation of artificial satellites (Kaula, 1961) as well as to the tidal evolution of the lunar orbit (Kaula, 1964), although it might complicate the assessment of the angular elements' variation in systems where both the primary and the secondary are contributing to the tidal evolution (Chyba et al., 1989; Boué and Efroimsky, 2019). Nevertheless, to characterise the star's position relative to the planet, we introduce three angles describing the planet's orientation relative to the orbital plane[7]: α, β, and γ. As indicated in Figure 1.2, the angle γ sets the position of the vernal point on the celestial equator and determines at what phase of the orbit the planet experiences vernal equinox. Angle β is the planet's obliquity, measured between the normal to the orbit and the planet's spin axis. Finally, α determines the initial position of the reference meridian (or the initial rotation of the planet around its spin axis). Variables introduced as Ω, i, and ω in the work of Kaula (1961, 1964) are thus substituted by the three new angles characterising the planet's orientation.

Tidal potential While the disturbing function in the previous subsection was a consequence of mere existence of the second planet, the disturbing function due to tides results from the tidally–induced deformation of the studied planet and from the changes in the gravitational potential of the deformed body. To determine the planet's deformation, we first need to express the *tidal potential*, under which it deforms. In our case, the tidal potential is induced by the gravitational action of the host star and its magnitude in an infinitesimal volume at radius ϱ, colatitude ϑ, and longitude φ of the studied planet can be decomposed as (Kaula, 1961, 1964)

$$\Phi^{\mathrm{tide,p}}(\varrho,\vartheta,\varphi) = \sum_{l=0}^{\infty}\sum_{m=0}^{l}\sum_{p=0}^{l}\sum_{q=-\infty}^{\infty} \Phi^{\mathrm{tide,p}}_{lmpq}(\varrho,\vartheta,\varphi)\ , \tag{1.27}$$

[7]Note that the frame defined by the orbital plane and its normal is not an inertial reference frame, since its orientation is subject to evolution. A description using the Euler angles with respect to the inertial frame is given in Boué and Efroimsky (2019). The counterparts of our angles $\{\alpha,\beta,\gamma\}$ in their notation are $\{\Omega',i',\omega'\}$.

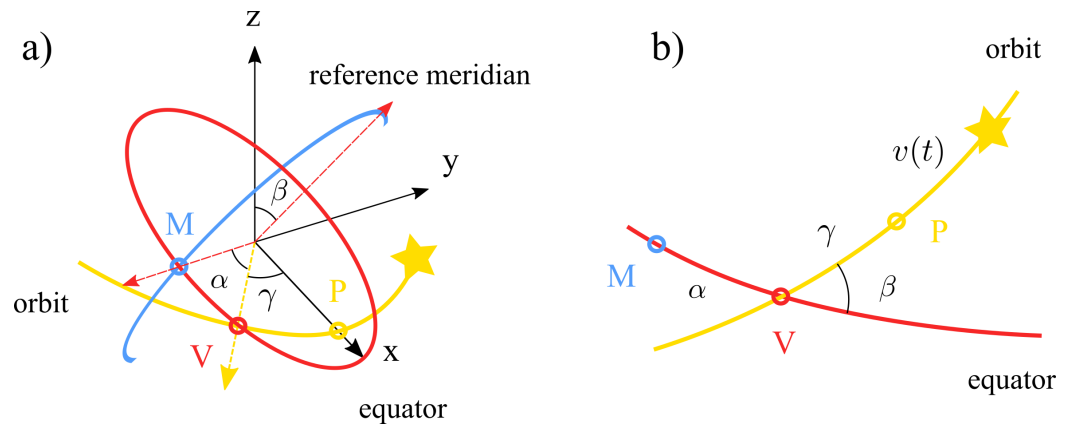

Figure 1.2: Orientation of the planet and the introduction of angles α, β and γ. (a) The orientation of the planet with respect to the orbital plane xy can be described by three consecutive rotations. Let the x-axis represent the direction towards the star in the pericentre P and let V indicate the position of the vernal point (the intersection of the equator with the orbit). Angle γ is then defined as the angular distance from P to V. Angle β characterises the planet's obliquity and measures the tilting of the equatorial plane with respect to the orbital plane. Finally, α defines the initial position of the reference meridian and is measured from the vernal point in the direction opposite to the planet's rotation. The star orbits counterclockwise along the yellow line. The planet rotates so that the point M, where the reference meridian crosses the equator, moves counterclockwise along the red line. (b) A close-up of the relevant region in the previous image; $v(t)$ is the true anomaly of the star. Adapted from Kaula (1961).

where

$$\Phi^{\mathrm{tide,p}}_{lmpq}(\varrho,\vartheta,\varphi) = \tilde{\mathcal{B}}_{lm}\,\tilde{\mathcal{C}}_{lmpq}\,\varrho^{l}\,\mathcal{P}_{lm}(\cos\vartheta)\,\begin{Bmatrix}\cos\\ \sin\end{Bmatrix}^{l-m\ \text{even}}_{l-m\ \text{odd}}[\tilde{\nu}_{lmpq} - m(\varphi+\tilde{\theta})] \tag{1.28}$$

and

$$\tilde{\mathcal{B}}_{lm} = \mathcal{G}m_{*}\,\frac{(l-m)!}{(l+m)!}\,\kappa_{m}\ ,$$

$$\tilde{\mathcal{C}}_{lmpq} = \frac{1}{\tilde{a}^{l+1}}\mathcal{F}_{lmp}(\tilde{\beta})\,\mathcal{G}_{lpq}(\tilde{e})\ .$$

$$\tilde{\nu}_{lmpq} = (l-2p)\tilde{\gamma} + (l-2p+q)\tilde{M} + m\tilde{\alpha}\ .$$

In the above definition, θ symbolises the sidereal time (the rotation angle of the planet) and the tilde marks variables describing the position of the tide–raising body relative to the planet's surface. As explained in the preface to the section on the Darwin–Kaula expansion, both Darwin (1880) and Kaula (1964) analysed the tidal evolution by studying the case of the Earth with two satellites. One of the satellites was thought of as tide–raising, while the other was thought of as experiencing the orbital evolution due to the tidal deformation of the Earth. Both

satellites were then identified with each other. Our variables with a tilde are thus bound to the first satellite in this description.

Tides in the planet The model planet deforms under the influence of the tidal potential (1.27) and the deformation gives rise to the disturbing potential—or the disturbing function. In the model of Darwin (1880) and Kaula (1964), the disturbing function determines the orbital variations of the second satellite. If we retain the same labelling as above, where the quantities with a tilde mark the orbital elements of the tide-raising satellite, the disturbing function influencing the orbital elements of the second satellite (without the tilde) is (Kaula, 1964)

$$\mathcal{R}^{\mathrm{tide,p}} = \sum_{l=0}^{\infty} \sum_{m=0}^{l} \sum_{p=0}^{l} \sum_{q=-\infty}^{\infty} \mathcal{R}^{\mathrm{tide,p}}_{lmpq} \,, \tag{1.29}$$

where[8]

$$\mathcal{R}^{\mathrm{tide,p}}_{lmpq} = k_l \, R^{2l+1} \, \tilde{\mathcal{B}}_{lm} \, \tilde{\mathcal{C}}_{lmpq} \sum_{p'=0}^{l} \sum_{q'=-\infty}^{\infty} \mathcal{C}_{lmp'q'} \cos[\tilde{\nu}_{lmpq} - \varepsilon_{lmpq} - m\tilde{\theta} - (\nu_{lmp'q'} - m\theta)] \,. \tag{1.30}$$

In equation (1.30) we introduced symbol R for the radius of the model planet and symbols k_l and ε_{lmpq} for the tidal *Love number* and the tidal *phase lag*, respectively. These two parameters quantify the relative change in the planet's gravitational potential resulting from its tidal deformation. The Love number and the phase lag depend on the interior structure, on the rheological parameters of the planet, and also on the loading frequency. Traditional as well as rheologically–motivated prescriptions of the two quantities will be discussed in one of the following paragraphs.

The argument of cosine in equation (1.30) can be explicitly rewritten as

$$\psi^{\mathrm{tide}} = (l-2p)\tilde{\gamma} - (l-2p')\gamma + (l-2p+q)\tilde{M} - (l-2p'+q')M + m(\tilde{\alpha}-\alpha) - m(\tilde{\theta}-\theta) - \varepsilon_{lmpq}$$

and if we introduced an analogy of the longitude of pericentre $(\alpha+\gamma)$ and the true longitude $(\alpha+\gamma+M)$ in the planetocentric elements of the host star $\{\alpha, \beta, \gamma\}$, the argument would closely resemble the case of the third–body perturbation (1.15). The only difference would result from the planet's rotation (the term with θ) and the lagging of the planet's deformation.

As was already emphasised, the tidal disturbing function (1.30) is expressed in elements defined with respect to the planet's equator. Since both the tide–raising and the perturbed satellites of Darwin (1880) and Kaula (1964) are, in our case, represented by the host star, the planetocentric elements of the "satellites" are equivalent to the angles describing the planet's orientation relative to the orbital plane. When studying the orbital evolution of the planet with respect

[8]This definition already contains the assumption $m_1 \ll m_*$. A more general expression for the disturbing function due to tides was presented by Boué and Efroimsky (2019).

to the (asterocentric) inertial reference frame, it would also be necessary to correctly convert the planetocentric elements $\{a, e, \beta, \gamma, \alpha, \sigma\}$ to the asterocentric elements $\{a, e, i, \omega, \Omega, \sigma\}$ used in the previous sections. The conversion consists in rotations of a planetocentric reference frame and results in nontrivial changes in the evolution equations for the angular variables. We will return to this point later when discussing the derivation of Boué and Efroimsky (2019).

Although the evolution of the angular elements should be treated carefully, the disturbing function introduced in equation (1.30) can be readily used in the Lagrange planetary equations for the semi–major axis and the eccentricity. The differentiation is then performed with respect to the elements without the tilde, i.e., corresponding to the second, perturbed satellite. After the derivation of the evolution equations, the two model satellites can be identified with each other, so that the quantities with a tilde are set equal to the quantities without the tilde.

As in the case of the third–body perturbation, we would like to study the tidal evolution in the long–term. Upon identifying M with $\tilde{M}$, γ with $\tilde{\gamma}$, and averaging over the mean anomaly and the precession angle[9] γ, the only nonzero terms in the Darwin–Kaula series are $p' = p$ and $q' = q$. Therefore, the argument of the secular evolution equations due to tidal loading reduces to $\psi^{\mathrm{sec,tide}} = -\varepsilon_{lmpq}$.

Effect of the interior structure We have already introduced the tidal Love number and the tidal phase lag as the two global parameters quantifying the planet's reaction to external loading. On the previous lines, we have also seen that the secular evolution equations only contain the argument $\sin \varepsilon_{lmpq}$. The role of the planet's interior is thus parameterised by the factor $k_l \sin \varepsilon_{lmpq}$, which is sometimes called the *kvalitet* (Makarov, 2015; Makarov et al., 2016; Frouard et al., 2016). The tidal Love number is defined as the ratio between the amplitude of the disturbing potential, induced by the tidal deformation of the planet, and the amplitude of the tidal potential, which is the source of the deformation. For the purpose of the definition, both potentials are measured at the surface R of the planet. The phase lag is then defined as the difference in phases of the two periodically changing potentials. Since the tidal and the disturbing potential can be decomposed into spherical harmonics, the Love number and the phase lag can also be defined with respect to a given harmonic. In equation (1.30), we use k_l to symbolise the degree–l Love number and ε_{lmpq} to mark lagging of the lm harmonic in the Fourier mode indexed as pq.

In addition to the Love number and the phase lag, we may also find in literature the quantity Q, or the *tidal quality factor* (e.g., MacDonald, 1964; Goldreich, 1966; Goldreich and Soter, 1966; Efroimsky and Lainey, 2007). The quality factor quantifies the energy dissipation in a planet: the higher it is, the less energy can be dissipated in each tidal loading cycle. The inverse quality factor is defined as the ratio between the energy lost ($\Delta\mathcal{E}$) and the maximum energy deposited ($2\pi\mathcal{E}$)

[9]The evolution of angle γ would correspond to the planet's axial precession. The second averaging is thus an averaging over the axial precession period.

during one loading cycle (e.g., Stacey, 1963; Sotin et al., 2009),

$$Q^{-1} = \frac{\Delta\mathcal{E}}{2\pi\mathcal{E}} , \tag{1.31}$$

and, in the tidal theory, it is related to the phase lag as (Efroimsky, 2012a)

$$Q^{-1}_{lmpq} = \sin\varepsilon_{lmpq}, \tag{1.32}$$

where Q_{lmpq} is the quality factor of the mode $lmpq$. In material science, a corresponding parameter is defined as tangent of the phase lag (Nowick and Berry, 1972). Nevertheless, the two definitions are almost equivalent for small values of ε_{lmpq}. In the Earth, the quality factor is measurable by the methods of seismology, gravimetry, and geodesy, which offers an insight into the behaviour of planetary material that should be also considered in tidal theory (Section 2.2).

The quantities k_l, ε_{lmpq}, and Q_{lmpq} depend on the interior structure and on the composition of the planet. As mentioned earlier, they also depend on the loading frequency. In reality, the frequency dependence of the kvalitet (either $k_l \sin\varepsilon_{lmpq}$ or k_l/Q_{lmpq}) is closely linked to the planet's rheology and stratification (e.g., Efroimsky and Lainey, 2007; Henning and Hurford, 2014; Tobie et al., 2019) and the prescription of a given frequency dependence is equivalent to the specification of a given rheological model for the planet. In the traditional tidal literature using the Darwin–Kaula expansion, we may find two basic concepts: the phase lags of the individual modes, ε_{lmpq}, are either treated as constant and equal to each other, or they are considered as linear functions of the loading frequencies

$$\omega_{lmpq} = (l-2p)\dot{\gamma} + (l-2p+q)\dot{M} + m\dot{\alpha} - m\dot{\theta} \approx (l-2p+q)n - m\dot{\theta} . \tag{1.33}$$

The first approach is known as the *constant phase lag model*, the second one as the *constant time lag model*. Both are valuable for their simple form, which endows them with the ability to serve as toy models in the basic considerations of the tidal evolution path. In certain restricted cases, they are also a good approximation of the system's actual behaviour. Nevertheless, neither of them is fully compatible with the rheology of realistic terrestrial bodies (Makarov and Efroimsky, 2013).

Constant phase lag model Although the constant phase lag model (e.g., Goldreich, 1963; Kaula, 1964; Yoder, 1982) is motivated by the negligible frequency dependence of the Earth's quality factor Q over a wide range of relevant frequencies, it leads to physically inappropriate behaviour in the vicinity of zero frequency. The kvalitet in the constant phase lag model reads as

$$k_l \sin\varepsilon_{lmpq} = k_\mathrm{c} \sin\varepsilon_\mathrm{c} \,\mathrm{Sgn}\{\omega_{lmpq}\} , \tag{1.34}$$

where k_c and ε_c are constants[10] and $\mathrm{Sgn}\{\cdot\} \in \{-1, 0, 1\}$ is a function returning

[10] In the traditional models, the Love number is often treated as constant. As we will see in Chapter 7, this assumption is in most cases correct: the Love number is approximately constant in the low–frequency region as well as in the high–frequency region and if all of the relevant tidal modes fall into one of these regions, the Love number does not necessarily need to be endowed with a frequency dependence.

the sign of its argument. Once the frequency of a dominant tidal mode crosses zero, as is the case for synchronously rotating bodies ($\dot{\theta} \approx n$) on eccentric orbits, the corresponding term in the Darwin–Kaula expansion immediately changes sign. In other words, the tidal bulge, first lagging behind the maximum of the tidal potential, immediately switches its position with respect to the radius vector centred in the star. Such a transition is unphysical and not related to any particular rheology. Nevertheless, the Darwin–Kaula expansion with the assumption of constant phase lags leads to qualitatively correct predictions for the planet's spin rate (Dobrovolskis, 2007).

Constant time lag model The constant time lag model (e.g., Darwin, 1880; Alexander, 1973; Hut, 1981; Mignard, 1979) avoids the step function at the zero frequencies by directly including the frequency dependence of the kvalitet,

$$k_l \sin \varepsilon_{lmpq} = k_\mathrm{c} \sin \omega_{lmpq} \Delta t \ , \tag{1.35}$$

where Δt is the time lag. This prescription of the frequency dependence is also known as the *weak friction approximation* (Alexander, 1973; Hut, 1981) and the main area of its application is the study of stellar tides in binary systems[11]. The constant time lag model is rheologically justified for planets with negligible rigidity, low average viscosity and/or planets loaded at very low frequencies (without the contribution of high–frequency modes). The equilibrium spin rate of such bodies is either the synchronous rotation on circular orbits or the *pseudo–synchronous rotation* on at least slightly eccentric orbits. As a consequence of the pseudo–synchronisation, the planets with nonzero orbital eccentricity are predicted to exhibit a rotation rate that is higher than the mean motion ($\dot{\theta} > n$), approximately described by the formula[12] (e.g., Dobrovolskis, 2007)

$$\frac{\dot{\theta}}{n} \approx 1 + 6e^2 \ . \tag{1.36}$$

However, due to the omission of the elastic and anelastic contributions to the

[11] Despite relatively good applicability to stars, the predictions of the constant time lag model are not always consistent with observation (e.g. Strassmeier et al., 2011). The tidal response of stars can be also affected by magnetic "rigidity" (e.g., Williams, 2004). For details and further discussion, see Makarov and Efroimsky (2013).

[12] A similar pseudo–synchronisation, characterised by $\dot{\theta}/n \approx 1 + 19/2\ e^2$ (Murray and Dermott, 1999), is also predicted by another class of tidal theories, not based on the Darwin–Kaula expansion. In this approach, attributed to MacDonald (1964) and dating back to Gerstenkorn (1955), the tidal lagging of the planet's reaction is described with respect to the two physical bulges, and not to the individual modes discussed earlier. The angle between the symmetry axis of the bulges and the line connecting the planet's centre with the perturber is then assumed to be constant: we are thus speaking about the *constant geometric/angular lag model*. However, the assumption of a constant geometric lag implies constant lagging in the true anomaly, a behaviour that cannot be reconciled with any rheological model (Ferraz-Mello, 2013). A corrected version of the constant angular lag model, introduced by Efroimsky and Williams (2009), corresponds to the constant time lag model.

tidal response, the constant time lag model is insufficient to represent the tidal effects in close–in moons or terrestrial planets (Makarov and Efroimsky, 2013).

Rheologically–motivated models An effort to reconcile the tidal parameters with the refined rheological models of planetary materials (Efroimsky and Lainey, 2007) can be seen in modern approaches, defining the Love number and the phase lag as the modulus and the phase of a complex number $\bar{k}_l(\omega_{lmpq})$. The kvalitet in such models is then expressible as

$$k_l \sin \varepsilon_{lmpq} = -\mathrm{Im}\{\bar{k}_l(\omega_{lmpq})\} \tag{1.37}$$

and the functional form of the *complex Love number* is defined in analogy with the Love number of an incompressible homogeneous elastic sphere as (Castillo-Rogez et al., 2011; Makarov and Efroimsky, 2013)

$$\bar{k}_l(\omega_{lmpq}) = \frac{3}{2(l-1)} \frac{1}{1+A_l} \ , \quad \text{where} \quad A_l = \frac{(2l^2+4l+3)\ \bar{\mu}(|\omega_{lmpq}|)}{lg\rho R}\, \mathrm{Sgn}\{\omega_{lmpq}\} \ . \tag{1.38}$$

In the above expression, g denotes the surface gravity, ρ is the average density, and $\bar{\mu}$ stands for the complex rigidity, or the inverse of the dynamic compliance $\bar{J}$, which will be introduced in Section 2.2. The rheologically–motivated tidal models, derived also in different forms by other authors (Ferraz-Mello, 2013; Correia et al., 2014; Ferraz-Mello, 2015; Frouard et al., 2016), successfully predict the tidal locking of close-in moons and planets on eccentric orbits into *spin-orbit resonances*. Furthermore, in contrast to the constant phase lag model, the correct prediction of the stable spin states in the rheologically–motivated models goes together with a continuous behaviour of the kvalitet around zero frequency. Finally, the complex Love number also enables a self–consistent calculation of the tidal dissipation. This topic will be treated in the next chapter.

Tides in the host star In the special cases of either a massive close-in planet or a highly dissipating primary, it is also necessary to consider the orbital evolution due to tidal deformation of the host star. The *lmpq* mode of the corresponding disturbing function is then

$$\mathcal{R}^{\mathrm{tide},*}_{lmpq} = k^*_l\ R^{2l+1}_*\ \tilde{\mathcal{B}}^*_{lm}\ \tilde{\mathcal{C}}^*_{lmpq} \sum_{p'=0}^{l} \sum_{q'=-\infty}^{\infty} \mathcal{C}^*_{lmp'q'} \cos[\tilde{\nu}^*_{lmpq} - \varepsilon^*_{lmpq} - m\tilde{\theta}^* - (\nu^*_{lmp'q'} - m\theta^*)] \tag{1.39}$$

with

$$\mathcal{B}^*_{lm} = \mathcal{G}m_1\ \frac{(l-m)!}{(l+m)!}\ \kappa_m \ ,$$

$$\mathcal{C}^*_{lmpq} = \frac{1}{a^{l+1}} \mathcal{F}_{lmp}(i)\ \mathcal{G}_{lpq}(e) \ ,$$

$$\nu^*_{lmpq} = (l-2p)\omega + (l-2p+q)M + m\Omega \ ,$$

where R_* is the star's radius. In the above expressions, we assumed that the host star's spin axis is stationary and perpendicular to the inertial reference plane. As a result, the inclination i in the expression for $\mathcal{C}^*_{lmpq}$ is referred to the equatorial plane of the host star.

The disturbing function due to the tidal deformation of the host star $\mathcal{R}^{\mathrm{tide},*}$ and the disturbing function due to the tidal deformation of the planet $\mathcal{R}^{\mathrm{tide,p}}$ are defined in different body–centred frames. Although we do not consider the contribution of the deformed star to the orbital evolution in this work, we would like to see how the tidal deformation of the planet affects the "asterocentric" Keplerian elements, instead of the planet orientation $\{\alpha, \beta, \gamma\}$. For this reason, let us finally look at the set of equations considering the difference in the reference frames.

Complete tidal equations The evolution equations for the semi–major axis, the eccentricity, and the inclination derived by Kaula (1964, p. 676) include the tidal contribution from the planet as well as from the satellite (here, the host star). While the first two equations are correct and they can be readily applied to the tidal evolution of the orbit, the third equation lacks the consideration of the non–inertiality of the satellite's equatorial plane, to which Kaula refers the relative inclination of the planet's orbit. Specifically, the equatorial plane and the orbital plane of the satellite are subject to precession and a proper derivation of the secular evolution equations should also account for appropriate averaging over the precession cycle. A straightforward approach to overcoming this difficulty was taken, e.g., by Chyba et al. (1989) in his analysis of the Neptune–Triton system. Chyba et al. (1989) derives the secular evolution equation for the inclination from the conservation of the z–component of the orbital angular momentum. As a result, he obtains a relation between the three quantities, a, e, and i, which enables him to derive a self–consistent expression for $\mathrm{d}i/\mathrm{d}t$ in terms of $\mathrm{d}a/\mathrm{d}t$ and $\mathrm{d}e/\mathrm{d}t$.

A different approach was taken by Boué and Efroimsky (2019), who chose to re–derive the equations of Kaula (1964) from scratch, with the help of classical theoretical mechanics. In their derivation, they strictly refer the position vectors and the Euler angles to the inertial frame. However, in order to make their results comparable to the work of Kaula (1964), they also transform their expressions to the body–centred elements and provide a complete set of Lagrange–type evolution equations[13] for either of the bodies. Since the study of Boué and Efroimsky (2019) aims to be as general as possible, the two bodies are also allowed to change the orientation of their spin axes: the obliquities with respect to the inertial frame are generally nonzero and the spin axes are precessing around the normal to the orbital plane. The respective body–centred elements are then defined in frames coprecessing with the planet or with the satellite. The reference directions are identified with descending nodes of the respective equatorial planes on an inertial

[13]The equations of Boué and Efroimsky (2019) differ from the Lagrange planetary equations (1.9) introduced earlier since they also include the effect of different reference frames.

plane (Boué and Efroimsky, 2019). For the star–planet system considered in this section of our work and for the angular variables defined with respect to the equatorial plane of the host star, we may write the evolution equations of Boué and Efroimsky (2019) as

$$\frac{\mathrm{d}a}{\mathrm{d}t} = \frac{2}{na}\frac{\partial \mathcal{R}^*}{\partial \sigma} + \frac{2}{na}\frac{\partial \mathcal{R}^\mathrm{p}}{\partial \sigma} \,, \tag{1.40a}$$

$$\frac{\mathrm{d}e}{\mathrm{d}t} = \frac{1-e^2}{na^2 e}\frac{\partial \mathcal{R}^*}{\partial \sigma} - \frac{\sqrt{1-e^2}}{na^2 e}\frac{\partial \mathcal{R}^*}{\partial \omega} + \frac{1-e^2}{na^2 e}\frac{\partial \mathcal{R}^\mathrm{p}}{\partial \sigma} - \frac{\sqrt{1-e^2}}{na^2 e}\frac{\partial \mathcal{R}^\mathrm{p}}{\partial \gamma} \,, \tag{1.40b}$$

$$\begin{aligned}\frac{\mathrm{d}i}{\mathrm{d}t} = {} & \frac{\mu}{C_* \dot{\theta}^* \sin i}\left(\frac{\partial \mathcal{R}^*}{\partial \omega} - \cos i \frac{\partial \mathcal{R}^*}{\partial \Omega}\right) - \frac{1}{na^2\sqrt{1-e^2}\sin i}\left(\frac{\partial \mathcal{R}^*}{\partial \Omega} - \cos i \frac{\partial \mathcal{R}^*}{\partial \omega}\right) - \\ & - \frac{\sin(\omega-\gamma)}{na^2\sqrt{1-e^2}}\frac{\partial \mathcal{R}^\mathrm{p}}{\partial \beta} - \frac{\cos(\omega-\gamma)}{na^2\sqrt{1-e^2}\sin\beta}\left(\frac{\partial \mathcal{R}^\mathrm{p}}{\partial \alpha} - \cos\beta \frac{\partial \mathcal{R}^\mathrm{p}}{\partial \gamma}\right) \,,\end{aligned} \tag{1.40c}$$

$$\begin{aligned}\frac{\mathrm{d}\Omega}{\mathrm{d}t} = {} & \frac{\mu \cos i}{C_* \dot{\theta}^* \sin i}\frac{\partial \mathcal{R}^*}{\partial i} + \frac{\mu \cos\delta}{C_* \dot{\theta}^* \sin\delta}\left(\sin\Omega \cot i \frac{\partial \mathcal{R}^*}{\partial \Omega} - \cos\Omega \frac{\partial \mathcal{R}^*}{\partial i} - \frac{\sin\Omega}{\sin i}\frac{\partial \mathcal{R}^*}{\partial \omega}\right) + \\ & + \frac{1}{na^2\sqrt{1-e^2}\sin i}\frac{\partial \mathcal{R}^*}{\partial i} + \frac{\cos(\gamma-\omega)}{na^2\sqrt{1-e^2}\sin i}\frac{\partial \mathcal{R}^\mathrm{p}}{\partial \beta} + \\ & + \frac{\sin(\omega-\gamma)}{na^2\sqrt{1-e^2}\sin i \sin\beta}\left(\cos\beta \frac{\partial \mathcal{R}^\mathrm{p}}{\partial \gamma} - \frac{\partial \mathcal{R}^\mathrm{p}}{\partial \alpha}\right) \,,\end{aligned} \tag{1.40d}$$

$$\begin{aligned}\frac{\mathrm{d}\omega}{\mathrm{d}t} = {} & -\frac{\mu}{C_* \dot{\theta}^* \sin i}\frac{\partial \mathcal{R}^*}{\partial i} + \frac{\sqrt{1-e^2}}{na^2 e}\frac{\partial \mathcal{R}^*}{\partial e} - \frac{\cos i}{na^2\sqrt{1-e^2}\sin i}\frac{\partial \mathcal{R}^*}{\partial i} + \frac{\sqrt{1-e^2}}{na^2 e}\frac{\partial \mathcal{R}^\mathrm{p}}{\partial e} - \\ & - \frac{\cos i \cos(\omega-\gamma)}{na^2\sqrt{1-e^2}\sin i}\frac{\partial \mathcal{R}^\mathrm{p}}{\partial \beta} - \frac{\cos i \sin(\omega-\gamma)}{na^2\sqrt{1-e^2}\sin i \sin\beta}\left(\cos\beta \frac{\partial \mathcal{R}^\mathrm{p}}{\partial \gamma} - \frac{\partial \mathcal{R}^\mathrm{p}}{\partial \alpha}\right) \,,\end{aligned} \tag{1.40e}$$

$$\frac{\mathrm{d}\sigma}{\mathrm{d}t} = -\frac{2}{na}\frac{\partial \mathcal{R}^*}{\partial a} - \frac{1-e^2}{na^2 e}\frac{\partial \mathcal{R}^*}{\partial e} - \frac{2}{na}\frac{\partial \mathcal{R}^\mathrm{p}}{\partial a} - \frac{1-e^2}{na^2 e}\frac{\partial \mathcal{R}^\mathrm{p}}{\partial e} \,, \tag{1.40f}$$

where μ is the reduced mass, δ is the obliquity of the star with respect to the reference plane in the inertial frame, C_* is the star's principal moment of inertia with respect to the spin axis, and the symbols $\mathcal{R}^*$, $\mathcal{R}^\mathrm{p}$ were used in place of $\mathcal{R}^{\mathrm{tide},*}$, $\mathcal{R}^{\mathrm{tide},\mathrm{p}}$, respectively. The set of equations (1.40) is expressed in the frame coprecessing with the primary's equator. Therefore, out of the angles describing the orientation of the host star, we only need to provide the evolution equation for δ (Boué and Efroimsky, 2019):

$$\frac{\mathrm{d}\delta}{\mathrm{d}t} = -\frac{\mu}{C_* \dot{\theta}}\left(\cos\Omega \cot i \frac{\partial \mathcal{R}^*}{\partial \Omega} + \sin\Omega \frac{\partial \mathcal{R}^*}{\partial i} - \frac{\cos\Omega}{\sin i}\frac{\partial \mathcal{R}^*}{\partial \omega}\right) \,. \tag{1.41}$$

Finally, the spin rate evolution of the host star is governed by

$$\frac{\mathrm{d}^2\theta^*}{\mathrm{d}t^2} = -\frac{\mu}{C_*}\frac{\partial \mathcal{R}^*}{\partial \Omega} \,. \tag{1.42}$$

An equivalent set of equations can also be written for the orbital elements of the

star referred to the frame coprecessing with the planet's equator. In that case, the equations for the longitude of the ascending node (1.40d), the inclination (1.40c), and the argument of pericentre (1.40e) would play the role of the equations for the evolution of the planet's orientation $\{\alpha, \beta, \gamma\}$ relative to the orbital plane. Equation (1.42) would describe the spin rate evolution of the planet, which will be discussed later.

As can be seen from the set of equations (1.40), the evolution of the asterocentric orbital elements depends on the contribution of both the deformed host star and the deformed planet. The relative magnitude of the two contributions can be deduced from a comparison of the two disturbing functions, $\mathcal{R}^{\mathrm{tide},*}$ and $\mathcal{R}^{\mathrm{tide,p}}$. The main difference between the tidal deformation of the two bodies lies in different masses, radii, and susceptibilities to tidal dissipation, quantified by the Love number and the phase lag (or the quality factor). Since the host star in our study is considerably more massive than the planet and its quality factor is expected to be higher, relative to the planet (see, e.g., Goldreich and Soter, 1966), we neglect the terms in (1.40) containing $\mathcal{R}^{\mathrm{tide},*}$. Nevertheless, the contribution of the host star is important in the case of massive exoplanets orbiting close to swiftly rotating and/or highly dissipative stars (e.g., Bolmont and Mathis, 2016; Veras et al., 2019).

With this last paragraph, we conclude the overview of the tidal theory in the Darwin–Kaula formalism and we are ready to go on to the practical aspects of the calculation.

1.3.3 Eccentricity and inclination functions

As we learned in the previous two subsections, Kaula (1961, 1962, 1964) expands the tidal potential and the disturbing function into a series, whose coefficients depend on the orbital eccentricity via the eccentricity functions $\mathcal{G}_{lpq}(e)$, $\mathcal{H}_{lpq}(e)$ and on the inclination (or obliquity) through the inclination functions $\mathcal{F}_{lmp}(i)$. The eccentricity functions, or eccentricity polynomials, arise due to the substitution of the non–linearly changing quantities (r, v) by the semi–major axis a and the linearly changing mean anomaly M. The inclination functions, on the other hand, contain all algebraic factors arising during the derivation of the disturbing functions, multiplied by the sines and cosines of inclination.

Both the eccentricity and the inclination functions can be calculated directly from the definition provided in Kaula (1961) or Allan (1965) (as will be introduced below). Kaula (1964) gives a table of $\mathcal{F}_{2mp}(i)$ and $\mathcal{G}_{2pq}(e)$, expressed up to the order $|q| = 2$ in eccentricity, and refers the reader to the tables of Cayley (1861), who calculated the coefficients of eccentricity functions up to the order $|q| = 7$. Since the precise knowledge of the disturbing function is crucial for the satellite theory, even higher–order expansions of the eccentricity functions were tabulated in the following years, such as the $|q| = 12$ expansion of Izsak et al. (1964) and Cherniack (1972). Several authors also explored the calculation of eccentricity functions for extremely elliptical orbits (Szeto and Lambeck, 1982; Wnuk, 1997; Celletti et al., 2017). As the need for the exact prediction of satellite orbits grew,

the original analytical formulae derived by the founders of the satellite theory made way for more practical recurrence relations, which also proved ideal for the calculation by a digital computer (e.g., Izsak et al., 1964; Cherniack, 1972; Giacaglia, 1977; Vakhidov, 2001).

Until we proceed to the introduction of one such recurrence formula, let us first mention the connection of the eccentricity functions to a more general function used in celestial mechanics. The eccentricity functions of Kaula are a special case of Hansen coefficients $X_j^{n,k}(e)$, defined as (e.g., Tisserand, 1889)

$$\left(\frac{r}{a}\right)^n \exp\{\mathrm{i}kv\} = \sum_j X_j^{n,k}(e) \exp\{\mathrm{i}jM\} \,, \tag{1.43}$$

and it holds that (Kaula, 1961, 1962)

$$\mathcal{G}_{lpq}(e) = X_{l-2p+q}^{-l-1,l-2p}(e) \tag{1.44}$$

and

$$\mathcal{H}_{lpq}(e) = X_{l-2p+q}^{l,l-2p}(e) \,. \tag{1.45}$$

An advantageous property of the Hansen coefficients is the possibility to expand them into a power series in eccentricity (Cherniack, 1972)[14],

$$X_j^{n,k}(e) = \sum_{\substack{\rho-\sigma=j-k \\ \rho,\sigma\geq 0}} X_{\rho,\sigma}^{n,k}\, e^{\rho+\sigma} \,, \tag{1.46}$$

where $X_{\rho,\sigma}^{n,k}$ are known as *Newcomb operators* (Newcomb, 1895). Newcomb operators are algebraic factors and as such, they can be calculated and tabulated in advance. The eccentricity functions for arbitrary value of eccentricity are then obtained from equation (1.46).

To obtain Hansen coefficients and, consequently, the eccentricity functions, we calculate the Newcomb operators using the Von Zeipel–Andoyer method (VZA; Andoyer, 1903; Von Zeipel, 1912), as described by Izsak et al. (1964) and Cherniack (1972). The calculation makes use of recurrent relations between the integer polynomials $J_{\rho,\sigma}^{n,k}$ and, as a result, it can be performed in integer arithmetic. However, it should be noted that the J–polynomials may rise to extreme values and the computer–assisted calculation of eccentricity functions for high indices ($|q| \geq 8$) may be corrupted by integer overflow. It is thus advisable to keep this difficulty in mind when initialising of the computation.

The integer polynomials $J_{\rho,\sigma}^{n,k}$ can be calculated as (Izsak et al., 1964; Cherniack, 1972)

$$J_{0,0}^{n,k} = 1 \,, \tag{1.47a}$$

[14]Cherniack (1972), in his equation (7), gives the limits of the summation as $(\rho-\sigma) = (j+k)$. However, it follows from a comparison with Izsak et al. (1964) that the correct condition should be $(\rho-\sigma) = (j-k)$.

$$J_{1,0}^{n,k} = 2k - n \;, \tag{1.47b}$$

$$J_{\rho,0}^{n,k} = (2k-n)J_{\rho-1,0}^{n,k+1} + (\rho-1)(k-n)J_{\rho-2,0}^{n,k+2} \;, \tag{1.47c}$$

$$J_{\rho,\sigma}^{n,k} = -(2k+n)J_{\rho,\sigma-1}^{n,k} - (\sigma-1)(k+n)J_{\rho,\sigma-2}^{n,k-2} - \rho(\rho-5\sigma+4+4k+n)J_{\rho-1,\sigma-1}^{n,k} +$$

$$+\rho(\rho-\sigma+k)\sum_{\tau\geq 2}^{\min(\rho,\sigma)} C_{\rho\sigma\tau}J_{\rho-\tau,\sigma-\tau}^{n,k} \;, \tag{1.47d}$$

with

$$C_{\rho\sigma\tau} = (\rho-1)(\rho-2)\ldots(\rho-\tau+1)(\sigma-1)(\sigma-2)\ldots(\sigma-\tau+1)C_\tau$$

and

$$C_\tau = (-1)^\tau \binom{3/2}{\tau} 2^{2\tau-1} \;.$$

The real–valued Newcomb operators are related to the integer–valued J–polynomials via

$$X_{\rho,\sigma}^{n,k} = \frac{J_{\rho,\sigma}^{n,k}}{2^{\rho+\sigma}\rho!\sigma} \;, \tag{1.48}$$

which holds for $\rho \geq \sigma$; the remaining operators, with $\rho < \sigma$, can be calculated from the symmetry

$$X_{\rho,\sigma}^{n,k} = X_{\sigma,\rho}^{n,-k} \;. \tag{1.49}$$

Going back to the Lagrange planetary equations (1.10), we see that the evolution equations for the longitude of periastron (ϖ) and the mean longitude at epoch (ϵ) also require the knowledge of derivatives of the eccentricity functions. Fortunately, the derivatives of Hansen coefficients can be easily related to the calculated values through (Giacaglia, 1977)

$$\frac{\mathrm{d}X_j^{n,k}}{\mathrm{d}e} = \frac{2k-n}{2}X_j^{n-1,k+1} - \frac{2k+n}{2}X_j^{n-1,k-1} - \frac{ke}{4(1-e^2)}\left(X_j^{n,k+2} - X_j^{n,k-2}\right) \;. \tag{1.50}$$

Once we have discussed the calculation of eccentricity functions, it is time to proceed to the inclination functions. The inclination functions of Kaula were originally derived using a nontrivial three–sum formula (Kaula, 1961)

$$\mathcal{F}_{lmp}(i) = \sum_{t=0}^{t_2} \frac{1}{2^{2l-2t}} \frac{(2l-2t)!}{t!(l-t)!(l-m-2t)!} \sin^{l-m-2t}(i) \sum_{s=0}^{m} \binom{m}{s} \cos^s(i) \times$$

$$\times \sum_{c=c_1}^{c_2} \binom{l-m-2t+s}{c} \binom{m-s}{p-t-c} (-1)^{c-k} , \tag{1.51}$$

where the upper limit for the first summation is $t_2 = \min(p, k)$ with k being the integer part of $(l-m)/2$, the lower limit for the last summation is $c_1 = \max(0, p-t-m+s)$, and the upper limit for the last summation is $c_2 = \min(l-m-2t+s, p-t)$. The limits of the summations were chosen in order to sum only over the nonzero terms (i.e., terms with nonzero binomial coefficients).

An alternative definition of the inclination functions, originating in the angular momentum theory in quantum mechanics, was presented by Allan (1965). Owing to the sole summation used in their formulation, Allan's inclination functions are better suited for numerical computation than the functions of Kaula and they are widely used in the literature (e.g., Gooding, 1971; Murray and Dermott, 1999). The functions were originally defined as complex and, in a newer convention, they require the introduction of the imaginary unit to the corresponding disturbing function (as is done in Murray and Dermott, 1999). Nevertheless, Allan (1965) also gives their relation to the classical Kaula's functions, which are real. Following the notation of Wnuk (1988), Allan's inclination functions, redefined to match the corresponding Kaula's functions, are

$$\mathcal{F}_{lmp}(i) = (-1)^{\delta} \frac{(l+m)!}{2^l\, p!\, (l-p)!} \sum_{j=j_1}^{j_2} (-1)^j \binom{2l-2p}{j} \binom{2p}{l-m-j} c^{2l-\alpha} s^{\alpha} \tag{1.52}$$

where δ is the integer part of $(l-m+1)/2$, the limits of the summation are $j_1 = \max(0, l-m-2p)$, $j_2 = \min(l-m, 2l-2p)$, and the goniometric functions are shortened as $c = \cos(i/2)$ and $s = \sin(i/2)$ with $\alpha = (m-l+2p+2j)$. Allan also derived a recurrence formula for the inclination functions, which was first published by Gooding (1971). For the redefined inclination functions (1.52), the recurrence formula reads as (Wnuk, 1988)

$$\begin{aligned} 2p\mathcal{F}_{lmp} = {} & s^2(l+m)(l+m-1)\mathcal{F}_{l-1,m-1,p-1} + \\ & + \; 2(-1)^{l-m} c\, s\, (l+m)\mathcal{F}_{l-1,m,p-1} - c^2\mathcal{F}_{l-1,m+1,p-1} \end{aligned} \tag{1.53}$$

for $p \neq 0$ and

$$\begin{aligned} 2(l-p)\mathcal{F}_{lmp} = {} & c^2(l+m)(l+m-1)\mathcal{F}_{l-1,m-1,p} - \\ & - \; 2(-1)^{l-m} c\, s\, (l+m)\mathcal{F}_{l-1,m,p} - s^2\mathcal{F}_{l-1,m+1,p} \end{aligned} \tag{1.54}$$

for $p \neq l$. The precision of the recurrent computation can be further increased by summing the two expressions above (Wnuk, 1988). To obtain the analytical formula for the derivations of inclination functions, which are required by the

evolution equations for ϖ and ϵ, we need to differentiate the expression (1.52) with respect to inclination. This results in the relation

$$\frac{\mathrm{d}\mathcal{F}_{lmp}}{\mathrm{d}i} = (-1)^{\delta}\,\frac{(l+m)!}{2^{l+1}\,p!\,(l-p)!}\sum_{j=j_1}^{j_2}(-1)^j\binom{2l-2p}{j}\binom{2p}{l-m-j}c^{2l-\alpha}s^{\alpha}\left[\alpha\frac{c}{s}-(2l-\alpha)\frac{s}{c}\right]\,. \tag{1.55}$$

Alternatively, the recurrence formula for the derivatives can be obtained by differentiating equations (1.53) and (1.54).

1.4 Nonsingular elements

Coordinate singularities The two sets of Lagrange planetary equations, (1.9) and (1.10), contain mathematical singularities in the limit cases of $e \to 0$, $i \to 0$ or $i \to \pi$. As can be shown by expressing the disturbing function $\mathcal{R}$ in the form of the Darwin–Kaula expansion, most of these discontinuities are only apparent. Focusing now on the second set of Lagrange planetary equations, (1.10), the only two discontinuities which do not vanish upon the explicit expression of the disturbing function, are present in equations (1.10d) and (1.10e), that is

$$\frac{\mathrm{d}\Omega}{\mathrm{d}t} = \frac{1}{na^2\sqrt{1-e^2}\sin i}\frac{\partial\mathcal{R}}{\partial i}$$

and

$$\frac{\mathrm{d}\varpi}{\mathrm{d}t} = \frac{\sqrt{1-e^2}}{na^2e}\frac{\partial\mathcal{R}}{\partial e} + \frac{\tan\frac{i}{2}}{na^2\sqrt{1-e^2}}\frac{\partial\mathcal{R}}{\partial i}\,.$$

Naturally, this kind of singularities is introduced by the choice of the coordinate system. The longitude of the ascending node Ω is defined only when the orbital plane intersects the inertial reference plane. When the two planes coincide, as is the case for $i \to 0$ or $i \to \pi$, the introduction of Ω lacks meaning. Similarly, the longitude of the periapsis ϖ can be found only on an orbit with clearly defined periapses. On circular orbit ($e \to 0$), where each point is in the same distance from the host star, the introduction of ϖ is ambiguous.

New set of elements The coordinate singularities in the two aforementioned equations can be overcome by introducing a new set of *nonsingular elements*, which would eliminate the vanishing terms in the denominator. We adopt the nonsingular elements defined by Nacozy and Dallas (1977) as

$$\begin{aligned}
\xi &= e\sin\varpi\,,\\
\eta &= e\cos\varpi\,,\\
\zeta &= \sin\frac{i}{2}\sin\Omega\,,\\
\nu &= \sin\frac{i}{2}\cos\Omega\,,
\end{aligned} \tag{1.56}$$

with the remaining two elements, a and ε, being the same as in the previous sections. Then, the evolution equations for the new nonsingular elements can be written either in the mixed form, using the chain rule,

$$\begin{aligned}
\frac{\mathrm{d}\xi}{\mathrm{d}t} &= \frac{\mathrm{d}e}{\mathrm{d}t}\sin\varpi + \eta\frac{\mathrm{d}\varpi}{\mathrm{d}t}\,, \\
\frac{\mathrm{d}\eta}{\mathrm{d}t} &= \frac{\mathrm{d}e}{\mathrm{d}t}\cos\varpi - \xi\frac{\mathrm{d}\varpi}{\mathrm{d}t}\,, \\
\frac{\mathrm{d}\zeta}{\mathrm{d}t} &= \frac{1}{2}\frac{\mathrm{d}i}{\mathrm{d}t}\cos\frac{i}{2}\sin\Omega + \nu\frac{\mathrm{d}\Omega}{\mathrm{d}t}\,, \\
\frac{\mathrm{d}\nu}{\mathrm{d}t} &= \frac{1}{2}\frac{\mathrm{d}i}{\mathrm{d}t}\cos\frac{i}{2}\cos\Omega - \zeta\frac{\mathrm{d}\Omega}{\mathrm{d}t}\,,
\end{aligned} \tag{1.57}$$

or in a self–consistent form, which, however, requires the expression of the disturbing function in the nonsingular elements. Although the desired disturbing function $\mathcal{R}(a,\xi,\eta,\zeta,\nu,\varepsilon)$ can be analytically derived, as was done by Nacozy and Dallas (1977) or Giacaglia (1977) in the case of geopotential, we retain the mixed form of the evolution equations (1.57). This decision enables us to calculate the eccentricity functions $\mathcal{G}_{lpq}(e)$ and $\mathcal{H}_{lpq}(e)$ using the existing recurrence relations.

Nonsingular evolution equations For the sake of clarity, we present here the complete set of evolution equations used in our calculations for Chapters 4 and 5. The partial derivatives of the disturbing functions due to due to the third–body perturbation are listed in Appendix C.2.

$$\frac{\mathrm{d}a}{\mathrm{d}t} = \frac{2}{na}\frac{\partial\mathcal{R}}{\partial\epsilon} \tag{1.58a}$$

$$\frac{\mathrm{d}\xi}{\mathrm{d}t} = \frac{\cos\varpi}{na^2}\left(\sqrt{1-e^2}\frac{\partial\mathcal{R}}{\partial e} + \frac{e}{\sqrt{1-e^2}}\tan\frac{i}{2}\frac{\partial\mathcal{R}}{\partial i}\right) - \frac{\sin\varpi}{na^2}\frac{\sqrt{1-e^2}}{e}\left[(1-\sqrt{1-e^2})\frac{\partial\mathcal{R}}{\partial\epsilon} + \frac{\partial\mathcal{R}}{\partial\varpi}\right] \tag{1.58b}$$

$$\frac{\mathrm{d}\eta}{\mathrm{d}t} = -\frac{\sin\varpi}{na^2}\left(\sqrt{1-e^2}\frac{\partial\mathcal{R}}{\partial e} + \frac{e}{\sqrt{1-e^2}}\tan\frac{i}{2}\frac{\partial\mathcal{R}}{\partial i}\right) - \frac{\cos\varpi}{na^2}\frac{\sqrt{1-e^2}}{e}\left[(1-\sqrt{1-e^2})\frac{\partial\mathcal{R}}{\partial\epsilon} + \frac{\partial\mathcal{R}}{\partial\varpi}\right] \tag{1.58c}$$

$$\frac{\mathrm{d}\zeta}{\mathrm{d}t} = \frac{\cos\Omega}{2na^2\sqrt{1-e^2}\cos\frac{i}{2}}\frac{\partial\mathcal{R}}{\partial i} - \frac{1}{2}\frac{\sin\Omega}{na^2\sqrt{1-e^2}}\left[\sin\frac{i}{2}\left(\frac{\partial\mathcal{R}}{\partial\epsilon} + \frac{\partial\mathcal{R}}{\partial\varpi}\right) + \frac{1}{2\sin\frac{i}{2}}\frac{\partial\mathcal{R}}{\partial\Omega}\right] \tag{1.58d}$$

$$\frac{\mathrm{d}\nu}{\mathrm{d}t} = -\frac{\sin\Omega}{2na^2\sqrt{1-e^2}\cos\frac{i}{2}}\frac{\partial\mathcal{R}}{\partial i} - \frac{1}{2}\frac{\cos\Omega}{na^2\sqrt{1-e^2}}\left[\sin\frac{i}{2}\left(\frac{\partial\mathcal{R}}{\partial\epsilon} + \frac{\partial\mathcal{R}}{\partial\varpi}\right) + \frac{1}{2\sin\frac{i}{2}}\frac{\partial\mathcal{R}}{\partial\Omega}\right] \tag{1.58e}$$

$$\frac{\mathrm{d}\epsilon}{\mathrm{d}t} = -\frac{2}{na}\frac{\partial\mathcal{R}}{\partial a} - \frac{\sqrt{1-e^2}}{na^2e}(1-\sqrt{1-e^2})\frac{\partial\mathcal{R}}{\partial e} + \frac{\tan\frac{i}{2}}{na^2\sqrt{1-e^2}}\frac{\partial\mathcal{R}}{\partial i}\,. \tag{1.58f}$$

A similar set of nonsingular equations can also be derived for the tidally–induced

orbital evolution. In that case, we transform the Lagrange–type equations (1.40) to the elements $\{a, e, i, \varpi, \Omega, \epsilon\}$ and insert them to the formulas for nonsingular evolution equations (1.57), with the partial derivatives of the disturbing function given by Appendix C.1.

Although the set of equations (1.58) is said to be nonsingular, it should be noted that it still contains apparent singularities. To understand their behaviour (or vanishing) in the limit cases of $e \to 0$ and $\sin i \to 0$, let us briefly discuss the leading terms in the Darwin–Kaula expansion.

Vanishing of apparent singularities The remaining apparent singularities in the above set of equations occur in one of the following forms:

$$\begin{gathered} \frac{\sqrt{1-e^2}}{e}\left[\left(1-\sqrt{1-e^2}\right)\frac{\partial \mathcal{R}}{\partial \epsilon}+\frac{\partial \mathcal{R}}{\partial \varpi}\right], \\ \frac{\sqrt{1-e^2}}{e}\left(1-\sqrt{1-e^2}\right)\frac{\partial \mathcal{R}}{\partial e}, \\ \frac{1}{\sin\frac{i}{2}}\frac{\partial \mathcal{R}}{\partial \Omega}. \end{gathered} \tag{1.59}$$

The critical prefactor

$$\frac{\sqrt{1-e^2}}{e}\left(1-\sqrt{1-e^2}\right)$$

in the terms containing partial derivatives with respect to ϵ and e becomes $e/2$ in the limit of $e \to 0$ and does not need to be confronted with the leading terms (corresponding to $q = 0$ for small eccentricities) in the expansion. The prefactor of $\partial\mathcal{R}/\partial\varpi$ is more delicate. However, remembering that (Subsection 1.3.3 and Appendix C)

$$\left(\frac{\partial \mathcal{R}}{\partial \varpi}\right)_{lmpq} \propto q\, e^{|q|}\, \sin^{|m-l+2p|}\frac{i}{2}, \tag{1.60}$$

we may see that the leading term ($q = 0$) is always zero and the other terms always depend on e with positive exponents. A similar argument holds in the last case, that becomes problematic at $i \to 0$. Since

$$\left(\frac{\partial \mathcal{R}}{\partial \Omega}\right)_{lmpq} \propto (m-l+2p)\, e^{|q|}\, \sin^{|m-l+2p|}\frac{i}{2}, \tag{1.61}$$

the prefactor of the partial derivative with respect to Ω in (1.59) only results in a mathematical singularity in the case of $|m - l + 2p| = 0$. The corresponding term is, however, zero.

1.5 Spin rate evolution

The secular evolution of the orbital elements is naturally interconnected with the evolution of the planet's orientation and of the spin rate. Strictly speaking, the

changes to the planet's orientation should be modelled by solving the Euler (or Euler–Liouville) rotation equations (e.g., Munk and MacDonald, 1960), with the individual components of the torque derived from the tidal disturbing function $\mathcal{R}^{\rm tide,p}$ and from the disturbing function due to the planet's permanent deformation (e.g., its rotational flattening).

Cassini states In the absence of tidal dissipation, the spin axis of the planet typically tends to one of the four (or less) equilibrium solutions known as the *Cassini states* (e.g., Colombo, 1966; Peale, 1969; Ward, 1975; Fabrycky et al., 2007; Correia, 2015). Cassini states are resonances between the precession frequency of the planet's equatorial plane and that of the orbital plane, characterised by nonzero obliquity of the planet's spin axis. Derived under the assumption of uniform orbit precession and constant inclination, the permitted obliquities β of the equilibrium states are prescribed implicitly by (Fabrycky et al., 2007)

$$0 = \dot{\Omega} \sin\left(\beta - i\right) + \dot{\alpha} \cos\beta \sin\beta \; . \tag{1.62}$$

Depending on the relative magnitude of the two precession frequencies, equation (1.62) has either two or four roots.

Conventionally, the Cassini states are numbered as follows (Winn and Holman, 2005): State 1 has a vanishingly small obliquity ($\beta \ll 1^\circ$) and the normals to the two precessing planes lie on the same side of the axis of precession. State 2 is characterised by a greater obliquity (such as that of the Moon, where $\beta = 6.5^\circ$) and the two normals lie on different sides of the axis of precession. State 3 allows stable retrograde rotation with obliquity close to 180° (as may be the case for Venus, see Correia and Laskar, 2003). Finally, the unstable state 4 is similar to state 1 with potentially extreme obliquity (up to 90°).

If the planet is also subject to tidal dissipation (e.g., Ward, 1975; Fabrycky et al., 2007), or if it is radially stratified (Boué, 2020), the positions of the equilibrium states may differ or there may be multiple stationary solutions to the corresponding equations of motion. While the locking into such generalised Cassini state may serve as an additional source of tidal dissipation in icy moons or close–in exoplanets (Chen et al., 2014; Winn and Holman, 2005), the high–obliquity (and highly dissipative) state 2 might not be stable in the long term (Fabrycky et al., 2007). Therefore, the most probable obliquities of strongly tidally–loaded exoplanets are close to zero[15].

Tidal locking The secular tidal evolution of the planet's spin rate is governed by the equation (Dobrovolskis, 2007; Efroimsky and Williams, 2009)

$$C \frac{\mathrm{d}^2\theta}{\mathrm{d}t^2} = -m_* \frac{\partial \mathcal{R}^{\rm p}}{\partial \alpha} = \mathcal{T} \; , \tag{1.63}$$

[15]In this work, we will always set $\beta = 0^\circ$.

where

$$\mathcal{T} = \frac{\mathcal{G} m_*^2}{a} \sum_{lmpq} \left(\frac{R}{a}\right)^{2l+1} \frac{(l-m)!}{(l+m)!}\, m\, \kappa_m \left[\mathcal{G}_{lpq}(e)\right]^2 \left[\mathcal{F}_{lmp}(\beta)\right]^2 k_l \sin \varepsilon_{lmpq} \tag{1.64}$$

is the secular tidal torque, C is the principal moment of inertia of the planet with respect to the spin axis, and symbol $\mathcal{R}^{\mathrm{p}}$ is used in place of $\mathcal{R}^{\mathrm{tide,p}}$. The sign of the tidal torque determines whether the planet's spin rate accelerates or decelerates. The magnitude of the tidal torque affects the steepness of the spin rate evolution. In response to the tidal loading, an initially quickly rotating planet decelerates until it reaches an equilibrium state, characterised by the vanishing of the secular tidal torque.

As we can see in equation (1.64), the secular tidal torque depends on the shape and the orientation of the star's orbit with respect to the planet's equatorial plane, on the stellar mass, and on the rheological parameters of the planet (along with its size). Specifically, the dependence of the tidal torque on the loading frequencies is given by the kvalitet $k_l \sin \varepsilon_{lmpq}$. Section 1.3.2 introduced three distinct assumptions on the frequency dependence of the kvalitet: constant phase lag (CPL), constant time lag (CTL), and rheologically–motivated models (RHEO). Recall that the three types of models predict different equilibrium spin rates of planets on non–circular orbits. The CTL model results in pseudo–synchronous rotation, while both the CPL and the RHEO models indicate that a tidally–loaded planet on eccentric orbit should end up in a spin-orbit resonance. For circular orbits (and low obliquities), the only stable spin state in all three types of models is the synchronous rotation.

The role of kvalitet The effect of the orbital eccentricity, the planet's obliquity, and the assumed frequency (in)dependence on the secular tidal torque is depicted in Figure 1.3. The x–axis of the individual plots represents the ratio between the planet's spin rate and its mean motion. We will call this quantity a *spin–orbit ratio*. Note that for planets with nonzero obliquity or orbital eccentricity, the spin–orbit ratio translates to a number of loading frequencies, whose contributions are captured by the Darwin–Kaula expansion. The RHEO model in our illustrations is represented by a differentiated rocky planet, whose mantle is governed by the Andrade rheology. Additional properties of the model planet are given in Table 3.1 of Chapter 3 (with $\eta_{\mathrm{m}} = 10^{21}\,\mathrm{Pa\,s}$ and $\mu_{\mathrm{m}} = 200\,\mathrm{GPa}$); here, we do not reprint them, since the planet was chosen only for the sake of illustration. The constant Love numbers of the CPL and the CTL models correspond to the calculated complex Love number of the RHEO model for the maximum and the minimum loading frequencies, respectively: As the CTL model, from its definition, describes the low–frequency, fluid–like behaviour of the planet, its degree–2 Love number was identified with the Love number of RHEO model at zero frequency ($k_{\mathrm{c}} = 1.3$). On the other hand, since the CPL model is motivated by the response of the Earth at seismic frequencies, its degree–2 Love number was identified with the

high–frequency value for the RHEO model, which is $k_c = 0.25$. The constant quality factor $Q \approx 100$ of the CPL model approximately corresponds to the typical phase lags of the RHEO model at the orbital frequency, while the constant time lag $\Delta t = 100\,\mathrm{s}$ of the CTL model was chosen arbitrarily for the sake of illustration.

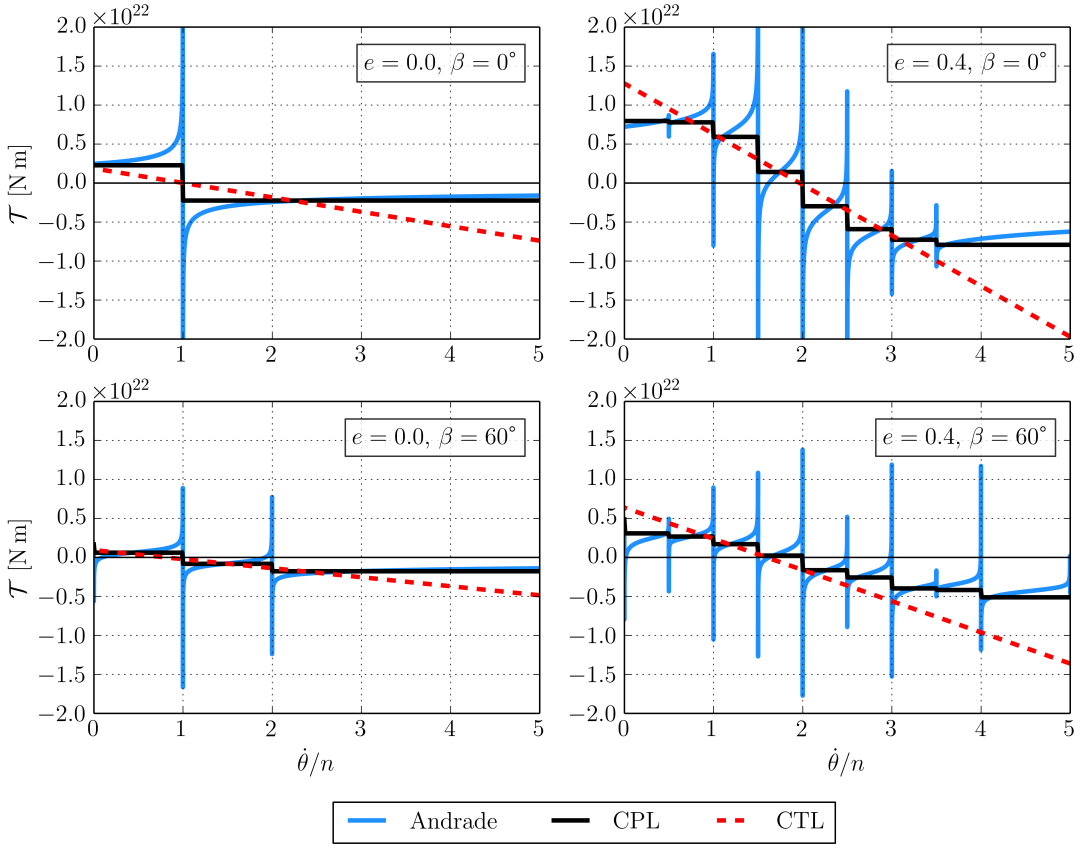

Figure 1.3: Secular tidal torque $\mathcal{T}$ (equation (1.64)) as a function of the spin rate $\dot{\theta}/n$. Individual panels show the effect of the orbital eccentricity e and the planet's obliquity β; different colours indicate three distinct choices of the kvalitet: constant time lag model (red, $k_c = 1.3$, $\Delta t = 100\,\mathrm{s}$), constant phase lag model (black, $k_c = 0.25$, $Q \approx 100$), and a rheologically–motivated model (blue, Andrade rheology, model planet from Chapter 3 with mantle viscosity $\eta_m = 10^{21}\,\mathrm{Pa\,s}$). Motivation for different choices of the Love number is explained in the text.

Several features in Figure 1.3 deserve a special mention: 1) The three considered assumptions for the kvalitet result in a different number of stable spin states. While the CTL and the CPL models predict a single intersection of the tidal torque with zero and, therefore, a single permissible equilibrium spin rate of the planet, the RHEO model shows multiple zero crossings. In other words, it permits more than one stable spin state for given orbital parameters, typically associated with spin–orbit resonances[16]. 2) The three models predict different

[16] A spin state in Figure 1.3 is stable, if the secular tidal torque crosses zero with a negative slope. Then, a "quickly–rotating" planet experiences negative secular torque and is dragged towards the stable point, while a "slowly–rotating" planet experiences positive torque and is being accelerated until it reaches the stable point.

functional dependence of the tidal torque on the spin–orbit ratio. The CTL model is represented by a line intersecting zero at the position of the corresponding pseudo–synchronous spin–orbit ratio. The CPL, on the other hand, exhibits a "staircase–like" behaviour, with steps at the positions of spin–orbit resonances. Finally, the RHEO model shows characteristic "kink-shaped" features around the stable spin states. The height of the peaks around each equilibrium spin state affects its stability against random perturbations. 3) Increase in the orbital eccentricity leads to an increase in the number of steps in the CPL "staircase" and in the multiplication of stable spin states in the RHEO model. For the CTL model, it shifts the position of the stable pseudo–synchronous rotation to higher spin–orbit ratios. 4) Increase in the planet's obliquity also results in the increased number of CPL steps and the increased number of stable spin states in the RHEO model, although with lower amplitude than in the case of nonzero eccentricity. Interestingly, in contrast to the effect of nonzero eccentricity, the increase in obliquity shifts the position of the stable pseudo–synchronous rotation in the CTL model to lower spin-orbit ratios.

1.6 Concluding remarks

The principal topic of Chapter 1 was the orbital evolution of a planet subjected either to the tidal loading or to the orbit perturbation by another body in the system. We have introduced two sets of orbital elements, glanced at the basics of the perturbation theory and at the Lagrange planetary equations, and given an overview of the Darwin–Kaula expansion. We have also looked at the practical aspects of the computation, discussing the recurrent relations for the eccentricity and inclination functions and introducing the nonsingular elements. Finally, the last section of the chapter illustrated the role of different parameterisations of the planet's tidal response in the calculation of the equilibrium spin rate.

In the context of our work, the shape and orientation of the orbit with respect to the planet's equatorial plane determine the amplitude and frequency of the tidal loading. In a broader sense, the planet's distance from the host star, along with other orbital elements, affects its surface conditions and the long–term evolution of its climate, thermal state, and potential habitability. Since the frequency of the tidal forcing (and, potentially, of a climate forcing) is also strongly influenced by the planet's spin rate, we will return to the discussion of the tidal torque and pay special attention to the stable spin states again in Chapter 3. However, until we do so, let us first focus on another part of the tidal picture: on the interior structure, thermal evolution, and rheological properties of rocky exoplanets.

2. Interior structure and dynamics

The second chapter of our work is dedicated to the other side of planetary dynamics. While in the first chapter, we gave an overview of the equations governing the long–term evolution of orbital elements, here we focus on the "inner life" of terrestrial bodies. To facilitate the transition to the new topic, we begin with an introductory section summarising current knowledge (or possible sources of knowledge) about the rocky exoplanets and their interior structure. Then, we step into the central part of this chapter, which is the discussion of rheological models and deformation mechanisms acting in planetary materials. Finally, in the last two sections, we contemplate the thermal evolution of the planet, i.e., the main heating and cooling mechanisms determining the interior temperature profile.

2.1 Interior structure of terrestrial exoplanets

The inner—or terrestrial—planets of the Solar System share several common characteristics: they are relatively small, compared to the jovian worlds and ice giants, they orbit closer to the Sun, they rotate relatively slowly, and their bulk composition is dominated by refractory elements. Most of these properties are also shared by large satellites of the gaseous planets, by dwarf planets, and by the Moon. While each of the celestial bodies is sculpted by the local environment and its unique dynamical history, a zero–order estimate of the interior properties can be derived from basic physical characteristics, as is the mean density or the presence of major heat sources. In the study of low–mass exoplanets—often labelled as *terrestrial exoplanets* in parallel to the rocky worlds of the Solar System—we are often left with very scarce information. For the majority of these objects, only the radius and the semi–major axis are known. Nevertheless, as we will see, a global picture of the class of terrestrial worlds can be obtained either by statistical methods or by theoretical considerations.

2.1.1 Detection and characterisation techniques

Most of the currently known extrasolar planets have been discovered by indirect detection techniques, which rely on the effects the orbiting planet has on other bodies in the system. Such methods are, however, highly unfavourable for low–mass exoplanets for an obvious reason: the smaller the planet, the lower its impact on the measured quantities. While the first detected exoplanets used to lie on the high–mass end of the actual exoplanetary statistics, the past fifteen years have witnessed a steep increase even in the number of known terrestrial worlds. The search for terrestrial exoplanets is greatly fueled by the desire to understand the uniqueness of the Earth and, specifically, by the more or less explicit search for extraterrestrial life.

Among the most widely used detection methods are the *transit photometry* and the *radial velocity* (RV) measurements (e.g., Santos, 2008; Wright and Scott, 2013; Santos and Faria, 2018). Each of these techniques assesses different quantities and makes use of different instrumentation. In addition to the two methods, planets can also be detected in gravitational microlensing events, by direct imaging, by astrometry or by analysing their mutual gravitational interaction (in a multiplanetary system) (e.g., Holman and Murray, 2005; Santos, 2008; Rice, 2014; Tsapras, 2018). In the following three paragraphs, we will overview the first two and the last one of the mentioned techniques.

Transit photometry Transit photometry is based on the observation of periodic occultations of a planet–hosting star by its planetary companion. As the planet moves in front of its host, it blocks part of the stellar flux, leading to a decrease in the star's relative magnitude. The shape of the photometric time series (or "light curve") is then a footprint of the star–planet system's condition. Since the amount of blocked flux depends on the size of the transiting planet, the relative drop in the observed magnitude is proportional to the relative radius of the planet with respect to the host star. The period of occultations relates, via Kepler's third law, to the semi–major axis of the planet and to the mass of the star, while the duration of each transit is also determined by the orientation of the planet's orbit and by the stellar radius.

It should be stressed that an exoplanet can be detected by transit photometry only when it is actually transiting: its orbital plane has to be oriented in such a way that the planet periodically passes in front of the star, as observed from the Earth, and effectively blocks the stellar flux. The geometric probability that a transit will occur is (Santos, 2008)

$$p = \frac{R_*}{a} \,, \tag{2.1}$$

where R_* is the stellar radius and a is the semi–major axis. Therefore, the technique strongly favours planets on close–in orbits. Due to the dependence of the relative drop in magnitude on the relative radius of the planet, it is also more sensitive to larger planets or to bodies orbiting smaller stars. Nevertheless, thanks to the space–based missions designed specifically to search for terrestrial exoplanets, namely the *CoRoT* (Baglin, 2003), *Kepler* (Basri et al., 2005), and *TESS* (Ricker et al., 2015), even smaller extrasolar worlds are being included in the continuously expanding statistical set.

While the observation of periodic transits remains an important detection technique, it can also be an invaluable tool in the characterisation of the planet's surface conditions. A transit signal measured in different wavelengths presents a gateway to the planet's atmospheric composition, surface temperature, cloud coverage, and possible habitability (e.g., Kreidberg, 2018). This spectroscopic method, known as the *transmission spectroscopy*, may also enable the reconstruction of the planet's rotation (Brogi et al., 2016) or serve as a complement to the measurements of thermal spectra, fundamental for the planet surface characterisation (Hu et al.,

2012). As we have seen in this brief overview, the combination of the transit light curve retrieval and the transmission spectroscopy is a source of extensive data. However, despite individual efforts still waiting for full realisation (de Wit and Seager, 2013), the mentioned techniques are insufficient for the estimation of the planet mass. For this reason, the transit photometry is often combined with a historically older detection method, the radial velocity measurement, or with *transit–timing variation* (TTV), which will be discussed later.

Radial velocity method The most famous application of the RV measurements in exoplanetary science was, without a doubt, the detection of the first planetary companion orbiting a Sun–like star (Mayor and Queloz, 1995; Mayor and Queloz, 1996). Searching for the periodic radial motion of stars orbiting a common barycentre with hypothetical substellar companions[1], the discoverers used a high–precision echelle spectrograph *ELODIE* to measure the Doppler shift of photospheric absorption lines in the stellar spectra. The unexpected discovery of a close–in Jupiter–mass exoplanet, 51 Pegasi b, not only ignited the scientific community's interest in the search for extrasolar worlds, but also raised important questions concerning the formation of planetary systems (Mayor and Queloz, 1995).

The dynamical effect of a substellar companion on the radial motion of its host strongly depends on the relative masses of the two bodies. The semi–amplitude A_{RV} of the varying radial velocity, proportional to the relative shift of the absorption lines with respect to their nominal wavelengths, is related to the observed system's properties by (e.g., Cochran and Hatzes, 1996; Wright, 2018)

$$A_{\mathrm{RV}} = \left(\frac{2\pi\mathcal{G}}{T_{\mathrm{orb}}}\right)^{1/3} \frac{1}{\sqrt{1-e^2}} \frac{m_{\mathrm{p}} \sin i_{\mathrm{obs}}}{(m_* + m_{\mathrm{p}})^{2/3}} , \tag{2.2}$$

where T_{orb} is the orbital period, e the orbital eccentricity, m_{p} and m_* denote the masses of the companion and the star, respectively, and i_{obs} symbolises the inclination of the orbital plane to the plane of the sky. As an illustration, the case of $i_{\mathrm{obs}} = 0°$ would indicate a face-on orbit with no radial component (Wright, 2018). An orbit perpendicular to the plane of the sky ($i_{\mathrm{obs}} = 90°$), on the other hand, presents the best–case scenario with the most precise information on the companion's mass. Since the inclination of a newly–detected object is often unknown, the RV method gives us rather the mass function $m_{\mathrm{p}} \sin i_{\mathrm{obs}}$, i.e., the minimum mass of the star's companion. Nevertheless, if the character of the system also enables the measurement of the companion's spectrum, it can be used to determine the inclination i_{obs} (e.g., Brogi et al., 2012). Alternatively, if the companion is also transiting, the RV method can be combined with transit photometry and the orbital elements—including the inclination—can be constrained by Bayesian analysis (e.g., Gillon et al., 2010; Bonfils et al., 2011) or by approximate analytical methods (e.g., Carter et al., 2008).

As we can see in equation (2.2), the radial velocity method favours the detection

[1]By "substellar companions" we mean either brown dwarfs or planets.

of short–period high–mass exoplanets orbiting around low–mass stars. The effect of the orbital eccentricity on the semi–amplitude of the varying radial velocity is relatively weak; however, the ability to determine its value is one of the important advantages of this method. The orbital eccentricity is imprinted into the shape of the RV time series and is usually fitted along with other parameters (e.g., Stassun et al., 2017). Equation (2.2) also indicates that the RV method can be used for the inference of the minimum mass $m_{\rm p} \sin i_{\rm obs}$ only if we already know the stellar mass. Similarly to the case of transit photometry, a precise characterisation of the planet (or brown dwarf) requires a precise independent characterisation of the host star, which can be achieved by a combination of high–resolution spectroscopy, asteroseismology, and stellar evolution models (for an overview, see, e.g., Adibekyan et al., 2018).

Transit timing variation Long time series of planetary transits not only contain the information about the relative radius and orbit orientation of the planet, but they can also indicate ongoing orbital evolution in the system. The evolution can be caused by tidal interaction with the star; in that case, the precise and continual measurements of transit light curves provide an insight into the dissipation in the two bodies (e.g., Chernov et al., 2017; Maciejewski, 2019; Bolmont et al., 2020). If, on the other hand, the evolution results from gravitational interaction with other—yet unknown—bodies in the system, the analysis of transit signal can be used as an additional detection technique: the transit timing variation (Holman and Murray, 2005; Agol et al., 2005).

Proposed in 2005 as a feasible method for the detection of Earth–sized exoplanets not producing a detectable transit signal, the TTV became particularly promising in the era of *Kepler*. The most notable applications of this method in the first years of the mission were the confirmation and refined characterisation of the multi–planetary system Kepler–9 (Holman et al., 2010), the first detection of a non–transiting companion in the system Kepler–19 with one transiting planet (Ballard et al., 2011), and the first complete orbital characterisation of a non–transiting planet Kepler–46 c (Nesvorný et al., 2012). Recently, TTV was also applied as an auxiliary method for the precise determination of masses and eccentricities in the seven–planet system TRAPPIST–1 (Gillon et al., 2017).

As the name suggests, the TTV is based on the measurement of variations in the intervals between successive transits (Holman and Murray, 2005; Agol et al., 2005). A single planet in a system would orbit its host star with a fixed period $T_{\rm orb}$. The photometric signal produced by its passages in front of the star would be strictly periodic. In the presence of other companions, however, the transiting planet is subjected to mutual gravitational interaction, resulting in variations in its orbital elements (Section 1.3.1). As follows from the perturbation theory, the timing variations become greatly amplified in systems of planets near mean–motion resonances[2]. In consequence, the TTV method favours resonant

[2]Empirically–derived statistics indicate that the members of close–in multiplanetary systems are more frequently found close to first–order mean–motion resonances than directly in the resonant locations (Lissauer et al., 2011; Fabrycky et al., 2014; Delisle and Laskar, 2014).

companions, preferentially around low–mass stars (Holman and Murray, 2005). The need for long time series also implies that the ideal targets for the timing variation analysis are short–period (close–in) systems. On the other hand, TTV is presently the only reliable method linking the transit light curves to the planetary masses (without the need of RV measurements) and it is also an important source of information on the orbital eccentricities in multiplanetary systems.

2.1.2 Mass-radius relations

In an ideal case of a transiting exoplanetary system and a well–characterised host star, the combination of the transit photometry with the RV method or, if applicable, with the TTV method enables a simultaneous determination of the masses and radii of the studied exoplanet(s). The mass and radius, combined to yield the average density, are the basic ingredients of any considerations regarding the planet's interior structure and composition. In reality, however, the two parameters are not always known at the same time and, especially for terrestrial exoplanets, the masses are often poorly constrained (e.g., Weiss and Marcy, 2014).

The problem of lacking data can be partially solved by resorting to the mass–radius relations of celestial bodies with already determined properties. Among such bodies are the Solar System moons, dwarf planets, and planets, as well as transiting extrasolar worlds with measured RVs or TTVs. Mass–radius relations can be constructed either by statistical means, based purely on the data (e.g., Weiss and Marcy, 2014; Wolfgang et al., 2016; Bashi et al., 2017; Chen and Kipping, 2017), or with the help of a physically–justified model, based on the equations of state for the expected planetary constituents[3] (e.g., Valencia et al., 2006; Zeng et al., 2016). Recent scaling laws also consider the scatter in radii for given masses (or vice versa) and the uncertainty in the measured quantities (Wolfgang et al., 2016; Chen and Kipping, 2017).

Additionally, the mass–radius relations can provide a basic insight into the exoplanets' types and compositions. As illustrated, e.g., in Chen and Kipping (2017, Figure 3), the slopes of the relation, as well as the variances, substantially differ between distinct mass intervals. The change of slope is most prominent around $100 M_\oplus$. In this region, the relation is characterised by a plateau, indicating that the radius of extrasolar gas giants is almost independent of their mass. Nevertheless, the area of our interest lies below $\sim 2 M_\oplus$, which was found by Chen and Kipping (2017) as the upper limit for the "Terran" mass–radius relation. Translated to radii, the upper limit for exoplanets with undoubtedly rocky composition should lie around $\sim 1.2 R_\oplus$. Less strict estimates predict that the upper limit in radii is around $1.5 R_\oplus$ (Weiss and Marcy, 2014; Rogers, 2015) and, in a very broad sense, the planet formation theory admits the existence of terrestrial worlds with masses up to $10 M_\oplus$ and corresponding radii up to $\sim 1.9 R_\oplus$ (Valencia et al., 2006).

An interesting feature arises when we focus on the dependence of planetary

[3] In Chapter 4 of this work, we adopt specifically the model of Zeng et al. (2016), which is based on the Preliminary Reference Earth Model (PREM; Dziewonski and Anderson, 1981).

radius on a fixed mass. Despite a large scatter of radii in the Neptunian range of Chen and Kipping (2017), refined exoplanetary statistics suggest that not all predicted mass–radius pairs are equally probable. Empirical mass–radius diagrams (e.g., Zeng et al. 2019; see also Fulton et al. 2017) reveal two distinct regions, divided by a scarcely–populated valley. The population with higher average densities belongs to *super–Earths*, or massive terrestrial exoplanets (theoretically, up to $10M_{\oplus}$). The population with lower average densities consists of *mini–Neptunes*: exoplanets with extended water vapour or hydrogen/helium atmospheres. Whether a newly formed planet remains terrestrial or it evolves to a small Neptunian world presumably depends on the individual formation history. Similarly, whether a Neptune–like exoplanet pertains its low–density atmosphere or it loses the volatiles to space may depend on the levels of instellation[4] (Fulton and Petigura, 2018; Swain et al., 2019). As the mass–radius diagram can be divided into regions inhabited by planets of different classes, a comparison of a newly–detected exoplanet with such a diagram permits the estimation of its character even in the absence of information on the mass (or on the radius, if mass is known).

2.1.3 Composition

The estimation of the average density, possibly with the help of an analytical or semi–empirical mass–radius relation, is only the first step in the characterisation of exoplanet interiors. The position of a planet on the mass–radius diagram can be approximately linked to its composition (see, e.g., Figure 2 in Zeng et al., 2019); such a characterisation is, however, often ambiguous. While a two–layered model, in which the planet is composed of a homogeneous core and a homogeneous mantle (or ocean) provides a unique fit to the planet's average density, any multi–layered models or models with more realistic mineralogy are inherently non–unique. Typically, there is a trade–off between the layers' compositions and thicknesses. To constrain the interior models of exoplanets with determined masses and radii, we would need additional information, coming either from observation or from numerical modelling.

Observational constraints Among the observational constraints are the spectrum of the host star, the spectrum of the planet, and the footprints of the planet's shape in the transit light curves or RV measurements. The spectrum of the host star contains information on the elemental abundances in its photosphere and, implicitly, on the building blocks of the surrounding planetary system (e.g., Dorn et al., 2015). The link between the stellar and the planetary composition is based on the evidence from our closest neighbourhood. Considering only the refractory, non–volatile elements, the composition of carbonaceous chondrites and the bulk composition of the Earth closely follow the relative elemental abundances in the solar photosphere (McDonough, 2003; Lodders, 2003). Specifically, the Mg:Si:Fe ratio determines the relative core size of the terrestrial planets and, together with

[4]The word "instellation" is used in parallel to "insolation" and denotes the incident flux at the planet's surface (e.g., Dobrovolskis, 2007, 2009).

the C:O ratio, it co–determines the mantle mineralogy (Thiabaud et al., 2014). Although the exact planetary composition depends on the processes acting during the planet formation (Thiabaud et al., 2014) and in the early violent stages of the planetary system evolution (e.g., Marcus et al., 2010), the stellar abundances can constrain the composition of planets in a given system at least by statistical means.

The transmission or emission spectrum of a terrestrial exoplanet's atmosphere may provide clues to the planetary water content (Tsiaras et al., 2019) or to ongoing volcanic activity (e.g., Kaltenegger et al., 2010). In the case of active silicate volcanism or maintenance of a surface magma ocean, the atmospheric composition is also linked to the composition of the solid body. On the other hand, the absence of absorption features in the transmission spectrum can be explained by the presence of clouds (Fortney, 2005; Kreidberg et al., 2014).

Another promising method probing the interior of close–in exoplanets is the search for the signal coming from the tidal or rotational deformation in long photometric or spectrometric time series. The tidal Love number k_2, introduced in the previous chapter, has a direct effect on the planet's apsidal precession[5], which proceeds on much shorter timescales than the tidal evolution of other orbital elements. In other words, the measurement of apsidal motion provides information about the planet's tidal deformation and, consequently, about its radial structure. For an elliptic orbit, the changes in the orientation of the periapsis with respect to the observer result in transit timing variations or radial velocity variations (Csizmadia et al., 2019). Specifically, Csizmadia et al. (2019) used archival RV measurements to estimate k_2 of the hot Jupiter WASP–18Ab and discussed the detectability of apsidal motion by TTV. Focusing on the tidal deformation of terrestrial worlds, Bolmont et al. (2020) analysed the effect of k_2 on the TTV of the innermost planets in the TRAPPIST–1 system. The authors found that the tidally–induced apsidal precession is comparable to the relativistic precession and the tidal contribution is potentially detectable, given the planets are covered by ocean.

In addition to the apsidal precession, the shape of a tidally– or rotationally–deformed transiting exoplanet also affects the apparent dimming and brightening of its host star, as observed from the Earth (or from the Earth's orbit). Analysis of photometric time series can thus provide clues not only to the dynamical effect of tides, through the apsidal motion reflected in TTV, but also to the actual deformation of the planet, through its influence on the shape of the light curve. Although hardly detectable by current instruments (however, see Hellard et al., 2020), the measurements of tidal deformation will hopefully become a new constraint on exoplanetary interiors upon the launch of future missions such as JWST or PLATO (Hellard et al., 2019). Furthermore, the detection of the planet's rotational flattening may give clues to its spin rate and thus constrain the rate of tidal dissipation in the interior (e.g., Seager and Hui, 2002; Zhu et al., 2014).

[5]In the context of works dedicated to close binary stars, the tidal Love numbers k_l, divided by two, are referred to as *apsidal motion constants* (e.g., Russell, 1928; Sterne, 1939; Kopal, 1953; Hut, 1981).

Constraints from numerical modelling Due to the inherent degeneracy of physically–motivated interior structure models, the numerical modelling alone provides only a loose constraint on the possible exoplanetary compositions. Nevertheless, in combination with the measurable parameters, such as the mass, radius, and distance from the host star, the information coming from theoretical efforts can help us to qualitatively determine how similar—or how dissimilar—are the individual exoplanets to the Solar System bodies.

As was said earlier, the planetary composition depends on the individual formation history, which can be hardly tracked down in a distant exoplanetary system (e.g., Thiabaud et al., 2014). Theoretical considerations can, however, set limits on the empirically–obtained mass–radius diagrams. For instance, the knowledge of the equilibrium surface temperature, based on the measured semi–major axis and stellar luminosity, indicates whether a planet is able to sustain an ice crust, a water ocean, or any water reservoirs at all (e.g., Leconte et al., 2013). Numerical simulations of giant impacts, on the other hand, give constraints on the maximum core mass fraction (CMF) in terrestrial exoplanets (Marcus et al., 2010) since a collision never strips a planet from the entire mantle[6]. Taking a yet different approach, Suissa et al. (2018) suggest that the maximum and minimum core size of planets with measured masses and radii can be estimated from synthetic planet interior models. The authors adopt the model grid of Zeng and Sasselov (2013), which was calculated using equations of state for iron and silicates, and use the measured radii as boundary conditions for interior structure models of planets with a given mass.

The last theoretical constraint that we are going to mention is the planetary systems' formation time. In short, younger systems were formed in an older—and chemically more evolved—Galaxy. The availability of heavy elements in the star–forming regions affects the initial heat budget of newly–forming terrestrial worlds, as well as their possible core sizes and mantle mineralogies (Frank et al., 2014; O'Neill et al., 2020). At the same time, the chemical composition of the interstellar medium (ISM) is subject to evolution. Material is being recycled in new and new generations of stars and the ISM is being gradually enriched in metals, including iron and long–lived radionuclides. Based on the galactic chemical composition models, Frank et al. (2014) predicts that terrestrial exoplanets formed in the early Galaxy might be more Lunar–like than Earth–like, that is, they might possess a smaller iron core. Newer planets, on the other hand, may resemble hypothetical "super–Mercuries". The core size, the related surface gravity, and the efficiency of radiogenic heating have further implications for the thermal and tectonic regime of a planet (Frank et al., 2014; O'Neill et al., 2020). The formation time may, therefore, determine whether an Earth–sized planet will be also Earth–like.

[6]Although the bulk density of terrestrial exoplanets might be constrained by giant–impact simulations, this lower limit is probably not always determining. Mocquet et al. (2014) point out at the existence of exotic planetary candidates with densities exceeding the density of iron and suggest that the objects can be naked cores of former giant planets which have migrated too close to their host star.

On the several pages behind us, we have reviewed the most successful detection and characterisation techniques used in exoplanetary science and we have discussed the types of information about the interiors of extrasolar worlds that can be obtained from observation or numerical modelling (with theoretical considerations). Now, we will briefly return to the Earth and to Earth–based laboratories with a quest for a rheologically–motivated description of tidal deformation.

2.2 Deformation mechanisms

Realistic parameterisation of the tidal response and of the subsequent tidal heat production requires a proper understanding of the underlying deformation mechanisms. Such knowledge can be obtained either by empirical measurements or by *ab initio* calculations. In this section, we are going to discuss the microscopic sources of global–scale deformation and introduce the rheological models used in planetary science.

The internal friction, or the magnitude of the energy dissipation, is commonly quantified by the (inverse) quality factor Q^{-1}, defined as (e.g., Stacey, 1963; Sotin et al., 2009)

$$Q^{-1} = \frac{\Delta\mathcal{E}}{2\pi\mathcal{E}} , \tag{2.3}$$

where $\Delta\mathcal{E}/\mathcal{E}$ is the fractional energy loss per loading cycle. In our case, this quantity presents the link between the internal mechanisms and the tidal response introduced in the previous chapter. Specifically, the tidal quality factor can be related to the tidal phase lag[7] as (Efroimsky, 2012a,b)

$$Q^{-1}(\omega_{lmpq}) = \sin\varepsilon_{lmpq}(\omega_{lmpq}) . \tag{2.4}$$

Since the difference between the seismic quality factor and the tidal quality factor of planetary bodies is only produced by the self–gravity (Goldreich, 1963; Efroimsky and Lainey, 2007), the frequency dependence of the latter quantity can be reasonably represented by the frequency dependence of the former.

In the following, we are going to use the words *anelasticity* and *viscoelasticity* with the meaning identical to their introduction in Karato and Spetzler (1990). Anelastic behaviour is thus a relaxation of the material to a uniquely defined equilibrium state, characterised by the relaxation time τ. Viscoelastic behaviour, on the other hand, lacks a uniquely defined equilibrium and results in infinite deformation at an infinite time (given the stress is constant).

[7]Note that this definition of the quality factor differs from the definition used in geophysics and material science, which would be $Q^{-1} = \tan\varepsilon$ (e.g., Nowick and Berry, 1972). The difference between the "seismic" and the "tidal" factor is due to the planet's self–gravity. For a detailed discussion, see Efroimsky and Lainey (2007) or Efroimsky (2012b).

2.2.1 Rheological models

The constitutive relation between the applied shear stress σ and the resulting strain ϵ in the medium is determined by our choice of the rheological model. Specifically, if the relation between the two quantities is linear, as is the case in geophysically–relevant materials at low stresses (e.g., Jackson, 2015), the rheological model is also said to be linear. The use of a linear rheology enables us to perform the Darwin–Kaula expansion (Section 1.3) as well as the normal mode expansion presented in Appendix A. In the time domain, we can define the *creep function* $J(t)$ (e.g., Nowick and Berry, 1972; Jackson, 2015), which represents the strain resulting from shear stress applied in the form of a step function at time "zero",

$$\sigma(t) = \begin{cases} 0 & \text{for } t < 0 \,, \\ 1 & \text{for } t \geq 0 \,. \end{cases} \tag{2.5}$$

As an example, a purely elastic body would respond by instantaneously occurring constant deformation ($J(t) \propto 1$), while a purely viscous body would respond by linearly growing deformation ($J(t) \propto t$). Nevertheless, since an important class of laboratory experiments as well as seismological measurements are concerned with the response of a material subjected to periodic loading, it is advantageous to express the relation between the strain $\bar{\epsilon}$ and stress $\bar{\sigma}$ in the frequency domain, using the Laplace transform of the creep function,

$$\bar{J}(\omega) = \mathcal{L}\big\{J(t)\big\} = \mathrm{i}\omega \int_0^\infty J(\xi) e^{-\mathrm{i}\omega\xi} \, \mathrm{d}\xi \,, \tag{2.6}$$

which is denoted as the *dynamic compliance* (Jackson, 2015). Alternatively, this quantity can also be defined as the Fourier transform (e.g., Makris, 2019).

Mechanical circuits In a simplified 1d case, the rheological model of a material can be represented by a mechanical circuit, in analogy to the alternating current (AC) circuits of electromagnetics. After substituting the scalar quantities σ and ϵ by the traceless stress tensor $\boldsymbol{\sigma}^{\mathrm{D}}$ and strain tensor $\boldsymbol{\epsilon}^{\mathrm{D}}$, the outcome of this analogy is also applicable to the general 3d case. The extension of the illustrated 1d mechanical models to the rheology of 3d continuum will be shown later in this subsection. A purely elastic response to periodic loading is symbolised by a Hookean spring with elastic (Young) modulus E. A purely viscous response is represented by a Newtonian dashpot with viscosity F, as illustrated on the following lines:

$$\epsilon(t) = \frac{\sigma(t)}{E} \qquad \bar{\epsilon}(\omega) = \frac{\bar{\sigma}(\omega)}{E} \qquad \tag{2.7}$$

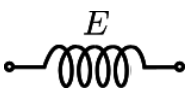

$$\epsilon(t) = \int_0^t \frac{\sigma(t')}{F} \mathrm{d}t' \qquad \bar{\epsilon}(\omega) = \frac{\bar{\sigma}(\omega)}{\mathrm{i}\omega F} \qquad \tag{2.8}$$

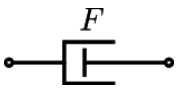

Maxwell and Kelvin–Voigt elements Figure 2.1 shows four linear rheological models applicable to geophysical phenomena. The first two models, namely Maxwell and Kelvin–Voigt, represent the simplest possible combinations of viscous and elastic elements. First, the Maxwell model, depicted as a spring and dashpot connected in series, describes irrecoverable, viscoelastic deformation. In response to applied stress, the spring deforms instantaneously, while the dashpot slides gradually until the stress is removed. Conversely, when a constant strain is applied to the Maxwellian circuit, the resulting stress decays with relaxation time $\tau_{\mathrm{M}} = F_1/E_1$. Similarly, the Kelvin–Voigt model, a spring and dashpot connected in parallel, can be characterised by a retardation time[8] $\tau_{\mathrm{KV}} = F_2/E_2$, which describes the retardation of strain upon the application of a constant stress. Due to the parallel connection, the Kelvin–Voigt model represents recoverable, anelastic deformation in the medium. Note that the elastic moduli and the viscosities of the two models are marked with different subscripts, since they symbolise different mechanisms.

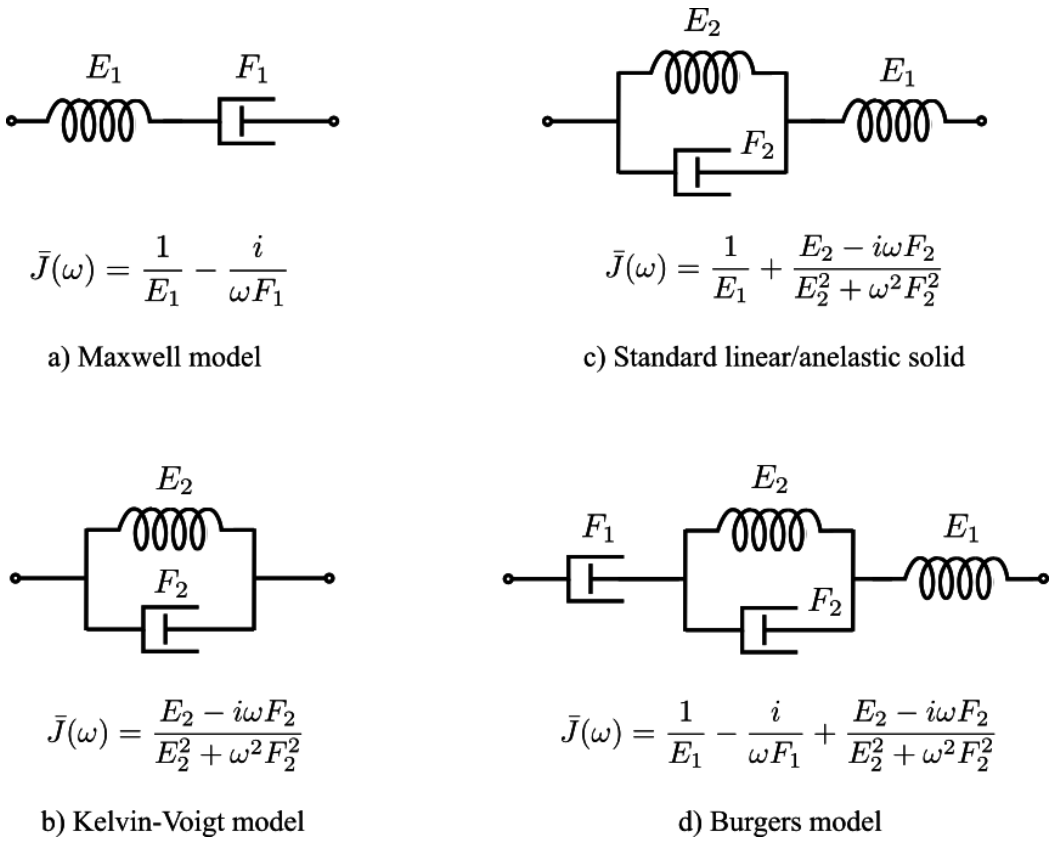

Figure 2.1: Overview of the simplest rheological models and their mechanical circuit analogues. Symbol E stands for the elastic (Young) modulus of a Hookean spring and F denotes the viscosity of a Newtonean dashpot.

[8]The relaxation time characterises the stress relaxation under a constant strain. The retardation time, on the other hand, characterises the strain retardation under a constant stress. For materials described by complex rheologies, the two timescales are generally different (Nowick and Berry, 1972).

Both the Maxwell and the Kelvin–Voigt models contain a contribution which is nonelastic, leads to a time–dependent behaviour, and in which the strain lags behind the stress. Such a behaviour results in the dissipation of mechanical energy in the system. The complex–valued dynamic compliance (2.6) can be divided into the real and imaginary part as (Nowick and Berry, 1972)

$$\bar{J}(\omega) = \bar{J}_1(\omega) - \mathrm{i}\bar{J}_2(\omega) = |\bar{J}(\omega)|e^{-\mathrm{i}\varepsilon} \,, \tag{2.9}$$

where $\bar{J}_1(\omega)$ is called the *storage compliance*, $\bar{J}_2(\omega)$ the *loss compliance*, $|\bar{J}(\omega)|$ the *absolute dynamic compliance*, and the "seismic phase lag" ε is, in this context, referred to as the *loss angle*. The energy dissipated in a full cycle of loading is related to the loss compliance by

$$\Delta\mathcal{E} = \pi\sigma_0^2\bar{J}_2(\omega) \,, \tag{2.10}$$

with σ_0 being the amplitude of applied periodic stress.

Standard anelastic solid A combination of the elastic and the anelastic behaviour can be most easily represented by the standard anelastic solid (SAS)—a model introduced by Zener (1948) and originally labelled as the "standard linear solid" (SLS). Here, we adopt the newer term, as it better captures the essence of the model: the SAS is required not only to provide a linear relationship between the strain and stress, but also to relax into a unique equilibrium after sufficient time. The mechanical analogue of SAS consists of a Hookean spring, representing the elastic deformation, and a Kelvin–Voigt element, representing the anelastic deformation. In the material science (e.g., Nowick and Berry, 1972), the creep function is conventionally divided into the unrelaxed part,

$$J_\mathrm{U} = J(t=0) = \frac{1}{E_1} \,, \tag{2.11}$$

and the relaxed part,

$$J_\mathrm{R} = J(t\to\infty) = \frac{1}{E_1} + \frac{1}{E_2}, \tag{2.12}$$

where the former characterises the instantaneous deformation after the exertion of stress in the circuit, while the latter characterises the equilibrium value of $J(t)$ after strain relaxation. Another quantity, used in line with the relaxation or retardation time[9] τ (e.g., Karato and Spetzler, 1990), is the *relaxation strength*

$$\Delta = \frac{J_\mathrm{R} - J_\mathrm{U}}{J_\mathrm{U}} = \frac{\delta J}{J_\mathrm{U}} \,. \tag{2.13}$$

[9]Strictly speaking, the timescale used for the characterisation of a material depends on the type of experiment conducted. The creep function is typically measured at constant stress (as follows from its definition). Therefore, the quantities J_U and J_R are used together with the retardation time. Conversely, the relaxation time is used in combination with the *stress relaxation function* $M(t)$ (Nowick and Berry, 1972). The unrelaxed part of this function is equal to $1/J_\mathrm{U}$. The relaxed part is equal to $1/J_\mathrm{R}$.

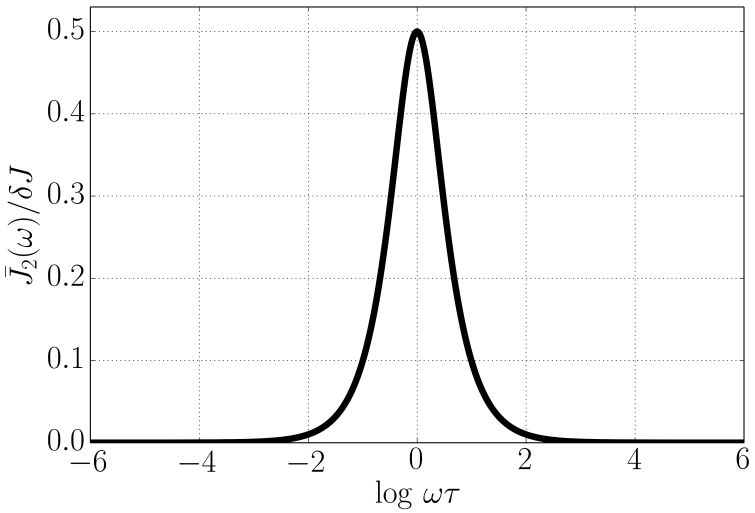

Figure 2.2: Sketch of the Debye peak arising in the relaxation spectrum of an anelastic material.

Using this notation, the relaxed and unrelaxed compliance can be related via $J_\mathrm{R} = J_\mathrm{U}(1 + \Delta)$.

If we rewrite the frequency–domain constitutive relation of SAS (Figure 2.1c) into these newly introduced variables, we arrive at

$$\bar{J}(\omega) = J_\mathrm{U} + \delta J \frac{1}{1+\omega^2\tau^2} - \mathrm{i}\delta J \frac{\omega\tau}{1+\omega^2\tau^2} \,. \tag{2.14}$$

Specifically, the imaginary part of equation (2.14), which stands for the dissipation in the medium, follows a distinct frequency dependence that is characteristic for the given material. When plotted against $\log\omega\tau$ the imaginary part forms a symmetric peak around $\omega\tau = 1$ (Figure 2.2), which is called the *Debye peak*. The laboratory measurements and characterisations of Debye peaks paved the way for advanced rheological models, which will be introduced in one of the following sections.

Burgers model The addition of a Newtonian dashpot to the mechanical analogue of the SAS model yields the Burgers model (Figure 2.1d). The main strength of the Burgers model when compared to SAS is, therefore, its ability to capture the viscous creep, in addition to the anelastic deformation. In analogy to equation (2.14), we may write the dynamic compliance of this model as

$$\bar{J}(\omega) = J_\mathrm{U} + \delta J \frac{1}{1+\omega^2\tau^2} - \mathrm{i}\left(\delta J \frac{\omega\tau}{1+\omega^2\tau^2} + \frac{J_\mathrm{U}}{\omega\tau_\mathrm{M}}\right) \,, \tag{2.15}$$

where τ_M is the previously mentioned Maxwell time.

Three–dimensional elastic case Up to now, we have introduced the basic rheological models using the 1d mechanical circuit analogue. Such toy models are useful for illustration purposes and they also have a role in laboratory experiments performed on metal wires (Andrade, 1910). However, in practical applications, the presented results need to be extended to a general 3d case. On the following lines, we are going to discuss the relationship between the incremental Cauchy stress tensor $\boldsymbol{\sigma}$ and the Eulerian strain tensor $\boldsymbol{\epsilon} = \frac{1}{2}\left(\nabla\mathbf{u} + \nabla^t\mathbf{u}\right)$, where $\mathbf{u}$ is the infinitesimal deformation. First, we will focus on the elastic case and then on the case of linear viscoelasticity or anelasticity.

The constitutive relation for a linear elastic solid can be expressed by the generalised Hooke's law (e.g., Martinec, 2019)

$$\boldsymbol{\sigma} = \mathbf{C} : \boldsymbol{\epsilon} \,, \tag{2.16}$$

where $\mathbf{C}$ is the fourth–order elastic tensor. In a general case of anisotropic solid, the elastic tensor is specified by 21 independent components (and the stress–strain relation is further characterised by six components of a reference stress tensor). In the more specific case of an isotropic solid, the number of independent elastic constant reduces to two and the generalised Hooke's law becomes

$$\boldsymbol{\sigma} = \lambda\,\mathrm{tr}(\boldsymbol{\epsilon})\,\mathbf{I} + 2\mu\,\boldsymbol{\epsilon} \,, \tag{2.17}$$

where $\mathrm{tr}(\cdot)$ denotes the trace of a tensor. Constants λ and μ are *Lamé's coefficients*. The second Lamé's coefficient, μ, is also called the *shear modulus* or the *rigidity*, depending on the context. The strain and the stress tensors can be further split into the spherical and the deviatoric ($\cdot^{\mathrm{D}}$) parts (Martinec, 2019):

$$\boldsymbol{\epsilon} = \frac{1}{3}\mathrm{tr}(\boldsymbol{\epsilon})\mathbf{I} + \boldsymbol{\epsilon}^{\mathrm{D}} \,, \qquad\qquad \boldsymbol{\sigma} = -p\mathbf{I} + \boldsymbol{\sigma}^{\mathrm{D}} \,, \tag{2.18}$$

with p being the mechanical pressure. Specifically, the deviatoric parts of both tensors are traceless and symmetric from the definition. Upon inserting the expressions (2.18) into equation (2.17), the generalised Hooke's law also splits to the spherical and deviatoric parts as

$$-p = k\,\mathrm{tr}(\boldsymbol{\epsilon}) \,, \qquad\qquad \boldsymbol{\sigma}^{\mathrm{D}} = 2\mu\boldsymbol{\epsilon}^{\mathrm{D}} \,. \tag{2.19}$$

Here, we defined the *bulk modulus*, or the *modulus of hydrostatic compression*, as $k = \lambda + \frac{2}{3}\mu$ (Landau et al., 1986; Martinec, 2019). If we continue the descent from the more general to the less general 3d case, we may further require that the linear elastic solid be not only isotropic but also incompressible. Then, it holds that

$$\begin{gathered} \mathrm{tr}(\boldsymbol{\epsilon}) = \nabla\cdot\mathbf{u} \to 0 \,, \qquad \lambda \to \infty \,, \qquad k \to \infty \,, \\ \boldsymbol{\sigma} = -p\,\mathbf{I} + 2\mu\,\boldsymbol{\epsilon}^{\mathrm{D}} \,, \end{gathered} \tag{2.20}$$

and the mechanical pressure becomes a new unknown function of coordinates, determined by solving the governing equations of the continuum (Landau et al., 1986).

Until we proceed to the linear viscoelastic or anelastic solid, it would be beneficial to contemplate the relationship between the Young modulus, used in the discussion of the 1d case, and the shear modulus, introduced in this paragraph. While the Young modulus characterises the stretching of a material subjected to uniaxial stress, the shear modulus describes the material's response to shear stress and it is related also to the forces acting in the direction perpendicular to the loading. As an example, the stretching of a wire is accompanied by its thinning. The ratio between the transversal compression and the longitudinal stretching is called the Poisson ratio ν and the Young modulus can be related to the shear stress by (Landau et al., 1986)

$$E = 2\mu(1+\nu) \,. \tag{2.21}$$

In practice, the Poisson ratio may vary between $\nu = -1$ and $\nu = 0.5$. However, the idealised mechanical models of Figure 2.1 are devoid of any deformation in the transversal direction and are considered as having $\nu := 0$.

Three–dimensional nonelastic case The constitutive relation for a linear viscoelastic or anelastic solid differs from the constitutive relation for an elastic solid by the dependence of the Cauchy stress tensor on the strain rate $\dot{\boldsymbol{\epsilon}}$ or the stress rate $\dot{\boldsymbol{\sigma}}$. Nevertheless, the linear nonelastic case can be readily rewritten to an analogue of the generalised Hooke's law by applying the principle of correspondence (Peltier, 1974). Therefore, for the Laplace (or Fourier) transform of the incremental Cauchy stress tensor $\bar{\boldsymbol{\sigma}}$ and of the incremental strain tensor $\bar{\boldsymbol{\epsilon}}$ in a linear isotropic incompressible solid, we may write

$$\bar{\boldsymbol{\sigma}}(\omega) = -p\,\mathbf{I} + 2\bar{\mu}(\omega)\,\bar{\boldsymbol{\epsilon}}^{\mathrm{D}}(\omega) \,, \tag{2.22}$$

where $\bar{\mu}(\omega)$ is the complex rigidity. Taking only the deviatoric part of the Cauchy stress tensor, the inverse relation reads as

$$2\bar{\boldsymbol{\epsilon}}^{\mathrm{D}}(\omega) = \bar{J}(\omega)\bar{\boldsymbol{\sigma}}^{\mathrm{D}}(\omega) \,. \tag{2.23}$$

Equation (2.23), in the form stated, is traditionally used in rheologically–justified models of tidal phenomena (e.g., Castillo-Rogez et al., 2011; Efroimsky, 2012b). In our case, however, it requires some caution, especially in relation to the factor 2 in front of the strain tensor and to our previous exposition. The complex compliance $\bar{J}(\omega)$ has been, up to now, defined in the 1d case with the Young modulus E and the 1d viscosity F. The 3d complex compliance, as introduced in equation (2.23), has exactly the same form as in Figure 2.1; the symbols E and F only need to be replaced by the symbols μ and η, where symbol η stands for the dynamic viscosity,

defined for a Newtonian fluid in analogy to the shear stress in a linear elastic solid. If we, instead, stated equation (2.23) without the factor 2, we would need to substitute $E = 2\mu$ and $F = 2\eta$ in the compliances given in Figure 2.1.

2.2.2 Microscopic processes as a source of macroscopic deformation

The global–scale deformation and energy dissipation in planetary bodies are determined by several distinct microscopic mechanisms, acting with variable importance at different depths of the core and mantle. Among the mechanisms likely to induce anelastic or viscoelastic deformation are the motion of point defects or dislocations, grain boundary migration and sliding, redistribution of intergranular fluids (such as melt or water), and local phase transitions (Jackson, 2015). Different deformation mechanisms are characterised by different characteristic (relaxation/retardation) times and different relaxation strengths (see, e.g., Zener, 1948). According to Karato and Spetzler (1990), the most important sources of seismic–wave attenuation in the Earth mantle are dislocation sliding and grain–boundary mechanisms. These two mechanisms can also contribute to the attenuation at the tidal frequencies and will be specifically reviewed in this section.

Movement of dislocations The theoretical background of dislocation motion was developed in the 1930s (e.g., Orowan, 1934; Taylor, 1934), although it was not earlier than in the 1950s when the dislocations were observed in the laboratory (Hirsch et al., 1956). The movement of a dislocation under applied stress is achieved in various ways. As an example, the *dislocation climb* consists in the migration of dislocation in a crystal, accompanied by the formation or annihilation of vacancies. Since the motion of vacancies depends strongly on temperature, dislocation climb is a thermally–activated mechanism (e.g., Hull and Bacon, 2011). On the other hand, the *dislocation glide* takes place without the assistance of vacancy diffusion and proceeds even at low temperatures.

The rheological properties of real materials are marked by the presence of multiple dislocations, characterised by the *dislocation density*. The dislocation density ϱ is defined as the total length of dislocations in a unit volume and its magnitude is particularly sensitive to long–term tectonic stresses, that is, to the past loading of the interior. An intersection of dislocations is one of the possible mechanisms responsible for the formation of kinks and jogs: the "defects inside a defect" impeding the movement of a dislocation. Specifically, the presence of jogs and other impurities in the slip plane may lead to a phenomenon called *dislocation pinning*. In a material subjected to forced oscillations, the dislocation usually moves between pinning points, which can be represented, in addition to jogs, also by other obstacles, such as impurity atoms or nodes. The material then deforms anelastically, with relaxation strength and characteristic time given by (Karato and Spetzler, 1990)

$$\Delta \sim \varrho l^2 \,, \tag{2.24}$$

$$\tau \sim \frac{l^2}{\mu b B} \,, \tag{2.25}$$

where l denotes the average distance between pinning points, b is the magnitude of Burgers vector[10], μ the shear modulus and B the mobility of dislocation. The last quantity is determined by the resistance to dislocation motion, such as phonon scattering, impurity or jog drag, the repulsive effect of lattice periodicity or interaction with other dislocation (Hirth and Lothe, 1992; Karato and Spetzler, 1990)

The anelastic behaviour, which is caused by dislocation pinning, changes at high temperatures, high stresses or low frequencies. Under such conditions, the pinning is no longer effective and the pinning agents may either be overcome, or they move along with dislocations. This phenomenon is called *dislocation unpinning* and leads to viscoelastic deformation (Karato and Spetzler, 1990; Karato, 1998). The frequency at which unpinning occurs is

$$\omega_{\mathrm{u}} = \omega_{\mathrm{char}} \exp\left\{-\frac{\mathcal{E}_{\mathrm{b}} - \sigma b^2 l}{R_{\mathrm{gas}} T}\right\} , \tag{2.26}$$

where ω_{char} symbolises the characteristic vibration frequency of a dislocation, $\mathcal{E}_{\mathrm{b}}$ is the binding energy of a dislocation to a pinning point, R_{gas} is gas constant, and, finally, T is the local temperature.

Grain-boundary mechanisms The movement of grain boundaries may proceed either in the direction perpendicular to its tangent plane, or in the parallel direction. In the former case, we are speaking about the *grain boundary migration*, while the latter case is known as the *grain boundary sliding* (e.g., Karato and Spetzler, 1990). The grain boundary migration consists in the emission of near-boundary atoms from one grain and their absorption by another grain, resulting in gradual shrinking or growth of the respective neighbouring grains (e.g., Gleiter, 1969). This mechanism, possibly induced by an applied stress and increased temperature, plays an active role in recrystallisation. However, since it does not generally cause strain, the grain boundary migration has negligible contribution to stress relaxation (Karato and Spetzler, 1990). Its action may, nevertheless, smoothen the boundaries of involved grains and facilitate grain boundary sliding.

Grain boundary sliding is a process consisting of the sliding of flat portions of the grain boundary and of the accommodation of grain boundary irregularities (Raj and Ashby, 1971; Karato and Spetzler, 1990). Here, the irregularities are a direct consequence of the grain shape and the most important of them is due to

[10]The Burgers vector compares the crystal with a dislocation to an idealised "perfect crystal". It can be introduced using the method of the Burgers circuit (Friedel, 2013), that is, by drawing an oriented curve around the area with dislocation and the same curve around the corresponding area in the perfect crystal. The difference between the two curves is the Burgers vector.

the neighbouring grains. Similar to the case of dislocation pinning, the presence of irregularities may impede the sliding of the boundaries, which can only be overcome at high temperatures or under low-frequency loading. When the motion of the grain boundary is restricted, the accommodation of the irregularities is said to be elastic and the resulting behaviour is anelastic. Interestingly, the relaxation strength Δ of grain boundary sliding is independent on the grain size and, therefore, also on the past stress field and thermochemical conditions. The characteristic time τ is related to the grain size d as (Nowick and Berry, 1972; Karato and Spetzler, 1990)

$$\tau = \frac{d}{B_{\mathrm{s}} E} \,, \tag{2.27}$$

with B_{s} being the sliding mobility and E denoting the elastic modulus, as in the previous subsection. The sliding mobility is sensitive to the temperature and to the presence of impurities or secondary phases (Raj and Ashby, 1971). At high temperatures and low frequencies, the deformation accommodation at irregularities is viscous and results in viscoelastic behaviour. The timescale of viscous accommodation is then given by diffusion creep and its dependence on the grain size and temperature is approximately (Karato and Spetzler, 1990)

$$\tau_{\mathrm{vis}} \propto d^2 T \,. \tag{2.28}$$

We have seen that the two most important mechanisms responsible for the nonelastic behaviour of Earth mantle at seismic–wave frequencies depend on the local thermochemical conditions (through thermal activation) and on the past stress field (through the dislocation density and grain size). Both mechanisms also result in the transition between anelastic and viscoelastic deformation at high temperatures and low frequencies. These features will be reminded in the next subsection, where we discuss the relationship between the previously introduced rheological models and the seismological and geodetic measurements.

2.2.3 Empirically–based models

According to seismological and geodetic observations on a variety of timescales, the response of the Earth to small–strain excitations cannot be described by a purely elastic behaviour (e.g. Lau and Faul, 2019). The intrinsic friction in the Earth mantle results in attenuation and velocity dispersion of seismic waves (Karato and Spetzler, 1990, e.g.,), increase in the period of Chandler wobble (Anderson and Minster, 1979, e.g.,), and broadening of free–oscillation peaks (e.g., MacDonald, 1961). The comprehension of the mechanisms lying behind the observed phenomena is the key to the information on the structure and composition of the mantle. The investigation of Q^{-1} in the Earth is, however, marked by a substantial difficulty: the trade–off between its depth and frequency dependence. Since the early investigations of the attenuation in the Earth were

mostly concerned with the depth dependence of the internal friction—and since the frequency dependence is relatively weak compared to the effect of varying depth—it became conventional to treat Q^{-1} as frequency–independent in a broad range of seismic frequencies.

Absorption band model The gradual increase in the accuracy of measurements required the introduction of frequency–dependent models able to fit the data more precisely. Building on the observational evidence available in 1970s, Don L. Anderson and his colleagues (Liu et al., 1976; Anderson and Minster, 1979; Anderson and Given, 1982) proposed a model in which the internal friction Q^{-1} exhibits the following dependence on the loading frequency ω (see also Figure 2.3):

- At low frequencies ($\omega < \omega_1$), the internal friction increases linearly with increasing frequency
$$Q^{-1} \sim \omega$$
- Inside a distinct absorption band ($\omega \in [\omega_1, \omega_2]$), the internal friction follows a weak frequency dependence
$$Q^{-1} \sim \omega^{-\alpha}$$
with α in the range $0.1 - 0.4$.
- At high frequencies ($\omega > \omega_2$), the internal friction decreases with increasing frequency
$$Q^{-1} \sim \omega^{-1}$$

Specifically, the boundaries of the absorption band (ω_1, ω_2) depend on the thermochemical conditions in the mantle and they shift with the increasing depth (Liu et al., 1976; Anderson and Minster, 1979; Anderson and Given, 1982).

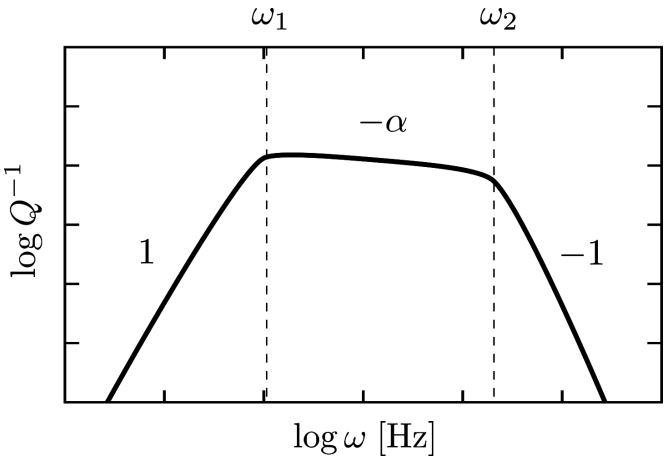

Figure 2.3: Schematic depiction of the absorption-band behaviour of the internal friction Q^{-1}.

High temperature background Since the attenuation in the Earth is closely related to the underlying microscopic mechanisms, an analogy of the seismic absorption band is also known in material science. Samples of various metals, when heated to sufficiently high temperatures below the melting point, exhibit exponential dependence of the internal friction on the temperature (e.g., De Batist, 1969; Castillo-Rodríguez et al., 2016). The same is also true for other materials, such as ceramics, silicates or ices (Schoeck et al., 1964; Lakki and Schaller, 1996; Farla et al., 2012; Cole, 2020). The full attenuation spectrum, plotted against the temperature, consists of Debye peaks (e.g., due to the presence of impurities) superimposed over the *high temperature background* (h.t.b.). The observations of h.t.b. in polycrystals can be attributed to the self–diffusion and the motion of dislocations in the entire sample (De Batist, 1969).

Written as a function of frequency, the internal friction corresponding to the h.t.b. can be expressed as (De Batist, 1969; Anderson and Minster, 1979)

$$Q^{-1}(\omega) = Q_0^{-1}(\omega\tau)^{-\alpha}\,, \tag{2.29}$$

where the characteristic time τ follows the Arrhenius–like dependence on temperature T,

$$\tau = \tau_0 \exp\left\{\frac{\mathcal{E}^*}{R_{\text{gas}}T}\right\}, \tag{2.30}$$

R_{gas} is gas constant, and $\mathcal{E}^*$ the activation energy for diffusion. This functional form of the internal friction corresponds to the *transient creep*, a phenomenon observed in microcreep experiments, where the sample is loaded by a constant (i.e., not periodic) stress (e.g., Andrade, 1910). The transient creep with time–dependent strain rate occurs in addition to the instantaneous elastic deformation and the steady–state viscous flow and leads to the following time dependence of the strain (Anderson and Minster, 1979):

$$\epsilon(t) = \epsilon_0 \left(\frac{t}{\tau_0}\right)^{\alpha} \exp\left\{-\frac{\alpha\mathcal{E}^*}{R_{\text{gas}}T}\right\}. \tag{2.31}$$

For the special choice of $\alpha = 0.3$, equation (2.31) is equivalent to the *Andrade creep equation* (Andrade, 1910; Anderson and Minster, 1979).

Viscoelasticity While the attenuation of seismic waves can be well approximated by the broad anelastic peak introduced in the absorption band model (e.g., Liu et al., 1976; Anderson and Minster, 1979; Minster and Anderson, 1981), the global response of the Earth at very low frequencies points out at the existence of a transition from the anelastic regime to a purely viscous behaviour (e.g., Yuen and Peltier, 1982). Among other arguments for the viscous deformation operating at long timescales, we should mention the maintenance of mantle convection—a phenomenon which is impossible under the assumption of anelastic rheology (Jeffreys, 1972, 1973). The transition from the anelastic behaviour to the viscous creep is also known from laboratory experiments (Nowick and Berry, 1972).

Yuen and Peltier (1982) note that while the conclusion that the long–term behaviour of the Earth mantle is viscous has been sufficiently confirmed by observation, an uncertainty still exists about the timescale of the anelastic–viscous transition and about the (non)linearity of the rheological law in the viscous regime. For instance, the characteristic timescale for mantle convection, where the mantle rheology is mostly viscous, are $1 - 100\,\mathrm{Myr}$ (Schubert et al., 2004). On the other hand, the timescale of global isostatic adjustment, $\sim 10^3\,\mathrm{yr}$, may be interpreted either as a manifestation of viscoelasticity or (although only marginally) as a manifestation of transient anelasticity (Peltier et al., 1980). The Chandler wobble, with a period of about 435 days, is already governed by the anelastic rheological law (Peltier et al., 1981; Sabadini and Vermeersen, 2004).

Owing to the enormous regions involved in the global deformation of the Earth and to the dependence of the relevant microscopic processes on the temperature, chemistry, and stress field, the viscoelastic behaviour may, in fact, act on all timescales of interest. Such consideration would soften the low–frequency cut–off at $\omega = \omega_1$ prescribed by the absorption band model. As suggested by Karato and Spetzler (1990), even the absorption band itself can be explained by dislocation unpinning and grain boundary sliding occurring at various times in the entire volume of the mantle. Different pinning points and irregularities may be overridden at different frequencies. Under this consideration, the transition from the anelastic to viscoelastic effect of grain boundaries and dislocations would be very gradual.

Extended mechanical models As we have seen earlier, the absorption band model represents the anelastic reaction of the mantle and is justified by the presence of various relaxation mechanisms with a range of characteristic times. Specifically, Minster and Anderson (1980) explain the seismic wave attenuation by the presence of dislocations with different lengths and lying in different depths (i.e., at different temperatures). To formalise the empirical conclusions, Anderson and Minster (1979) relates the absorption band model to a generalisation of the standard anelastic solid (SAS), prescribing an arbitrary distribution of characteristic times $\mathcal{D}(\tau)$. In accordance with equation (2.14), the dynamic compliance of the generalised SAS model is

$$\bar{J}(\omega) = J_\mathrm{U} + \delta J \int_0^\infty \mathcal{D}(\tau)\, \frac{1 - \mathrm{i}\omega\tau}{1 + \omega^2\tau^2}\, \mathrm{d}\tau\,. \tag{2.32}$$

A reconciliation of the observed absorption–band behaviour with the presumed viscoelasticity of the Earth at long periods can be achieved by introducing the generalised (or extended) Burgers model, as was initially done by Peltier et al. (1981) and Yuen and Peltier (1982). Identically to the "simple" Burgers model (equation (2.15)), the generalisation predicts a Maxwell–like behaviour at long timescales ($t \gg \tau_\mathrm{M}$). The response at short timescales is the same as in the case of the generalised SAS. The dynamic compliance of the generalised Burgers model

is thus (Faul and Jackson, 2005)

$$\bar{J}(\omega) = J_{\mathrm{U}} - \mathrm{i}\frac{\delta J}{\omega\tau_{\mathrm{M}}} + \delta J \int_0^\infty \mathcal{D}(\tau)\, \frac{1-\mathrm{i}\omega\tau}{1+\omega^2\tau^2}\, \mathrm{d}\tau\ . \tag{2.33}$$

The strong side of both the generalised SAS and the generalised Burgers model is the arbitrariness of $\mathcal{D}(\tau)$. The distribution of relaxation times can be prescribed to fit the observations or laboratory measurements, which may be composed not only of the h.t.b. but also from individual Debye peaks. Specifically, a peak in the distribution may arise due to plastic deformation or due to the presence of impurities in a sample (e.g., Karato and Wenk, 2018). On the other hand, owing to the necessity to prescribe the entire distribution, the two models may prove unwieldy for the application in pure numerical modelling of the global–scale behaviour of a planetary mantle. An alternative to the description using the spectrum of relaxation times is the original empirical model of transient creep introduced by Andrade (1910). In his work, Edward N. da Costa Andrade studied the stretch of metal wires subjected to constant tensile stress, which transitions from the instantaneous elastic deformation, through transient creep (labelled as "β–creep" by the author), to the steady–state viscous flow. He also noted that the effect of the transient phase is less prominent at higher temperatures (162 °C for a lead wire). The dynamic compliance corresponding to the previously mentioned Andrade creep equation is (Jackson, 2015)

$$\bar{J}(\omega) = J_{\mathrm{U}} - \mathrm{i}\frac{\delta J}{\omega\tau_{\mathrm{M}}} + \beta\Gamma(1+\alpha)(\mathrm{i}\omega)^{-\alpha} \tag{2.34}$$

where α and β are empirical parameters. The value of α used by Andrade (1910) was 0.3.

While the Andrade model was introduced as purely empirical, its few–parameter approach was also followed by Sundberg and Cooper (2010), who presented a rheological description of fine–grained peridotite. The authors based the model both on torsion oscillation and microcreep experiments and on theoretical considerations. Specifically, they included the effect of elastically accommodated grain boundary sliding and of transient diffusion creep. Sundberg and Cooper (2010) argue that neither the Andrade model nor the traditionally used version of generalised Burgers model (e.g., Minster and Anderson, 1981) are capable of properly describing the diminishing of h.t.b. and the occurrence of an attenuation peak at high frequencies ($\omega \gg 1\,\mathrm{Hz}$) or low temperatures. Although this is usually not the case for tidal loading of a planetary mantle (however, cf. Renaud and Henning, 2018), we include the Sundberg–Cooper rheology to our overview of physically justified models and write its dynamic compliance as (Renaud and Henning, 2018)

$$\bar{J}(\omega) = J_{\mathrm{U}} - \mathrm{i}\frac{\delta J}{\omega\tau_{\mathrm{M}}} + \beta\Gamma(1+\alpha)(\mathrm{i}\omega)^{-\alpha} + \delta J_{\mathrm{KV}}\frac{1-\mathrm{i}\omega\tau_{\mathrm{KV}}}{1+\omega^2\tau_{\mathrm{KV}}^2}\ . \tag{2.35}$$

As can be seen in equation (2.35), the Sundberg–Cooper model is a superposition of

the Andrade model and a Kelvin–Voigt element, characterising the high–frequency Debye peak. In addition to $J_{\rm U}$, δJ and $\tau_{\rm M}$, it is described by four parameters: by the original α and β of the Andrade rheology and by the compliance defect $\delta J_{\rm KV}$ and retardation time $\tau_{\rm KV}$ of the Kelvin–Voigt component.

2.2.4 Proper description of the tidal response

In the context of celestial mechanics, the tidal evolution of planetary or lunar orbits has traditionally been described by simplified models based on certain geophysical assumptions (Section 1.3.2). The fact that the internal friction Q^{-1} in the Earth mantle is almost frequency–independent on a wide range of seismic frequencies served as a justification for the *constant phase lag* and *constant geometric lag* models (e.g., Gerstenkorn, 1955; Goldreich, 1963; MacDonald, 1964; Kaula, 1964; Goldreich and Soter, 1966; Murray and Dermott, 1999). Similarly, the presumed inverse dependence of the internal friction on the frequency at long timescales was consistent with the *constant time lag* model (e.g., Alexander, 1973; Mignard, 1979; Hut, 1981; Correia and Laskar, 2010), which is otherwise inspired by the treatment of tides in binary stars. However, as explained in Section 1.3.2, the applicability of the traditional models is limited and the proper description of tidal phenomena requires the introduction of a rheologically–motivated tidal theory.

Maxwell model To begin with, a planet loaded at sufficiently low frequencies—or a body whose mantle viscosity is sufficiently small—can be conveniently characterised by the Maxwell viscoelastic model. Extending the 1d dynamical compliance from Figure 2.1c) to a 3d case, we arrive at

$$\bar{J}(\omega) = \frac{1}{\mu} - \frac{i}{\eta\omega} \,. \tag{2.36}$$

Note that we have now parameterised the rheological model by the dynamic viscosity η and the rigidity μ instead of the Maxwell time $\tau_{\rm M} = \eta/\mu$. The present formalism will be used throughout the rest of this work, if not stated otherwise. Interestingly, the application of Maxwell rheology to tidal phenomena dates back to Sir George H. Darwin. Darwin (1879) first derived a viscous counterpart to the theory developed by Lord Kelvin for the treatment of deformation of an elastic sphere subjected to a bodily force (Thomson and Tait, 1895). Then, using an equivalent of the principle of correspondence (considered, however, as a correspondence between the viscous and the "elasto–viscous" problem), he derived the yielding of a viscoelastic solid Earth and its implication for the height of the ocean tide.

Although the linear viscoelastic model of Darwin (1879) was not considered in later Darwin's work—and most of the twentieth–century tidal models included simplified constant–tide–lag assumptions[11]—the idea of deriving the tidal deformation from basic rheophysical considerations was revived by Ferraz-Mello (2013). In

[11]It should be, however, noted that in the studies dedicated solely to tidal heating, the Maxwell viscoelastic rheology was commonly in use (e.g., Peale and Cassen, 1978; Poirier et al., 1983; Segatz et al., 1988; Tobie et al., 2005b).

an approach labelled as the *creep tide theory*, the author studies the deformation and spin–orbital evolution of a sphere governed by Newtonian viscosity, and later superimposes his results over the contribution of elastic tide (Ferraz-Mello, 2013, 2015; Ferraz-Mello et al., 2020). Proceeding in a similar direction, Correia et al. (2014) apply the aforementioned Darwin's correspondence principle and consider the Maxwell model from the beginning. The authors also derive the equations for time–dependent gravity field coefficients and, similarly to Ferraz-Mello (2015), explore the stable spin states (resonant or pseudo-synchronous), the orbital evolution, and the shape of a tidally– and rotationally–deformed planet. The results of Correia et al. (2014) were later extended to planets with arbitrary obliquity by Boué et al. (2016).

Earth-like rheology In the context of the Darwin–Kaula theory (Darwin, 1880; Kaula, 1964, see also Section 1.3), the use of rheologically–motivated models was pioneered by Efroimsky and Lainey (2007). Efroimsky and Lainey point out at the parameterisation of seismic wave attenuation based on geophysical observations and remind the reader that the internal friction Q^{-1} is no longer considered as constant in seismological literature, neither is it considered as proportional to ω at tidal frequencies. The authors also provide arguments for the choice of the law $Q^{-1} \sim \omega^{-\alpha}$ at frequencies higher than $\sim 1\,\mathrm{yr}^{-1}$, based on empirical measurements. Building on the rheologically–motivated description, Castillo-Rogez et al. (2011) study the despinning of Iapetus assuming a composite model, in which they adopt Maxwell rheology at loading periods greater than the Maxwell time and Andrade rheology at shorter periods. Efroimsky (2012b) reparameterises the Andrade model (2.34) as

$$\bar{J}(\omega) = \frac{1}{\mu} - \frac{\mathrm{i}}{\eta\omega} + \frac{\mu^{\alpha-1}}{(\mathrm{i}\,\zeta\eta\omega)^{\alpha}}\,\Gamma(1+\alpha)\,, \tag{2.37}$$

where ζ is the ratio between the Andrade time τ_{A} and the Maxwell time τ_{M}, so that

$$\beta = \frac{\mu^{\alpha-1}}{(\zeta\eta)^{\alpha}}\,. \tag{2.38}$$

The magnitude of ζ (or of the Andrade time) depends on the damping mechanisms involved at given loading frequencies and amplitudes (Efroimsky, 2012b). We will follow the parameterisation with α and ζ in Chapters 3 to 5 and Chapter 7.

Complex Love numbers While the traditional tidal models (e.g., Kaula, 1964) assume that the Love number k_2 and the quality factor Q (or phase lag) are two independent quantities, the rheologically–motivated models imply that the height and the orientation of the tidal bulges are introduced in a consistent way. In the introduction to this section, we have mentioned that the internal friction Q^{-1} presents a link between the tidal response and the underlying microscopical mechanisms. However, it would be more appropriate to say that the understanding

of global dynamics of the Earth provides the key to the proper inclusion of the planet's reaction to tidal equations—the planet's reaction being parameterised by both the Love number and the quality factor (or phase lag). This is most naturally done by introducing the complex Love numbers (e.g., Castillo-Rogez et al., 2011, see also Section 1.3.2 around equation (1.38)). For a homogeneous spherical planet of radius R, surface gravity g, and average density ρ, the degree–l complex Love number can be calculated as

$$\bar{k}_l(\omega_{lmpq}) = \frac{3}{2(l-1)} \frac{1}{1+A_l} , \quad \text{where} \quad A_l = \frac{(2l^2+4l+3)\, \bar{\mu}(|\omega_{lmpq}|)}{lg\rho R} \, \mathrm{Sgn}\{\omega_{lmpq}\} . \tag{2.39}$$

In the above equation, reprinted from Section 1.3.2, we have used the already introduced complex rigidity $\bar{\mu}(\omega)$, which is related to the complex compliance by

$$\bar{\mu}(\omega) = \frac{1}{\bar{J}(\omega)} . \tag{2.40}$$

In the case of radially–stratified spherical bodies, the Love numbers cannot be calculated by the simple formula (2.39). Even for a two–layered interior model, we would need to take into account the contribution of both layers and the corresponding analytical formula would become impractically complex (Henning and Hurford, 2014). Nevertheless, the deformation and stress field, together with the additional potential induced by boundary deflections, can be calculated using the normal–mode theory (Takeuchi and Saito, 1972; Wu and Peltier, 1982; Sabadini and Vermeersen, 2004; Tobie et al., 2005b). Consequently, the complex Love number can be constructed from parameters corresponding to the incremental gravitational potential. A brief overview of this method, which will be also applied to the problems discussed in Chapters 3 to 5, is given in Appendix A.

2.3 Heat sources

The efficiency of microscopic processes lying behind the global dynamics depends on the local temperature. Planetary interiors are heated at their birth by the gravitational energy released upon their formation and differentiation; the remnant heating is then complemented by other heating mechanisms acting during the planet's lifetime. A principal source of energy, competing with the remnant heating in relevance (e.g., Korenaga, 2008), is the decay of radioactive isotopes. Additional sources acting in the Earth interior are also the latent heat extracted at exothermic phase transition and the compositional energy transformed to heat during the crystallisation and chemical separation of the inner core (Jaupart et al., 2007). Finally, for strongly tidally–loaded worlds, such as the close–in moons or exoplanets, the dominant heating mechanism is the tidal dissipation. In the following two subsections, we will review the calculation of radiogenic and tidal heating, the latter being of crucial importance in the rest of this work.

2.3.1 Radiogenic heating

Mantle convection in terrestrial planets of the Solar System is kept alive by the radioactive decay of elements and by the secular cooling of the interior[12] (Schubert et al., 2004). According to measurements of elemental abundances in the samples of CI carbonaceous chondrites and of the upper mantle minerals (Jaupart et al., 2007), the most important isotopes controlling the present–day radiogenic heating are ^{238}U, ^{235}U, ^{232}Th, and ^{40}K. Since all of the mentioned radioactive elements are incompatible, i.e., they resist inclusion into rock–forming minerals and they readily go into the liquid phase upon partial melting, the highest concentration of heat–generating radionuclides is found in the crust.

The total volumetric heat rate generated by radioactive decay can be expressed as (e.g., Schubert et al., 2004)

$$h^{\mathrm{rg}}(\vartheta,\varphi,r) = \sum_j h^{\mathrm{rg}}_{0,j}(\vartheta,\varphi,r)\ \exp\{-\lambda_j\ t\}\ , \tag{2.41}$$

where $\lambda_j = \log 2/\tau_{1/2,j}$ is the decay constant of radionuclide j and $\tau_{1/2,j}$ is the corresponding half–life. Symbol $h^{\mathrm{rg}}_{0,j}$ stands for the volumetric heat rate due to radionuclide j at time $t = 0$. The half–lives of uranium, thorium, and potassium are long enough ($\sim 1\,\mathrm{Gyr}$) to contribute to the planet's thermal evolution billions of years after its formation. Nevertheless, in the toddler years of the Solar System, the heat budget of the young planets was probably also controlled by short–lived isotopes, such as ^{26}Al or ^{60}Fe. The contribution of these elements might have been especially important for the early melting, differentiation, and outgassing of the planetary bodies (Lugaro et al., 2018).

2.3.2 Tidal heating

The second heating mechanism to be discussed in this section is the tidal dissipation. Although not relevant for present–day Earth, the importance of tidal dissipation rises drastically in bodies on close–in eccentric orbits. As an illustration, the averaged global heat flux from the surface of Jupiter's moon Io, orbiting approximately at 6 Jovian radii, is $> 2.5\,\mathrm{W\ m^{-2}}$, as compared to the same quantity for much bigger Earth, which is $0.09\,\mathrm{mW\ m^{-2}}$ (Veeder et al., 1994; Davies and Davies, 2010). Tidal dissipation is presumably also the leading source of energy on close–in terrestrial exoplanets orbiting on tighter orbits than the innermost Solar System planet, Mercury. Moreover, while the previously discussed radiogenic heating dies out with time, as the radioactive isotopes decay into stable isotopes, tidal heating may prevail even for the entire lifetime of the system, provided the planet is protected from orbital circularisation, spin–orbit synchronisation, and/or alignment of its spin axis with the normal to the orbital plane.

Global heat rate The average heat rate produced by the dissipation in the entire volume of the planet over one orbital period can be written as (Segatz et al.,

[12]The radiogenic contribution to the heat flux measured at the Earth surface is usually expressed by the convective Urey ratio *Ur* (Christensen, 1985).

1988; Efroimsky and Makarov, 2014)

$$\bar{P}^{\rm tide} = -\sum_{l=2}^{\infty} \frac{(2l+1)\,n}{8\pi^2 \mathcal{G} R} \int_0^{T_{\rm orb}} \int_S \delta\Phi_l(R,\vartheta,\varphi,t)\, \frac{\partial \Phi_l(R,\vartheta,\varphi,t)}{\partial t}\, {\rm d}S\, {\rm d}t\,, \tag{2.42}$$

where Φ_l and $\delta\Phi_l = |\bar{k}_l(\omega)|\,\Phi_{l,\rm lag}$ are the degree–l tidal and additional potential evaluated at the planet's surface[13]. The subscript "lag" indicates that the argument of the disturbing potential should be complemented with the tidal phase lag ε. If we express the two potentials in the form of a Darwin–Kaula expansion, make use of the orthogonality of associated Legendre polynomials, and average the tidal heat rate over the precession period of the planet's spin axis, equation (2.42) can be rewritten into an analytical form

$$\bar{P}^{\rm tide} = -\frac{\mathcal{G} m_*^2}{a} \sum_{lmpq} \left(\frac{R}{a}\right)^{2l+1} (2-\delta_{m0})\, \frac{(l-m)!}{(l+m)!} \left[\mathcal{G}_{lpq}(e)\right]^2 \left[\mathcal{F}_{lmp}(\beta)\right]^2 \omega_{lmpq}\, {\rm Im}\{\bar{k}_l(\omega_{lmpq})\}\,. \tag{2.43}$$

The full derivation of this formula can be found in Efroimsky and Makarov (2014)[14]. A special case of $l = 2$, used in our work, is provided in Appendix B.1. Note that equation (2.43) holds for an arbitrary obliquity and orbital eccentricity as well as for an arbitrary spin rate, provided that the overall deformation can be described by a linear tidal theory.

Heat rate per unit volume A detailed analysis of thermal evolution may also require the assessment of tidal dissipation in different depths of the planet (e.g., Tobie et al., 2005a; Beuthe, 2013; Henning and Hurford, 2014) or even on a computational grid spanning the entire mantle (e.g., Běhounková et al., 2010). For the sake of completeness, we also discuss here the calculation of volumetric tidal heating, which is implemented in our numerical model, although not applied to the studies presented in Chapters 3 through 5. From the definition of volumetric energy dissipation in viscoelastic continuum (e.g., Schubert et al., 2004), we have (see also Tobie et al., 2005a; Sotin et al., 2009)

$$h^{\rm tide}(\vartheta,\varphi,r,\omega) = {\rm Re}\Big\{\bar{\boldsymbol{\sigma}}^{\rm D}(\vartheta,\varphi,r,\omega) : \dot{\bar{\boldsymbol{\epsilon}}}^{\rm D}(\vartheta,\varphi,r,\omega)\Big\}\,, \tag{2.44}$$

where $\bar{\boldsymbol{\sigma}}^{\rm D} = 2\bar{\mu}\bar{\boldsymbol{\epsilon}}^{\rm D}$ is the deviatoric part of the incremental Cauchy stress tensor and $\dot{\boldsymbol{\epsilon}}$ is the deviatoric part of the incremental strain rate tensor. The components

[13]Here, we assume that the degree–l additional potential is proportional to the degree–l tidal potential (at earlier time t), the coefficient of proportionality being the corresponding Love number. In other words, we are using the linear tidal theory, as introduced by Darwin (1880) and Kaula (1964). It should be noted that the assumption of linearity is violated at very high tidal strains or if the planet's internal friction depends on the amplitude (Goldreich, 1963). Furthermore, the Darwin–Kaula expansion cannot be applied to planets with considerable lateral heterogeneities, which would require the use of 3d interior models. Here, we only consider homogeneous or radially–stratified bodies, i.e., models of 1d interior structure.

[14]Specifically, the full derivation is given in the Appendix H of the *arXiv* version of Efroimsky and Makarov (2014).

of the strain tensor can be related to the local tidal potential and to the local deformations and tractions, calculated with the help of the normal mode theory. For the sake of clarity, we refer the reader to Appendix B.2, which provides the details of the calculation. A more elaborate derivation of volumetric heating, also based on the normal mode theory and applicable mainly to synchronously–rotating bodies, was presented by Tobie et al. (2005a).

2.4 Mantle convection

In addition to the primordial or externally–induced heating mechanisms, the planet's heat budget is controlled by cooling through the surface. Depending mainly on the planet's size, presence of heat sources, and on the core–surface temperature contrast, the heat can be carried either by conduction[15] or by convection, with possible contributions from large–scale volcanism and melt migration. Here, we briefly discuss mantle convection, as it plays a primary role in the thermal evolution of terrestrial planets and large moons across the Solar System (e.g., Schubert et al., 2004).

Stated simply, the global energy balance of the planetary mantle can be expressed by the equation (e.g., Schubert et al., 2004; Breuer and Spohn, 2006)

$$\rho_{\mathrm{m}} c_{\mathrm{m}} V_{\mathrm{m}} \frac{\partial T}{\partial t} = V_{\mathrm{m}} h_{\mathrm{m}} - q_{\mathrm{m}} A_{\mathrm{m}} + q_{\mathrm{c}} A_{\mathrm{c}} \,, \tag{2.45}$$

where ρ_{m} is the average mantle density, c_{m} the specific heat of the mantle, V_{m} marks the volume of the mantle, T the volume–averaged mantle temperature, and h_{m} is the volumetric heat rate of arbitrary origin. Moreover, A_{c}, A_{m} denote the outer surface area of the core and the mantle, respectively, and q_{c}, q_{m} are the corresponding average heat fluxes, the first flowing from the core to the mantle and the second from the mantle to the planet's surface. As we can deduce from equation (2.45), the thermal evolution of a planet depends on a multitude of factors, including the efficiency of heat transfer through the surface and the core–mantle boundary (CMB), the temperature– and pressure–dependent mineralogical composition, the presence and significance of various heating mechanism, and, of course, the size of the mantle.

The heat transfer from the core into the mantle or from the mantle to the outer surface is controlled by the thicknesses and conductivities of the thermal boundary layers (TBLs). Thermal boundary layers, transferring heat mainly by conduction, are responsible for the steepest changes of temperature in the system and the analysis of their stability provides a basic insight into the mantle dynamics. Although the thermal and chemical convection in planetary mantles is better treated by 3d numerical modelling, the use of parameterised models based on the boundary layer theory permits the understanding of its main aspects and

[15] If permitted by the transparency of minerals in the IR, the heat can be also transferred by radiation. This contribution might be particularly important in the lower mantle (e.g., Matyska and Yuen, 2005).

the incorporation of the thermal evolution to coupled simulations (see also the discussion in Chapter 4). In the parameterised models, the thickness of TBLs can be related to the *Rayleigh number* (e.g., Solomatov, 1995), which expresses the vigour of convection[16],

$$Ra = \frac{\alpha_{\mathrm{m}} \rho_{\mathrm{m}} g_0 \Delta T d^3}{\eta_{\mathrm{m}} \kappa_{\mathrm{m}}} \,. \tag{2.46}$$

In the above definition, α_{m} stands for the thermal expansivity of mantle material, g_0 is the surface gravity, ΔT symbolises the temperature drop across the convecting layer, d is the convecting layer's thickness, η_{m} the mantle viscosity, and κ_{m} the diffusivity.

Mantle convection is enabled by the viscous flow of material under high pressures and high temperatures. In the upper TBL, where temperature decreases steeply towards the surface, the material becomes stiff and behaves elastically. Depending on the level of participation of the upper TBL on the global dynamics, the convection regime can be divided into *stagnant–lid* and *mobile–lid*[17] (e.g., Weller et al., 2015). In the stagnant–lid regime, which is most common among the Solar System planets and large moons, only the lowermost parts of the upper TBL participate in the convection and the surface heat flux is thus strongly controlled by the conductivity of the "lid". The stagnant–lid regime arises as a consequence of strong temperature dependence of the mantle viscosity (e.g., Solomatov, 1995), that can be described by the Arrhenius law:

$$\eta_{\mathrm{m}} = \eta_0 \exp\left\{ \frac{\mathcal{E}^* + pV^*}{R_{\mathrm{gas}} T} \right\} \,, \tag{2.47}$$

where η_0 is a reference viscosity (a pre–exponential factor), $\mathcal{E}^*$ and V^* are activation energy and volume, respectively, R_{gas} is universal gas constant, and p denotes pressure. In the mobile–lid regime, the entire upper TBL participates in the convection and the thermal evolution of the mantle is also affected by the descent of the cold slabs formed by the near–surface material. As such, cooling in the mobile–lid regime is more efficient than cooling in the stagnant–lid regime (Schubert et al., 2004). Furthermore, the recycling of the entire upper TBL also guarantees the maintenance of important geochemical cycles, stabilising the planet's climate (e.g., Walker et al., 1981).

A manifestation of the mobile–lid convection in the Earth is the plate tectonics: the upper TBL, i.e., the lithosphere, is broken into a number of plates that are continuously being created at mid–ocean ridges and consumed by the mantle at

[16]We note that the given definition of the Rayleigh number characterises a system heated from below. This definition is also used by the parameterised models that will be adopted in Chapters 4 and 5. An alternative definition of the *internal heating Rayleigh number*, which quantifies the contribution of volumetric heat sources to the vigour of convection, is given, e.g., in Schubert et al. (2004).

[17]In addition to the two regimes, there is the possibility of an episodic or quasi–periodic character of convection, in which the periods of stagnant–lid are combined with periods of mantle overturn (Moresi and Solomatov, 1998; Weller et al., 2015).

subduction zones (Schubert et al., 2004). The motion of the lithospheric plates is—for most of their life—horizontal. On the other hand, the lowermost continental lithosphere may be recycled by vertical motion, through delamination.

With respect to terrestrial exoplanets, neither the probability of plate tectonics, nor the actual mantle convection regime can be uniquely determined. The dynamical processes in the mantle depend on too many unknowns and it is not even possible to draw conclusions from the size of the planet. For the simple parameterised models, the vigour of convection—and the stresses in the lithosphere, leading to its eventual breaking—can be estimated from the Rayleigh number (2.46). Such estimates would lead to the assumption, that terrestrial exoplanets bigger than the Earth should strongly favour plate tectonics (e.g., Valencia et al., 2007; Valencia and O'Connell, 2009). An opposing view, presented, e.g., by the numerical simulations of O'Neill and Lenardic (2007), predicts that the low convective stresses at the upper mantle of large terrestrial bodies decrease the probability of mobile–lid convection. The mantle dynamics can be also affected by other factors, such as the interior structure, depth–dependence of viscosity, and the evolution of volumetric heating (e.g, van Heck and Tackley, 2011; Stamenković et al., 2012; Noack and Breuer, 2014; Noack et al., 2014). We will thus conclude that the nature of convection on terrestrial exoplanets is—and most probably also will be in the near future—an unresolved question.

2.5 Concluding remarks

Although the information about the surface and interior conditions of terrestrial exoplanets is still very scarce, a combination of promising characterisation techniques and numerical modelling provides an insight into the basic characteristics of these distant worlds. Since we are particularly interested in the tidal response of rocky bodies, a large portion of this chapter was dedicated to the deformation mechanisms acting in the Earth and to their rheological description. We have seen that the tidal response at the relevant frequencies is weakly frequency–dependent and out of several rheological models, it is most practically described by the few–parameter Andrade rheology. In the rest of the chapter, we have discussed the radiogenic and tidal heating, that enters the simplified equation of energy balance (2.45) and presents an important driving mechanism for mantle convection. The overview was then closed by several thoughts about the thermal evolution.

By finishing Chapter 2, we have also come to the end of the theoretical part of this work. The following chapters are dedicated to the applications of the theoretical tools introduced up to now. Specifically, the next chapter serves as a transition between the grey theory and the green tree of thermal–orbital calculations: We will explore the parameter dependence of the tidal torque and tidal dissipation. The keywords that will be carried from Chapter 2 to Chapter 3 are the Maxwell and Andrade rheology, the core mass fraction, and the tidal heat rate.

3. Tidal torque and tidal heat rate

Interweaving the information given in the first two chapters of this work, we may slowly approach the exploration of the tidal effects in viscoelastic (and anelastic) bodies. The first part of the third chapter is dedicated to the analysis of the secular tidal torque in the Maxwell and the Kelvin–Voigt rheologies. In particular, we will be interested in the frequency dependence of the tidal torque and in the effect of the planet's size and rheological parameters. The second part then focuses on a model planet described by the Andrade rheology, which will be explored by a numerical model. The aim of this study is to gain intuition in the parameter space relevant to the tidal evolution of terrestrial exoplanets.

We note that most of Chapter 3 was adapted from Section 6 and Appendix B of Walterová and Běhounková (2020).

3.1 Parameter dependence of the tidal torque

A degree–2 secular tidal torque acting on a moon or planet with zero obliquity can be expressed from equation (1.64) as an infinite sum

$$\mathcal{T}_2 = \sum_{q=-\infty}^{\infty} \mathcal{T}_{220q} = -K \sum_{q=-\infty}^{\infty} \left[\mathcal{G}_{20q}\right]^2 \mathrm{Im}\left\{\bar{\mathrm{k}}_{220\mathrm{q}}(\omega_{220\mathrm{q}})\right\} , \tag{3.1}$$

with

$$K = \frac{3}{2}\frac{\mathcal{G}m_*^2 R^5}{a^6} .$$

On the following lines, we will explore the parameter dependence of the tidal torque in the most simple rheological models introduced in Section 2.2.1: the Maxwell model and the Kelvin-Voigt model.

Maxwell rheology In the simplified case of a homogeneous spherical body governed by the Maxwell rheology, we may write the imaginary part of the complex Love number as (e.g., Castillo-Rogez et al., 2011)

$$\mathrm{Im}\left\{\bar{\mathrm{k}}_2(\omega)\right\} = -\frac{57}{4}\left(\frac{\rho \mathrm{g R}\eta\omega}{\mu^2} + \frac{19\eta\omega}{\mu} + \frac{361}{4}\frac{\eta\omega}{\rho \mathrm{g R}} + \frac{\rho \mathrm{g R}}{\eta\omega}\right)^{-1} , \tag{3.2}$$

where ω is the tidal frequency of the given mode (equation (1.33)).

To emphasise the frequency dependence of this expression and analyse the stability of higher spin–orbit resonances, we further simplify the notation of

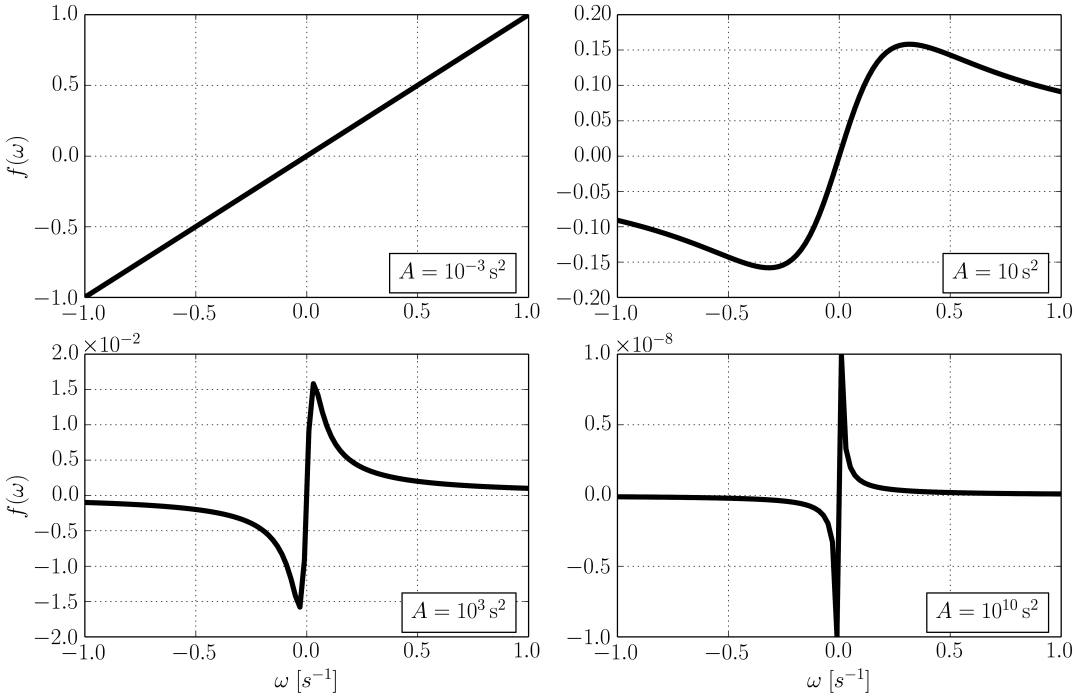

Figure 3.1: Frequency dependence of the kink–shaped function $f(\omega) = 1/(A\omega + \omega^{-1})$ for four values of A. Note the different y–ranges of the individual panels.

equation (3.2) and rewrite it to the form

$$\mathrm{Im}\left\{\bar{\mathrm{k}}_2(\omega)\right\} = -\mathrm{K}'\,\mathrm{f}(\omega) = -\frac{\mathrm{K}'}{\mathrm{A}\omega + \frac{1}{\omega}}\ , \tag{3.3}$$

where we substituted

$$K' = \frac{57}{4}\frac{\eta}{\rho g R} \qquad \text{and} \qquad A = \frac{\eta^2}{\mu^2}\left(1 + \frac{19}{2}\frac{\mu}{\rho g R}\right)^2\ .$$

The function $f(\omega)$ is responsible for a kink–shaped torque around spin–orbit resonances, which ensures their stability in linear viscoelastic or anelastic rheological models (Makarov and Efroimsky, 2013; Noyelles et al., 2014). Specifically, the functional dependence of $f(\omega)$ on the frequency ω is given by the coefficient A, i.e., by a combination of rheological and physical parameters of the planet. An illustration of the frequency dependence of $f(\omega)$ for different values of A is given in Figure 3.1. Depending on the relative magnitude of these quantities, we may delimit two regions in the parameter space (see also Efroimsky, 2012b):

$$\frac{19}{2}\frac{\mu}{\rho g R} \ll 1 \qquad \text{self–gravity–dominated regime} \qquad A \approx \tau_{\mathrm{M}}^2\ ,$$

$$\frac{19}{2}\frac{\mu}{\rho g R} \gg 1 \qquad \text{rheology–dominated regime} \qquad A \approx \left(\frac{19}{2}\frac{\eta}{\rho g R}\right)^2\ .$$

For Earth–like planets, the boundary between the self–gravity–dominated and

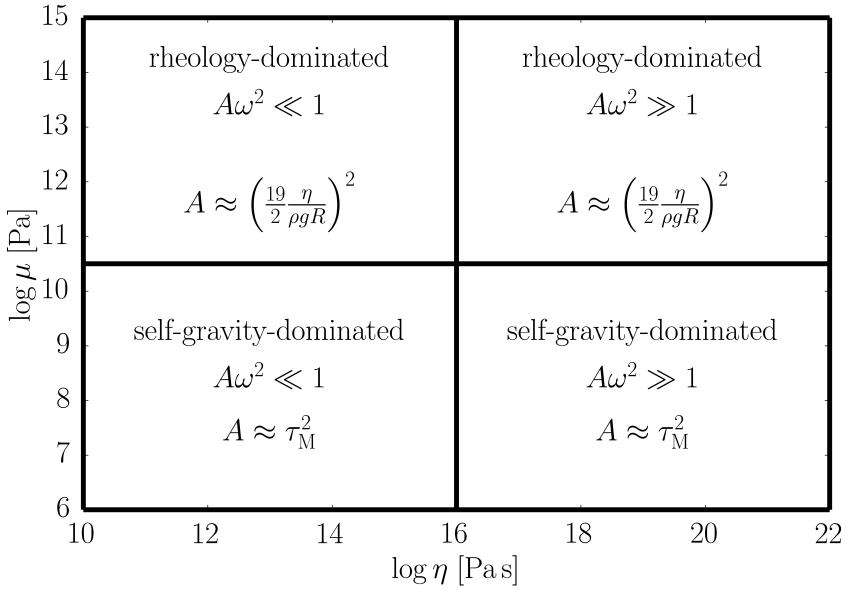

Figure 3.2: Estimate of the regions corresponding to different rheological and frequency regimes for an Earth–sized planet described by the Maxwell model. The x–range and y–range were chosen to match the ranges of parameters considered in Figures 3.3 to 3.5. The exact position of the boundary between the low–frequency and the high–frequency regime depends on the loading frequency.

rheology–dominated regions lies at $\mu \approx 10^{10}\,\mathrm{Pa}$. In the rheology–dominated regime, tidal torque is determined solely by the planet's viscosity and does not depend on the rigidity. The same behaviour is also predicted for small bodies, such as asteroids (Efroimsky, 2015), as long as their reaction can be described by the Maxwell rheology. In the self–gravity–dominated regime, on the other hand, the shape of the kink function (3.3) is determined by the Maxwell time $\tau_{\mathrm{M}} = \eta/\mu$. While the parameter dependence of A in the two regimes might be different, the same value of A should always yield the same behaviour of $f(\omega)$ around zero.

Depending on the absolute magnitude of A and on the loading frequency ω, we may also distinguish two limit cases,

$$\begin{aligned} A\omega^2 \ll 1 \qquad &\Rightarrow \qquad f(\omega) \approx \omega \,, \\ A\omega^2 \gg 1 \qquad &\Rightarrow \qquad f(\omega) \approx \frac{1}{A\omega} \,. \end{aligned}$$

The first case, if attained in the self–gravity–dominated regime, corresponds to the weak friction approximation, used originally for the description of tides in binary stars (e.g., Alexander, 1973; Hut, 1981), or to the constant time lag model (e.g., Mignard, 1979; Correia and Laskar, 2010). A summary of the two rheological regimes and the two frequency regimes is sketched in Figure 3.2, which indicates the expected behaviour of the model planet studied later in this chapter (Table 3.1).

The secular tidal torque (3.1) is, in fact, a weighted sum of the kink–shaped functions $f(\omega)$, centred around frequencies ω_{220q}. Standing alone, each kink would cross zero exactly at a half–integer spin–orbit resonance, such as 1:1, 3:2, and so on. However, when multiplied by the coefficients $[\mathcal{G}_{20q}(e)]^2$ and summed together, the positions of their zero crossings get slightly shifted from the exact resonances—and, in some cases, they do not cross zero at all. Later in this chapter, we will explore the highest spin–orbit resonances for which the tidal torque for prescribed model parameters still crosses zero.

For the sake of illustration, let us also derive a stability criterion for the 3:2 resonance. Assuming a homogeneous spherical planet governed by the Maxwell rheology, we may rewrite the secular tidal torque expanded to the second order in orbital eccentricity as

$$\mathcal{T}_2 = K_2 \left\{ f(2n - 2\dot{\theta}) + e^2 \left[\frac{1}{4} f\left(n - 2\dot{\theta}\right) - 5f\left(2n - 2\dot{\theta}\right) + \frac{49}{4} f\left(3n - 2\dot{\theta}\right) \right] \right\} , \tag{3.4}$$

where

$$K_2 = K\,K' . \tag{3.5}$$

The frequencies $\left(n - 2\dot{\theta}\right)$, $\left(2n - 2\dot{\theta}\right)$ and $\left(3n - 2\dot{\theta}\right)$ correspond to the 1:2, 1:1 and 3:2 resonances, respectively. Note that in the low–eccentricity case, when $e \lesssim 0.1$, the largest term in the expansion is the 1:1 resonance with prefactor $(1 - 5e^2)$. To the right from this resonance, $f(2n - 2\dot{\theta})$ is negative. Since the stability of the 3:2 resonance requires that $\mathcal{T}_2$ crosses zero in its vicinity, we are seeking the parameters for which the maximum of the 3:2 kink is nonnegative. If we neglect the contribution of the term corresponding to the 1:2 resonance, the problem reduces to a comparison between the 1:1 and the 3:2 components. The maximum of the 3:2 component lies at $\dot{\theta} = \frac{3}{2}n - \frac{1}{2}\sqrt{\frac{1}{A}}$. Thus, the 3:2 resonance is theoretically stable whenever

$$(1 - 5e^2)\, f\left(-n + \sqrt{\frac{1}{A}}\right) + \frac{49}{4} e^2\, f\left(\sqrt{\frac{1}{A}}\right) > 0 . \tag{3.6}$$

If we further require that the maximum of the 3:2 component is positioned to the right from the 1:1 resonance, the above inequality is solved with

$$\sqrt{A} > \frac{29e^2 + 4 + 4\sqrt{1 - 10e^2 - \frac{2001}{16}e^4}}{49e^2 n} \approx \frac{8}{49e^2 n} . \tag{3.7}$$

We recall that this condition has been derived with the explicit assumption of small eccentricity ($e \lesssim 0.1$) and holds only for a homogeneous body governed by the Maxwell rheology. A similar analysis can also be performed for higher eccentricities and other spin–orbit resonances (with a higher–order expansion of the secular tidal torque), as well as for different rheological models. Specifically, the additional terms in the Andrade model, when compared to the Maxwell model, make the stability criterion stricter and more complex than in this illustrative case.

Kelvin–Voigt rheology Although the overall response of planetary bodies is better described by rheological models accounting for gradual creep, it might be illustrative to also derive the tidal torque for the Kelvin–Voigt rheology, which accounts for anelastic attenuation in the medium. In this case, we may write the imaginary part of the complex Love number as

$$\mathrm{Im}\left\{\bar{\mathrm{k}}_2(\omega)\right\} = -\mathrm{K}''\,\mathrm{g}(\omega) = -\frac{\mathrm{K}''}{\omega + \frac{\mathrm{B}}{\omega}} \tag{3.8}$$

with

$$K'' = \frac{3}{19}\frac{\rho g R}{\eta} \qquad \text{and} \qquad B = \frac{\mu^2}{\eta^2}\left(\frac{2}{19}\frac{\rho g R}{\mu}\right)^2\left(1 + \frac{19}{2}\frac{\rho g R}{\mu}\right)^2 .$$

Note that function $g(\omega)$ exhibits the same kind of behaviour around zero as function $f(\omega)$ and it contributes to similar stabilisation of the spin–orbit resonances. However, the two limit cases, corresponding to the self–gravity–dominated and the rheology–dominated regimes, are quite different. The character of the two regimes can be deduced from the following expressions:

$$\begin{aligned}
&\frac{19}{2}\frac{\mu}{\rho g R} \ll 1 \qquad \text{self–gravity–dominated regime} \qquad && B \approx \left(\frac{2}{19}\frac{\rho g R}{\eta}\right)^2 , \\
&\frac{19}{2}\frac{\mu}{\rho g R} \gg 1 \qquad \text{rheology–dominated regime} && B \approx \tau_{\mathrm{KV}}^{-2} .
\end{aligned}$$

Contrary to the Maxwell model, which predicts that the reaction of a body in the rheology–dominated regime does not depend on the rigidity, the Kelvin–Voigt model concludes the same for the self–gravity–dominated regime. Moreover, in the rheology–dominated regime of the Kelvin–Voigt body, the shape of the kink function $g(\omega)$ is determined by the retardation time[1] $\tau_{\mathrm{KV}} = \eta/\mu$. As in the case of the Maxwell model, the combination of parameters leading to the same value of B should also result in the same tendency of $g(\omega)$ around zero—and in the stability of the same spin states.

Finally, let us divide the frequency range into two regimes:

$$\begin{aligned}
&\frac{\omega^2}{B} \ll 1 \qquad \Rightarrow \qquad g(\omega) \approx \frac{\omega}{B} , \\
&\frac{\omega^2}{B} \gg 1 \qquad \Rightarrow \qquad g(\omega) \approx \frac{1}{\omega} .
\end{aligned}$$

Here, the slope of the linear frequency dependence of $g(\omega)$ in the low–frequency regime is modulated by B, while in the high–frequency regime, the function $g(\omega)$ approximately equals $1/\omega$. For very high values of B, the planet operates in the

[1]The relaxation time of the Maxwell model and the retardation time of the Kelvin–Voigt model were introduced in Chapter 2. Note that although we use the same notation for the viscosity η and the rigidity μ in the two rheologies, the physical mechanism behind these quantities differs between the Maxwell and the Kelvin–Voigt model.

"low–frequency" regime for a wide range of frequencies and the planet is prone to pseudo–synchronisation.

Although we have only focused on the parameter dependence of the secular tidal torque, the individual rheological models also imply distinct parameter dependencies of the tidal heating. A thorough overview of the tidal heating maps for all relevant rheological models can be found in Henning et al. (2009) and Renaud and Henning (2018). The specific case of tidal heating and highest stable spin states in the Andrade rheology will be discussed in the following section.

3.2 Tidal locking and tidal heating

In this section, we are going to investigate the effect of rheological and orbital parameters on the tidal dissipation and tidal locking of a generic terrestrial exoplanet hosted by a red dwarf (an M–type star). Planetary systems around M–type stars are a particularly interesting target, since their conventional habitable zone lies very close to the primary and, therefore, overlaps with the region of strong tidal loading (e.g., Běhounková et al., 2011). Knowledge of the thermal and orbital state of such bodies may serve as additional information for the evaluation of planetary habitability (e.g., Wandel, 2018; Godolt et al., 2019).

The secular thermal and orbital evolution of close–in exoplanets is determined by the rate of the energy dissipation and by the planet's spin rate. Furthermore, the rotation state in which the planet resides also affects its surface conditions and, potentially, the evolution of the climate and habitability prospects. Tidal locking into synchronous rotation with its extreme insolation pattern results in essentially different climate forcing than faster, nonsynchronous rotation (e.g., Dobrovolskis, 2007, 2013, 2015). To better understand the general parametric dependencies of the tidal dissipation and of the spin rate, we perform several numerical studies, in which we only explore the parameter space: therefore, we do not take into account the planet's internal dynamics, variations of orbital elements, and changes of the interior structure (as will be done in Chapter 4). Throughout this section, the only variables evolving in time are the spin rate and the tidal heating. The quantities plotted in the subsequent figures are stationary states to which the model planet evolves.

Our model planet consists of three layers: a liquid core with low, finite viscosity, a viscoelastic[2] mantle governed by the Andrade rheology, and an elastic lithosphere of constant thickness. The rheological properties of the planet, as well as other model parameters, are listed in Table 3.1. Among other parameters with obvious meaning, Table 3.1 includes the core mass fraction CMF, which is defined as the ratio of the core mass to the total mass of the planet. The top radii of the core and of the mantle with given densities are chosen to match the total radius and the given CMF.

[2]Since the Andrade model also accounts for the steady–state viscous creep, it can be classified as a viscoelastic rheology.

Table 3.1: Parameters of the generic terrestrial exoplanet

Parameter	Definition	Value	Unit
m_*	Mass of the host star	0.1	$m_\odot$
a	Semi–major axis	0.04	AU
e	Eccentricity	0.0 to 0.5	—
ρ_c	Core density	9000	kg m^{-3}
η_c	Core viscosity	10^{-3}	Pa s
μ_c	Core rigidity	10^{-10}	Pa
ρ_m	Mantle density	5000	kg m^{-3}
η_m	Mantle viscosity	10^{10} to 10^{22}	Pa s
μ_m	Mantle rigidity	10^{6} to 10^{15}	Pa
ρ_lid	Lithosphere density	3000	kg m^{-3}
μ_lid	Lithosphere rigidity	7×10^{10}	Pa
d_lid	Lithosphere thickness	50	km
CMF	Core mass fraction	0.1 to 0.7	—
R	Outer radius of the planet	0.2 to 1.5	$R_\oplus$
α	Parameter of the Andrade model	0.3	—
ζ	Parameter of the Andrade model	1	—

Throughout the parametric studies, the planet is first allowed to despin from an arbitrarily chosen initial spin–orbit ratio $\dot{\theta}/n = 5.6$ to the first (i.e., highest) stable spin state, in which the derivative $\ddot{\theta}$ decreases below a given limit $\delta = 10^{-16}$. Tidal heating in the equilibrium spin state is then calculated by formula (2.43) for $l = 2$. In order to normalise the tidal heat rate to the planet's surface, we introduce the average surface tidal heat flux,

$$\Phi_\mathrm{tide} = \frac{\bar{P}^\mathrm{tide}}{4\pi R^2} \,, \tag{3.9}$$

which facilitates the comparison with total heat flux at the surface of the Earth (0.09 mW m^{-2}; Davies and Davies, 2010) or Io (> 2.5 W m^{-2}; Veeder et al., 1994).

3.2.1 Effect of the rheological parameters

In this subsection, we consider an Earth–sized model planet ($R = 1R_\oplus$) with Earth–like core mass fraction (CMF = 0.3) and investigate the effect of varying mantle rigidity and viscosity for three different orbital eccentricities: 0.05, 0.2 and 0.4. Figures 3.3–3.5 depict the regions of the parametric space with different highest stable spin states and the corresponding surface tidal heat fluxes. Although in most of the cases the model planet despins into a spin–orbit resonance, we note that at very low mantle viscosities, the stable spin state is pseudo–synchronous,

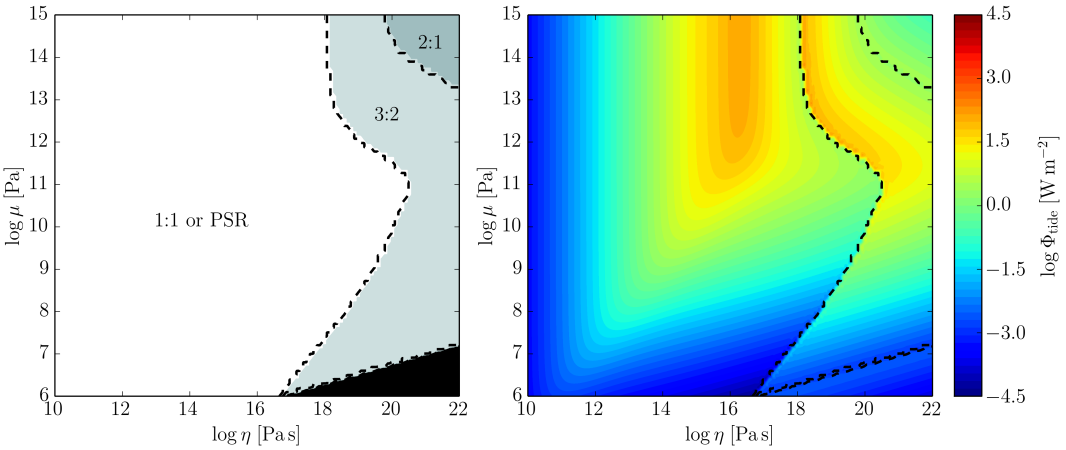

Figure 3.3: The highest stable spin-state (*left*) and the surface tidal heat flux (*right*) of the model planet with orbital eccentricity $e = 0.05$. The caption "PSR" corresponds to pseudo–synchronous rotation with spin-orbit ratio $\dot{\theta}/n \approx 1.015$. Triangular region in the lower right corner of both panels indicates combinations of parameters for which the tidal despinning takes more than 1 Gyr.

with spin–orbit ratio approximately given by (e.g., Dobrovolskis, 2007)

$$\frac{\dot{\theta}}{n} \approx 1 + 6e^2 \,. \tag{3.10}$$

Nevertheless, in the illustrations, we include the region of pseudo–synchronous rotation ("PSR") into the region of the closest spin–orbit resonance.

A common feature of all the model cases is the complex shape of boundaries between different stable spin states. While for high mantle rigidities ($> 10^{12}$ Pa) the first stable spin state depends almost exclusively on the viscosity, for low mantle rigidities ($< 10^{10}$ Pa) it depends on both of the rheological parameters. If evolving from this region, a planet with initially low mantle rigidity would be more susceptible to tidal locking into a high spin–orbit resonance, which could be eventually destabilised by an increase in the rigidity at constant viscosity. The transition between the two tendencies in tidal locking is characterised by a heap in the boundary between different high spin–orbit resonances. The behaviour decribed can be understood by investigating the parameter dependence of tidal torque (1.64), as we have done earlier for the simplest nonelastic models (see Figure 3.2). Specifically, the low–rigidity case corresponds to a self–gravity–dominated deformation regime, while the high–viscosity case is governed by the planet's rheology.

Another pattern observable in Figures 3.3-3.5 is the eccentricity dependence of width of the regions with different highest stable spin state. At high orbital eccentricity ($e = 0.4$) and for an arbitrarily chosen rigidity of 10^{12} Pa, the change in the mantle viscosity from 10^{18} to 10^{16} Pa s would result in a steep cascade of spin state transitions. For less eccentric orbits, on the other hand, the evolution

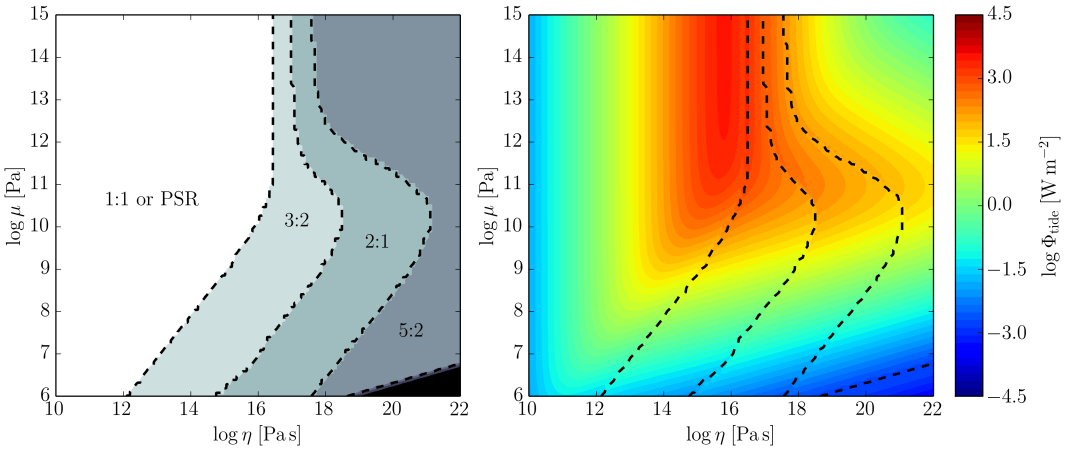

Figure 3.4: Same as Figure 3.3, but for orbital eccentricity $e = 0.2$. PSR corresponds to $\dot{\theta}/n \approx 1.24$.

of spin rate would be much more gradual.

The effect of the mantle rigidity and viscosity on the surface tidal heat flux of synchronously rotating moons and exoplanets has already been discussed extensively in the literature (e.g., Fischer and Spohn, 1990; Moore, 2003; Henning et al., 2009; Renaud and Henning, 2018). Here, we only mention that the role of the mantle rigidity and viscosity is considerably stronger than the effect of different spin states and orbital eccentricities. However, in the model cases with low orbital eccentricity, the surface tidal heat flux apparently depends on the spin–orbit ratio (Figure 3.3). A transition between the $3 : 2$ spin–orbit resonance and the synchronous rotation may result in order of magnitude drop in the surface tidal heat flux, which would be probably succeeded by a significant change in the surface and interior conditions.

3.2.2 Effect of the eccentricity

In the second parametric study, we set the mantle rigidity to a constant value of $\mu_\mathrm{m} = 200\,\mathrm{GPa}$ and vary the mantle viscosity and the orbital eccentricity. The remaining parameters are the same as in the previous section. To ensure the precision of the computation, we chose the cut–off degree of the Kaula's eccentricity functions $\mathcal{G}_{lpq}(e)$ with respect to the actual eccentricity. Specifically, we required that the truncation error of the disturbing potential and evolution equations be lower than 10^{-4} and we continued to increase the upper limit for index q of the Darwin–Kaula expansion from $q_\mathrm{max} = 1$ for the lowest eccentricities up to $q_\mathrm{max} = 7$ for $e = 0.5$.

Figure 3.6 unveils two distinct regions, which are characterised by a different type of stable spin states and a different parameter dependence of the tidal dissipation. The boundary between these two regions is due to the change in

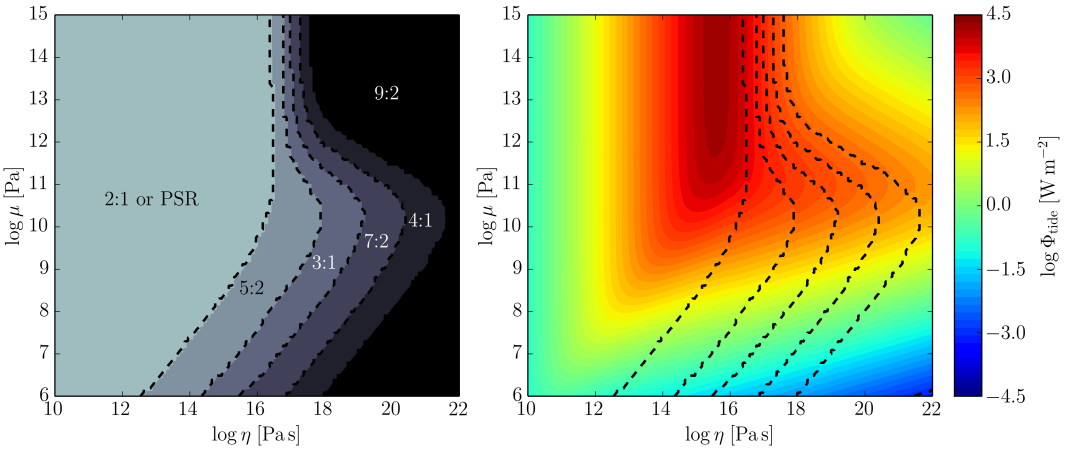

Figure 3.5: Same as Figure 3.3, but for orbital eccentricity $e = 0.4$. PSR corresponds to $\dot{\theta}/n \approx 1.96$.

behaviour of the viscoelastic material at different tidal frequencies, which can be related to its Maxwell time. In general, planets are loaded on a variety of frequencies; however, for the simplest case of a synchronously rotating body on a slightly eccentric orbit, the tidal frequency is approximately equal to the orbital frequency. Since the orbital parameters of our model system yield $T_{\mathrm{orb}} = 9.24\,\mathrm{days}$, it follows that planets with mantle viscosity higher than $10^{17}\,\mathrm{Pa\,s}$ are loaded on periods shorter than their Maxwell time and behave more viscoelastically, while planets with considerably lower mantle viscosities can be considered as purely viscous.

The first of the two regions, at low mantle viscosities, is, therefore, characterised by pseudo–synchronous rotation and by tidal dissipation, which smoothly increases with increasing orbital eccentricity or proximity to the boundary between the zones (below $\eta_{\mathrm{m}} \approx 10^{16}\,\mathrm{Pa\,s}$). In this region, the surface tidal heat flux is determined primarily by the mantle viscosity, with a comparably weaker contribution of the orbital eccentricity. On the contrary, the rotational evolution of a solid body lying in the second (high–viscosity) region is marked by transitions between stable spin–orbit resonances. Their stability is given predominantly by the orbital eccentricity, with more eccentric orbit resulting in higher first stable resonance, but it can also be affected by changing the viscosity, as was the case in the previous section.

Looking at the tidal dissipation, the average surface tidal heat flux of a planet locked in a given spin–orbit resonance is only weakly dependent on the orbital eccentricity and changes mainly due to the variations in the viscosity (see also Běhounková et al., 2011), with the exception of the transition to synchronous rotation. This behaviour is very different from the viscous region and can be

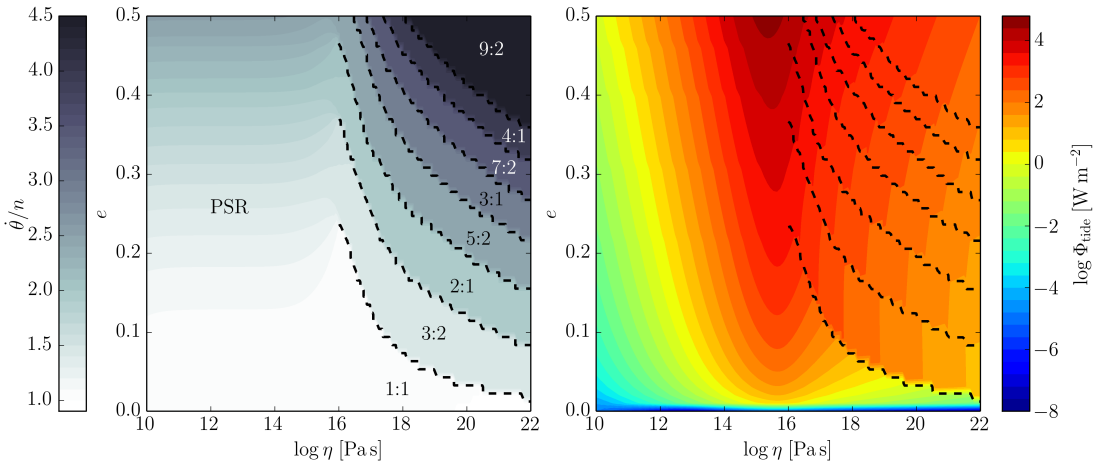

Figure 3.6: The highest stable spin–state (*left*) and the surface tidal heat flux (*right*) for a model planet with mantle rigidity $\mu_{\mathrm{m}} = 200\,\mathrm{GPa}$.

derived from the expression for the average tidal heat rate[3].

3.2.3 Effect of the core size

In order to investigate the role of the planet's radius and CMF on the stability of spin–orbit resonances and on the tidal heating, we again set the mantle rigidity to a fixed value $\mu_{\mathrm{m}} = 200\,\mathrm{GPa}$, as in the previous section. Additionally, we consider an Earth–like value of the mantle viscosity $\eta_{\mathrm{m}} = 10^{21}\,\mathrm{Pa\,s}$ and two possible values of the orbital eccentricity, $e = 0.05$ or $e = 0.2$. The densities of all interior layers are considered constant, as listed in Table 3.1.

Figure 3.7 depicts the average surface tidal heat flux with inscribed boundaries between the different highest stable spin states, as well as a simplified mass–radius diagram of the model ensemble. Focusing first on the spin rate evolution, we see that the main feature of the results is the higher susceptibility of planets with small radii or low core mass fractions to tidal locking into higher spin–orbit resonances. This observation also means that the lower the planet's mass for a given radius, the higher the probability that the planet rotates non–synchronously. For higher orbital eccentricities, the model planet always gets locked into higher

[3]The average tidal heat rate (2.43), written in the form of the Darwin–Kaula expansion, contains products of the eccentricity polynomials $\mathcal{G}_{lpq}(e) \in o(e^{|q|})$. Since we restricted our study to the case of zero obliquity, the only nonzero terms in the expansion are $\{lmpq\} = \{220q\}$ and $\{lmpq\} = \{201q\}$, for which the higher the index q, the weaker the contribution of the term to the total sum. Specifically, the term with $q = 0$ is independent of the eccentricity. Each term of the expression (2.43) is also multiplied by the tidal frequency ω_{lmpq}, which can be in our case either $\omega_{220q} = (2+q)n - 2\dot{\theta}$ or $\omega_{201q} = qn$. For a synchronously rotating body ($\dot{\theta} = n$), both of the considered frequencies are zero for $q = 0$, and the leading term is, therefore, $q = 1$. For a higher spin–orbit resonance, the frequency ω_{2200} is nonzero and the leading term does not depend on the eccentricity.

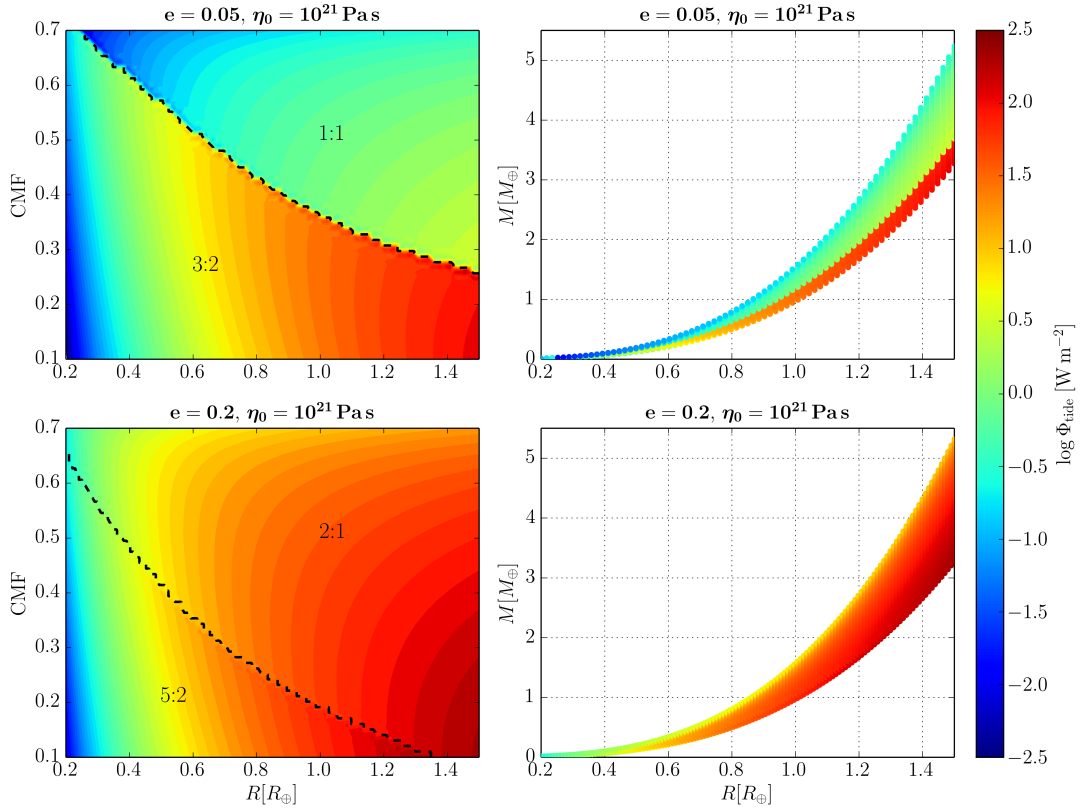

Figure 3.7: Surface tidal heat flux as a function of the planet's radius and CMF (*left*) and the same figure plotted into a mass–radius graph (*right*). Dashed line demarcates the boundaries between regions with different highest stable spin state. The mantle viscosity was set to $\eta_\text{m} = 10^{21}$ Pa s and the orbital eccentricity to $e = 0.05$ (*upper row*) or $e = 0.2$ (*lower row*).

than synchronous resonances; however, the effect of the small radius or low core mass fraction on the spin–orbit ratio remains qualitatively the same.

Again, the planet's spin state cooperates with other model parameters on determining the rate of energy dissipation. Similarly to the previous results, we may see that the effect of tidal locking on the tidal heating is most prominent in the case of planets with low orbital eccentricity (upper row in Figure 3.7), where trespassing the boundary between the synchronous and nonsynchronous rotation results in two orders of magnitude change in the surface tidal heat flux. A common feature of all model cases is increasing surface tidal heat flux with increasing planetary radius at constant CMF. This pattern is a simple consequence of the differing volume of the dissipating mantle and of the increase in the tidal force with R. On the other hand, the effect of increasing CMF is slightly less intuitive. For higher planetary radii ($R > 1\,R_\oplus$), the surface tidal heat flux typically increases with decreasing CMF (for a given spin state), in line with the previous result for increasing planetary radius: lower CMF is equivalent to a larger dissipative mantle. However, for lower planetary radii ($R < 1\,R_\oplus$), the heat flux slowly decreases

with decreasing CMF. This feature probably results from the greater flexure of a thinner mantle above a larger liquid core.

3.3 Concluding remarks

The stability of individual spin–orbit resonances within the Andrade model is a complex function of the rheological parameters and the eccentricity. The resulting pattern depends on the interplay between the self–gravity and the rheological parameters and on the role of viscoelasticity at given tidal frequencies. Especially at low orbital eccentricities, the despinning from higher spin–orbit resonance to the synchronous rotation results in a significant drop in the tidal heating. The secular tidal torque also depends on the planet's mass and radius. Planets with smaller radii and/or low core mass fractions (CMF) tend to get locked into higher spin–orbit resonances than larger and/or more massive planets with the same rheological and material parameters of the interior layers.

As we have now overviewed the main aspects of the tidal heating and tidal locking of a generic low–mass exoplanet, we are ready to continue to the central chapter of this work. Chapter 4 will introduce a coupled model of long–term thermal–orbital evolution, which will be applied to the case of three model bodies inspired by three of the currently known close–in terrestrial exoplanets. Among the results of the next chapter, we will also see the consequence of transitions between different spin–orbit resonances as well as the effect of an emergent magma ocean on the thermal and orbital dynamics.

4. Coupled thermal and orbital evolution of low–mass exoplanets

The entire chapter was adapted from Walterová and Běhounková (2020).

4.1 Introduction

Internal dynamics of close–in exoplanets and large moons in the Solar System are closely linked to their tidal interaction with the primary. As an effective heat source, tidal dissipation can sustain liquid oceans under the surface of large icy moons (e.g., Hussmann et al., 2010; Chen et al., 2014) or maintain the extreme volcanic activity of Jupiter's moon Io (e.g., Peale et al., 1979; Segatz et al., 1988). Beyond the realms of the Solar System, tidal heating is believed to transform close–in rocky exoplanets into lava worlds (e.g., Běhounková et al., 2011; Barr et al., 2018; Henning et al., 2018), influence their tectonic regime (Zanazzi and Triaud, 2019), alter the boundaries of the conventional habitable zone for exoplanets or exomoons (e.g., Jackson et al., 2008; Heller and Barnes, 2013; Dobos et al., 2017; Renaud and Henning, 2018), and it is also one of the suggested mechanisms responsible for the existence of inflated hot Jupiters (e.g., Bodenheimer et al., 2001; Jermyn et al., 2017).

Tidal loading and the subsequent transfer of angular momentum and orbital energy are also the cause of long–term orbital evolution, accompanied by the disturbed body's despinning into spin–orbit synchronisation, pseudo–synchronisation or a higher spin–orbit resonance (e.g., Ferraz-Mello, 2013; Makarov and Efroimsky, 2013; Correia et al., 2014; Ferraz-Mello, 2015). As a consequence of the spin–orbital dynamics, close–in moons and exoplanets are expected to tend toward circular orbit and synchronous rotation, unless they are disturbed by other bodies in the system or by the tidal response of a rapidly rotating primary (e.g., Bolmont and Mathis, 2016). The rate of tidally induced orbital evolution depends on the moon's or planet's ability to dissipate mechanical energy. Different interiors support different dissipation mechanisms. While the dissipation inside terrestrial bodies or rocky parts of gas giants is dominated by large–scale viscous flow (Ferraz-Mello, 2013), jovian worlds are typically heated by inertial waves and turbulent convection in their massive atmospheres (Ogilvie and Lin, 2004). Owing to their higher tidal quality factor Q, they are also a few orders of magnitude less susceptible to tidally–induced spin and orbital evolution (Goldreich and Soter, 1966). Since the interior structure and dissipation mechanisms of extremely heated bodies depend on the varying interior temperature (e.g., Henning et al., 2009; Renaud and Henning, 2018), the rate of orbital evolution is presumably also a function of time.

The feedback between the thermal and orbital evolution has been investigated particularly in the context of large Solar System satellites. Ojakangas and Stevenson (1986) assessed mutual interconnection between the varying interior

temperature of Jupiter's moon Io and the evolution of its orbital eccentricity, which is affected both by tides and by the Laplace resonance with other Galilean satellites. Assuming heat loss by mantle convection and heat generation by viscoelastic tidal dissipation, they described a process of periodic cooling down and heating up of the satellite, controlled by inverse dependence of the tidal quality function k/Q on the temperature. Several years later, Fischer and Spohn (1990) extended the model by considering partial melting of the interior. The presence of melt decreases the moon's average rigidity and further reduces the tidal dissipation. In addition to the oscillatory state described by Ojakangas and Stevenson (1986), the authors identified an approximate thermal and dynamical equilibrium, in which the moon can be temporarily stabilised. The equilibrium is characterised by a very low rate of change in the eccentricity and interior temperature. Further studies of coupled thermal–orbital evolution with more complex models of the interior have since then been presented by a number of authors (e.g., Hussmann and Spohn, 2004; Tobie et al., 2005a; Neveu and Rhoden, 2019).

Partial melting is also likely to be an important regulating mechanism in the case of close–in terrestrial exoplanets. Identically to the case of Solar System satellites, the emergence of melt yields an abrupt change of rheological parameters and decreased tidal dissipation, which prevents runaway heating of the mantle (Makarov et al., 2018). For multiplanetary systems in mean–motion resonances, the coupled thermal–orbital evolution follows a pattern similar to the evolution of large Saturnian or Jovian satellites. In single-planetary systems or systems without substantial eccentricity forcing, on the other hand, the decreased dissipation may be reflected in the unexpected orbital parameters. Specifically, it has been argued (e.g., Henning et al., 2009; Henning and Hurford, 2014; Makarov, 2015) that partial melting may explain nonzero orbital eccentricities of exoplanets for which the standard tidal theories predict rapid circularisation.

Shoji and Kurita (2014) and Driscoll and Barnes (2015) investigated the long–term thermal–orbital evolution of single–planetary systems around low–mass stars. Both studies focused on small, synchronously rotating exoplanets in the habitable zone and implemented a combined model of parameterised mantle convection with global melting, viscoelastic tidal dissipation and simplified orbital evolution. Shoji and Kurita (2014) assumed a stagnant–lid convection regime and predicted two possible evolution branches of the planets in question. Depending on the initial orbital eccentricity and the stellar mass, the planet either undergoes runaway cooling, with increasing mantle viscosity and gradually terminating mantle convection, or it is affected by runaway heating, which is eventually stopped by partial melting. In either of these states, the semi–major axis and the orbital eccentricity change very slowly over several billions of years and may allow the planet to remain habitable for a considerable time. In contrast, Driscoll and Barnes (2015) prescribed a mobile–lid regime, in which the planet's lithosphere participates in the convection. As a consequence of more efficient energy dissipation, they found rapid decay of the eccentricity of close-in exoplanets and relatively low importance of tidal heating on long timescales. The authors also performed plenty of parametric studies, in which they illustrated the complex

dependence of the tidal heat rate and other quantities on the initial orbital parameters.

While the assumption of synchronous rotation, taken in the cited studies, is well justified in low eccentricity cases, the evolution of exoplanets on eccentric orbits is most probably marked by tidal locking into higher than synchronous resonances or pseudo–synchronous rotation (e.g, Dobrovolskis, 2007; Ferraz-Mello, 2013; Correia et al., 2014). A self–consistent model of an eccentric exoplanetary system requires not only the coupling between thermal and orbital evolution but also the simultaneous assessment of the stable spin state. In the specific case of the multiplanetary system TRAPPIST–1, the influence of a tidally induced change of interior properties on the stability of higher spin states has been discussed by Makarov et al. (2018). The authors identified that, as a consequence of an abrupt change in the mantle's rheological parameters, the planet might leave its initially high spin–orbit resonance and evolve toward synchronisation or toward pseudo–synchronisation, expected for molten rocky worlds on eccentric orbits (Makarov, 2015). Both the melting and the change of equilibrium spin state result in substantially decreased tidal dissipation.

In this study, we investigate the coupled thermal and orbital evolution of model bodies inspired by three currently known low–mass exoplanets with nonzero eccentricity, namely Proxima Centauri b, GJ 625 b, and GJ 411 b. This goal is accomplished by implementing a semi–analytical model including spin–orbital evolution of a layered viscoelastic planet with emerging subsurface magma ocean, self–consistently calculated tidal heat generation, and a simplified parameterised mantle convection in the stagnant–lid regime. As in the previous chapter, we first explore the dependence of tidal heating and highest stable spin states on the rheological parameters. Then, we analyse the evolution of the three planets in the coupled thermal–orbital model. Finally, we discuss the model assumptions that might have affected the results and we conclude the chapter with a summary of the main implications.

4.2 Orbital evolution

Our model system consists of a spherical star with mass m_* and a single rocky planet with mass $m_\mathrm{p} \ll m_*$, whose trajectory is defined by the semi–major axis a and the eccentricity e. The planet, considered here as an extended body, deforms in the heterogeneous gravitational field of the host star and its orbital parameters undergo secular tidal evolution. Additional potential due to the planet's deformation, which presents a perturbation to the standard two–body problem (e.g. Murray and Dermott, 1999), can be expressed in the form of a disturbing function. Following the linear tidal theory developed by Darwin (1880) and Kaula (1961), we expand the disturbing function into a Fourier series in space and time and insert it into Lagrange planetary equations for the semi–major axis and the eccentricity. The secular evolution equations are then written as a linear combination of individual tidal modes (Kaula, 1964):

$$\dot{a} = -\sum_{lmpq} \frac{2\mathcal{G}m_*}{na} \frac{R^{2l+1}}{a^{2l+2}} (l-2p+q) \frac{(l-m)!}{(l+m)!} (2-\delta_{0m}) \left[\mathcal{G}_{lpq}(e)\right]^2 \left[\mathcal{F}_{lmp}(\beta)\right]^2 k_l \sin\varepsilon_{lmpq} , \tag{4.1}$$

$$\dot{e} = -\sum_{lmpq} \frac{\mathcal{G}m_*}{na^2} \frac{\sqrt{1-e^2}}{e} \frac{R^{2l+1}}{a^{2l+2}} \left[\sqrt{1-e^2}(l-2p+q) - (l-2p)\right] \times \\ \times \quad \frac{(l-m)!}{(l+m)!} (2-\delta_{0m}) \left[\mathcal{G}_{lpq}(e)\right]^2 \left[\mathcal{F}_{lmp}(\beta)\right]^2 k_l \sin\varepsilon_{lmpq} . \tag{4.2}$$

In the above equations, $\mathcal{G}$ is the Newton's gravitational constant, n stands for the planet's mean motion and R symbolises the planet's outer radius. The quantities $\mathcal{G}_{lpq}(e)$ and $\mathcal{F}_{lmp}(\beta)$ are Kaula's functions of orbital eccentricity and inclination relative to the planet's equator (e.g., Kaula, 1961, 1964; Allan, 1965). In our case, the "inclination" is equal to the planet's obliquity β, which we set to zero. The tidal response of the planet, determined by its rheological properties and interior structure, is represented by the frequency–dependent tidal Love number $k_l = k_l(\omega_{lmpq})$ and by the tidal phase lag $\varepsilon_{lmpq} = \varepsilon_{lmpq}(\omega_{lmpq})$. While the former quantifies the ratio between the amplitude of the additional potential and the amplitude of the tidal potential, the latter characterises the lagging between the two potentials in the frequency domain. When working with viscoelastic models of the interior, it is also appropriate to introduce the complex Love number $\bar{k_l}(\omega_{lmpq})$ (e.g., Castillo-Rogez et al., 2011), whose relation to the two quantities is

$$\bar{k_l}(\omega_{lmpq}) = k_l \exp\left\{-\mathrm{i}\varepsilon_{lmpq}\right\} . \tag{4.3}$$

Finally, the frequencies of the individual modes $\{l, m, p, q\}$ are

$$\omega_{lmpq} = (l-2p+q)n - m\dot{\theta} , \tag{4.4}$$

where $\dot{\theta}$ stands for the planet's spin rate. Similarly to the calculation of the semi–major axis and the eccentricity, the secular evolution of the spin rate can be also written as a sum of individual modes (e.g., Dobrovolskis, 2007; Efroimsky and Williams, 2009),

$$\ddot{\theta} = \frac{\mathcal{G}m_*^2}{C} \sum_{lmpq} \frac{R^{2l+1}}{a^{2l+2}} \frac{(l-m)!}{(l+m)!} (2-\delta_{0m})\, m \left[\mathcal{G}_{lpq}(e)\right]^2 \left[\mathcal{F}_{lmp}(\beta)\right]^2 k_l \sin\varepsilon_{lmpq} , \tag{4.5}$$

with C being the principal moment of inertia with respect to the rotational axis. For the sake of simplicity, we set C equal to the moment of inertia of a sphere with the same mass and radius as the planet. While it is also possible to accommodate the Darwin–Kaula theory for the study of secular evolution of the planet's obliquity (Boué and Efroimsky, 2019), we do not include this effect in our model and consider only the planar case with $\beta = 0°$. A nonzero

initial obliquity would temporarily affect the stability of higher than synchronous spin–orbit resonances (Boué et al., 2016) and would be an additional source of tidal heating, complementing the eccentricity tides (e.g., Peale and Cassen, 1978). However, when the planet's spin–orbital evolution is shaped only by tides, the obliquity in stable spin states usually tends toward zero (Boué et al., 2016).

For the sake of completeness, we note that the spin and orbital evolution might be also induced by the deformation of the star under the gravitational action of the planet. However, due to the large difference between masses and to lower typical dissipation rates in stars, compared to the terrestrial planets (e.g., Hansen, 2010), the star's contribution to the system's tidal evolution is neglected in this study, and we consider only the dissipation in the companion. Nevertheless, tides raised by the planet on the host star play an important role in the evolution of hot Jupiters orbiting fast–rotating stars (Bolmont and Mathis, 2016), in which case they should be taken into account.

4.3 Tidal deformation

The reaction of a tidally loaded exoplanet with a given mass and radius is determined by its interior structure and rheological properties. The mineralogical composition of the mantle, as well as the existence of a liquid core or a subsurface ocean, translates into the previously introduced complex Love numbers $\bar{k}_l(\omega_{lmpq})$. For a homogeneous body with averaged interior properties, the complex Love numbers can be expressed by a relatively simple analytical formula (Castillo-Rogez et al., 2011, see also equation 1.38 in Chapter 1 of the present work). This approach facilitates the qualitative examination of the problem; however, the assumption of a homogeneous interior might not always be justified. As has been shown by a number of studies (e.g., Castillo-Rogez et al., 2011; Beuthe, 2013; Henning and Hurford, 2014; Folonier et al., 2015; Tobie et al., 2019), the tidal deformation and dissipation vary between different models of interior structure and the radial stratification cannot be generally neglected.

Here, we focus on planets with a liquid core and emerging magma ocean, i.e., we are concerned with a layered interior. To calculate the complex Love numbers of a differentiated planet, we follow in the steps of the previous tidal studies and adopt the normal mode theory (e.g., Takeuchi and Saito, 1972; Wu and Peltier, 1982; Sabadini and Vermeersen, 2004; Tobie et al., 2005b). A draft of the method is presented in Appendix A. This calculation assumes that each interior layer is endowed with its own material and rheological properties. Specifically, the mantle is described by linear viscoelastic rheology, which predicts instantaneous deformation on seismological timescales and gradual creeping on geological timescales. In the following, we discuss the chosen rheological model and the calculation of tidal dissipation.

4.3.1 Rheological models

According to the principle of correspondence, the equations of motion for a linear viscoelastic continuum in the frequency domain are analogous to the equations governing the motion of an elastic material. The static rigidity μ only needs to be rewritten to its complex and frequency–dependent counterpart $\bar{\mu}(\omega)$. Similarly to the elastic case, the complex rigidity characterises the relation between the deviatoric part of the incremental strain tensor $\bar{\boldsymbol{\epsilon}}^{\mathrm{D}} = \frac{1}{2}\left(\nabla\mathbf{u} + \nabla^t\mathbf{u}\right)$ and the deviatoric part of the incremental Cauchy stress tensor $\bar{\boldsymbol{\sigma}}^{\mathrm{D}}$,

$$\bar{\boldsymbol{\sigma}}^{\mathrm{D}} = 2\bar{\mu}(\omega)\,\bar{\boldsymbol{\epsilon}}^{\mathrm{D}} \,, \tag{4.6}$$

where $\mathbf{u}$ stands for the incremental displacement. Alternatively, we may use the dynamic compliance $\bar{J}(\omega)$, defining the will of a material to deform under applied stress,

$$2\bar{\boldsymbol{\epsilon}}^{\mathrm{D}} = \bar{J}(\omega)\,\bar{\boldsymbol{\sigma}}^{\mathrm{D}} \,. \tag{4.7}$$

The simplest viscoelastic model used in the planetary science is the Maxwell model, represented by a Hookean spring and a Newtonian dashpot connected in series and accounting for a linear viscoelastic response. However, owing to the variety of deformation mechanisms observed in real solids, the accurate description of the planet's response requires the introduction of more complex, rheologically–motivated models, consistent with laboratory experiments and seismological or geodetic measurements (for an overview, see, e.g., Efroimsky and Lainey, 2007; Henning et al., 2009; Castillo-Rogez et al., 2011, or Section 4.3 of the present work). The best fit to experimental data for polycrystalline materials is presented by three rheological models: Andrade (Andrade, 1910), extended Burgers (Faul and Jackson, 2005), and Sundberg–Cooper (Sundberg and Cooper, 2010), each of which entails a different anelastic extension to the simple linear viscoelasticity of the Maxwell model. The desire to keep the number of model parameters at a minimum while retaining a sufficiently accurate description of the deformation leads us to prefer the Andrade rheology, whose complex compliance is

$$\bar{J}(\omega) = \frac{1}{\mu} - \frac{\mathrm{i}}{\eta\omega} + \frac{\mu^{\alpha-1}}{(\mathrm{i}\,\zeta\eta\omega)^{\alpha}}\,\Gamma(1+\alpha) \,. \tag{4.8}$$

The last term in equation (4.8) stands for a transient, anelastic creep, which dominates the material's response at high[1] frequencies. Symbols α and ζ stand for empirical parameters characterising the duration of transient creep and the ratio of material's relaxation time to the Maxwell time η/μ, respectively. Both parameters depend on the prevalent deformation mechanism at given stresses,

[1] According to Karato and Spetzler (1990), Andrade rheology is applicable to the Earth's response at frequencies higher than $\sim 1\,\mathrm{yr}^{-1}$. However, the exact position of the frequency threshold between the anelastic and viscoelastic regimes depends exponentially on the temperature and may vary greatly with the thermal state of the mantle.

temperatures, and chemical compositions (Karato and Spetzler, 1990).

As we have seen in the previous chapters, a characteristic feature of viscoelastic tidal models is the occurrence of distinct stable spin states, i.e. distinct stationary solutions to equation (4.5), associated either with spin–orbit resonances or with pseudo–synchronous rotation (e.g., Correia et al., 2014; Ferraz-Mello, 2015; Makarov, 2015). Additionally, complex viscoelastic models are endowed with increased tidal heating at high frequencies and they enable the planet to remain tidally active for long periods (Renaud and Henning, 2018).

4.3.2 Tidal heating

Periodic deformation of a viscoelastic body is accompanied by the dissipation of mechanical energy, which results in tidal heating. The average heat rate produced by the dissipation in the entire volume of the planet over one orbital is calculated as (Efroimsky and Makarov, 2014, see also derivation for $l = 2$ in Appendix B.1)

$$\bar{P}^{\rm tide} = -\frac{\mathcal{G}m_*^2}{a} \sum_{lmpq} \left(\frac{R}{a}\right)^{2l+1} (2-\delta_{m0}) \frac{(l-m)!}{(l+m)!} \left[\mathcal{G}_{lpq}(e)\right]^2 \left[\mathcal{F}_{lmp}(\beta)\right]^2 \omega_{lmpq} \, \mathrm{Im}\{\bar{k}_l(\omega_{lmpq})\} \, . \tag{4.9}$$

Equation (4.9) holds for an arbitrary obliquity and orbital eccentricity as well as for arbitrary spin rate, provided that the overall deformation can be described by a linear tidal theory.

4.4 Thermal evolution

The thermal state of planetary bodies is controlled by a combination of heating and cooling mechanisms, differing in their significance and in their characteristic timescales. Internal heat sources include remnant gravitational energy released at the time of the planet's formation and differentiation, latent heat extracted during phase transitions, radiogenic heating of the crust and mantle, and tidal dissipation. Secular cooling of the planetary interior is realised mainly by mantle convection and conduction, depending on the size, temperature gradient, and rheological properties of the mantle.

The following section contains several important assumptions. Keeping in mind the wealth of possible thermal histories of the exoplanets, including, for instance, the occurrence of plate tectonics or episodic resurfacing events, we focus specifically on the stagnant–lid convection. This gives us the advantage of a relatively simple parametric description, allowing for a systematic parametric study. Furthermore, given the lack of information on the tectonic regimes of exoplanets and the scarcity of plate tectonics in the Solar System, the stagnant–lid convection is often considered as a conservative guess (e.g., Shoji and Kurita, 2014; Tosi et al., 2017).

Since the main subject of this work is the evolution of strongly tidally loaded exoplanets, we also restrict the mantle–heating mechanisms to the initial core–mantle temperature difference and to the volumetric tidal dissipation. The contribution of latent heat to the overall energy balance is, however, included in the adopted equations. Although the radiogenic heating may be an important source in the elastic lithosphere (and crust) and it might slow down the cooling of the mantle, its contribution would be most pronounced in the initial stages of the evolution, which are, however, also dominated by tidal heating.

The last important assumption is the absence of melt extraction from the mantle. Low efficiency of the heat transport through the stagnant lid, together with immense heating of planets on eccentric orbits, may lead to partial melting of the interior and formation of a subsurface magma ocean. Current studies using parameterised stagnant–lid convection consider either perfect mixing of the interior (e.g., Henning et al., 2009; Shoji and Kurita, 2014; Driscoll and Barnes, 2015) or instantaneous melt extraction accompanied by crustal production (e.g., Breuer and Spohn, 2006; Tosi et al., 2017). Although the subsurface magma can be extracted from the interior by heat pipe volcanism (Spohn, 1991; Moore et al., 2017), we do not consider any melt transport mechanisms in this study, and we instead include the effect of the emerging magma ocean into the tidal model.

4.4.1 Parameterised mantle convection

To inspect the long–term thermal evolution of the planet, we adopt a 1d parameterised model of mantle convection in the stagnant–lid regime (e.g., Breuer and Spohn, 2006; Grott and Breuer, 2008). The evolution of the temperature on the top of the convecting mantle T_m and at the core–mantle boundary T_c is governed by the energy balance in the tidally heated planet (Breuer and Spohn, 2006),

$$\rho_\mathrm{m} c_\mathrm{m} V_\mathrm{m} (1 + St) \frac{\mathrm{d}T_\mathrm{m}}{\mathrm{d}t} = -q_\mathrm{m} A_\mathrm{m} + q_\mathrm{c} A_\mathrm{c} + \bar{P}^\mathrm{tide} \,, \tag{4.10}$$

$$\rho_\mathrm{c} c_\mathrm{c} V_\mathrm{c} \frac{\mathrm{d}T_\mathrm{c}}{\mathrm{d}t} = -q_\mathrm{c} A_\mathrm{c} \,, \tag{4.11}$$

where ρ_m and ρ_c are the mean density in the mantle and in the core, respectively, and c_m and c_c are the corresponding specific heat capacities. The symbol St stands for the Stefan number related to the latent heat L_m consumed or generated during partial melting or solidification,

$$St = \frac{L_\mathrm{m}}{c_\mathrm{m}} \frac{\mathrm{d}\phi_\mathrm{m}}{\mathrm{d}T_\mathrm{m}} \,, \tag{4.12}$$

where ϕ_m signifies the total melt fraction in the mantle. Additionally, A_c, A_m, V_c and V_m are the total surface areas and volumes of the core and the mantle, and q_c and q_m are the heat fluxes from the core to the mantle and from the mantle to the lithosphere, respectively. The last two quantities can be expressed as

$$q_\mathrm{c} = k_\mathrm{m} \frac{T_\mathrm{c} - T_\mathrm{b}}{\delta_\mathrm{c}} \tag{4.13}$$

and

$$q_\mathrm{m} = k_\mathrm{m} \frac{T_\mathrm{m} - T_\mathrm{l}}{\delta_\mathrm{u}} \,, \tag{4.14}$$

where k_m is the thermal conductivity of the mantle, T_b is the temperature on the bottom of the convecting mantle, T_l stands for the temperature at the base of the lithosphere and δ_c and δ_u are the thicknesses of the lower and upper thermal boundary layers (TBLs), given by the boundary layer theory. The temperatures throughout the convective mantle follow the adiabatic profile. According to the chosen stagnant–lid parameterisation, the boundary layer thicknesses should be determined by the ratio of the local Rayleigh number to the critical Rayleigh number (Tosi et al., 2017). However, as explained in the following section, we calculate the thickness of the upper TBL using the "mean Rayleigh number", corresponding to the average mantle viscosity. This choice enables us to mimic the role of a magma ocean.

In the presented model, the thermal evolution of the planet affects the interior structure and the tidal response in three ways. First, the increasing or decreasing temperature at the top of the mantle regulates the heat flux into the lithosphere and, as a result, determines the thickness of the stagnant lid D_l (Grott and Breuer, 2008),

$$\rho_\mathrm{m} c_\mathrm{m} (T_\mathrm{m} - T_\mathrm{l}) \frac{\mathrm{d}D_\mathrm{l}}{\mathrm{d}t} = -q_\mathrm{m} - k_\mathrm{m} \left.\frac{\partial T}{\partial r}\right|_{r=R_\mathrm{l}} . \tag{4.15}$$

The second term on the right–hand side, which is being evaluated at the stagnant–lid base with radius R_l, can be obtained analytically (e.g. Carslaw and Jaeger, 1959) from the heat conduction equation

$$\frac{1}{r^2}\frac{\partial}{\partial r}\left(r^2 k_\mathrm{l} \frac{\partial T}{\partial r}\right) = 0 , \tag{4.16}$$

where we have neglected heat sources in the elastic—and thus nondissipative—lithosphere. The surface temperature T_s of the model planets is held constant.

As the second of the coupling mechanisms, the variations of the interior temperature influence the rheological properties of mantle minerals. Specifically, the temperature dependence of the local mantle viscosity η can be expressed by the Arrhenius law as

$$\eta(T) = \eta_0 \exp\left(\frac{\mathcal{E}^*}{R_\mathrm{gas}} \frac{T_0 - T}{T_0 T}\right) , \tag{4.17}$$

where η_0 is the reference viscosity at reference temperature $T_0 = 1600\,\mathrm{K}$ (Grott and Breuer, 2008), $\mathcal{E}^*$ stands for the activation energy, and R_gas is the gas constant. In addition to the temperature dependence, mantle rheology should also be determined by the local pressure, whose role in shallow depths of the mantle is to increase the viscosity. The effect of extreme pressures in the lower mantle of massive terrestrial exoplanets is, however, still a question of debate (e.g., Karato, 2011; Stamenković et al., 2012). Here, we do not include the pressure dependence of the mantle viscosity explicitly, but we instead assume several different values of the reference viscosity η_0 in order to cover all possible viscosity models.

The third and last of the discussed mechanisms is partial melting in the shallow regions of the mantle, possibly followed by the formation of a magma ocean. The presence of melt, associated with an additional change in the local viscosity and rigidity, alters the planet's response to external loading and affects the efficiency of energy dissipation. The melt fraction at a given radius $\phi(r)$ depends on the local temperature $T(r)$, given by the mantle temperature profile, and on the chemical and mineralogical composition, which determines the solidus and liquidus temperatures throughout the planet,

$$\phi(r) = \frac{T(r) - T_{\mathrm{sol}}(r)}{T_{\mathrm{liq}}(r) - T_{\mathrm{sol}}(r)} \,. \tag{4.18}$$

The melting curves of mantle materials at pressures relevant to planetary science are determined by fitting laboratory data. Here, we follow Monteux et al. (2016), who use empirical data from two experimental studies performed in two different pressure ranges and adjust the parameters of the fitted function to avoid discontinuities at the boundary of the two ranges. At pressures lower than $P = 20\,\mathrm{GPa}$, the solidus and liquidus temperatures can be obtained as (Herzberg and Zhang, 1996)

$$T_{\mathrm{sol}} = 1661.2 \left(\frac{P}{1336 \times 10^9} + 1 \right)^{1/7.437} , \tag{4.19}$$

$$T_{\mathrm{liq}} = 1982.1 \left(\frac{P}{6.594 \times 10^9} + 1 \right)^{1/5.374} , \tag{4.20}$$

while at pressures above $P = 20\,\mathrm{GPa}$, deeper in the mantle, the following relations are used (Andrault et al., 2011):

$$T_{\mathrm{sol}} = 2081.8 \left(\frac{P}{101.69 \times 10^9} + 1 \right)^{1/1.226} , \tag{4.21}$$

$$T_{\mathrm{liq}} = 2006.8 \left(\frac{P}{34.65 \times 10^9} + 1 \right)^{1/1.844} . \tag{4.22}$$

Once the local temperature exceeds the local solidus, the mantle rocks begin to melt. The molten material, first encapsulated in isolated cavities, gradually builds up a system of interconnected channels, and as the local melt fraction reaches the disaggregation point ϕ_{D} (40%-60%; e.g., Moore, 2003), it assumes the leading role in the rock's rheology. While the gradual formation of drops of partial melt in solid material does not substantially affect its rigidity and only accelerates the Arrhenius–like decrease in viscosity, reaching the disaggregation point is accompanied by several orders of magnitude drop in both quantities. In order to characterise the described behaviour by a smooth and qualitatively adequate function, we adopt the following dependence of the rheological parameters on the melt fraction

$$\log \mu(\phi) = \log \mu_{\max} - \frac{1}{2} \left(\frac{2}{\pi} \arctan \frac{\phi - \phi_{\mathrm{D}}}{\Delta_\mu} + 1 \right) \log \frac{\mu_{\max}}{\mu_{\min}} \,, \tag{4.23}$$

$$\log \eta(\phi, T) = \log \eta(T) - \frac{1}{2}\left(\frac{2}{\pi} \arctan \frac{\phi - \phi_{\mathrm{D}}}{\Delta_\eta} + 1\right) \log \frac{\eta(T)}{\eta_{\min}} , \tag{4.24}$$

where $\mu_{\max}$ and $\mu_{\min}$ are the rigidity of the solid and entirely molten rock, respectively, $\eta(T)$ is the temperature-dependent viscosity given by the Arrhenius law (4.17), $\eta_{\min}$ is the minimum viscosity, were it determined only by the melt fraction, and Δ_j stands for the disaggregation width of quantity j. Relations (4.23) and (4.24) follow the temperature and melt fraction dependence similar to the empirically justified expressions used in literature (e.g. Fischer and Spohn, 1990; Abe, 1997; Moore, 2003), while ensuring relatively steep but smooth parameter changes.

4.5 Numerical implementation

The long–term evolution of a planet in our model settings consists of processes with substantially different characteristic timescales. The shortest timescale is associated with the rotational evolution, and specifically with tidal despinning from the initial spin state to the closest equilibrium spin state (e.g., a spin–orbit resonance). Depending on the rate of tidal dissipation, the initial despinning operates on the scale of thousands or millions of years. On the other hand, the longest timescale is usually associated with the evolution of the semi–major axis and the orbital eccentricity. It may span from hundreds of millions to tens of billions of years. In between these two extreme cases stands the mantle convection with a characteristic timescale of millions of years.

When choosing the adequate time step for the spin–orbital evolution model, it is necessary to take into account the precision of the calculation as well as its speed. The step should be short enough to correctly capture the changes of the spin rate and long enough to describe the long–scale processes in a reasonable time. In order to fulfill both of these requirements, we divide the calculation into two cycles. The *short cycle* is dedicated to finding the equilibrium spin rate for a given semi–major axis, orbital eccentricity, and interior structure, which are—on the short timescale—usually treated as constant. The *long cycle*, on the other hand, takes steps in the orbital elements, assuming a temporarily constant spin–orbit ratio.

The flow of the computation is schematically depicted in Figure 4.1 and proceeds as follows. In the beginning, we initialise the planetary and stellar masses, spin and orbital parameters and prescribe the planet's interior structure. The computation then starts with the short cycle in a specific *despinning mode*. During the despinning, we evolve not only the spin rate but also the semi–major axis and the eccentricities, following equations (4.1) to (4.5). Although the orbital parameters change very slowly on the short timescale, we include their evolution into the despinning mode in order to find the first stable spin state with high precision. Since the spin rate changes on relatively short timescales, the step size Δt_{S} in the short cycle is initialised to a few orbital periods. To solve the equations,

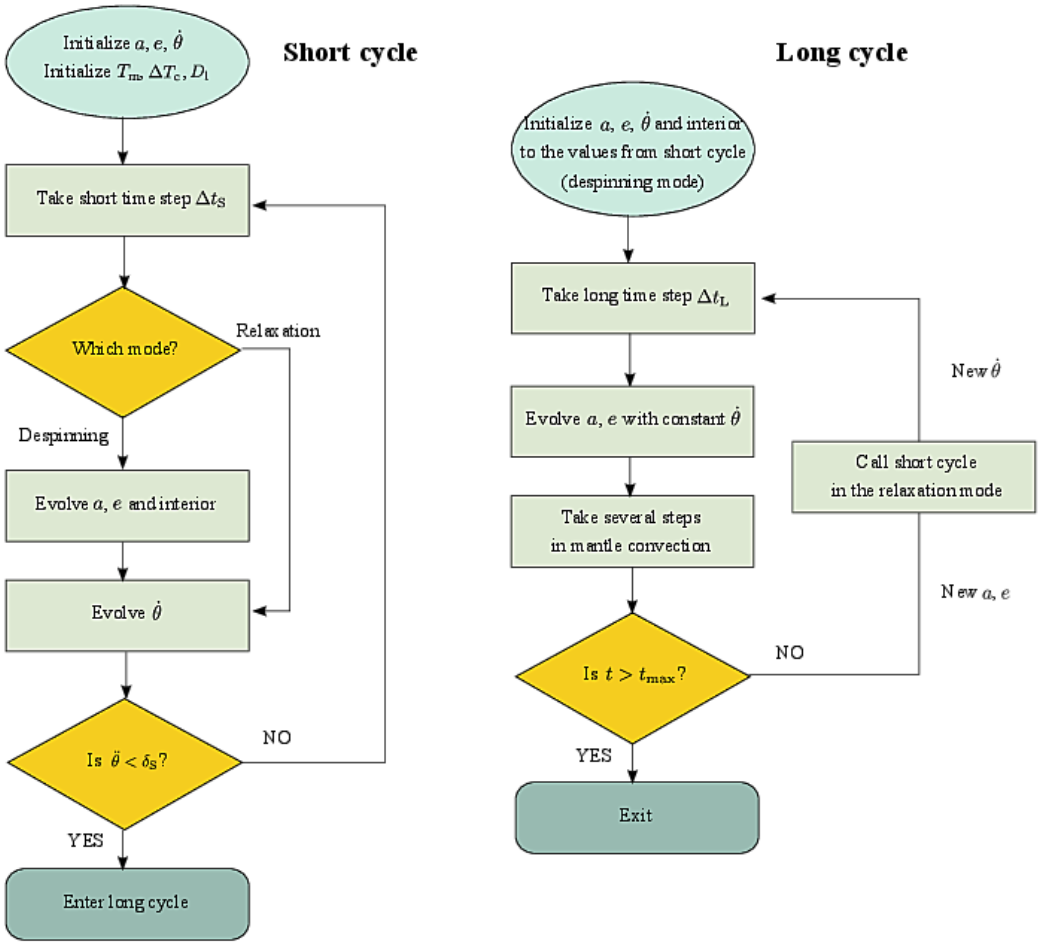

Figure 4.1: Schematic depiction of the computation flow. The short cycle proceeds with short time steps Δt_S and it is designed to find a stable spin state. During its first run, it operates in the *despinning mode*, which allows for the coupled evolution of the orbital elements and the spin rate. In later calls, it is set to the *relaxation mode*, which serves to find the spin rate consistent with a given (constant) semi–major axis and eccentricity. The long cycle takes long time steps Δt_L and calculates the evolution of the orbital parameters and thermal state for a constant spin rate. During the computation, we alternate between steps in the long cycle and runs of the short cycle in the relaxation mode.

we employ a fourth–order predictor–corrector integration scheme (the Hamming's method) with a variable step size controlled by the local error ϵ_{S} in the spin rate $\dot{\theta}$ (see, e.g., Ralston, 1965).

The calculation in the short cycle is performed as long as the derivative $\ddot{\theta}$ exceeds a given limit $\delta_{\mathrm{S}} \times \dot{\theta}$. When the spin rate reaches the equilibrium value, we leave the short cycle and take one step in the long cycle. At this stage, the equilibrium spin–orbit ratio is considered constant, and the step size Δt_{L} is set equal to the last step in the despinning mode of the short cycle. After the step in the long cycle, we recalculate the equilibrium spin rate using the short cycle in a *relaxation mode*, in which the semi–major axis and the eccentricity are considered constant. For the rest of the computation, we alternate between taking one step in the long cycle and running the short cycle in the relaxation mode. Identically to the short cycle, the long cycle utilises a predictor–corrector scheme with step size controlled by the maximum local error in orbital parameters ϵ_{L}. Depending on the planet's rheology and loading frequency, the long step size may gradually become several orders of magnitude larger than the step size of the short cycle. This combined integration scheme allows us to take relatively large steps in the evolution of orbital parameters while still keeping a precise value of the current spin state.

During the despinning mode of the short cycle, as well as in each step of the long cycle, we also evolve the planet's thermal state and interior structure. For the sake of clarity, let Δt_{orb} symbolise the current step size in either of the orbital evolution cycles from which we call the convection module. Equations (4.10) and (4.11), controlling the interior temperature, and equation (4.15), which describes the evolution of the stagnant lid, are solved explicitly with a step size equal to $\min(\Delta t_{\mathrm{orb}}, 10^4\,\mathrm{yr})$. As the interior temperature evolves, we also actualise the mantle viscosity and rigidity and inspect whether the planet contains a magma ocean.

Since our model consists of two parts—a tidal module and a convection module—we seek the mantle viscosity and rigidity in two different forms. In order to calculate the mean Rayleigh number, which is used for the calculation of the upper thermal boundary thickness, we require the mantle viscosity averaged over the entire mantle. The tidal model, on the other hand, enables us to divide the planetary mantle into several layers and endow each of them with its own, locally–averaged rheological parameters. Specifically, in the case of a strongly tidally heated planet, the mantle can be divided into a solid region, with zero or relatively low melt fraction ($\phi < \phi_{\mathrm{D}}$), and a magma ocean, in which the melt fraction exceeds the disaggregation point ($\phi > \phi_{\mathrm{D}}$).

The viscosity and the rigidity are calculated in different depths of the mantle, following relations (4.23) and (4.24) and assuming an adiabatic temperature profile. The average mantle viscosity $\bar{\eta}_{\mathrm{m}}$, which enters the convection module, is then obtained as the geometric mean of the radially dependent values. At the same time, we inspect the radially dependent melt fraction (4.18). If it never exceeds the disaggregation point, the mantle is solid and the tidal model consists of a single

mantle layer, whose viscosity is equal to $\bar{\eta}_\mathrm{m}$. Conversely, if the melt fraction at any radius r exceeds the disaggregation point, the model should contain a magma ocean. In this case, we seek the lower boundary of the ocean and divide the mantle in the tidal model into two layers. The average viscosity and rigidity of these layers are then calculated from the radially dependent quantities individually.

Although the parameterised mantle convection model includes the evolution of the stagnant–lid thickness, we do not consider the melting of the planet's surface. Once the lid thickness decreases to a prescribed minimum value $D_\mathrm{l,min}$, it is set constant. The lithosphere is then allowed to evolve only after the planet begins to cool down. Similarly, in case the temperature at the bottom of the convecting mantle T_b exceeds the temperature at the core–mantle boundary T_c, we set the thickness of the lower boundary layer to a constant value $\delta_\mathrm{c,par}$. The heat flux from the mantle to the core is then calculated using equation (4.13) with the parameter $\delta_\mathrm{c,par}$ instead of δ_c.

A list of the numerical parameters used in this study is given in Table 4.1.

Table 4.1: Parameters of the numerical scheme

Parameter	Definition	Value or interval
ϵ_S	Local error in the short cycle	$[10^{-12}, 10^{-10}]$ or lower
ϵ_L	Local error in the long cycle	$[10^{-10}, 10^{-8}]$
δ_S	Upper limit on $\ddot{\theta}/\dot{\theta}$ in the short cycle	10^{-16}

4.6 Application to low-mass exoplanets

Extrasolar planets with radii below 1.5 $R_\oplus$ (Weiss and Marcy, 2014) or masses below 2−4 $M_\oplus$ (Chen and Kipping, 2017) are expected to have a rocky composition, similarly to the terrestrial worlds of the Solar System. At the same time, many of these terrestrial exoplanets orbit very close to their host star and their thermal and orbital evolution has been presumably marked by a period of substantial tidal dissipation. Since the theoretically predicted final state of a tidally evolved exoplanet is a circular orbit and synchronous rotation, attention has been recently drawn to the number of bodies whose orbital eccentricity seems to be, despite their proximity to the host star, still nonzero.

Among other explanations, such as observational bias, low age of the system, gravitational scattering or eccentricity excitation by mean–motion resonances, it has been proposed (e.g., Henning et al., 2009; Makarov, 2015) that the nonzero eccentricities can be maintained by the thermal state of the planet. This mechanism has been illustrated in several studies (e.g., Henning et al., 2009; Shoji and Kurita, 2014; Driscoll and Barnes, 2015) and can be also deduced from Figures 3.3-3.5 of the previous chapter. If a rocky planet with initial mantle viscosity 10^{21} Pa s and rigidity 200 GPa begins to melt, the decrease in viscosity

leads it close to the region of maximum, runaway heating, which is, in our case, around 10^{16} Pa s. As a consequence of the increased heat generation, the lattice of mantle minerals is disrupted and the mantle begins to melt. At this stage, the mantle viscosity and rigidity decrease abruptly and terminate the period of extreme tidal heating. Furthermore, the change in the rheological parameters might also result in the change of the planet's spin state (Makarov et al., 2018).

In this section, we are going to perform the parametric study of the rheological properties for the models of three low–mass exoplanets: GJ 625 b (Suárez Mascareño et al., 2017), GJ 411 b (Díaz et al., 2019), and Proxima Centauri b (Anglada-Escudé et al., 2016). As in Chapter 3, we explore here only the effect of instantaneous rheological and orbital parameters on the tidal locking and dissipation, i.e., we consider neither the thermal nor the orbital evolution. The planets have been chosen on the grounds of their masses, proximities to the host star, nonzero eccentricities, and presumed absence of strong perturbations by other bodies in the system. Since all of these exoplanets were found by radial velocity measurements and only their minimum masses are known, we calculate the (minimum) radii from the mass–radius relation of Zeng et al. (2016),

$$\left(\frac{R}{R_\oplus}\right) = (1.07 - 0.21 \cdot \mathrm{CMF}) \left(\frac{M}{M_\oplus}\right)^{1/3.7} \tag{4.25}$$

and assume that they have an Earth–like core mass fraction CMF = 0.3. The average core density is set to $\rho_\mathrm{c} = 10,000\,\mathrm{kg\,m^{-3}}$ in the case of Proxima Centauri b and to $\rho_\mathrm{c} = 12,000\,\mathrm{kg\,m^{-3}}$ for the other two exoplanets and the respective average mantle densities are calculated to match the prescribed masses and radii. The numerical values of all parameters used for the following study are listed in Table 4.2.

Table 4.2: Model parameters of the studied exoplanets

Parameter	Proxima Centauri b	GJ 625 b	GJ 411 b
m_* $[m_\odot]$	0.12	0.30	0.39
a [AU]	0.0485	0.0784	0.0785
m_p $[m_\oplus]$	1.27	2.82	2.99
R $[R_\oplus]$	1.074	1.333	1.354
ρ_c [kg m^{-3}]	10000	12000	12000
ρ_m [kg m^{-3}]	4797	5502	5589

4.6.1 GJ 625 b

The exoplanet GJ 625 b is about three times more massive than the Earth and lies on the inner edge of the habitable zone of its host star (Suárez Mascareño et al., 2017). Depending on its cloud coverage and albedo, it might or might not be able

to support the existence of liquid surface water. Although no other planets have been discovered in the system, the orbital eccentricity of GJ 625 b was estimated as $e = 0.13^{+0.12}_{-0.09}$ (Suárez Mascareño et al., 2017), which may point to the effect of mechanisms other than eccentricity excitation by mean–motion resonance.

Figure 4.2 shows the effect of the mantle viscosity and rigidity on the planet's spin state and surface tidal heat flux. The parametric study is performed for the mean and limit values of orbital eccentricity, that is, $e = 0.04$, 0.13, and 0.25. Considering, for the sake of illustration, a reference Earth-like viscosity $\eta_\mathrm{m} = 10^{21}$ Pa s and rigidity $\mu_\mathrm{m} = 200$ GPa, we see that the planet always despins into higher than synchronous spin–orbit resonance and retains significant surface tidal heat flux. Since the tidal heat flux for all studied values of eccentricity exceeds the surface heat flux at Io, the planet in this model setting is not expected to be habitable, independently of the incident flux from the host star. A more favourable situation would arise if the average mantle viscosity and rigidity were reduced either due to a different mineralogical composition or due to the presence of subsurface melt or water. In the case of, e.g., $\eta_\mathrm{m} = 10^{19}$ Pa s and $\mu_\mathrm{m} = 100$ MPa, the surface tidal heat flux becomes comparable to the total heat flux at the Earth and the tidal effects do not present a substantial threat to potential habitability. Only in the case of the lowest considered eccentricity ($e = 0.04$) does this combination of rheological parameters result in tidal locking into the synchronous rotation, the effect of which on the surface conditions is ambiguous (e.g. Kite et al., 2011; Checlair et al., 2019).

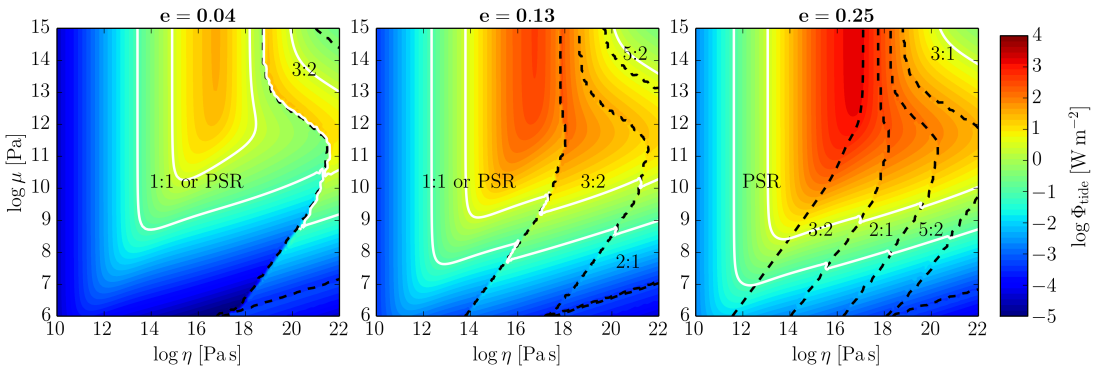

Figure 4.2: Surface tidal heat flux of a model of GJ 625 b for three plausible orbital eccentricities. Dashed lines delimit boundaries between the regions with different highest stable spin state. The solid white lines indicate the total surface heat flux on the Earth (~ 0.09 W m^{-2}) and on Io (~ 2.5 W m^{-2}). The triangular region in the lower right corners of the panels indicates combinations of parameters for which the despinning takes more than 10 Gyr.

4.6.2 GJ 411 b

The red dwarf GJ 411 belongs to the closest stars from the Sun, and it is also one of the brightest M–dwarfs on the Earth sky (Lépine and Gaidos, 2011). As

for December 2020, it is known to harbour one confirmed exoplanet, whose mass might be compatible with rocky composition (Díaz et al., 2019). The planet, GJ 411 b, orbits the star with a 12.95 day period and its equilibrium surface temperature lies between 256 and 350 K, depending on the albedo. It is, therefore, not expected to be habitable. Furthermore, its presumably nonzero eccentricity $e \in [0.00, 0.44]$, with most likely value of $e = 0.22 \pm 0.13$, (Díaz et al., 2019) makes it susceptible to immense tidal loading.

Figure 4.3 depicts the role of rheological parameters in the thermal–rotational evolution of GJ 411 b. Since the considered eccentricities are relatively high, the planet with a reference Earth–like composition would be most probably locked in a spin–orbit resonance between 3 : 2 and 3 : 1. Partial melting, which generally sets the planet to the central (red) part of the graph, would lead, in the case of small eccentricity, to pseudo–synchronous rotation. For higher eccentricities, however, even a molten planet with low mantle rigidity and decreased viscosity keeps a resonant spin state. The pattern of tidal heating is very similar to the previous case, and the surface tidal heat flux for realistic combinations of rheological parameters again exceeds the surface heat flux at Io. Combined with the high insolation, the tidal dissipation may contribute to transforming GJ 411 b into a lava planet.

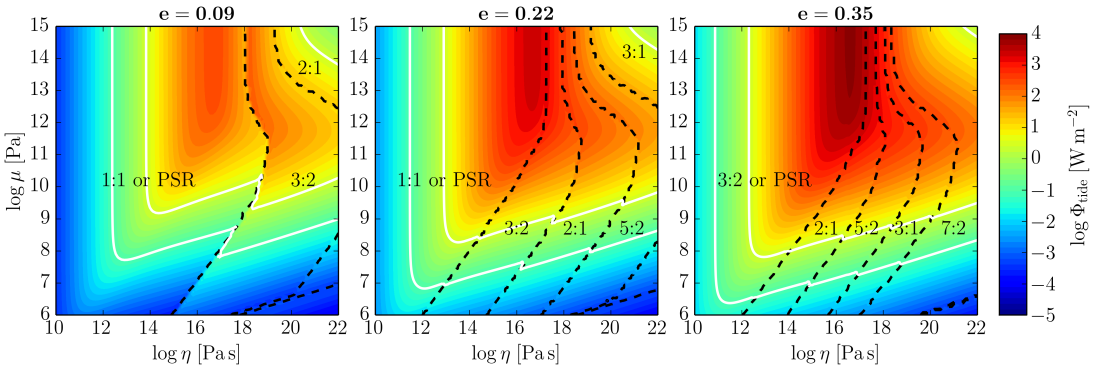

Figure 4.3: Same as Figure 4.2, but for GJ 411 b.

4.6.3 Proxima Centauri b

The discovery of an Earth-mass planet on the orbit around Proxima Centauri (Anglada-Escudé et al., 2016) has drawn a lot of attention mainly due to its astrobiological significance. Not only does the planet dwell in the traditional habitable zone, but its proximity also makes it a suitable target for direct imaging in the near future (Turbet et al., 2016). The orbit of Proxima Centauri b indicates a small remnant eccentricity of $e = 0.08^{+0.07}_{-0.06}$ (Jenkins et al., 2019) and, depending on the efficiency of tidal dissipation, the planet is expected to be locked either in the state of synchronous rotation or in the 3 : 2 spin–orbit resonance (Ribas et al., 2016). In a recent analysis of new radial velocity data for the system, Damasso et al. (2020) found that Proxima Centauri may also host another low–mass exoplanet on a wide orbit. However, since the orbital period of the new exoplanet

candidate is two orders of magnitude higher than the orbital period of Proxima Centauri b, it is not expected to affect the dynamics of the latter significantly.

The results of our last parametric study with constant parameters are illustrated in Figure 4.4. In accordance with the study of Ribas et al. (2016), the planet on the least eccentric orbit tends to the synchronous rotation for most of the considered pairs of rheological parameters. Only the combination of Earth–like viscosity ($> 10^{20}$ Pa s) and very low ($< 10^{8}$ Pa) or high ($> 10^{12}$ Pa) rigidity may allow the preservation of the 3 : 2 spin–orbit resonance even on an almost circular orbit. In the case of low rigidity, however, the tidal dissipation is almost negligible, resulting in a rather long period of despinning (on the scale of billions of years) and, in the most extreme situation, even preventing the planet from reaching stable spin state during the first 10 Gyr. For the other two considered eccentricities, the planet with Earth–like parameters despins first into higher spin–orbit resonance (3 : 2 or 2 : 1) and is able to maintain surface heat flux much higher than Io, which would later entail its melting and further despinning. In the view of the parametric study with fixed interior, we conclude that the habitability prospects of Proxima Centauri b are strongly dependent on the orbital eccentricity and for even mildly eccentric orbits they may be limited.

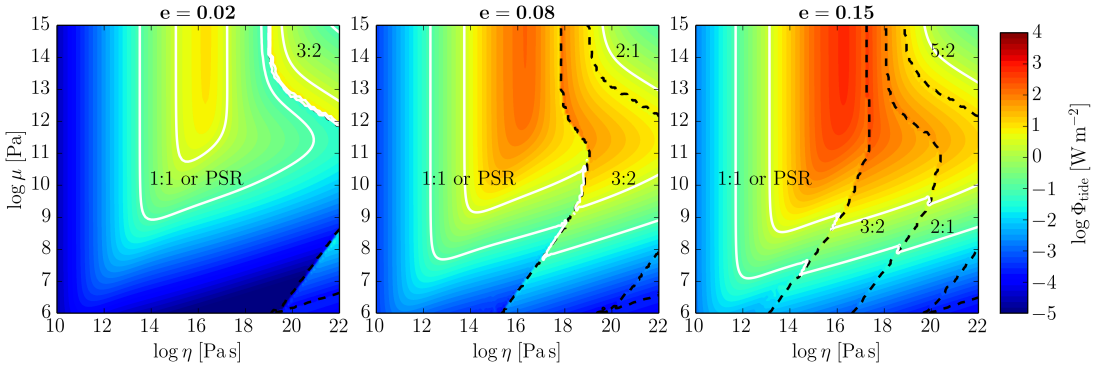

Figure 4.4: Same as Figure 4.2, but for Proxima Centauri b.

4.7 Coupled thermal–orbital evolution

Previous sections have shown that tidal heating on the three model planets is a complex function of various orbital and rheological parameters. The same complexity is also reflected by other phenomena affected by energy dissipation. Namely, it marks the rate of orbital evolution and the vigour of mantle convection. Stepping away from the parametric studies with constant orbital elements and interior structure, we are ready to discuss the results of the fully coupled model with an emerging magma ocean.

The following two subsections are dedicated to the long–term evolution of the exoplanets described in Table 4.2. However, since we are now also considering the thermal evolution, it is necessary to include several new quantities to the analysis,

such as the initial temperatures and the parameters of the convection model (Table 4.3). In all model cases, we assume that the planet's mantle is initially solid, and the temperature at the top of the convective layer is $T_{\mathrm{m},0} = 1500\,\mathrm{K}$. The tidal evolution of real exoplanets would presumably initiate in the magma ocean state, when at least part of the planet is still molten due to the heat released during its formation. The interior temperatures would be, therefore, much higher. To account for these initial conditions, we also conducted numerical experiments for initial temperatures $T_{\mathrm{m},0} = 2000\,\mathrm{K}$ and $T_{\mathrm{m},0} = 2500\,\mathrm{K}$; however, all cases led to a rapid equilibration of T_{m} around the same value. The effect of the initial temperature at the top of the convecting mantle is, in the long term, minimal. We also tested different values of the disaggregation widths Δ_η and Δ_μ, which affect the transition of a partially molten layer from a solid–like behaviour to a liquid–like behaviour around the disaggregation point Φ_{D}. Higher Δ corresponds to a more gradual transition between the two regimes. On the base of these numerical experiments, we chose the value $\Delta_\eta = \Delta_\mu = 0.01$, since it best describes the abrupt change considered in other studies (e.g., Fischer and Spohn, 1990) and since a further decrease in Δ does not substantially affect the results.

4.7.1 Evolutionary paths of Proxima Centauri b

Figure 4.5 shows the coupled thermal–orbital evolution in the model case of Proxima Centauri b. For illustration purposes, we assume that the planet begins on a mildly eccentric orbit ($e = 0.2$), and its initial semi–major axis is set to its presently observed value[2]. To include the unknown effect of pressure on the lower mantle viscosity, we consider four possible reference viscosities η_0 in the range from 10^{19} to $10^{22}\,\mathrm{Pa\,s}$. In addition to mimicking different pressure dependencies, the range of viscosities also accounts for different possible mineralogical compositions of the mantle. To identify the effect of the evolving interior, we further run two additional simulations, in which the interior temperature profile and the rheological properties are held constant while the orbital parameters evolve (dashed lines in Figure 4.5). The comparison between the coupled model and the constant–interior model is discussed at the end of this subsection.

In the beginning, the planet despins rapidly into the first stable spin–orbit resonance. Depending on the reference viscosity, it ends up either in the 2 : 1 resonance ($\eta_0 = 10^{21}$ or $10^{22}\,\mathrm{Pa\,s}$) or in the Mercury–like 3 : 2 resonance ($\eta_0 = 10^{19}$ or $10^{20}\,\mathrm{Pa\,s}$). The despinning phase is, furthermore, marked by a rapid increase in the interior temperature—a consequence of the relatively high orbital eccentricity and nonsynchronous rotation. Due to its orbital configuration, the planet undergoes considerable tidal loading, and the dissipated heat remains in the mantle because it cannot be efficiently taken away by the convection. This

[2]The present–day semi–major axis a_{now} and the present–day eccentricity e_{now} are related to the initial values by $a_{\mathrm{now}}(1-e_{\mathrm{now}}^2) = a_0(1-e_0^2)$. Nevertheless, since the present–day eccentricity of the exoplanets, as well as the age of their host stars, is known with relatively large errors, we cannot exactly trace back the a_0 corresponding to the chosen values of e_0. Although it would be possible to test different initial semi–major axes, we decided to set a_0 for all model cases of a given system to the same value and to vary only the initial eccentricity.

Table 4.3: Parameters of the mantle convection model

Parameter	Definition	Value	Unit
$T_{\mathrm{m},0}$	Initial temperature at the top of the convecting mantle	1500	K
$\Delta T_{\mathrm{cmb},0}$	Initial temperature drop over the core–mantle boundary	1500	K
$T_{\mathrm{s},0}$	Surface temperature (constant)	500	K
$D_{\mathrm{l},0}$	Initial stagnant–lid thickness	50	km
$D_{\mathrm{l,min}}$	Minimum stagnant–lid thickness	1	km
$\delta_{\mathrm{c,par}}$	Lower thermal boundary layer thickness for the overheated mantle	10	km
k_{m}	Thermal conductivity of the mantle	1	$\mathrm{W\,m^{-1}K^{-1}}$
k_{l}	Thermal conductivity of the lithosphere	1	$\mathrm{W\,m^{-1}K^{-1}}$
α_{m}	Thermal expansivity of the mantle	2×10^{-5}	$\mathrm{K^{-1}}$
c_{m}	Specific heat capacity of the mantle	1200	$\mathrm{J\,K^{-1}kg^{-1}}$
c_{c}	Specific heat capacity of the core	800	$\mathrm{J\,K^{-1}kg^{-1}}$
$\mathcal{E}^*$	Activation energy	10^5	$\mathrm{J\,mol^{-1}}$
η_{min}	Minimum mantle viscosity due to melting	0.1	Pa s
μ_{max}	Maximum mantle rigidity	2×10^{11}	Pa
μ_{min}	Minimum mantle rigidity due to melting	10^{-7}	Pa
Δ_η	Disaggregation width for viscosity	0.01	—
Δ_μ	Disaggregation width for rigidity	0.01	—
Φ_{D}	Disaggregation point	0.4	—

period of overheating is, however, only transient. As can be seen in the lower row of Figure 4.5, the increase in the interior temperature is accompanied by a similarly steep decrease in the average mantle viscosity and rigidity. We note that in these model settings, the top of the mantle melts shortly after the beginning; the melting temperature at the relevant pressures is around $T_{\mathrm{m}} = 1900\,\mathrm{K}$. The melt is predominantly concentrated below the lid as both solidus and liquidus temperatures increase considerably with depth.

The increase in the upper mantle temperature and decrease in the average viscosity and rigidity continues until the mantle reaches an equilibrium state. Once the viscosity decreases to a value that enables the efficient transport of the generated heat to the surface, the interior temperature stops rising and—independently of the reference viscosity—stabilises around 2350 K. Increased

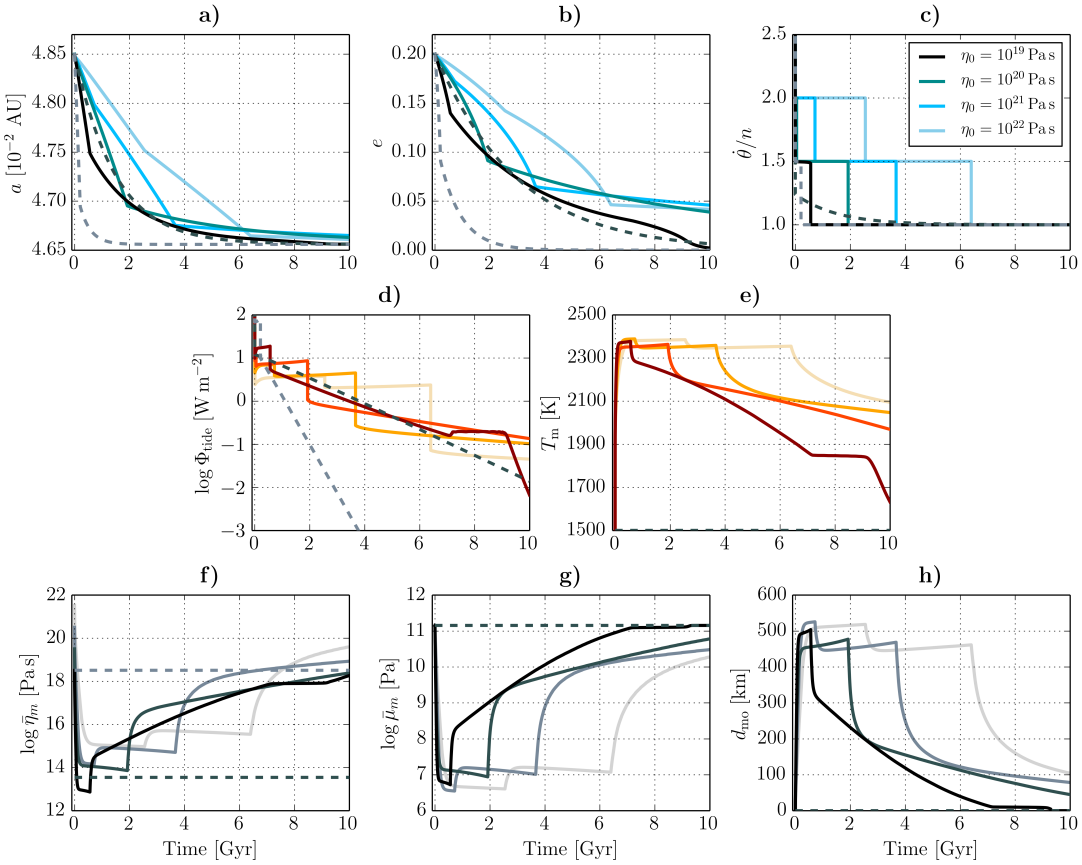

Figure 4.5: Simultaneous evolution of the spin–orbital parameters (*upper row*), thermal state (*middle row*) and interior properties (*lower row*) of Proxima Centauri b. Going from the upper–left corner to the lower–right corner, the individual panels depict a) the semi–major axis, b) the orbital eccentricity, c) the spin–orbit ratio, d) the surface tidal heat flux, e) the mantle temperature measured under the stagnant lid, f) the average mantle viscosity, g) the average mantle rigidity, and h) the thickness of the magma ocean. The initial eccentricity was set to $e_0 = 0.2$, and the reference viscosity spans from $\eta_0 = 10^{19}$ Pa s (darkest colours) to $\eta_0 = 10^{22}$ Pa s (lightest colours). For comparison, the dashed lines indicate the spin–orbital evolution and the surface tidal heat flux for a model with constant (non–evolving) temperature profile. The dark gray dashed line corresponds to the reference viscosity $\eta_0 = 10^{14}$ Pa s and the light gray dashed line to the reference viscosity $\eta_0 = 10^{19}$ Pa s.

mantle temperatures also affect the efficiency of heat transfer from the core. As the mantle reaches thermal equilibrium at high temperatures, such as in this model case, the cooling rate of the core substantially decreases and the core attains a quasi-equilibrium. At this moment, the planet possesses a $400 - 500$ km thick magma ocean, and the global melt fraction in the mantle is about 25 %. How long the interior remains in the equilibrium state depends on the evolution of the spin–orbital parameters. Decreased mantle viscosity and evolving eccentricity act

together in destabilising the actual spin–orbit resonance. As was already illustrated in the previous subsections, the regions of stability for distinct stable spin states depend on the average mantle viscosity (or rigidity) and on the eccentricity. Different model cases in Figure 4.5 thus undergo the transition to lower spin–orbit resonances at different times.

Each transition between stable spin–orbit resonances is accompanied by a drop in the tidal heat rate. The decreased heat rate results in slower orbital evolution (noticeable as a change of the slope in the first two panels) and in the fast cooling of the vigorously convecting mantle. The subsequent fate of the planet's interior depends on the new spin state. If the planet despinned into yet another nonsynchronous spin–orbit resonance, such as 3 : 2 for the higher considered viscosities, the tidal dissipation remains an important, almost eccentricity–independent heat source (see Figure 3.6). In this case, the interior promptly acquires a new equilibrium thermal state at a slightly lower temperature and higher average viscosity. On the other hand, if the planet despins directly into the synchronous rotation, the tidal heat rate becomes strongly dependent on the eccentricity. The interior first cools down to a quasi–equilibrium state, in which the mantle temperature continues to decrease. The long–term cooling is then controlled by the decaying eccentricity.

A noteworthy feature of the depicted evolutionary paths is the late thermal equilibrium of the model case with $\eta_0 = 10^{19}\,\mathrm{Pa\,s}$. The sudden increase in the surface tidal heat flux, which occurs after 7 Gyr, is associated with the partial crystallisation of the remnant magma ocean. Once the magma layer begins to crystallise and the local rigidity in the upper mantle increases, it becomes a significant source of tidal dissipation, able to counterbalance the gradual cooling. The period of thermal equilibrium is, however, terminated after 2 Gyr. By the end of this transient phase, the average melt fraction in the magma layer decreases to 0.4 and the rigidity slowly increases. At 9.2 Gyr, the ocean eventually disappears. After leaving the equilibrium, the planet follows a path of gradual cooling down with an even steeper slope.

The presented model of Proxima Centauri b illustrates, in the first place, the principal role of tidal locking in the long–term thermal and orbital evolution. Despinning into a new spin–orbit resonance affects all other studied quantities and enables abrupt changes in the slope of the semi–major axis and the eccentricity. The eccentricity, in turn, complements the effect of the planet's rotation in determining the tidal heat rate.

The combined effect of the two parameters is most prominent in the evolution of the average surface tidal heat flux (panel "d" in Figure 4.5). In the beginning, the highest rate of tidal heating is observed in the model case with the lowest reference viscosity. The highest viscosity case, on the other hand, dissipates the lowest amount of energy. Since the eccentricity of both cases is comparable and the rotation is nonsynchronous, the difference lies in the different susceptibility to tidal deformation. After 5 Gyr, however, the situation almost reverses. While the highest reference viscosity case remains in the 3 : 2 resonance for a considerable

time and supports persistent tidal heating, the lowest reference viscosity case has already despinned into the synchronous rotation and dissipates order of magnitude less energy. The former case also retains more than two times higher orbital eccentricity than the latter, which further contributes to the increased tidal dissipation.

Another interesting observation can be made by comparing the orbital eccentricities over the last 4 Gyr. Independently of the interior properties, the three highest–viscosity cases end up on very similar orbits. The same tendency was also observed in additional model runs with different initial eccentricities ($e = 0.05$, 0.1 or 0.4). The resulting eccentricities after 10 Gyr of evolution tend either to a similar nonzero value (between 0.03 and 0.05) or—in the lowest reference viscosity cases—toward circular orbit. However, as was illustrated in this subsection, the earlier evolution of all model parameters is relatively complex and cannot be described by a simple rule.

Compared to the model with fixed interior properties (dashed lines in Figure 4.5), the coupled model generally maintains higher orbital eccentricities. To illustrate this, we first focus on the evolution of the "fixed–interior" model case with reference viscosity $\eta_0 = 10^{19}$ Pa s. In the beginning, the chosen model case is confronted with much higher tidal dissipation than any of the other model cases. Since it is not moderated by a decrease in the rheological parameters, this overheating results in the rapid circularisation of the orbit and tidal locking into synchronous rotation within the first billion of years. The surface tidal heat of the chosen model case then quickly becomes negligible.

The orbital evolution of the second fixed–interior case, with $\eta_0 = 10^{14}$ Pa s, resembles the pattern of the evolving–interior model with $\eta_0 = 10^{19}$ Pa s. However, while the latter possesses a relatively stiff mantle, whose average viscosity is reduced only by the presence of a magma ocean, the former has low mantle viscosity by definition. Hence, while the evolving-interior model gets locked early into the 1:1 resonance, which reduces its rate of orbital evolution, the fixed-interior model remains in stable pseudo–synchronous rotation. Although the two model cases in question provide similar results for both of the studied orbital parameters, the difference in the rotation history would yield substantially different atmospheric forcing and different surface conditions. This example illustrates that, when studying the spin rate evolution of partially molten bodies, the assumption of homogeneous versus layered mantle may lead to qualitatively different results.

4.7.2 Thermal and orbital state of evolved low–mass exoplanets

The long–term evolution of all chosen exoplanets follows similar tendencies. Depending on the initial orbital eccentricity, they experience one or more spin–orbit lockings and possibly also a series of thermal equilibria. In the previous subsection, we inspected the evolutionary path of Proxima Centauri b over 10 Gyr. The actual age of the system is, however, much lower. According to asteroseismic observations

of the α Centauri binary (Thévenin et al., 2002), it originated 4.85 Gyr ago and, therefore, is only a few hundred million years older than the Sun. Since the age of the other two exoplanets is—to the best of our knowledge—currently unknown, we now focus on the evolutionary outcome of several model cases after 5 Gyr.

For each of the three studied exoplanets, we consider four possible initial eccentricities ($e_0 = 0.05$, 0.1, 0.2, and 0.4) and four reference viscosities identical to the previous subsection. The tidally evolved eccentricity after 5 Gyr, together with the spin–orbit ratio and the surface tidal heat flux, is depicted in Figures 4.6 to 4.8. To sort out the model outcomes which do not comply with the eccentricity derived from current observations, we indicate the plausible eccentricities by a red line in the colour bar and by the light blue background on the individual panels.

Figure 4.6 illustrates the possible evolution outcomes of GJ 625 b: a planet that lies on the inner edge of the habitable zone. Its instantaneous, tidally evolved eccentricity follows a predictable pattern, which is only mildly affected by the reference viscosity. The higher the initial eccentricity, the higher its value after 5 Gyr. Since the uncertainty of the empirically determined eccentricity is relatively high, the majority of the models comply with the observation. Model cases initialised to the highest considered eccentricity, possibly due to external excitation, are, however, excluded. The second panel of the figure indicates that the planet is most probably locked in the synchronous rotation. Only in the rare case of high–eccentricity start with an Earth–like mantle viscosity does the planet sustain the 3 : 2 resonance. A consequence of the resonance locking is further reflected in the nontrivial dependence of the surface tidal heat flux on the reference viscosity. While in the lower eccentricity cases the resulting heat flux monotonically increases with decreasing viscosity, for $e_0 = 0.2$ and $e_0 = 0.4$ the rheological parameters play a lesser role than the rotation state. The values of the tidal heat flux also indicate that the evolved planet is most probably less volcanically active than Io. If rotating synchronously, its thermal output due to tides might be hypothetically comparable with other internal sources of heat (e.g., radiogenic heating or remnant heat from accretion).

Due to the similar orbital periods and masses, the conclusions given for the model of GJ 625 b are also applicable to the case of GJ 411 b (Figure 4.7). The difference, however, lies in the eccentricities. For GJ 411 b, the mean value of the empirically given eccentricity is higher than 0.2, which points at the currently high surface tidal heat flux and nonsynchronous rotation. Were the present–day orbit influenced only by tides, the planet would have to originate on a highly eccentric trajectory. The evolved spin rate predicted by the coupled model ranges from the 1 : 1 spin–orbit resonance for low reference viscosities up to the 5 : 2 resonance for higher viscosity values. Accordingly, the surface tidal heat flux is expected to surpass the activity of Io.

The orbital and physical parameters of the Proxima Centauri system are rather unlike the two previously described exoplanets. First of all, its lower mass and lower predicted orbital eccentricity make it akin to the Earth. Figure 4.8 suggests that independently of the initial eccentricity and the reference viscosity,

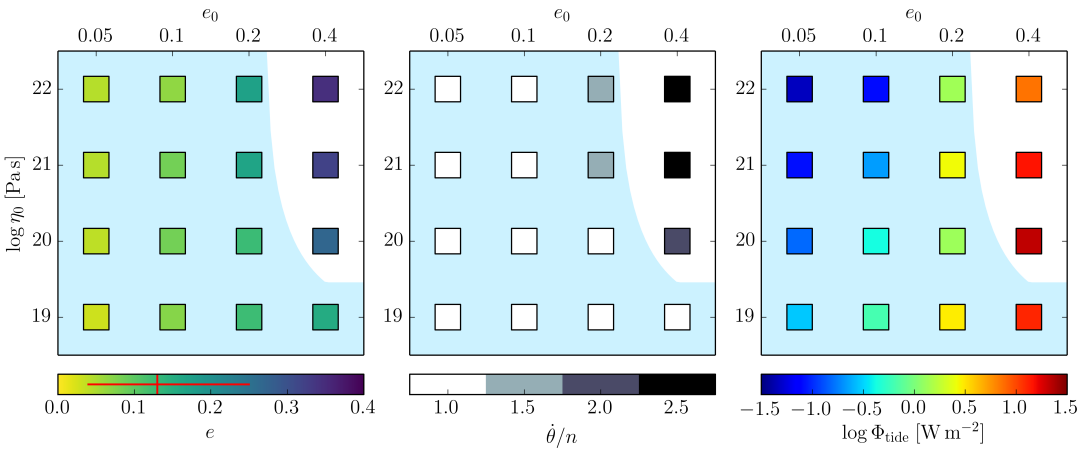

Figure 4.6: Orbital and thermal characteristics of GJ 625 b after 5 Gyr of evolution. Depending on the initial orbital eccentricity e_0 (x-axes) and the reference mantle viscosity η_0 (y-axes), the individual panels illustrate the evolved eccentricity (*left*), the spin–orbit ratio (*middle*) and the surface tidal heat flux (*right*). The light blue areas correspond to the model parameters for which the evolved eccentricity complies with the observation (Suárez Mascareño et al., 2017). The range of the empirically given values is also indicated by the red line in the first colour bar.

the planet's orbit tends to a relatively low eccentricity below $e = 0.1$. Hence, the majority of the cases comply with the current observations. As a consequence of the low resulting eccentricity, the model predicts the prevalence of synchronous rotation. The only exception from this pattern is the 3 : 2 resonance expected for a high reference viscosity model with initial eccentricity of $e_0 = 0.2$ (see also Figure 4.5). As most of the model cases end up in the same rotation state, the thermal output of Proxima Centauri b is usually determined by the actual eccentricity and the rheological parameters. Especially for low initial eccentricities, the surface tidal heat flux is comparable to the total heat flux on the Earth and, depending on the other heat sources and on the effect of the subsurface magma layer, it might not present an obstacle for the hypothetical habitability.

In addition to the presented diagrams, it is worth noting that the majority of the model cases support a long–lived magma ocean. The only case in which the ocean disappears during the first 5 Gyr is Proxima Centauri b with the lowest considered initial eccentricity and reference viscosity. However, since the effect of the subsurface magma ocean on the surface conditions is beyond the scope of this work, we postpone the discussion of this phenomenon to a more detailed study of the interior evolution.

4.8 Discussion

The spin–orbital dynamics of a tidally loaded exoplanet interact with its interior evolution in an intricate way. Throughout the previous section, we attempted

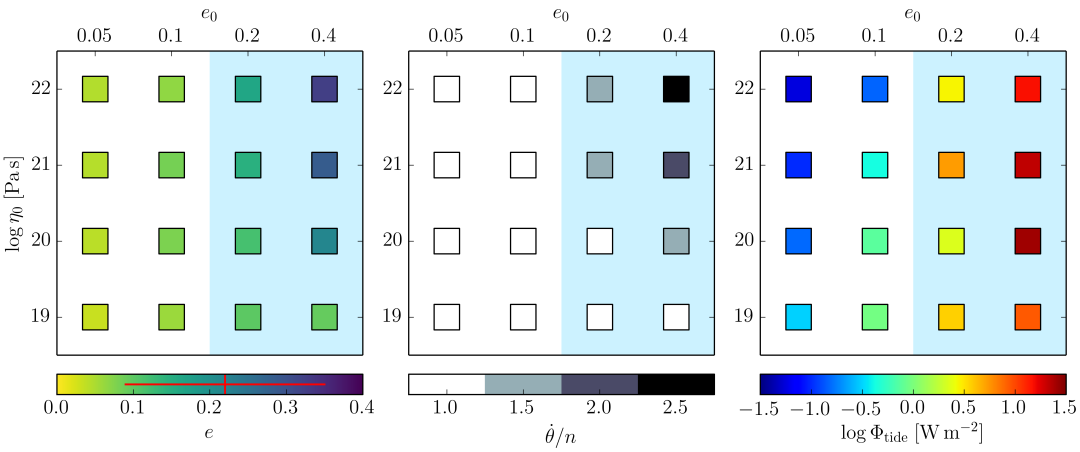

Figure 4.7: Same as Figure 4.6, but for GJ 411 b. The span of empirically given eccentricities is taken from Díaz et al. (2019).

to illustrate the complexity of the coupled model, which is given primarily by the viscoelastic rheology and the evolution of the interior structure. Although the complexity is inherent to the nature of the problem, the exact results and predictions depend on the assumptions made. In this section, we focus on the main features of the model which might have affected its outcome, and we also discuss the implications of our results.

4.8.1 Stable spin states

The thermal and orbital evolution of viscoelastic planets on eccentric orbits is interrelated with the evolution of their spin state. As a consequence of the viscoelastic behaviour, planets with rocky interiors tend to the proximity of spin–orbit resonances, whose stability is given by the frequency of tidal loading and by the rheological parameters (e.g., Ferraz-Mello, 2013; Makarov and Efroimsky, 2013; Correia et al., 2014; Ferraz-Mello, 2015). Different orbital configurations (e.g., the eccentricity) yield a different spectrum of loading frequencies and determine the actual stable spin state. Although the basic aspects of the coupled system's dynamics can be captured by models with synchronous rotation (e.g., Henning et al., 2009), the results of Sections 4.6 to 4.7, as well as Chapter 3, show that the consideration of higher spin–orbit resonances is important, especially in the case of planets with low orbital eccentricity. In this case, the eccentricity tides are already weak, and the tidal dissipation is sustained primarily by nonsynchronous rotation. The time at which the planet undergoes a transition to the synchronous rotation determines the values of the terminal, slowly evolving orbital parameters.

The stable spin state of real moons and close-in planets is given not only by the gravitational tides but also by the thermal atmospheric tides (e.g., Gold and Soter, 1969; Auclair-Desrotour et al., 2019) and/or by their permanent deformation (e.g., Goldreich, 1966). In the presence of a significant atmosphere, as is the case for the planet Venus, the dayside experiences higher temperatures and lower atmospheric

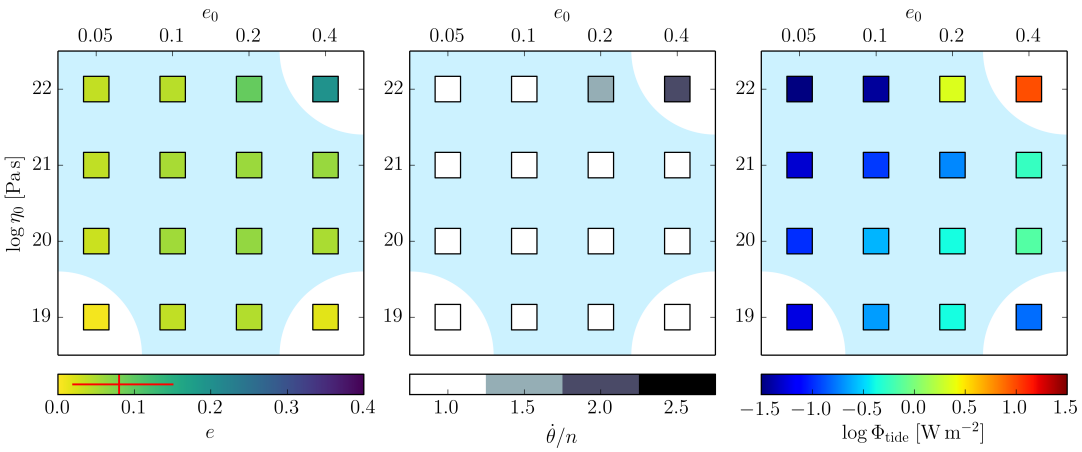

Figure 4.8: Same as Figure 4.6, but for Proxima Centauri b. The span of empirically given eccentricities is taken from Jenkins et al. (2019).

pressures than the nightside. As a consequence of the periodic thermal forcing and the redistribution of atmospheric masses, the planet becomes subjected to additional tidal torque acting on its atmosphere. The competition between the gravitational and thermal tidal torques destabilises spin–orbit resonances and drives the planet to nonsynchronous rotation (e.g., Leconte et al., 2015). Similarly, in the case of a triaxial planet, the tidal torque is counterbalanced by a torque acting on the permanent deformation. The inherent triaxiality may either stabilise the planet in an otherwise unstable synchronous rotation (e.g., Goldreich, 1966; Goldreich and Peale, 1966) or, conversely, it may prevent the planet from exact synchronisation by locking it into a higher spin–orbit resonance (e.g., Makarov, 2012; Zanazzi and Lai, 2017).

When calculating the stable spin state, we also assumed that the spin axis is perpendicular to the orbital plane. The tidal effects in our study were, therefore, only due to the nonzero eccentricity. In general, the rotation state is determined by the planet's figure and interior structure and its equilibrium obliquity corresponds to one of the Cassini states (e.g., Peale, 1969; Boué, 2020). The stability of individual Cassini states also depends on the configuration of the planetary system. A planet with nonzero obliquity might be attracted to different spin–orbit resonances (Boué et al., 2016), and its thermal budget is then enhanced by obliquity tides (e.g., Peale and Cassen, 1978). Both of these effects contribute to long-term evolution. As a first-order approximation, the ratio of the obliquity heating to the eccentricity heating can be expressed as (e.g., Peale and Cassen, 1978; Chyba et al., 1989; Murray and Dermott, 1999)

$$\frac{P_\beta^{\mathrm{tide}}}{P_e^{\mathrm{tide}}} \simeq \frac{\sin^2 \beta}{7e^2} \,. \tag{4.26}$$

Stable nonzero obliquity may, therefore, prevent runaway cooling once the orbital eccentricity decreases to a negligible value. A test calculation with both sources

of tidal heating and a constant obliquity of 20° indicates that increased tidal heat rate stabilises the interior at a higher temperature, with a thicker magma ocean. The orbital evolution is marked both by the increased dissipation and by the earlier destabilisation of higher spin–orbit resonances due to low mantle viscosity. However, in the long term, the obliquity of strongly tidally loaded exoplanets (e.g., Fabrycky et al., 2007) tends to zero.

4.8.2 Sources of orbital eccentricity

The orbital eccentricities of moons and planets in the Solar System are shaped mainly by mutual interactions between the bodies. A well–known example of this effect is planet Mercury, whose eccentricity may rise up to 1 due to the gravitational action of other planets (e.g., Laskar, 1994; Batygin and Laughlin, 2008; Laskar and Gastineau, 2009; Lithwick and Wu, 2011; Boué et al., 2012), and large satellites of gas giants, with orbital parameters forced by orbital resonances (e.g., Schubert et al., 2010). A considerable change of the satellites' orbits might have also been caused by transient events, such as close encounters of giant planets during the period of planet migration (e.g., Deienno et al., 2014). In analogy with the Solar System, the detection of nonzero orbital eccentricities among close–in exoplanets is often a consequence of ongoing gravitational perturbations by other bodies (e.g., Takeda and Rasio, 2005; Pu and Lai, 2018; Van Eylen et al., 2019) or a relic of past catastrophic events, such as planet–planet scattering (e.g., Petrovich et al., 2014; Huang et al., 2017). In single–planetary systems or systems without substantial gravitational forcing, the orbital eccentricity can be explained by initial conditions during planet formation and by subsequent evolution in a gas disk (e.g., Kley and Nelson, 2012; Ragusa et al., 2018), as well as by formation in an unstable multiplanetary system. Another possible source of nonzero orbital eccentricity is the tidal interaction of a close–in planet with a rapidly rotating host star (Boué and Efroimsky, 2019, equation (156)). For a detailed overview of the eccentricity excitation mechanisms, we refer the reader to, e.g., Namouni (2007).

In this chapter, we assumed that the planet begins on an eccentric orbit and evolves only under the action of tides. The three studied exoplanets, GJ 625 b, GJ 411 b and Proxima Centauri b, were also chosen on the grounds of absent, negligible or yet–unknown gravitational forcing by a third body. Applying the tidal model to such exoplanets may help to shed light on the initial conditions in the system or constrain the previous gravitational forcing the system underwent. The results of the parametric study presented in Section 4.7.2 indicate that the empirically given eccentricities can be reconciled with a wide range of initial eccentricities and reference viscosities. In the case of exoplanets GJ 625 b and GJ 411 b, this is mainly due to the large error bars of the current eccentricities. For Proxima Centauri b, the reason also lies in the similar tendencies of the test cases, all of which evolve toward a similar, mild eccentricity after 5 Gyr.

The most specific of the studied exoplanets is GJ 411 b. Its high present–day eccentricity determines it either to a high–eccentricity start or to eccentricity excitation in the past. An additional constraint on the initial conditions would be

given by the age of the host star, which is currently unknown. Although GJ 411 b, discovered in 2019, is the only confirmed exoplanet in the system, the star GJ 411 had been for a long time suspected to host a planetary companion. However, none of the previously reported detections has been confirmed, and the existence of other bodies in the system is putative (see also discussion and references in Díaz et al., 2019). In the presence of strong eccentricity forcing by a second planet, the thermal evolution of GJ 411 b would be affected by periods of high tidal dissipation, and its evolution would resemble that of resonant moons in the Solar System.

4.8.3 Parameterised convection and melting model

In Section 4.7, we observed that the coupled thermal–orbital evolution proceeds as a sequence of thermal equilibria. In each equilibrium, the heat sources due to the tidal dissipation are entirely compensated by the heat loss by mantle convection. However, the heat loss is determined by the selected convection regime. A different cooling rate would yield different equilibrium states, different temperature profiles and, most importantly, different rheological properties. Here, we shall discuss our choice of the convection regime and its impact on the resulting cooling rates.

First of all, we note that the choice of the convection regime is a very complex problem that should be ideally addressed by numerical modelling. The thermal or thermo–chemical convection on Earth and other Solar System bodies is discussed in extensive literature. Despite the scarcity of information on exoplanets, numerical models are used to investigate the scaling of mantle convection with mass and radius (including the effect of extreme pressure) and to describe the convection regimes in massive terrestrial exoplanets ("super-Earths"; e.g., van den Berg et al., 2010; Čížková et al., 2017). The probability of plate tectonics on super-Earths was investigated by, e.g., van Heck and Tackley (2011), Foley et al. (2012), and Noack and Breuer (2014). Van Summeren et al. (2011) studied the mantle convection in tidally locked terrestrial planets with large surface temperature contrasts. The presence of huge volumetric heating or hot conditions, as experienced by close–in planets, brings additional challenges due to large–scale melting and the emergence of magmatic ponds and oceans. Vilella and Kaminski (2017) used a systematic approach to build a diagram providing conditions for partial melting based on the planet size and internal heating. An ideal solution accounting for substantial internal heating or extreme temperatures on close-in exoplanets is a 3d multiphase convection with tidal dissipation as a source of volumetric energy. Nevertheless, the inclusion of the melt–solid phase interaction, such as the melt migration, melt production, and recrystallisation, requires complex description (e.g., Bercovici et al., 2001) and possibly leads to extremely computationally–demanding simulations.

Any 3d/2d modelling efforts are thus beyond the scope of this study. In order to understand the main aspects of secular thermal–orbital coupling, we follow here a traditional approach of parameterised convection, where we have to account for possibly significant melting. Depending on the size of the planet and the

magnitude of internal heating, the incorporation of melt into the model can be treated in different ways. Parametric studies of mantle convection in Mars or stagnant–lid Earth (Breuer and Spohn, 2006; Tosi et al., 2017), on which we base our interior evolution model, assume that the melt with positive buoyancy is instantaneously extracted from the mantle and becomes a building material for the crust. This approach might result in the depletion of the mantle material and in its dehydration (e.g., Plesa and Spohn, 2012), which increases the upper mantle solidus and regulates the further production of the melt. Coupled thermal–orbital models focused on small terrestrial exoplanets (Henning et al., 2009; Shoji and Kurita, 2014; Driscoll and Barnes, 2015), on the other hand, assume a well–mixed mantle with evenly distributed melt and decreased viscosity and rigidity of the entire planet. However, the neglection of radial stratification of the planet might substantially affect the resulting tidal heating pattern (Beuthe, 2013; Henning and Hurford, 2014).

A realistic parameterisation of the subsurface melt dynamics would take into account the permeability of the lithosphere (e.g., Spiegelman, 1993, and references therein) and the melt buoyancy, which is a complex function of the mantle composition. According to experimental studies with floating olivine in silicate liquids, the melt becomes neutrally buoyant around $7 - 12\,\mathrm{GPa}$, at the density crossover of the two phases (e.g., Agee and Walker, 1993; Ohtani et al., 1995; Agee, 2008). Specifically, in the upper mantle of the Earth, the existence of a density crossover might enable the formation and maintenance of hydrous melts above the 410 km discontinuity (Agee, 2008). In a general case, the position of this transition depends on the water content, the mineralogy of the mantle, and the local temperature. Since all of these parameters vary with depth, the realistic incorporation of melt migration would require a much more detailed study. Another important mechanism, which affects the cooling rate of the planet, is global–scale volcanism (e.g., O'Neill et al., 2007). As proposed by Moore et al. (2017), moons and planets with overheated and partially molten mantles might be effectively cooling down by heat–pipe volcanism, before they transition to the stagnant–lid or mobile–lid regime. Strongly tidally loaded bodies, such as Jupiter's moon Io (Moore, 2003), or large terrestrial exoplanets (Moore et al., 2017) might remain in the stage of heat pipe for billions of years.

We opted here for parameterised stagnant–lid convection with a very simplistic treatment of the melt. The model does not consider any melt migration and, conversely, assumes a stable magma layer in the range of depths where the local temperature exceeds the disaggregation point. This assumption enables us to assess the dynamical effect of a liquid, almost nondissipative layer above a much more viscous lower mantle. The liquid layer also decouples the lithosphere and the rest of the mantle, which is then more susceptible to tidal deformations. Nevertheless, while we consider the magma ocean in the tidal model, it is included only in a simplified manner in the mantle convection. The maintenance of the magma ocean can be understood as a limit case for interior evolution, maximising the effect of partial melting. The presence of melt decreases the upper boundary layer thickness via the geometric average of the mantle viscosity and allows for

large heat flux into the lithosphere. This results in faster cooling of the mantle, as expected for any presence of melt. The partial melting and the formation of magma ocean also help to regulate the thermal runaways through the following two mechanisms: i) the consumption of a part of the tidal heat by the phase transitions and ii) the change of the rheological properties. During the cooling part of the evolution, the magma ocean can delay the cooling due to recrystallisation and latent heat.

Finally, we should note that our model neglects any circulation in the magma ocean. The tidal response of fluid is essentially different from the response of solid layers and should be calculated by a different set of tidal equations (such as Laplace tidal equations; see, e.g., Tyler et al., 2015). Dissipation in the liquid layers is directly affected by the rotation rate and is characterised by the formation of inertial waves (e.g., Rovira-Navarro et al., 2019). Several recent studies have investigated the tidal response of realistic liquid layers in Io or icy satellites of Solar System gas giants. The importance of tidal dissipation in subsurface oceans generally depends on the thickness of the ocean and the thickness of the overlying shell, which tends to dampen the ocean tides (Beuthe, 2016; Matsuyama et al., 2018). Additional heat can be also produced by turbulent dissipation, internal gravity waves in the ocean, and interaction of the fluid with the ocean basin topography.

4.8.4 Habitability of tidally evolving exoplanets

Two of the planets chosen for our parametric study, namely GJ 625 b and Proxima Centauri b, are reported to reside in the conventional habitable zone of their host star (Anglada-Escudé et al., 2016; Suárez Mascareño et al., 2017). The habitable zone is conventionally defined as the range of orbital distances that allow the planet to sustain liquid surface water under certain atmospheric conditions (Kasting et al., 1993). The boundaries of a habitable zone are given by the incident flux and thus depend on the stellar type. Later refinements of the original definition relate the boundaries of the habitable zone to additional parameters, such as the planetary mass, atmosphere, and orbital eccentricity (e.g., Seager, 2013; Kopparapu et al., 2013, 2014; Palubski et al., 2020), or restrict the range of plausible temperatures to allow for the formation of complex organics (Wandel, 2018; Wandel and Gale, 2020) or even complex life (Schwieterman et al., 2019). Although the orbit's location inside the habitable zone may serve as an initial guess on the surface conditions of an exoplanet, it is not sufficient to determine its potential to harbour life. Planetary habitability is influenced by a combination of many effects, some of which are also altered by tides (e.g., Seager, 2013; Kane and Torres, 2017; Lingam and Loeb, 2018; Del Genio et al., 2019).

Tidal evolution affects habitability in both positive and negative ways. Secular shrinking and circularisation of the orbit may drive the planet inside or outside the habitable zone (Barnes et al., 2009; Palubski et al., 2020), and the tidal alignment of the spin axis may principally influence its climate (Heller et al., 2011). Tidal strain in the lithosphere can be vital in developing plate tectonics on close–in worlds (Zanazzi and Triaud, 2019), while strong tidal dissipation is able to transform the planet into an inferno (Barnes et al., 2013). An essential question determining

the habitability of tidally evolving exoplanets is the effect of spin–orbit coupling on the planetary climate and surface conditions. Synchronous rotation, which is the most probable spin state of planets with low orbital eccentricities, yields extreme differences in the insolation of the surface and in the surface temperatures (Dobrovolskis, 2007). Uneven heating of the atmosphere, combined with active volcanism, may trigger various feedbacks able to destabilise the climate (e.g., Kite et al., 2011). However, it may also prevent the planet from going through periods of global glaciation (Checlair et al., 2019).

Another tidal phenomenon able to affect planetary habitability is the overheating and melting of the interior. Partial melting and the subsequent volcanic outgassing can gradually enrich the planetary atmosphere in greenhouse gases, such as CO_2 (Dorn et al., 2018), which may be vital for planets whose atmospheres were eroded during the early active phase of stellar evolution (e.g., Loyd et al., 2018). Although secular partial melting also results from radiogenic heating, tidal dissipation may be an important additional source, especially in the mantles of higher–mass terrestrial planets ($>3\ M_\oplus$), whose solidus temperatures are increased due to higher subsurface pressures (Noack et al., 2017; Dorn et al., 2018). Outgassing and melt extraction also play an important role in the recycling of planetary material. The carbon–silicate cycle, which contributes to the long-term climate stability of the Earth, is enabled by the interplay between active volcanism and temperature-dependent weathering (Walker et al., 1981). Carbon, outgassed to the atmosphere by volcanism, is later deposited into the crust and returned to the mantle by subduction. On rocky exoplanets in the stagnant–lid regime, recycling may be limited by the absence of an efficient mechanism drawing carbon down from the atmosphere. Nevertheless, the maintenance of the carbon–silicate cycle on such planets is not completely excluded (Foley and Smye, 2018; Valencia et al., 2018).

In this study, we assumed that the model planets operate in the stagnant–lid regime and that the melt is not extracted by volcanism. While the conclusions of the coupled thermal–orbital model are marked by these assumptions and their answer to the question of planetary habitability might be limited, the results of our parametric study with fixed parameters give us some insight into the tidal effect on the surface conditions of GJ 625 b and Proxima Centauri b. If the melt was extracted from the upper mantle and the model planets retained Earth-like rheological parameters (i.e., $\eta_\mathrm{m} \approx 10^{21}\,\mathrm{Pa\,s}$ and $\mu_\mathrm{m} \approx 10^{11}\,\mathrm{Pa}$), their surface would be potentially habitable only for low values of orbital eccentricity. On even slightly eccentric orbits, consistent with the observation, the surface tidal heat flux would exceed the values measured for Io. However, it should be noted that the orbital eccentricity of such strongly dissipating exoplanets would need to be maintained by external forcing, in order not to disappear during the first 1 Gyr of tidal evolution. In terms of the present–day surface tidal heat flux, the results of the coupled thermal–orbital model seem more optimistic than the results of the model with fixed parameters. For mild initial eccentricities, the surface tidal heat flux tends to values comparable with the total heat production of the Earth and tidal dissipation alone does not pose a serious obstacle for potential habitability.

4.9 Concluding remarks

In this chapter, we investigated the interconnection between the spin–orbital dynamics and thermal evolution of low–mass exoplanets around M–type stars. The planets were modeled as differentiated bodies with three or four homogeneous layers, whose mantle is described by the Andrade viscoelastic model. Consistently with the evolution of the mantle temperature profile, the model bodies were allowed to build up a stable subsurface magma ocean, which influenced the effectivity of heat transport as well as the tidal response. In addition to the coupled model, we also conducted parametric studies with fixed interior structure (without the magma ocean), exploring the effect of various mantle viscosities and rigidities on the highest stable spin state and on the surface tidal heat flux of the three planets. The following summary highlights the main conclusions of this chapter:

- For the range of eccentricities consistent with observation, the three studied low–mass exoplanets (GJ 625 b, GJ 411 b, and Proxima Centauri b) are able to maintain higher than synchronous spin–orbit resonances. Locking into such a spin state would provide the planetary surface with relatively uniform insolation, which might have important consequences for the dynamics of the atmosphere and for the hypothetical habitability of the planet. However, as far as we consider a model with a homogeneous solid mantle (Section 4.6), this vital effect of the higher spin–orbit resonances may interfere with the increased tidal dissipation at even mild orbital eccentricities. For illustration, the model of Proxima Centauri b with a reference Earth-like rheology ($\eta_\mathrm{m} = 10^{21}\,\mathrm{Pa\,s}$, $\mu_\mathrm{m} = 200\,\mathrm{GPa}$, no magma ocean) might be locked into 3:2 resonance for $e = 0.08$ and into 2:1 resonance for $e = 0.15$. Nevertheless, in both cases, the surface tidal heat flux exceeds the values reached on Io. A more optimistic result is obtained either at the lowest considered orbital eccentricity $e = 0.02$ (with 1:1 resonance) or with a partially molten interior.

- In the coupled thermal–orbital simulations, we do not observe any pseudo–synchronisation of strongly tidally heated exoplanets with a magma ocean. Since the solidus temperature increases with pressure, the melt is emerging only under the lithosphere and—in our model—it remains in the same place as long as the local temperature exceeds solidus. The zone of substantially reduced viscosity and rigidity is thus concentrated only in the upper mantle, while the lower mantle remains solid and maintains a relatively high average viscosity. As the molten layer is almost nondissipative, its formation effectively reduces the volume in which the mechanical energy transforms to heat. This mechanism is then responsible for the reduced rate of tidal dissipation and orbital evolution (see also Henning and Hurford, 2014).

- The long–term thermal–orbital evolution of tidally loaded rocky exoplanets is strongly interconnected with the evolution of their spin rate. For higher

than synchronous spin–orbit resonances, the thermal state promptly evolves into an equilibrium, which is stable as long as the planet remains in the same resonance. The equilibrium temperature profile ensures that the heat sources are effectively compensated by the heat loss. As the tidal dissipation at higher than synchronous resonances depends mainly on the spin rate and only weakly on the eccentricity, the thermal equilibria are stable for a considerable time ($\sim$ Gyr in some cases), almost independently of the evolving orbital parameters. Each transition between spin–orbit resonances is then accompanied by a transition between thermal equilibria. Once the planet despins to synchronous rotation, the tidal heat rate becomes sensitive to the orbital eccentricity and the planetary mantle cools down gradually.

Understanding the complex relationship between the interior dynamics and the quantities that can be theoretically measured may help us to better constrain the conditions on extrasolar worlds. Although the spin rate of the studied low–mass exoplanets is currently beyond the limits of observational techniques, it might be measurable by the upcoming ground–based or space-based missions, such as JWST or E–ELT (see, e.g., Kane et al., 2017, for the discussion of observational prospects of Proxima Cetauri b). The surface tidal heat flux, which is not directly measurable, may affect the rate of volcanic activity and outgassing. The footprints of increased interior heating would then be observable in the planet's transmission spectra or, possibly, in the infrared light curves (e.g., Demory et al., 2012; Selsis et al., 2013; Meadows et al., 2018).

In the following chapter, we are going to complement the model introduced here with an additional source of orbital perturbation. Returning to the "generic" terrestrial world from Chapter 3, we will study the orbital evolution in the presence of a gas giant orbiting on an outer, highly inclined trajectory (with respect to the orbital plane of the model planet). The thermal evolution, if considered, will be described by the same parameterisation as in the present chapter.

5. Effect of an inclined outer perturber

Up to now, we have studied the tidal dynamics of a single terrestrial exoplanet orbiting a single star. The orbital elements of the planet were evolving due to the tidal dissipation alone and the efficiency of this process was governed by the thermal evolution of the mantle. In the present chapter, we add another source of perturbation to the system: the generic model planet on a close–in orbit, which served as an illustrative case in the parametric studies of Chapter 3, will be disturbed by a massive sub–stellar companion on an outer orbit. In the following exploration of the system's long–term evolution, special attention will be paid to secular perturbations and secular orbit–orbit resonances. Namely, we will discuss the case of large mutual inclinations of the two orbits, which may give rise to the Kozai–Lidov cycles. The results presented in this chapter were calculated using strictly Newtonian physics; the contribution of the relativistic precession, which is a dominant mechanism for close–in eccentric orbits, is only discussed at the end.

5.1 Introduction

Owing to the great variety of orbital configurations found among the exoplanetary systems, we may expect that some of the close–in rocky exoplanets are subjected not only to tides but also to periodic perturbations caused by other bodies in the system. The most commonly considered perturbations with a direct effect on the tidal dynamics (and *vice versa*) are mean–motion resonances, such as those existing between the satellites of giant planets or between the satellites of Pluto. Mean–motion resonances force the orbital eccentricity to retain nonzero values, causing the planet to remain tidally active in the long term. The feedback between the forced eccentricity and the tidal dissipation results in varying episodes of increased and decreased melt production in icy satellites as well as to periodic variations in the surface heat flow of Io (e.g., Ojakangas and Stevenson, 1986; Fischer and Spohn, 1990; Hussmann and Spohn, 2004). Among close–in exoplanetary systems, the tidal heating resulting from nonzero forced eccentricities may greatly influence the internal dynamics as well as the atmospheric evolution and, similarly to the case of Solar System satellites, it may determine the surface conditions and habitability prospects of the individual planets (e.g., Dobos et al., 2017; Barr et al., 2018). On the other hand, the tidal evolution might also have had an important role in the past orbital dynamics of the satellite or planetary system, which eventually resulted in the observed configuration (e.g., Goldreich, 1965; Makarov et al., 2018; Papaloizou et al., 2018).

The proximity of the planet's orbit to a mean–motion resonance results in potentially large–amplitude oscillations in the eccentricity and the semi–major axis. The period of these oscillations is few orders of magnitude longer than the orbital period (e.g., Murray and Dermott, 1999); nevertheless, it is still considerably

shorter than the typical timescale of tidal evolution. The study of a coupled thermal–orbital evolution in the long term, accounting for such large–amplitude short–scale effects, requires the use of relatively short time steps and becomes very challenging. Therefore, for practical reasons, we do not consider mean–motion resonances in this work, but we instead study the interconnection between tidal evolution and third–body perturbation in the *secular approximation*: considering a disturbing function averaged over the mean longitudes λ_1 and λ_2. Specifically, we treat the case of large mutual inclinations between the two orbits.

As was recently rediscovered by Ito and Ohtsuka (2019), the dynamics of bodies at high mutual inclinations were first analysed by Hugo von Zeipel in 1910 (von Zeipel, 1910). Nevertheless, all of the present theoretical work builds on the independent derivations of Lidov (1962) and Kozai (1962), who approached the problem in two different contexts[1]. Lidov (1962), motivated by considerable orbital evolution of three artificial satellites influenced by the gravitational attraction of the Moon, derived Gauss's planetary equations for the satellite's orbit, averaged them over the satellite's and the Moon's orbital period, and found three constants of motion, defining the dynamical state of the system. Depending on the initial orbital elements, he analysed the satellite's dynamics and derived, *inter alia*, a condition for its collision with the Earth. Kozai (1962), on the other hand, studied the orbital evolution of asteroids under the gravitational influence of Jupiter. Working in Hamiltonian formalism, he found that the asteroid's orbital variations may operate in two regimes; the actual regime being determined by the z–component of the angular momentum, or by the constant of motion $\Theta = (1 - e^2)\cos^2 i$, where e is the orbital eccentricity and i is the orbital inclination relative to Jupiter's orbital plane. Depending on the ratio between the semi–major axes of the asteroid and the semi–major axis of Jupiter, Kozai (1962) derived the limit values of the constant, Θ_0. Below the critical value, the system librates about a stationary solution and is said to be in a resonance (Thomas and Morbidelli, 1996): the perihelium precession of the asteroid ceases and the orbital eccentricity and inclination undergo large–amplitude oscillations. Above the critical value, the perihelium precesses uniformly and the oscillations are small. Specifically, for an asteroid with an initially circular orbit and short semi–major axis, the critical initial inclination needed to enter the resonant regime is 39°.

The discoveries of exoplanets orbiting widely–separated binary stars or dwelling in multi–planetary systems raised the questions about the stability of exotic orbital configurations under the described Kozai–Lidov mechanism (for an overview of the topic, see, e.g., Naoz, 2016). Funk et al. (2011) explored the effect of inclined jovian worlds on the dynamical stability of inner low–mass exoplanets and characterised the dynamical state of the system by the maximum eccentricity (ME) and a chaos indicator[2]. The authors studied the role of different quantities, such as the

[1] A thorough overview of the starting positions, motivations, and results of von Zeipel's, Lidov's, and Kozai's work can be found in Ito and Ohtsuka (2019).

[2] In general, low–eccentricity orbits (ME < 0.2) tend to be stable, while high–eccentricity orbits (ME > 0.8) tend to be unstable, or chaotic. The range of intermediate maximum eccentricities permits the existence of both stable and unstable orbits (Funk et al., 2011).

orbital eccentricity of the perturber, perturber–star mass ratio, ratio of semi–major axes, and the mutual inclination of the two planets. They found that for higher eccentricity or higher mass of the perturber, a smaller portion of the inclination—semi–major axis parameter space permits the existence of low-eccentricity orbits and, consequently, a smaller region of the parameter space is expected to be stable. The conclusion drawn for systems with an eccentric perturber from the numerical simulations of Funk et al. (2011) were later derived analytically and discussed by Libert and Delsate (2012). Libert and Tsiganis (2009) explored the stability of several systems under possible Kozai–Lidov resonance and reported high sensitivity of the systems' dynamics to a change in the initial orbital parameters (illustrating the role of observational uncertainties).

A number of studies have also focused on the combined effect of resonant eccentricity excitation and tidal damping. This mechanism, called the *Kozai–Lidov migration* (e.g., Wu and Murray, 2003), has been proposed as one of the explanations for the formation of close binaries in triple–star systems (e.g., Fabrycky and Tremaine, 2007; Naoz and Fabrycky, 2014; Bataille et al., 2018) or hot Jupiters, possibly on highly eccentric orbits (e.g., Wu and Murray, 2003; Socrates et al., 2012; Petrovich et al., 2014; Wang et al., 2017). The idea of the Kozai–Lidov migration is based on extreme eccentricity excitation, complemented by strong tidal dissipation during periastron passages. The effect of oscillating eccentricity on the tidal evolution depends on the relative timescales of the two processes (Petrovich, 2015; Wang et al., 2019). If the tidal timescale is much longer than the period of Kozai–Lidov oscillations, and if the amplitude of the oscillations is large, the tidal evolution is slowed down: the episodes of high dissipation are confined to small time windows around the maxima of mean eccentricity (Petrovich, 2015). If, on the contrary, the timescales are comparable—or the tidal timescale is relatively shorter than the oscillation period—the planet evolves quickly to a close–in circular orbit. As the most efficient tidal dissipation operates when the orbital eccentricity attains its maximum and the inclination is at its minimum value, the Kozai–Lidov tidal migration also results in damping the mutual inclination and equilibrating it around its minimum (Fabrycky and Tremaine, 2007; Correia et al., 2013).

Since the models of Kozai–Lidov migration are usually applied to stars or gaseous giants, they mostly utilise the constant time lag model (CTL) of tidal response, in which the tidal lag is proportional to the tidal frequency. However, there are exceptions to this rule. In works dedicated to the high–eccentricity migration of jovian worlds, Storch and Lai (2014) and Storch and Lai (2015) consider the tidal dissipation in a viscoelastic core of the planet (see also Remus et al., 2012) and prescribe the rheology via the imaginary part of the Love number. The authors show that the inclusion of a core described by the Maxwell model may speed up the tidal circularisation of highly eccentric orbits and better explain the number of observed hot Jupiters. In addition, the authors also discuss the existence of multiple stable spin states of such planets.

In this chapter, we first briefly introduce the circular restricted three–body problem, in which a massive outer perturber orbits on a circular trajectory and only the orbit of the inner planet is permitted to evolve. Then we present several additions to the numerical model of Chapter 4 and, finally, we explore the effect of an inclined Jupiter–mass perturber on the tidal evolution of a terrestrial planet. As in the previous two chapters, the terrestrial planet is assumed to be fully differentiated and its interior dynamics are coupled to the orbital evolution through the temperature dependence of rheological parameters.

Finally, we should note that the resonant motion and the stability of planetary systems is traditionally treated in the Hamiltonian formalism (using canonical orbital elements), which provides an invaluable insight into the dynamics of the system (e.g., Kozai, 1962; Thomas and Morbidelli, 1996; Murray and Dermott, 1999; Bataille et al., 2018). Although such an approach is, in most cases, preferable, in this study we solve the non–singular evolution equations (1.58) derived from the Lagrange planetary equations for the set of Keplerian elements with longitudes, $\{a, e, i, \varpi, \Omega, \epsilon\}$. This option was chosen for the sake of consistency with the rest of this work, especially with Chapter 4.

5.2 Secular resonances at high mutual inclinations

Let us consider a system consisting of a host star with mass m_*, a giant outer planet with mass m_2, and a small inner planet with mass m_1. Let the outer planet orbit in the reference plane ($i_2 \approx 0$) on a nearly circular orbit ($e_2 \approx 0$). As in the previous chapter, we expand the disturbing function for the inner planet into the Darwin–Kaula series (Kaula, 1962), that we introduced in Section 1.3.1, as

$$\mathcal{R}_1 = \frac{\mathcal{G}m_2}{a_2} \sum_{l=2}^{\infty} \sum_{m=0}^{l} \sum_{p,p'=0}^{l} \sum_{q,q'=-\infty}^{\infty} \kappa_m \frac{(l-m)!}{(l+m)!} \left(\frac{a_1}{a_2}\right)^l \mathcal{F}_{lmp}(i_1)\mathcal{F}_{lmp'}(i_2)\mathcal{H}_{lpq}(e_1)\mathcal{G}_{lp'q'}(e_2)\cos\psi \,, \tag{5.1}$$

with argument

$$\psi = (l-2p'+q')\lambda_2 - (l-2p+q)\lambda_1 - q'\varpi_2 + q\varpi_1 + (m-l+2p')\Omega_2 - (m-l+2p)\Omega_1 \,. \tag{5.2}$$

Before we proceed to the details of the implementation and to the results of our model, let us stop for a while to discuss the secular resonances in the circular restricted three–body problem.

Away from mean–motion resonances, and after double averaging over quickly–changing variables λ_1 and λ_2, the condition for a secular resonance is

$$\dot{\psi}_{\rm sec} = -q'\dot{\varpi}_2 + q\dot{\varpi}_1 + (m+q')\dot{\Omega}_2 - (m+q)\dot{\Omega}_1 \approx 0 \,. \tag{5.3}$$

As the outer planet revolves around the star on a nearly circular orbit in the

reference plane, the contribution of the terms corresponding to $q' \neq 0$ and $(m + q') \neq 0$ becomes negligible. Therefore, the condition of resonance in our case turns to

$$\dot{\psi}_{\rm sec} = q(\dot{\varpi}_1 - \dot{\Omega}_1) = q\dot{\omega}_1 \approx 0 \tag{5.4}$$

with $\psi_{\rm sec} = q\omega_1$ being the resonant argument. We may expect that the dynamics of a system locked into this type of secular resonances will be characterised by libration around a distinct argument of periapsis. The doubly–averaged disturbing function reads as

$$\langle \mathcal{R}_1 \rangle = \frac{\mathcal{G}m_2}{a_2} \sum_{l=2}^{\infty} \sum_{q=-\infty}^{\infty} \left(\frac{a_1}{a_2} \right)^l \mathcal{F}_{l0p}(i_1) \mathcal{F}_{l0p'}(0) \mathcal{H}_{lpq}(e_1) \cos q\omega_1 \ , \tag{5.5}$$

where we already set $e_2 = 0$ and $i_2 = 0$ for illustration purposes. In the above expression, the values of (non–negative) indices p and p' are given by $2p = l + q$ and $2p' = l$. These constraints require that l and q be even. A direct implication of the constraints given by double averaging is, therefore, the necessity to expand the disturbing function at least to e_1^2 in order to encounter the secular resonance. Since the argument of the averaged disturbing function (5.5) only depends on the argument of periapsis ω_1, the orbital evolution of the inner planet can be obtained from the first set of Lagrange planetary equations (1.9). Upon rewriting the relevant equations for the circular restricted three–body problem, we obtain

$$\frac{{\rm d}a_1}{{\rm d}t} = 0 \ , \tag{5.6a}$$

$$\frac{{\rm d}e_1}{{\rm d}t} = -\frac{\sqrt{1 - e_1^2}}{n_1 a_1^2 e_1} \ \frac{\partial \langle \mathcal{R}_1 \rangle}{\partial \omega_1} \ , \tag{5.6b}$$

$$\frac{{\rm d}i_1}{{\rm d}t} = \frac{\cot i_1}{n_1 a_1^2 \sqrt{1 - e_1^2}} \ \frac{\partial \langle \mathcal{R}_1 \rangle}{\partial \omega_1} \ , \tag{5.6c}$$

$$\frac{{\rm d}\Omega_1}{{\rm d}t} = \frac{1}{n_1 a_1^2 \sqrt{1 - e_1^2} \sin i_1} \ \frac{\partial \langle \mathcal{R}_1 \rangle}{\partial i_1} \ , \tag{5.6d}$$

$$\frac{{\rm d}\omega_1}{{\rm d}t} = \frac{\sqrt{1 - e_1^2}}{n_1 a_1^2 e_1} \ \frac{\partial \langle \mathcal{R}_1 \rangle}{\partial e_1} - \frac{\cot i_1}{n_1 a_1^2 \sqrt{1 - e_1^2}} \ \frac{\partial \langle \mathcal{R}_1 \rangle}{\partial i_1} \ . \tag{5.6e}$$

Obviously, the mean semi–major axis remains constant under the influence of a secular perturbation, while the mean orbital eccentricity and mean inclination evolve in a synchronised way. The relation between the mean eccentricity and mean inclination can be obtained by dividing equation (5.6b) by equation (5.6c), which yields

$$\frac{{\rm d}e_1}{{\rm d}i_1} = -\frac{1 - e_1^2}{e_1} \ \tan i_1 \ . \tag{5.7}$$

Integrating (5.7), we get the constraint

$$\sqrt{1-e_1^2}\,\cos i_1 = \text{const.} \tag{5.8}$$

This constraint is equivalent to the conservation of z–component of the inner orbit's angular momentum, given the semi–major axis is constant (as guaranteed by equation (5.6a)). The square of expression (5.8) is equal to Kozai's parameter Θ, mentioned in the introduction.

For the circular restricted three–body problem, the dynamics of the system can be well represented in the $(e\cos\omega, e\sin\omega)$ plane (e.g., Thomas and Morbidelli, 1996; Funk et al., 2011) or in the $(2\omega, 1-e^2)$ plane, as was originally done by Kozai (1962). Here, we choose the first option. In this representation, the distance from the origin denotes the mean eccentricity of the inner planet, while the angle between the x–axis and the radius vector marks the mean argument of periapsis. An illustration[3] of possible trajectories in the $(e\cos\omega, e\sin\omega)$ for different values of the initial eccentricity and of the z–component of the angular momentum is presented in Figure 5.1 (see also Thomas and Morbidelli, 1996).

5.3 Implementation

The tidal effects on the two planets' orbital elements are calculated using the full set of tidal equations (1.40), derived in Boué and Efroimsky (2019), where we neglected the contribution due to the tidal dissipation in the host star. The set of equations describing the third body perturbation is given by (1.58), with the derivatives of the disturbing function written explicitly in Appendix C.2. The accuracy of the implemented model for orbital evolution under the third–body perturbation was tested against the symplectic N–body integrator *Rebound* (Rein and Liu, 2012).

In contrast to the calculation of the tidal evolution, where the character of the problem permitted the neglection of degrees other than $l = 2$, the present problem may require the consideration of several more terms in the Darwin–Kaula expansion. As was outlined in Chapter 1, the magnitudes of the individual terms in the disturbing function are given by (see also Murray and Dermott, 1999)

$$\mathcal{R}_{lmpp'qq'} \sim \left(\frac{a_1}{a_2}\right)^l e_1^{|q|} e_2^{|q'|} \left(\sin\frac{i_1}{2}\right)^{|m-l+2p|} \left(\sin\frac{i_2}{2}\right)^{|m-l+2p'|}, \tag{5.9}$$

where a_1 and a_2 are the semi–major axes of the inner and the outer planet, respectively, and e_1, e_2, i_1, i_2 symbolise the orbital eccentricities and inclinations. Hence, the maximum degree l of the expansion needed to achieve the required precision depends on the ratio of the semi–major axes and on the inclinations of the two planets. Although our present work focuses on systems with relatively

[3]The illustration was calculated using the same semi–analytical model as in the rest of this chapter (and in Chapters 3 and 4). Only the tidal terms in the evolution equations were set the zero.

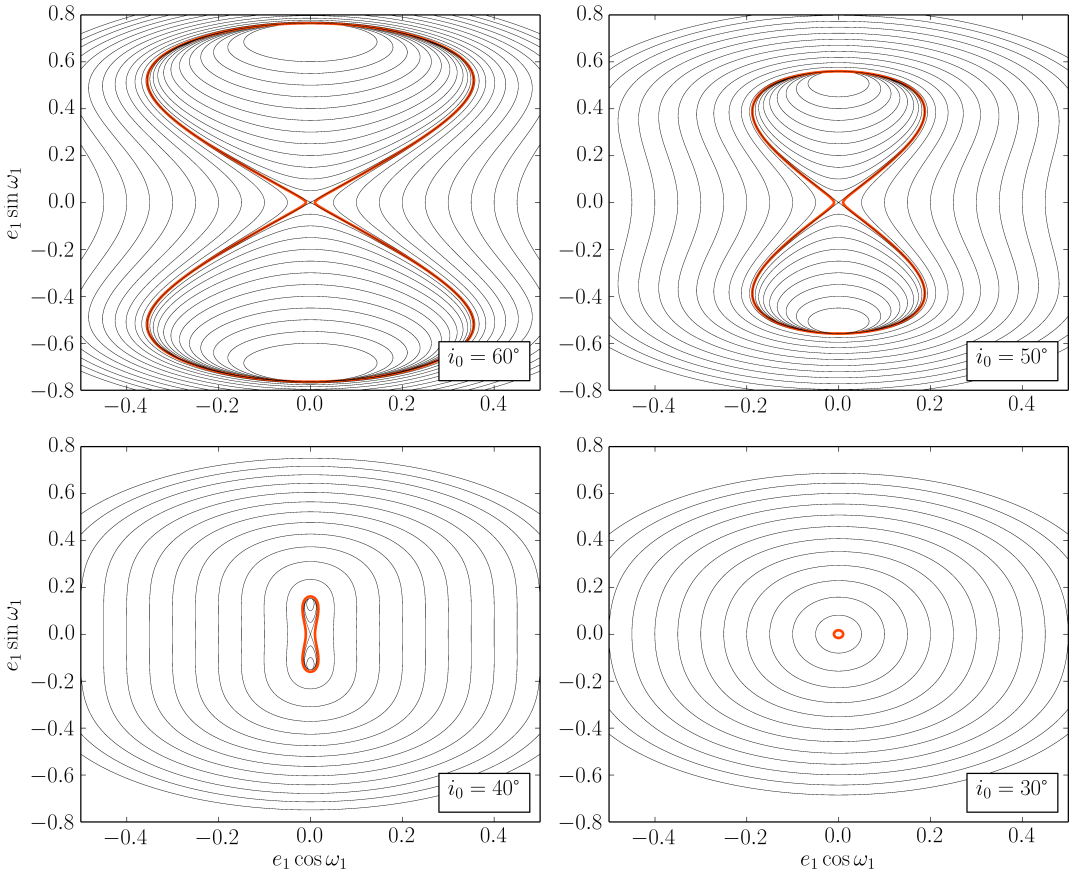

Figure 5.1: Isolines of Kozai's parameter Θ for our model system with outer Jupiter–mass companion at $a_2 = 1$ AU. Individual plots correspond to different initial inclinations i_1. The orange line indicates the trajectory which would be taken by the system used in our calculations (initial conditions: $e_1 = 0.01$, $\omega_1 = 0°$) in the absence of tides. Note the different ranges of x–axes and y–axes.

large distances between the planets—and we expand the evolution equations only up to degree $l = 5$—a desire to implement the method in a more general manner (e.g., to also enable the consideration of low–order mean–motion resonances in future studies) prompted us to modify the scheme used in the previous chapter and to facilitate the computation of higher–degree ($l > 10$) expansion.

The computation of the Darwin–Kaula series for high degrees becomes increasingly time–demanding. Therefore, to accelerate the program runs, we calculate the tables of inclination and eccentricity functions and their derivatives for various values of i and e in advance. During the individual steps of the model runs, the functions for the actual elements are obtained by polynomial interpolation (using a fourth–order polynomial). As in the previous chapter, we integrate the spin–orbital evolution equations using two computational cycles with different time steps: the *short cycle* and the *long cycle*. However, contrary to the previous chapter, we use the predictor–corrector scheme only in the short cycle, while

the long cycle is integrated using the fourth–order Runge–Kutta algorithm with variable step size, as implemented by Press et al. (1992).

5.4 Results

5.4.1 Model parameters

In the following, we study the evolution of a system consisting of an M–type star with mass $m_* = 0.1\ m_\odot$, an Earth–mass inner planet and a Jupiter–mass outer planet ($m_2 = 10^{-3}\ m_\odot$). The interior structure of the inner planet is identical to Chapter 3 and the model parameters are given in Table 3.1. For the model runs with mantle convection, we use the parameters from Table 4.3. Although the model settings permit the calculation of full orbital evolution of the system, we set the time derivatives of the exo–Jupiter's orbital elements to zero and mimic the dynamics of almost circular restricted three–body problem. Note that the restriction of the outer planet's evolution breaks the conservation of total angular momentum in the system. Have we chosen to calculate the full orbital evolution, the angular momentum would be exchanged between the two orbits.

For the outer planet, we prescribe a small, arbitrarily chosen constant orbital eccentricity $e_2 = 10^{-4}$ and zero inclination with respect to the inertial reference plane. In other words, the inertial reference plane and the outer planet's orbital plane are identical. The initial orbital eccentricity of the inner planet is $e_1 = 0.01$. The initial values of the longitudes of periapsis (ϖ_1, ϖ_2) and the longitude of the inner orbit's ascending node (Ω_1) are zero for simplicity. The longitude of the outer orbit's ascending node is undefined. We consider three possible values of the outer orbit's semi–major axis ($a_2 = 1$ AU, 5 AU or 10 AU) and two values of the inner orbit's inclination with respect to the reference plane (40° or 50°). Note that the former of the chosen inclinations marks a system just below the critical value of Θ for a possible resonant state.

A model planet at initially almost circular orbit, perturbed by a highly–inclined companion, will experience large synchronised oscillations in the orbital eccentricity (Figure 5.1) and inclination. Before we proceed to the presentation of the results, let us again note that the increase in the orbital eccentricity is a consequence of the decrease in the model planet's orbital angular momentum. In a two–planetary system, the total angular momentum would be periodically exchanged between the inner and the outer orbit; in the restricted three–body problem, the angular momentum is periodically removed and returned to the system. At the same time, the tidal evolution alone proceeds at constant angular momentum. In the combined problem of tidal and third–body perturbation, the tidal evolution becomes most effective at the periods of highest eccentricity—and lowest orbital angular momentum (see also Socrates et al., 2012). An important consequence of these facts will be illustrated in Figure 5.4.

5.4.2 Close perturber: tidal contribution to secular resonance

First, we will concentrate on a system with a close perturber: The Earth–mass model planet, orbiting on a mildly eccentric orbit with semi–major axis $a_1 = 0.04\,\mathrm{AU}$, will be perturbed by a Jupiter–mass companion at 1 AU. In the case of the higher initial mutual inclination ($i_1 = 50°$), the period of Kozai–Lidov oscillations is $\sim 50,000\,\mathrm{yr}$, and since the model planet orbits very close to its host star, this timescale is also shared by the tidal despinning[4]. For the lower mutual inclination ($i_1 = 40°$), the period of Kozai–Lidov oscillations is $\sim 100,000\,\mathrm{yr}$ and the concurrence of this mechanism with the tidal despinning is even more significant. On the other hand, the typical timescale of the orbital evolution induced by the third–body perturbation is orders of magnitude lower than the timescale for tidal evolution of a_1 and e_1. We should, therefore, expect that in the system with a close perturber, the orbital evolution will be governed mainly by the third–body perturbation, the effect of tides being only secondary.

Figures 5.2–5.5 confirm this expectation. In the beginning, the model planet's evolutionary path in the $(e\cos\omega, e\sin\omega)$ plane approximately follows the isolines of Kozai's parameter Θ (i.e., of the z–component of the orbital angular momentum, represented by the thin black lines) corresponding to the initial mutual inclination between its orbital plane and the orbital plane of the perturber. Since the angular momentum is slowly drained from the system, the trajectories taken by the planet in later stages of the evolution do not follow the thin black lines exactly, but the change is relatively slow, compared to the timescale of the eccentricity oscillations. Each triplet of panels in Figures 5.2 and 5.3 is plotted for the time range which captures the entire orbital evolution of the model case with the lowest mantle viscosity (and fastest tidal decay). Figure 5.5 shows the evolution over an arbitrarily[5] chosen time interval of 1 Gyr. Therefore, the colour–coded time ranges are different for different Figures.

Figure 5.2 depicts the trajectory of a model planet with initial inclination $i_1 = 40°$ and constant mantle structure and rheological properties. In this case, we do not consider the thermal evolution of the interior. As a consequence of the outer planet's gravitational action, the model planet's initially low eccentricity increases to $e_1 \sim 0.15$ and the planet becomes subjected to tidal dissipation. Tidal dissipation then acts to reduce the orbital eccentricity and "pushes" gradually the plotted trajectory closer to the centre of the panel. The combined tidally– and externally–induced orbital evolution is, therefore, marked by Kozai–Lidov oscillations in the orbital eccentricity and inclination with gradually decreasing amplitude. Since the third–body perturbation forces the inclination to evolve

[4]The period of Kozai–Lidov oscillations, as well as the timescale of tidal despinning, was obtained "empirically" from our numerical results. Furthermore, the period of Kozai–Lidov oscillations was also compared with the N–body integrator *Rebound* (Rein and Liu, 2012).

[5]The choice of the relatively short interval (1 Gyr) was also motivated by practical reasons. The calculation of the coupled evolution with short–scale eccentricity forcing is highly time–demanding.

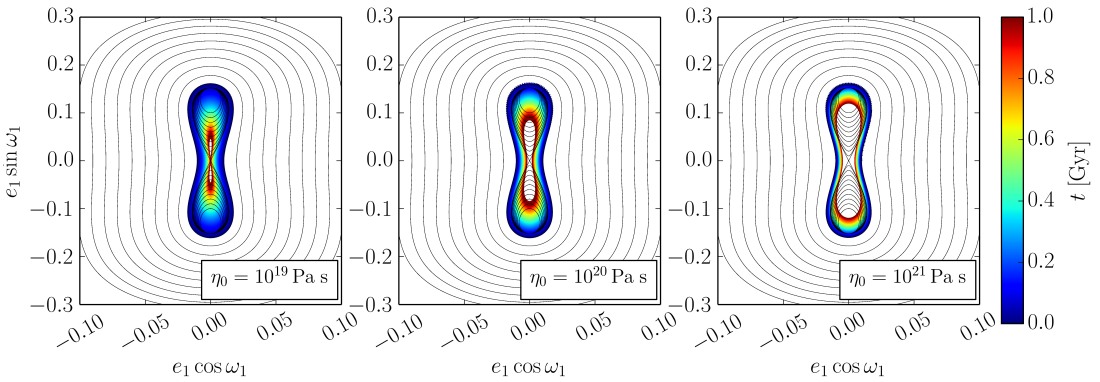

Figure 5.2: Evolutionary paths of a system with close perturber ($a_2 = 1\,\mathrm{AU}$) for three reference viscosities ($\eta_0 = 10^{19}\,\mathrm{Pa\,s}$, $10^{20}\,\mathrm{Pa\,s}$ and $10^{21}\,\mathrm{Pa\,s}$). Model with non–evolving interior and initial mutual inclination $i_1 = 40°$. Thin black lines correspond to isolines of Kozai's parameter Θ.

together with the decaying eccentricity, the mutual inclination decreases as well and the system no longer follows the isolines corresponding to the initial state, as was said earlier. A final state of the combined evolution is a model planet on a circular orbit with $i_1 < 40°$. The efficiency of tidal dissipation increases with decreasing viscosity; thus, the lowest–viscosity case undergoes complete decay of orbital eccentricity on a much shorter scale than the highest–viscosity case.

Focusing now on the dynamically more interesting case with initial mutual inclination $i_1 = 50°$, we may turn to the evolutionary paths depicted on Figure 5.3. As in the previous case, we are considering a model without the thermal evolution of the interior. The basic interpretation of the depicted trajectories is similar to the previous illustration, with two important differences: the amplitudes of the eccentricity and inclination oscillations are now considerably higher than in the case with $i_1 = 40°$ and the tidal dissipation at the periods of high orbital eccentricity results in the system's locking into the Kozai–Lidov resonance. Depending on the model planet's viscosity (i.e., on the efficiency of tidal dissipation), the crossing of the separatrix and the resonant locking happens at different times. Since our initial condition for the argument of periapsis is $\omega_1 = 0°$ and the orbit in these model cases precesses (ω_1 increases with time), the lowest–viscosity case gets locked into the resonance associated with $\omega_1 = 90°$. The other two cases, where the tidal decay of eccentricity proceeds more slowly, get locked into the resonance associated with $\omega_1 = 270°$.

Once locked in the resonance, the model planet's orbit undergoes large–amplitude oscillations in eccentricity and inclination, while the argument of periapsis librates around the resonant location. Nevertheless, the planet is still subjected to immense tidal loading and the orbital evolution continues. The gradual decrease in the eccentricity is accompanied by the gradual decrease in the inclination (the latter being induced by the third–body perturbation, not by tides), and as the inclination decreases to $\sim 40°$, the system crosses the separatrix once again, leaving the Kozai–Lidov resonance. The subsequent evolution is identical

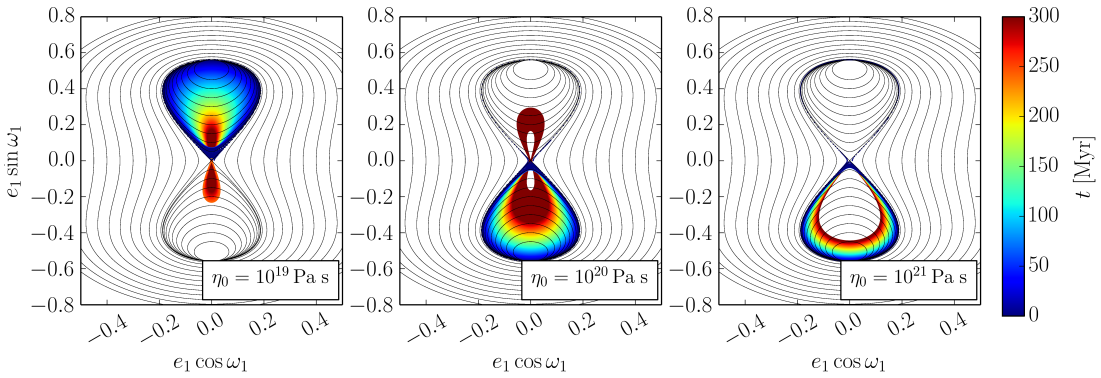

Figure 5.3: As in Figure 5.2, but for initial mutual inclination $i_1 = 50°$.

to the case with lower initial inclination.

Now, we can go back to the discussion about the system's angular momentum. Since the tidal evolution acts most effectively at the periods of increased orbital eccentricity—and the tidal evolution proceeds at constant angular momentum—the system is gradually subjected to the loss of angular momentum. In the absence of the third–body forcing, the tidal evolution would lead the model planet to a circular orbit with semi–major axis $a_{1,\mathrm{fin}} = a_{1,\mathrm{ini}}(1 - e_{1,\mathrm{ini}}^2)$. As the initial eccentricity in our models is very low, $e_{1,\mathrm{ini}} = 0.01$, the shrinking of the semi–major axis would be only mild. However, once we also consider the third–body perturbation at high mutual inclinations, the semi–major axis tends to a considerably lower value, approximately given by $a_{1,\mathrm{fin}} = a_{1,\mathrm{emax}}(1 - e_{1,\mathrm{max}}^2)$, where $e_{1,\mathrm{max}}$ is the maximum value of the oscillating eccentricity and $a_{1,\mathrm{emax}}$ is the corresponding semi–major axis. This mechanism lies behind the Kozai–Lidov migration, mentioned in the introduction (e.g., Wu and Murray, 2003).

The orbital evolution of the particular model case with initial mutual inclination $i_1 = 50°$ and reference viscosity is also depicted in Figure 5.4. We may see the tidally–decaying short–period oscillations of e_1 and i_1, as well as the gradual migration of the model planet towards the host star. On the lowermost panel, we see the rapid locking into the Kozai–Lidov resonance, with the argument of periapsis librating around 90°. Once the eccentricity and the inclination decrease to sufficiently low values, the argument ω_1 begins to precess. However, at almost zero orbital eccentricity and at mutual inclination just above 39°, the system returns to a resonant state, alternating between the two resonant positions ($\omega_1 = 90°$ and 270°).

Finally, to appreciate the role of the interior evolution in this combined problem, let us briefly comment on Figure 5.5. The three panels of this figure illustrate the evolution paths of the system with initial mutual inclination $i_1 = 50°$, as in Figure 5.3, but now including the thermal evolution of the interior. Recall that the increased tidal heating of planets on eccentric orbits (Chapter 4) results in partial melting of the interior, the formation of a subsurface magma ocean, and, effectively, a tidal shutdown. The same behaviour can be also seen in this model case. The planet starts as a tidally active body and, under the influence of the

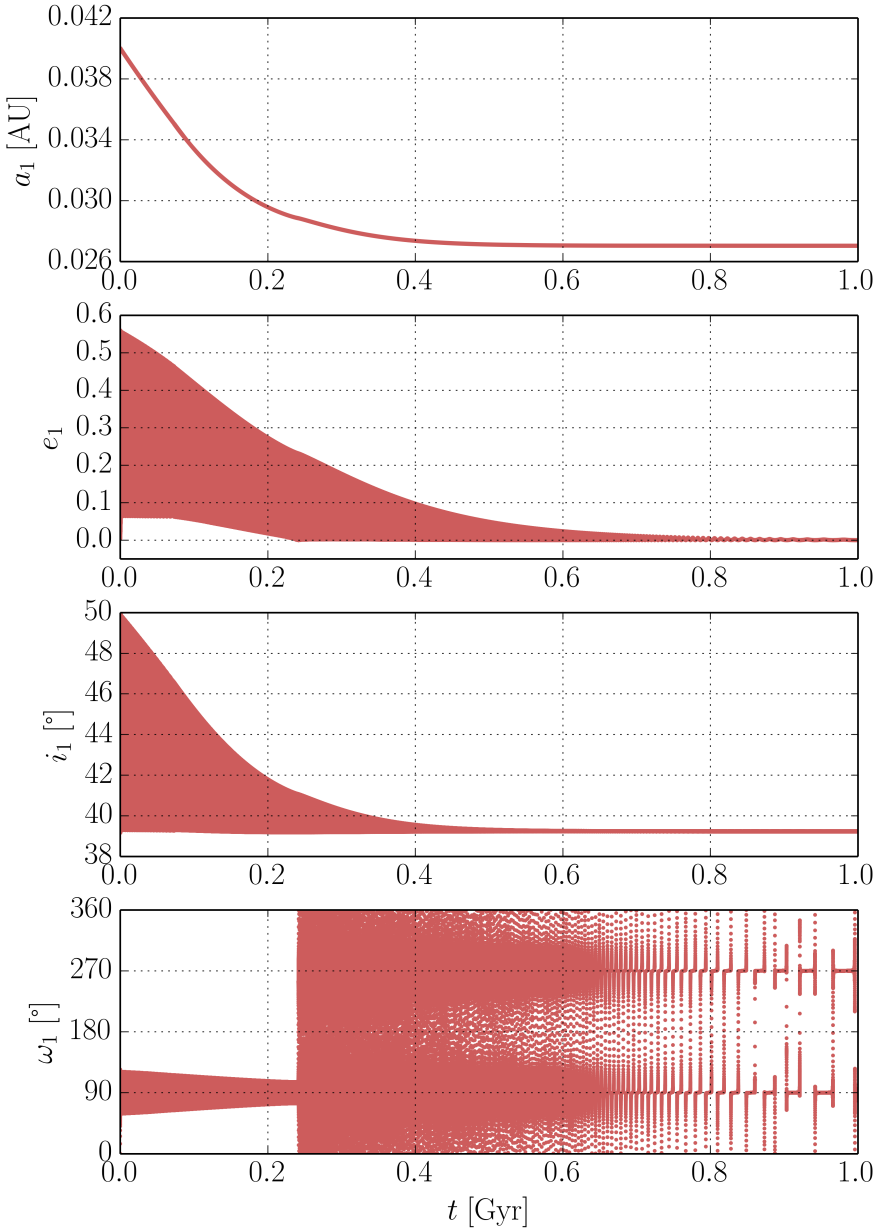

Figure 5.4: Orbital evolution of the model planet subjected to tides and third–body perturbation by a close perturber ($a_2 = 1\,\mathrm{AU}$) at high mutual inclination ($i_1 = 50°$). Model with non–evolving interior and reference mantle viscosity $\eta_0 = 10^{19}\,\mathrm{Pa\,s}$ (as on the left panel of Figure 5.3). Over the span of 1 Gyr, we may see, from top to bottom, the evolution of the semi–major axis, the orbital eccentricity, the inclination, and the argument of periapsis.

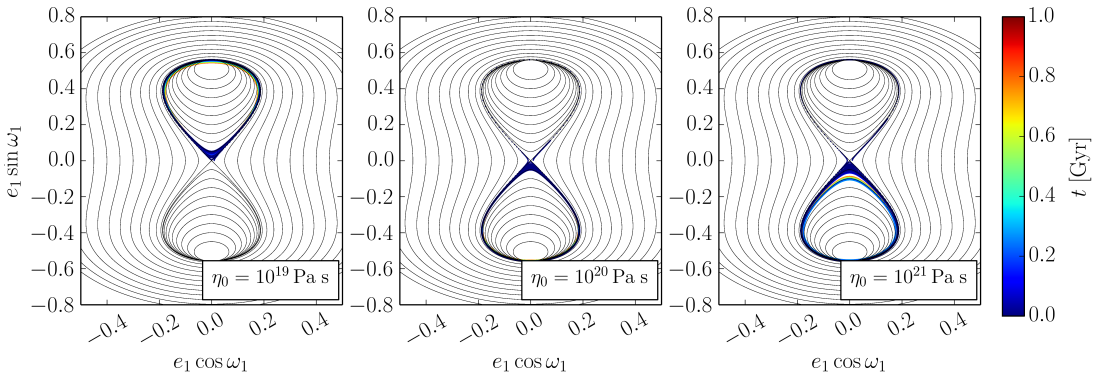

Figure 5.5: As in Figure 5.3 ($i_1 = 50°$), but for evolving interior.

Kozai–Lidov mechanism, it gets locked to the resonant state (as in the previous example). However, due to the high amplitude of the eccentricity oscillations, the temperature at the top of the planet's mantle promptly exceeds the solidus and the mantle begins to melt. As a result, the orbit remains confined to the resonant state. The orbital eccentricity (as well as the inclination) keeps its high–amplitude oscillations and the tidal evolution becomes negligible, compared to the evolution induced by the third–body perturbation.

5.4.3 Distant perturber: tidal breaking of secular resonance

On the previous images, we have seen the orbital evolution in the regime with prevailing third–body perturbation. In this regime, the tidal decay of the orbital eccentricity acts as a secondary effect, possibly leading the planetary orbit to a resonant state. Increasing the semi–major axis of the perturber unveils another type of the combined model's behaviour. As the timescale of eccentricity forcing gets closer to the tidal timescale, the influence of tides on the orbital dynamics becomes quite intricate. To capture the main aspects of the orbital evolution at different relative timescales, we will now discuss only the lowest–viscosity and highest–inclination case ($\eta_0 = 10^{19}$ Pa s, $i_1 = 50°$). Changing the reference viscosity affects the efficiency of tidal dissipation; therefore, it determines the exact time when the tidally–induced eccentricity decay quenches the Kozai-Lidov cycles. Decreasing the initial mutual inclination affects the maximum and minimum eccentricities reached.

Let us first discuss the model case with constant interior structure (i.e., without the thermal evolution of the planet). Figure 5.6 depicts the model planet's trajectory in the $(e \cos \omega, e \sin \omega)$ plane for three considered values of the outer planet's semi–major axis: 1 AU, 5 AU, and 10 AU. The left panel is identical to Figure 5.3 and, as on the previous images, it also contains a "grid" of trajectories with constant Θ. On the middle and right panels, the grid is omitted for the sake of clarity. A glance at the triplet of panels reveals an expectable rule: increasing the distance of the perturber decreases the importance of Kozai–Lidov mechanism

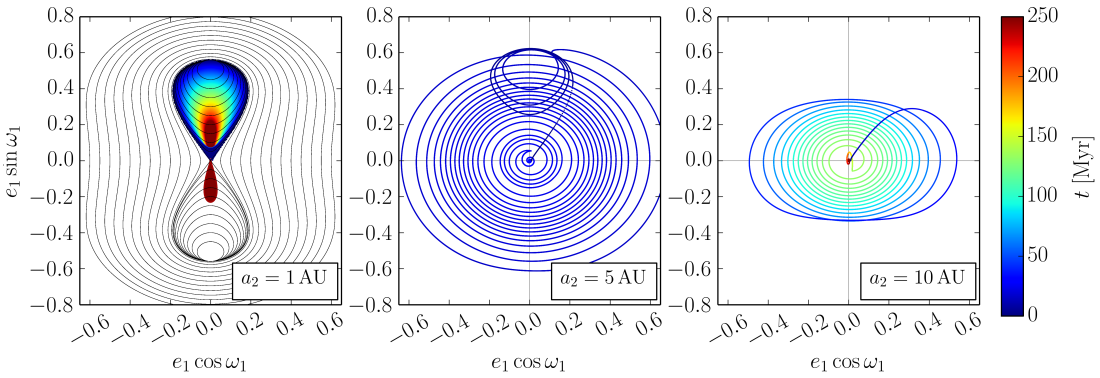

Figure 5.6: Evolutionary paths of a model planet with reference mantle viscosity $\eta_0 = 10^{19}$ Pa s for different semi–major axes of the outer perturber ($a_2 = 1$ AU, 5 AU, and 10 AU). Model with non–evolving interior and with initial mutual inclination $i_1 = 50°$. Thin black lines on the first panel correspond to isolines of Kozai's parameter Θ.

in driving the system's orbital dynamics. The further the perturber, the stronger the relative effect of tides.

The beginning of the trajectory in the middle panel of Figure 5.6 ($a_2 = 5$ AU) resembles the behaviour of the model case on the left ($a_2 = 1$ AU). The orbital eccentricity increases under the action of the perturber, until the planet becomes subjected to strong tidal dissipation. Then, the tidal decay of eccentricity "flicks" the system to a Kozai-Lidov resonance around $\omega_1 = 90°$. While in the case with $a_2 = 1$ AU, we observed a gradual, synchronised decrease in the eccentricity and inclination, in the present case with $a_2 = 5$ AU, we can see quite different evolution. The eccentricity decay is extremely fast, relative to the Kozai–Lidov cycles, and the system quickly converges to the resonance still corresponding to the initial inclination (and initial value of Θ). However, as the stable point in this case corresponds to extremely high eccentricity (~ 0.5), the system is soon destabilised by the immense tidal dissipation and the planet embarks on a journey of tidal circularisation. Note that the argument of periapsis at this stage recedes and the evolution is very rapid, compared to the other two model cases. Only at very low orbital eccentricity, when the planet despins to synchronous rotation, does the apsidal motion change again in a prograde direction. The entire tidal circularisation proceeds in less than 50 Myr.

On the right panel, depicting the case with $a_2 = 10$ AU, we may see a simplified version of the evolution described in the previous paragraph. In this case, the tidal dissipation prevails even earlier and the system does not even tend to the Kozai–Lidov resonance. However, due to lower eccentricities attained, the tidal circularisation takes more than 100 Myr.

To understand the intricate case of $a_2 = 5$ AU better, we also plot a close–up on the inner planet's orbital evolution over the first 50 Myr (Figure 5.7). This figure can also be compared with Figure 5.4, which shows the evolution of the

same model planet, but for a closer perturber. The dynamics depicted on the four panels of Figure 5.7 can be divided into three stages. During the first $\sim 15\,\mathrm{Myr}$, the system slowly librates around the Kozai–Lidov resonance at $\omega_1 = 90°$. The maxima of the inner planet's eccentricity at this stage are approximately constant, while the minima become higher and higher. This phenomenon, accompanied by a gradual decrease in the mutual inclination, is a consequence of the loss of angular momentum. Once the inclination becomes too low, the system leaves the resonance. The escape from resonance is marked by a further increase in the eccentricity and a steep decrease in the inclination: the system is now far away from the region relevant to Kozai-Lidov dynamics. It is subjected to non-resonant secular perturbation and tides.

In the second stage of evolution, the system undergoes rapid tidal circularisation and migration to the host star. The inner planet's semi–major axis decreases to less than 50% of its initial value. As we have noted in Figure 5.6, the argument of periapsis now recedes and the rate of its recession increases with decreasing eccentricity. The eccentricity decay also affects the planet's spin rate. While the millions of years spent on the eccentric orbit locked the planet's spin state to the $2:1$ resonance, the decrease in the eccentricity below $e_1 = 0.2$ despins it first to the $3:2$, which is later lost in favour of the synchronous rotation[6] (at $e_1 = 0.05$). The despinning marks a transition to the third stage of the orbital evolution. A planet locked in the synchronous rotation dissipates much less energy and, therefore, the tidal circularisation becomes very gradual. The sudden change in the dissipation is also visible in the evolution of the semi–major axis and it translates to the apsidal motion as well. Upon the despinning, the argument of periapsis begins to precess at a decreased rate. The system slowly tends to a final, stationary state at zero eccentricity.

Moving on to the model with ongoing thermal evolution (Figure 5.8), we may notice a surprising difference between the cases with different distance of the perturber. While the $a_2 = 1\,\mathrm{AU}$ and $a_2 = 10\,\mathrm{AU}$ panels correspond to the expected conclusion that thermal evolution and formation of a magma ocean leads to a tidal shutdown, the $a_2 = 5\,\mathrm{AU}$ panel seems to negate this expectation. The orbit in this case undergoes full tidal circularisation in $\sim 4\,\mathrm{Gyr}$. The first hint of an explanation can be obtained from comparing Figure 5.8 with Figure 5.6: note that even in the case without thermal evolution, the orbital circularisation on the middle panel proceeds on a considerably shorter timescale than in the other cases. To shed light on this difference, Figure 5.9 shows the evolution of tidal heating over

[6]Since we are studying the evolution of the same model planet as in Chapter 3, the stability of individual spin states—and the corresponding tidal heating—can also be compared with Figure 3.6. Note, however, that Figure 3.6 depicts the *highest stable spin state* attained by a planet despinning from $\dot{\theta}/n = 5.6$ at a fixed orbital eccentricity. In the present example, the planet despins from its initial spin state at a time when the eccentricity is close to 0 and its later spinning–up is a consequence of the increase in the eccentricity and destabilisation of the lower–order resonance. In other words, the higher–order spin–orbit resonances are now reached "from below". Therefore, even though the actual eccentricity may enable much higher stable spin states, the planet spins up only to the *lowest stable spin state*.

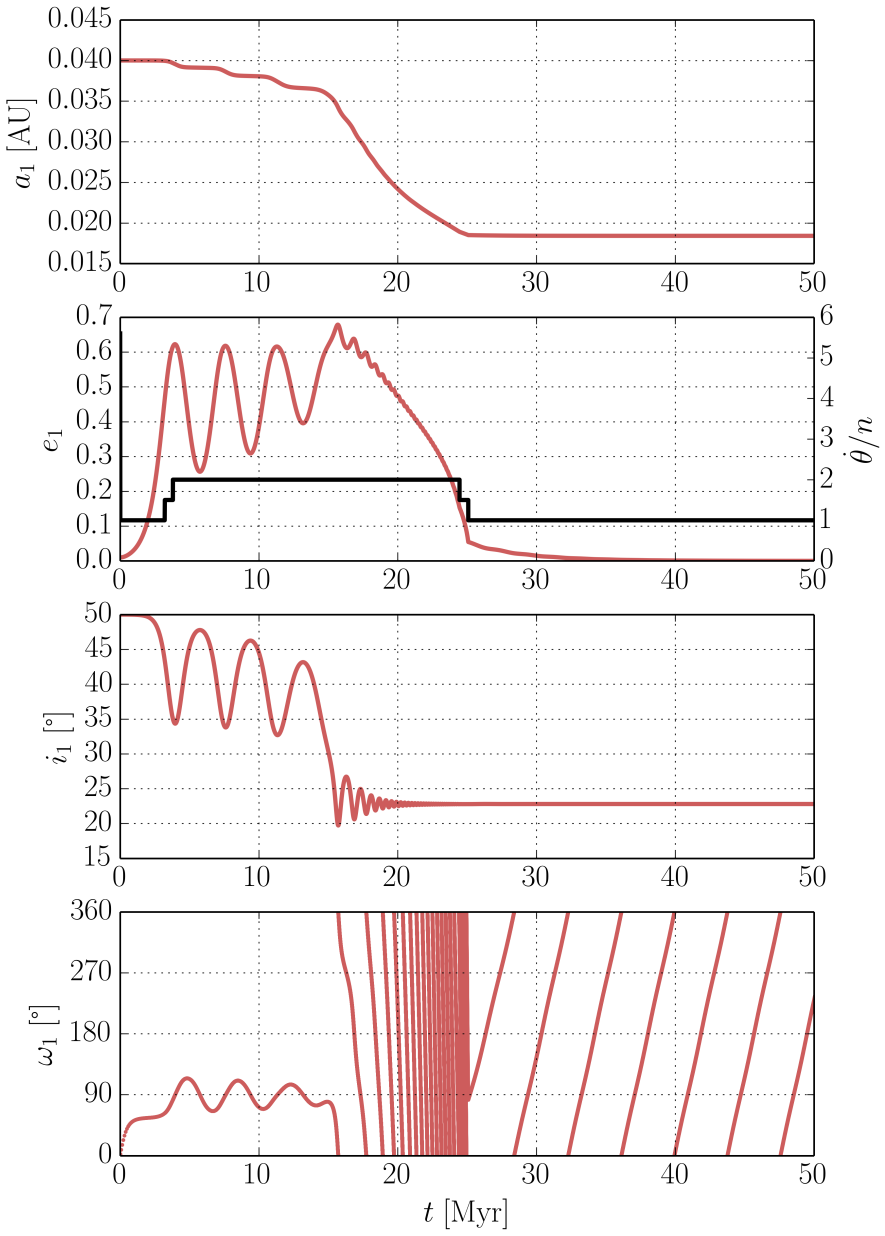

Figure 5.7: Orbital evolution of the model planet subjected to tides and third–body perturbation by a perturber at $a_2 = 5\,\mathrm{AU}$ and $i_1 = 50°$. Model with non–evolving interior and reference mantle viscosity $\eta_0 = 10^{19}\,\mathrm{Pa\,s}$ (as on the middle panel of Figure 5.6). The individual panels illustrate, from top to bottom, the evolution of the semi–major axis, the orbital eccentricity and spin–orbit ratio (black line), the inclination, and the argument of periapsis.

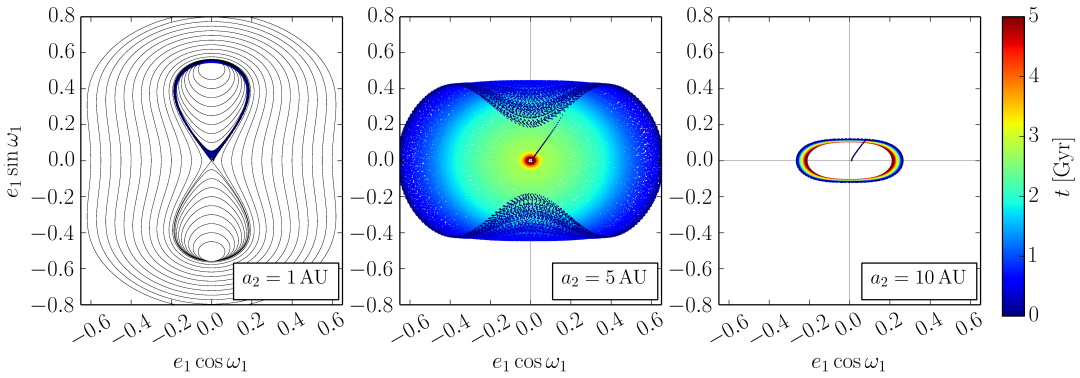

Figure 5.8: As in Figure 5.6 ($i_1 = 50°$), but for evolving interior.

a timescale relevant to each individual case. As the eccentricity in the $a_2 = 1$ AU case oscillates with a large amplitude and the minima are below $e_1 = 0.1$, the tidal dissipation is not efficient enough to overcome the effect of the partial melting (after ~ 250 kyr) and the tidally–induced evolution is effectively stopped. On the other hand, in the $a_2 = 5$ AU case, both the maxima and minima of eccentricity are not only higher but also maintained for a longer period of time (note the different timescales of the individual panels). Therefore, the tidal dissipation in the solid part of the planet is still efficient enough to induce considerable tidal evolution even after the formation of a magma ocean. Finally, in the $a_2 = 10$ AU case, the maxima of eccentricity are maintained for a long period of time, but they are few orders of magnitude lower than in the previous two cases. Although the tidal evolution is still more efficient than in the $a_2 = 1$ AU case, it cannot compete with the $a_2 = 5$ AU case in the rate of orbital circularisation.

Another interesting phenomenon illustrated on the middle panel of Figure 5.8 is a phase shift in the e_1–i_1–ω_1 oscillations, compared to the standard Kozai–Lidov mechanism without tides (Figure 5.1). While in the standard case, the maxima of the eccentricity (and the minima of the inclination) are reached at the same time when ω_1 goes through 90° or 270°, in the system with tidally evolving semi–molten planet, the same is true for $\omega_1 = 0°$ or $\omega_1 = 180°$. Furthermore, the maxima of eccentricity are higher (and the corresponding minima of inclination are lower) than in the standard case. The same "phase shift" can be also seen in the $a_2 = 10$ AU case with or without thermal evolution. In contrast to Figure 5.6, the initial trajectory that would correspond to the evolution without tides in the middle and right panels of Figure 5.6 is left much earlier. The escape from this trajectory—and the change from apsidal precession to apsidal recession—occurs at the same time as the formation of a subsurface magma ocean. Therefore, the sudden change in trajectory results from the sudden change in the rate of tidally-induced orbital evolution.

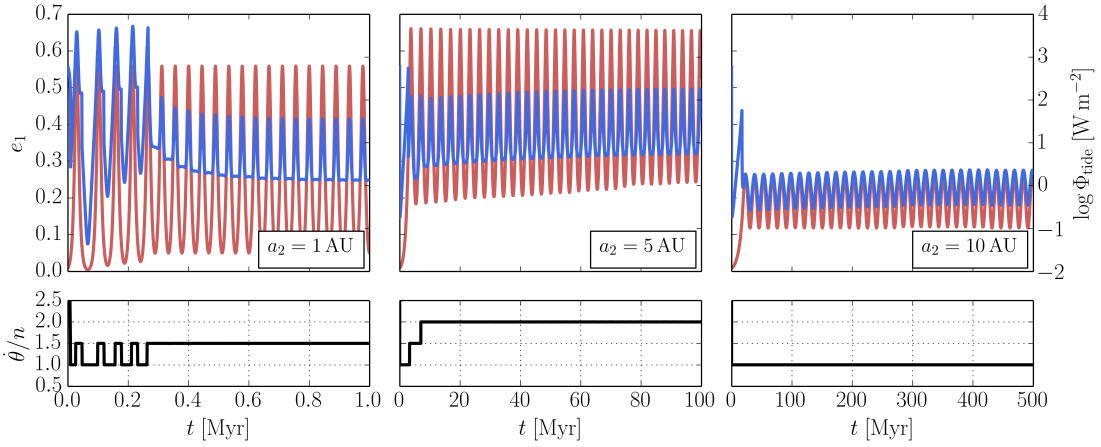

Figure 5.9: Initial evolution of the eccentricity (red), the surface tidal heat flux (blue), and the spin–orbit ratio (black) for the three considered semi–major axes of the perturber. Model with evolving interior and mutual inclination $i_1 = 50°$ (as in Figure 5.8). Note the different timescales of the three cases.

5.5 Discussion

The combined calculation of the tidally– and externally–induced orbital evolution, including possibly also the thermal evolution of the planet, is a very challenging problem. To facilitate the implementation of this model, we have made several assumptions that reduced the number of degrees of freedom present in the actual physical system. The simplifications introduced to the thermal evolution part have been already discussed in Chapter 4. Here, we mainly focus on the orbital and rotational evolution.

As in the previous two chapters, the spin axis of the planet was assumed to be always perpendicular to the orbital plane. Therefore, we implicitly neglected any dissipation resulting from obliquity tides. In reality, the high inclination of the model planet's orbit with respect to the reference plane, and the vivid dynamics of the system as well, would make the spin axis susceptible to large obliquity excursions (e.g., Wang et al., 2019). Non–zero obliquity would not only directly increase the total tidal dissipation, but it would also permit tidal locking of the planet to different spin–orbit resonances (Boué et al., 2016). In consequence, the inclusion of the obliquity evolution might have an effect on all the phenomena linked to tidal synchronisation; namely, on the sharp change in the slope of a_1 and e_1 evolution and on the direction of apsidal motion depicted in Figure 5.7.

While we attempted to include the self–consistent evolution of the spin rate into the model, the orbital evolution was still calculated using the two–cycle scheme from Chapter 4. In this scheme, we assume that the timescale of spin rate evolution is substantially shorter than the timescale of orbital evolution. After the initial "despinning mode", during which we calculate both the evolution of $\dot{\theta}$ and the evolution of the orbital elements, the short cycle is being called

in the "relaxation mode", which finds the equilibrium spin state for the actual orbital elements. The orbital elements in the relaxation mode are considered constant and the finding of the corresponding stable spin state is achieved without advancing in time. The time only runs in the despinning mode and in the long cycle. Although this computational scheme is justifiable when the evolution is solely due to tides, it might not be sufficient in the context of externally–induced eccentricity oscillations. In particular, when the spin evolution timescale becomes comparable to the period of oscillations (as in the $a_2 = 1\,\mathrm{AU}$ case), the alternation of the spin rate between different resonances should be more gradual. Therefore, in place of the "square wave" shown in the lower–left panel of Figure 5.9 for the first $\sim 250\,\mathrm{kyr}$, we should see a slightly smoother picture, possibly resembling a sinusoidal wave.

Another couple of problems stems from the model planet's vicinity to the host star. At small semi–major axes and large orbital eccentricities, the apsidal motion contains a contribution from the relativistic precession, which is given by (Eggleton and Kiseleva-Eggleton, 2001)

$$\frac{\mathrm{d}\omega_{1,\mathrm{GR}}}{\mathrm{d}t} = \frac{3\mathcal{G}m_* n_1}{a_1 c^2 (1-e_1^2)}\,, \tag{5.10}$$

where c is the speed of light. In our case, the rate of relativistic precession for the most extreme eccentricities ($e_1 = 0.7$, $a_1 = 0.04\,\mathrm{AU}$) would be $\sim 10^{-12}\,\mathrm{s}^{-1}$. This value is comparable to the precession induced by the second planet in the $a_2 = 1\,\mathrm{AU}$ case and few orders of magnitude higher than the precession rate in a system with a more distant perturber. Therefore, the relativistic precession, although not included in our study, should be considered as a dominant effect, possibly quenching the Kozai–Lidov oscillations and further increasing the rate of tidally–induced orbital evolution (see also Naoz et al., 2013; Petrovich, 2015).

An additional contribution to the apsidal motion would also result from the tidal deformation of the host star and from the rotational flattening of both the star and model planet. However, since the planet–star mass ratio is $\sim 10^{-5}$, the tidal effect of the model planet on the host star can be neglected. The apsidal motion induced by the host star's flattening is, in our case, $\sim J_{2,*} \times 10^{-9}\,\mathrm{s}^{-1}$, where $J_{2,*}$ is the second gravitational moment of the host star (e.g., Murray and Dermott, 1999). The gravitational moment depends on the stellar spin rate and interior structure and its typical values range from $\sim 10^{-7}$ for Sun–like stars to $\sim 10^{-4}$ for rapid rotators (e.g., Spalding and Millholland, 2020, and references therein). For very young stars, this value can be even higher, up to $\sim 10^{-2}$. Since the spins of low–mass stars (below $0.35\,m_\odot$) span a broad range of periods (Irwin et al., 2011), we can conclude that the precession induced by stellar J_2 might be important in the case of rapidly rotating host star and distant perturber (see also Spalding and Millholland, 2020). Likewise, the contribution of the model planet's rotational flattening to apsidal motion would be $\sim J_{2,\mathrm{p}} \times 10^{-11}\,\mathrm{s}^{-1}$, where $J_{2,\mathrm{p}}$ is the second gravitational moment of the planet. For the Earth, the gravitational moment is $\sim 10^{-3}$ (Petit and Luzum, 2010); however, for a tidally locked planet,

it can be expected to be lower. The effect of the planet's rotational flattening is thus potentially important only in the case of a distant perturber.

The close approaches to the host star during periastron passages may also raise questions regarding the planet's integrity under the extreme tidal forces endured. The theoretical distance to the host star below which the planet begins to disintegrate, is given by the Roche limit, defined as (e.g., Murray and Dermott, 1999)

$$r_{\mathrm{Roche}} = \left(\frac{9 m_*}{4 \pi \bar{\rho}} \right)^{1/3} , \tag{5.11}$$

with $\bar{\rho}$ being the planet's mean density. In our case, the Roche limit is $\sim 0.002\,\mathrm{AU}$ and it is reached neither during periastron passages nor after the Kozai–Lidov migration. Although the planet should not be subjected to disintegration, the close approaches to the host star may lead to extreme tidal deformation, possibly violating the assumption of linearity taken in the Darwin–Kaula theory. If this is the case, the orbital evolution might be better described by an alternative approach, for example by a mass–spring N–body model of the planet (e.g., Frouard et al., 2016).

5.6 Concluding remarks

In this chapter, we have explored the combined effect of tides and of the Kozai–Lidov mechanism, which occurs in systems with high mutual orbital inclinations ($> 39°$). Depending on the relative timescale of the two phenomena, the tidal evolution may either contribute as a minor effect to the Kozai–Lidov dynamics, or it can substantially alter the trajectory of the system, compared to a model without tides. Furthermore, the tidal evolution of a planet subjected to external eccentricity forcing leads to migration to the vicinity of the host star and to more or less gradual decrease in the mutual inclination in the system. As in the previous chapter, we have also seen the consequence of the model planet's thermal evolution. In a system with a close perturber ($a_2 = 1\,\mathrm{AU}$), the formation of a subsurface magma ocean results in a decrease in the tidal dissipation and in a "tidal shutdown". The variations in the planet's orbital elements are then governed almost exclusively by the third–body perturbation and, in the absence of other mechanisms, the planet may remain in a secular resonance for billions of years. In a system with a distant perturber, the feedback between the thermal evolution, the tidal effects, and the eccentricity forcing becomes much more complex.

The end of this chapter marks a transition from the semi–analytical studies of the thermal–orbital evolution of exoplanets to two additional independent analyses. First, we will follow in the steps of Kaula (1961) and derive an analytical expression for the tidal potential induced between individual planets in tightly–packed systems. Then, we will present an alternative study of tidal torques and tidal heating, using a fully numerical model. The relation of the following two chapters to the previous work is very loose and they are only included for the sake of completeness.

6. Planet–planet tides in tightly packed systems

The dynamics of tightly packed systems, such as is the planetary system around TRAPPIST–1 (Gillon et al., 2017) or the satellite systems around giant planets, may be affected not only by tides raised by the host star—and by the third–body perturbation—but also by tidal interaction between the individual secondaries. The possible importance of planet–planet tides was first discussed by Lingam and Loeb (2018), who pointed out at the astrobiological implications of this phenomenon. According to their estimations, the tidal elevation on the TRAPPIST–1 planets, caused by planet–planet tides, should be comparable to the elevation caused on the Earth by the tidal action of the Moon. Moreover, this effect would be greatly enhanced during multiple conjunctions, since the TRAPPIST–1 system constitutes a resonant chain. Were the planets' surfaces partially covered by ocean, the complex tidal modulation caused by the conjunctions would have interesting consequences for abiogenesis and further evolution of life (Lingam and Loeb, 2018).

In a context that is more related to the topic of our work, the role of planet–planet tides in the TRAPPIST–1 system was estimated by Wright (2018). Wright (2018) argues that the tidal strain and the tidal heat rate produced in planet g due to the action of planet f may, in fact, be even greater than the deformation and dissipation induced by the tidal interaction with the host star. For the other planets (except b), according to the estimates, the ratio between the strain due to planet–planet tides and the star–planet tides is always higher than 10%; the same ratio for the tidal dissipation being above 1%. A detailed study of the planet–planet tidal loading in the TRAPPIST–1 system was conducted by Hay and Matsuyama (2019). The authors discussed the role of viscosity and orbital eccentricity on the relative effect of planet–planet tides (compared to the star–planet tides) and reported lower values for the contribution to overall heating than estimated by Wright (2018). Nevertheless, for planet g, they still predicted that planet–planet tidal heating may participate by up to 20% to the total tidal heating. In a recent study, focused on the Galilean satellites, Hay et al. (2020) suggest that planet–planet (or moon–moon) tides may be particularly important in ocean worlds, where they can excite resonant response and thus alter the system's dynamics.

The main purpose of this chapter is to provide the tidal potential due to planet–planet loading, transformed to a planetocentric coordinate system and expressed by means of Keplerian elements. Derivation of the tidal potential (Section 6.1) follows the steps of Kaula (1961) and could be understood as a Fourier decomposition. In Section 6.2, we further derive the tidal torque resulting from planet–planet tides and potentially contributing to physical libration of the planets. Finally, Section 6.3 includes an illustration of the problem.

6.1 Derivation of the tidal potential

Consider a system consisting of a host star and two planets, denoted as planet A and planet B. Each of the planets orbits the star on a Keplerian trajectory described by a set of six elements $\{a, e, i, \omega, \Omega, \sigma\}$: the semi–major axis, the orbital eccentricity, the inclination of the orbit to a reference plane, the argument of the periapsis, the longitude of ascending node and the mean anomaly at epoch, respectively. Although we have also derived a general form of the planet–planet tidal potential, with arbitrary orientation of both orbits and arbitrary obliquities of the planets' spin axes, the complexity of the resulting formula is extremely high. Here, for the sake of illustration, we restrict our attention to a simple yet meaningful case of coplanar orbits and zero obliquity and we present the main steps of the derivation.

Let A be the planet of our interest, whose deformation is to be studied, and let B be the perturber. The instantaneous position of the two bodies in their respective orbits is described by the radial distance from the host star, r_A and r_B, and by the true anomaly, v_A and v_B. The angle between position vectors of their periapses—or the relative longitude of B's pericentre—will be denoted by $\varpi = (\omega_A - \omega_B) + (\Omega_A - \Omega_B)$. Our goal is to express the external potential sensed at any point of A due to the presence of B as a function of the orbital elements a_A, a_B, e_A, e_B, ϖ, the mean anomalies $M_A = n_A t + \sigma_A$ and $M_B = n_B t + \sigma_B$, and time t. Symbols n_A and n_B stand for the mean motions of the two planets.

We begin with expressing the external potential acting on infinitesimal volume of planet A as a linear combination of spherical harmonics (Kaula, 1961)

$$\mathcal{U} = \sum_{l=0}^{\infty} \frac{1}{r^{l+1}} \sum_{m=0}^{l} \mathcal{P}_{lm}(\cos\vartheta) \left(\mathcal{A}_{lm} \cos m\varphi + \mathcal{B}_{lm} \sin m\varphi \right) , \tag{6.1}$$

where (r, ϑ, φ) are planetocentric equatorial coordinates of the perturber referred to the centre of planet A, functions $\mathcal{P}_{lm}(\cos\vartheta)$ are the associated Legendre polynomials of degree l and order m, which can be defined by the following formula (e.g., Kaula, 1961; Novotný, 1998),

$$\mathcal{P}_{lm}(x) = \frac{(1-x^2)^{\frac{m}{2}}}{2^l l!} \sum_{t=0}^{\frac{l-m}{2}} \frac{(2l-2t)!}{(l-m-2t)!} \binom{l}{t} (-1)^t x^{l-m-2t} , \tag{6.2}$$

and $\mathcal{A}_{lm}$ and $\mathcal{B}_{lm}$ stand for a combination of physical parameters and algebraic terms arising from the addition theorem,

$$\mathcal{A}_{lm} = (2-\delta_{m0}) \frac{(l-m)!}{(l+m)!} \mathcal{G} m_B (r')^l \, \mathcal{P}_{lm}(\cos\vartheta') \, \cos m\varphi' ,$$

$$\mathcal{B}_{lm} = (2-\delta_{m0}) \frac{(l-m)!}{(l+m)!} \mathcal{G} m_B (r')^l \, \mathcal{P}_{lm}(\cos\vartheta') \, \sin m\varphi' .$$

In the last two expressions, $\mathcal{G}$ is Newton's gravitational constant, m_B mass of

the perturber and $(r', \vartheta', \varphi')$ coordinates of the "observer" (i.e., of the perturbed infinitesimal volume). Following Kaula (1961), we now rewrite the planetographic longitude of the sub–perturber point in terms of three new angles: the initial angular distance α_0 of planet A's zero meridian from the reference direction[1], the instantaneous angular distance α of planet B from the reference direction as observed from planet A (the "right ascension") and the sidereal time θ,

$$\varphi = \alpha - \alpha_0 + \alpha_0 - \theta \,. \tag{6.3}$$

It follows that the goniometric functions in (6.1) can be rewritten as

$$\begin{aligned} \cos m\varphi &= \cos m(\alpha - \alpha_0)\, \cos m(\alpha_0 - \theta) - \sin m(\alpha - \alpha_0)\, \sin m(\alpha_0 - \theta) \,, \\ \sin m\varphi &= \sin m(\alpha - \alpha_0)\, \cos m(\alpha_0 - \theta) + \cos m(\alpha - \alpha_0)\, \sin m(\alpha_0 - \theta) \end{aligned} \tag{6.4}$$

and with the help of trigonometric identities (3) and (4) of Kaula (1961),

$$\begin{aligned} \cos mx &= \Re\left\{ \sum_{s=0}^{m} \binom{m}{s} \mathrm{i}^s \cos^{m-s} x \sin^s x \right\} , \\ \sin mx &= \Re\left\{ \sum_{s=0}^{m} \binom{m}{s} \mathrm{i}^{s-1} \cos^{m-s} x \sin^s x \right\} , \end{aligned} \tag{6.5}$$

we can write

$$\begin{aligned} \mathcal{A}_{lm} \cos m\varphi + \mathcal{B}_{lm} \sin m\varphi = \Re\Bigg\{ \sum_{s=0}^{m} \binom{m}{s} \mathrm{i}^s \cos^{m-s}(\alpha - \alpha_0) \sin^s(\alpha - \alpha_0) \quad \times \\ \times \quad \left(\mathcal{A}_{lm} - \mathrm{i}\mathcal{B}_{lm}\right) \exp\left[\mathrm{i}\, m(\alpha_0 - \theta)\right] \Bigg\} , \end{aligned} \tag{6.6}$$

where $\Re$ symbolises the real part. As a consequence of the coplanarity of both orbits and the zero obliquity of A's spin axis, planet B is always located above a point with colatitude $\vartheta = \frac{\pi}{2}$, while the longitude of sub–B point depends only on the two true anomalies and the instantaneous mutual distances between the three bodies (two planets and a star) in the system. The goniometric functions of planet B's position above A's surface can be rewritten in the terms of asterocentric polar coordinates as

$$\begin{aligned} \cos(\alpha - \alpha_0) &= \frac{r_A \cos v_A - r_B \cos(v_B + \varpi)}{r \sin\vartheta} \\ \sin(\alpha - \alpha_0) &= \frac{r_A \sin v_A - r_B \sin(v_B + \varpi)}{r \sin\vartheta} \\ \cos\vartheta = 0 \qquad & \qquad \sin\vartheta = 1 \end{aligned} \tag{6.7}$$

[1]The quantity α_0 is equal to $(\alpha + \gamma)$ from Chapter 1. The reference direction is the direction from the centre of planet A towards the host star in the periapsis.

where r is the instantaneous distance between the two planets, or

$$r = \sqrt{r_A^2 + r_B^2 - 2\, r_A\, r_B\, \cos(v_B - v_A + \varpi)}\,. \tag{6.8}$$

The only non–zero terms in the explicit definition of associated Legendre polynomials (6.2) are those with $t = \frac{l-m}{2}$, where t is an integer. This condition implies that polynomials with odd $(l-m)$ are identically zero,

$$\mathcal{P}_{lm}(\cos\vartheta = 0) = 0 \qquad \Longleftrightarrow \qquad (l-m) \quad \text{odd}\,, \tag{6.9}$$

while polynomials with even $(l-m)$ simplify to

$$\mathcal{P}_{lm}(\cos\vartheta = 0) = \frac{1}{2^l}\,\frac{(l+m)!}{l!}\binom{l}{\frac{l-m}{2}}(-1)^{\frac{l-m}{2}} \qquad \Longleftrightarrow \qquad (l-m) \quad \text{even}\,. \tag{6.10}$$

In the next step, we further expand equation (6.6), which includes expressions $\cos^{m-s}(\alpha-\alpha_0)$ and $\sin^s(\alpha-\alpha_0)$. Applying binomial theorem on the first two equations of (6.7) and setting $\sin\vartheta = 1$, we obtain

$$\begin{aligned}
\cos^{m-s}(\alpha-\alpha_0) &= \frac{1}{r^{m-s}}\sum_{c_1=0}^{m-s}(-1)^{c_1}\binom{m-s}{c_1}\, r_A^{m-s-c_1}\, r_B^{c_1}\, \cos^{m-s-c_1} v_A\, \cos^{c_1}(v_B+\varpi) \\
\sin^{s}(\alpha-\alpha_0) &= \frac{1}{r^{s}}\sum_{d_1=0}^{s}(-1)^{d_1}\binom{s}{d_1}\, r_A^{s-d_1}\, r_B^{d_1}\, \sin^{s-d_1} v_A\, \sin^{d_1}(v_B+\varpi)
\end{aligned} \tag{6.11}$$

Product of the two terms expanded in (6.11) contains products of goniometric functions with the same argument: v_A or $(v_B+\varpi)$. This kind of expressions can be rewritten with the help of another goniometric identity, namely equation (5) of Kaula (1961),

$$\sin^a x \cos^b x = \frac{(-\mathrm{i})^a}{2^{a+b}}\sum_{c=0}^{a}\sum_{d=0}^{b}\binom{a}{c}\binom{b}{d}(-1)^c\big[\cos(a+b-2c-2d)x + \mathrm{i}\sin(a+b-2c-2d)x\big]\,. \tag{6.12}$$

The resulting products of goniometric functions are

$$\begin{aligned}
\cos^{c_1}(v_B+\varpi)\, \sin^{d_1}(v_B+\varpi) &= \frac{(-\mathrm{i})^{d_1}}{2^{c_1+d_1}}\sum_{h_1=0}^{d_1}\sum_{h_2=0}^{c_1}\binom{d_1}{h_1}\binom{c_1}{h_2}\times \\
&\qquad \times\ (-1)^{h_1}\ \exp\Big[\mathrm{i}\,(c_1+d_1-2h_1-2h_2)(v_B+\varpi)\Big] \\
\cos^{m-s-c_1} v_A\ \sin^{s-d_1} v_A &= \frac{(-\mathrm{i})^{s-d_1}}{2^{m-c_1-d_1}}\sum_{k_1=0}^{s-d_1}\sum_{k_2=0}^{m-s-c_1}\binom{s-d_1}{k_1}\binom{m-s-c_1}{k_2}\times \\
&\qquad \times\ (-1)^{k_1}\ \exp\Big[\mathrm{i}\,(m-c_1-d_1-2k_1-2k_2)v_A\Big]
\end{aligned} \tag{6.13}$$

Including both of these expansions into (6.6 and consequently into (6.1) leads us to a preliminary form of the tidal potential,

$$\mathcal{U}_{lm} = \frac{1}{r^{l+m+1}} \frac{(l+m)!}{2^{l+m}\, l!} \binom{l}{\frac{l-m}{2}} (-1)^{\frac{l-m}{2}} \sum_{s=0}^{m} \binom{m}{s} \sum_{c_1=0}^{m-s} \sum_{d_1=0}^{s} \binom{m-s}{c_1} \binom{s}{d_1} r_B^{c_1+d_1}\, r_A^{m-c_1-d_1} \times$$

$$\times (-1)^{c_1+d_1} \sum_{h_1=0}^{d_1} \sum_{h_2=0}^{c_1} \binom{d_1}{h_1} \binom{c_1}{h_2} (-1)^{h_1} \sum_{k_1=0}^{s-d_1} \sum_{k_2=0}^{m-s-c_1} \binom{s-d_1}{k_1} \binom{m-s-c_1}{k_2} (-1)^{k_1} \times$$

$$\times \Bigg\{ \mathcal{A}_{lm} \cos\Big[(c_1+d_1-2h_1-2h_2)(v_B+\varpi) + (m-c_1-d_1-2k_1-2k_2)v_A + m(\alpha-\theta)\Big] +$$

$$+ \mathcal{B}_{lm} \sin\Big[(c_1+d_1-2h_1-2h_2)(v_B+\varpi) + (m-c_1-d_1-2k_1-2k_2)v_A + m(\alpha-\theta)\Big] \Bigg\} . \tag{6.14}$$

In the following, we intent to simplify the above expression by changing the indices:

$$\begin{aligned} c_1 &= p_1 - d_1 \,, \qquad & p_1 &\in [0, m] \,, \\ h_2 &= p_2 - h_1 \,, \qquad & p_2 &\in [0, p_1] \,, \\ k_2 &= p_3 - k_1 \,, \qquad & p_3 &\in [0, m - p_1] \,. \end{aligned} \tag{6.15}$$

Together with setting the limits for the new indices p_1, p_2 and p_3, we shall also update the limits for the old indices d_1, h_1 and k_1, because some combinations of the new and the old indices result in zero binomial coefficients in (6.14). Updated intervals of the old indices' values are

$$\begin{aligned} \max(0, p_1 - m + s) \;&\leq d_1 \;\leq\; \min(s, p_1) \,, \\ \max(0, p_2 - p_1 + d_1) \;&\leq h_1 \;\leq\; \min(d_1, p_2) \,, \\ \max(0, p_3 + p_1 - m + s - d_1) \;&\leq k_1 \;\leq\; \min(s - d_1, p_3) \,. \end{aligned} \tag{6.16}$$

Up to now, we have succeeded in rewriting the planetographic longitude and latitude of the sub–perturber point in terms of the desired variables related to the instantaneous position of both planets and the orientation of planet A. The last term to be transformed is the mutual distance between the two bodies r, introduced by equation (6.8). Specifically, we are seeking a serie expansion of the function $r^{-\lambda}$, which is equivalent to the generating function of Gegenbauer polynomials (e.g., Reimer, 2003),

$$\frac{1}{\left(\sqrt{1+t^2-2xt}\right)^{\lambda}} = \sum_{n=0}^{\infty} t^n\, \mathcal{C}_n^{\left(\frac{\lambda}{2}\right)}(x) \tag{6.17}$$

with $\lambda \in \mathbb{R}$, $\lambda > -1$ and $\lambda \neq 0$. Gegenbauer polynomials are defined as

$$\mathcal{C}_n^{(\frac{\lambda}{2})}(x) = \sum_{u=0}^{\left[\frac{n}{2}\right]} (-1)^u \, \frac{\Gamma\left(n-u+\frac{\lambda}{2}\right)}{\Gamma\left(\frac{\lambda}{2}\right) \, u!(n-2u)!} \, (2x)^{n-2u} \, . \tag{6.18}$$

Applying expansions (6.17) and (6.18) to our case, we obtain the following equality

$$\frac{1}{r^{l+m+1}} = \frac{1}{r_>^{l+m+1}} \, \sum_{n=0}^{\infty} \left(\frac{r_<}{r_>}\right)^n \, \sum_{u=0}^{\left[\frac{n}{2}\right]} (-1)^u \, \frac{\Gamma\left(n-u+\frac{l+m+1}{2}\right)}{\Gamma\left(\frac{l+m+1}{2}\right) \, u!(n-2u)!} \left[2\cos(v_B - v_A + \varpi)\right]^{n-2u} \, , \tag{6.19}$$

where $r_>$ and $r_<$ indicate the larger and the smaller of the two instantaneous distances between each planet and the host star. Once again, we apply the trigonometric identity (6.12) on the function $\Big[\cos(v_B - v_A + \varpi)\Big]^{n-2u}$ and obtain the final expansion of (6.19),

$$\begin{aligned} \frac{1}{r^{l+m+1}} = \frac{1}{r_>^{l+m+1}} \, \sum_{n=0}^{\infty} \left(\frac{r_<}{r_>}\right)^n \, \sum_{u=0}^{\left[\frac{n}{2}\right]} (-1)^u \, \frac{\Gamma\left(n-u+\frac{l+m+1}{2}\right)}{\Gamma\left(\frac{l+m+1}{2}\right) \, u!(n-2u)!} \, \times \\ \times \, \sum_{j=0}^{n-2u} \binom{n-2u}{j} \, \exp\Big[\mathrm{i}\,(n-2u-2j)(v_B - v_A + \varpi)\Big] \, . \end{aligned} \tag{6.20}$$

Similarly to the previous expansion, it is convenient to introduce a new index, p_4, and to update the limits for the summation over u:

$$\begin{aligned} j &= p_4 - u \, , \qquad p_4 \in [0, n] \, , \\ 0 \; &\leq \; u \; \leq \; \min\left(\left[\frac{n}{2}\right], p_4, n - p_4\right) \, . \end{aligned} \tag{6.21}$$

Finally, we insert (6.20) into the preliminary form of the tidal potential (6.14) and gather all algebraic prefactors into an analogy of Kaula's functions of inclination, $\mathcal{F}^0_{lmn\bar{p}}$, where the superscript 0 indicates that we are in the limit of coplanar orbits and zero obliquities and $\bar{p}$ stands for the multiindex $\{p_1, p_2, p_3, p_4\}$. The tidal

potential can then be rewritten as

$$\mathcal{U}_{lm} = \sum_{n=0}^{\infty} \sum_{p_1=0}^{m} \sum_{p_2=0}^{m-p_1} \sum_{p_3=0}^{p_1} \sum_{p_4=0}^{n} \frac{r_B^{p_1}\, r_A^{m-p_1}}{r_>^{l+m+1}} \left(\frac{r_<}{r_>}\right)^n \mathcal{F}^0_{lmn\bar{p}} \times$$

$$\times \left[\begin{Bmatrix} \mathcal{A}_{lm} \\ -\mathcal{B}_{lm} \end{Bmatrix}_{l-m \text{ odd}}^{l-m \text{ even}} \cos\Big[(m-p_1-2p_3-n+2p_4)v_A + (p_1-2p_2+n-2p_4)(v_B+\varpi) + m(\alpha-\theta)\Big] + \right.$$

$$\left. + \begin{Bmatrix} \mathcal{B}_{lm} \\ \mathcal{A}_{lm} \end{Bmatrix}_{l-m \text{ odd}}^{l-m \text{ even}} \sin\Big[(m-p_1-2p_3-n+2p_4)v_A + (p_1-2p_2+n-2p_4)(v_B+\varpi) + m(\alpha-\theta)\Big] \right] \tag{6.22}$$

with

$$\mathcal{F}^0_{lmn\bar{p}} = \frac{1}{2^{l+m}} \frac{(l+m)!}{l!} \binom{l}{\frac{l-m}{2}} (-1)^{\frac{l-m}{2}} \sum_{s=0}^{m} \binom{m}{s} \sum_{d_1} \binom{m-s}{p_1-d_1} \binom{s}{d_1} (-1)^{p_1} \times$$

$$\times \sum_{h_1} \sum_{k_1} (-1)^{h_1+k_1} \binom{d_1}{h_1} \binom{p_1-d_1}{p_2-h_1} \binom{s-d_1}{k_1} \binom{m-s-p_1+d_1}{p_3-k_1} \times \tag{6.23}$$

$$\times \sum_{u} (-1)^u \frac{\Gamma\left(n-u+\frac{l+m+1}{2}\right)}{\Gamma\left(\frac{l+m+1}{2}\right) u!\,(n-2u)!} \binom{n-2u}{p_4-u}$$

and limits of summation over d_1, h_1, k_1 and u given by (6.16) and (6.21), respectively. We also note that the above expression holds only for $(l-m)$ even, as the terms $\mathcal{U}_{lm}$ for odd $(l-m)$ equal zero.

Equation (6.22) can be readily used for the computation of planet–planet tidal potential in the case of circular orbits. For general eccentric orbits, we need to expand the instantaneous distances of both planets from the host star and the true anomalies into series containing the respective semi–major axes a_i and the mean anomalies M_i. Let $X_k^{b,c}$ denote Hansen's coefficients (e.g., Murray and Dermott, 1999). Then,

$$\left(\frac{r_i}{a_i}\right)^b e^{icv_i} = \sum_{k=-\infty}^{\infty} X_k^{b,c}(e_i) e^{ikM_i} \,. \tag{6.24}$$

Here, the Hansen's coefficients play the role of Kaula's short-period functions of eccentricity $\mathcal{G}_{lpq}(e)$. In order to assign correct values to the exponent b, it is necessary to distinguish two particular cases. The instantaneous distance of planet B from the host star is either always larger than the distance of planet A,

$$a_B > a_A \frac{1+e_A}{1-e_B} \,, \tag{6.25}$$

or it is always smaller, hence

$$a_A > a_B \frac{1+e_B}{1-e_A} \,. \tag{6.26}$$

In the first case, we may substitute

$$b_A = m + n - p_1 \qquad b_B = -m - n + p_1 - l - 1$$

and in the second case

$$b_A = -n - p_1 - l - 1 \qquad b_B = n + p_1 \, .$$

The other two indices are

$$\begin{aligned} c_A &= m - p_1 - 2p_3 - n + 2p_4 & c_B &= p_1 - 2p_2 + n - 2p_4 \\ k_A &= m - p_1 - 2p_3 - n + 2p_4 + q_1 & k_B &= p_1 - 2p_2 + n - 2p_4 + q_2 \, . \end{aligned}$$

Introducing functions of eccentricity $\mathcal{G}^A_{lmn\bar{p}\bar{q}}(e_A) = X^{b_A,c_A}_{k_A}(e_A)$ and $\mathcal{G}^B_{lmn\bar{p}\bar{q}}(e_B) = X^{b_B,c_B}_{k_B}(e_B)$, we may write down the final form of the tidal potential due to planet–planet tides as

$$\begin{aligned} \mathcal{U}_{lm} = &\sum_{n=0}^{\infty} \sum_{p_1=0}^{m} \sum_{p_2=0}^{m-p_1} \sum_{p_3=0}^{p_1} \sum_{p_4=0}^{n} \sum_{q_1=-\infty}^{\infty} \sum_{q_2=-\infty}^{\infty} \frac{1}{a_>^{l+1}} \left(\frac{a_<}{a_>}\right)^{\varrho} \mathcal{F}^0_{lmn\bar{p}} \, \mathcal{G}^A_{lmn\bar{p}\bar{q}}(e_A) \, \mathcal{G}^B_{lmn\bar{p}\bar{q}}(e_B) \times \\ \times \Bigg[&\begin{Bmatrix} \mathcal{A}_{lm} \\ -\mathcal{B}_{lm} \end{Bmatrix}^{l-m \text{ even}}_{l-m \text{ odd}} \cos\Big[(m - p_1 - 2p_3 - n + 2p_4 + q_1)M_A + (p_1 - 2p_2 + n - 2p_4 + q_2)M_B + \\ &+ (p_1 - 2p_2 + n - 2p_4)\varpi + m(\alpha - \theta)\Big] + \\ + &\begin{Bmatrix} \mathcal{B}_{lm} \\ \mathcal{A}_{lm} \end{Bmatrix}^{l-m \text{ even}}_{l-m \text{ odd}} \sin\Big[(m - p_1 - 2p_3 - n + 2p_4 + q_1)M_A + (p_1 - 2p_2 + n - 2p_4 + q_2)M_B + \\ &+ (p_1 - 2p_2 + n - 2p_4)\varpi + m(\alpha - \theta)\Big]\Bigg] \end{aligned} \tag{6.27}$$

with the algebraic prefactors $\mathcal{F}^0_{lmn\bar{p}}$ given by (6.23). The exponent ϱ depends on geometry of the two orbits. If A is the inner planet, perturbed by outer B, then $\varrho = m + n - p_1$. In the opposite case of outer A, we have $\varrho = n + p_1$.

6.2 Tidal torque

Equation (6.27) presents harmonic expansion of the tidal potential acting on infinitesimal volume of planet A due to the presence of planet B. As a consequence of nonhomogeneity of the tidal potential, planet A deforms and its departure

from a perfectly spherical shape gives rise to disturbing potential $\delta\mathcal{U}$, whose value exterior to the body reads as (Kaula, 1964)

$$\begin{aligned}\delta\mathcal{U}^B_{lmn\bar{p}\bar{q}}(\mathbf{r}') &= \left(\frac{R_A}{r'}\right)^{l+1} k_l(\omega_{lmn\bar{p}\bar{q}})\Big[\mathcal{U}_{lmn\bar{p}\bar{q}}(R_A)\Big]_{\rm lag} \\ &= k_l(\omega_{lmn\bar{p}\bar{q}})\,\frac{R_A^{2l+1}}{(r')^{l+1}}\,B^B_{lm}\,C^B_{lmn\bar{p}\bar{q}}\,\mathcal{P}_{lm}(\cos\vartheta')\begin{Bmatrix}\cos\\ \sin\end{Bmatrix}^{l-m\ \text{even}}_{l-m\ \text{odd}}\Big[\nu_{lmnpq}-\varepsilon_{lmnpq}-m(\varphi'+\theta)\Big]\end{aligned} \tag{6.28}$$

where the subscript "lag" reminds us that in order to compute the disturbing potential of non–elastic body at time t, we need to express the tidal potential at time $t-\Delta t_{lmn\bar{p}\bar{q}}$, where $\Delta t_{lmn\bar{p}\bar{q}}=\varepsilon_{lmn\bar{p}\bar{q}}/\omega_{lmn\bar{p}\bar{q}}$ is a mode–specific tidal time lag. Parameters k_l and $\varepsilon_{lmn\bar{p}\bar{q}}$ are, respectively, the tidal Love number and the tidal phase lag: two quantities, whose magnitude and frequency dependence characterises the internal structure and the rheology of the planet. In (6.28), we also introduced the traditional notation for the non–rotational part of signed tidal frequency,

$$\begin{aligned}\nu_{lmn\bar{p}\bar{q}} = m\alpha + (m-p_1-2p_3-n+2p_4+q_1)\,M_A + (p_1-2p_2+n-2p_4+q_2)\,M_B + \\ + (p_1-2p_2+n-2p_4)\,\varpi\ ,\end{aligned} \tag{6.29}$$

and the two prefactors,

$$B^B_{lm} = \mathcal{G}m_B\,\frac{(l-m)!}{(l+m)!}\,(2-\delta_{m0}) \tag{6.30}$$

$$C^B_{lmn\bar{p}\bar{q}} = \frac{1}{a_>^{l+1}}\,\left(\frac{a_<}{a_>}\right)^{\varrho}\,\mathcal{F}^0_{lmn\bar{p}}\,\mathcal{G}^A_{lmn\bar{p}\bar{q}}(e_A)\,\mathcal{G}^B_{lmn\bar{p}\bar{q}}(e_B) \tag{6.31}$$

Planet A is also deformed by its tidal interaction with the host star, in which case we express the disturbing potential as

$$\begin{aligned}\delta\mathcal{U}^*_{lm}(\mathbf{r}') = \sum_{p=0}^{l}\sum_{q=-\infty}^{\infty} k_l(\omega_{lmpq})\,\frac{R_A^{2l+1}}{(r')^{l+1}}\,B^*_{lm}\,C^*_{lmpq}\,\mathcal{P}_{lm}(\cos\vartheta')\,\times \\ \times\ \begin{Bmatrix}\cos\\ \sin\end{Bmatrix}^{l-m\ \text{even}}_{l-m\ \text{odd}}\Big[\nu_{lmpq}-\varepsilon_{lmpq}-m(\varphi'+\theta)\Big]\end{aligned} \tag{6.32}$$

with

$$\nu_{lmpq} = m\alpha + (l-2p+q)\,M_A + (l-2p)\,\varpi\ , \tag{6.33}$$

$$B^*_{lm} = \mathcal{G}m_*\,\frac{(l-m)!}{(l+m)!}\,(2-\delta_{m0}) \tag{6.34}$$

and

$$C^*_{lmpq} = \frac{1}{a_A^{l+1}}\, \mathcal{F}_{lmp}(0)\, \mathcal{G}_{lpq}(e_A)\,. \tag{6.35}$$

where $\mathcal{F}_{lmp}$ and $\mathcal{G}_{lpq}$ are Kaula's functions of inclination and eccentricity and m_* is the stellar mass.

In the model system consisting of three bodies—the host star and the two planets—we may think of four components to the tidal torque influencing planet A's spin rate. The leading component is obviously the torque raised by the host star on the deformation induced by the star itself, which leads the planet either into a spin–orbit resonance or toward pseudo–synchronisation. Second, there are two "cross components": planet B acting on the tidal bulge raised by the host star, and vice versa. These two terms are presumably non–negligible only around the mutual conjunctions of the two planets. Last, there is also a tiny component due to planet B's action on the deformation caused by the planet–planet tides.

The tidal torque acting on a planet with zero obliquity due to the host star or due to another body in the same orbital plane is orthogonal to the planetary equator. It induces changes in the spin rate (including physical libration) but has no effect on the axial tilt. Each term $\mathcal{T}_{lm}$ of the torque's harmonic expansion can be computed as (Efroimsky and Williams, 2009)

$$\mathcal{T}_{lm} = m'\, \frac{\partial}{\partial\theta}\Big[\delta\mathcal{U}_{lm}(\mathbf{r}')\Big]\,, \tag{6.36}$$

where m' is mass of the spin–perturbing body located at $\mathbf{r}'$.

On our way towards the derivation of all planetary contributions to the total tidal torque, we will begin with the cross components. In order to express the disturbing potential sensed at the instantaneous position of planet B due to the deformation of planet A induced by stellar tides, we apply the harmonic expansion derived in the previous section on the terms of (6.32) containing r', ϑ' and φ'. This results in

$$\begin{aligned}\delta\mathcal{U}^*_{lm}(\mathbf{r}')\Big|_{\mathbf{r}'=\mathbf{r}} = &\sum_{h=0}^{l}\sum_{j=-\infty}^{\infty} k_l(\omega_{lmhj})\, R_A^{2l+1}\, B^*_{lm}\, C^*_{lmhj}\,\times \\ &\times \sum_{n}\sum_{\bar{p}}\sum_{\bar{q}} C^B_{lmn\bar{p}\bar{q}}\, \cos\Big[(\nu_{lmhj} - m\theta) - (\nu_{lmn\bar{p}\bar{q}} - m\tilde{\theta}) - \varepsilon_{lmhj}\Big]\,,\end{aligned} \tag{6.37}$$

where $\tilde{\theta}$ is the sidereal time with respect to the rotation of perturbed planet A. Note that θ and $\tilde{\theta}$ are essentially the same quantity and here (as well as in Kaula, 1964) they are labelled separately only for the sake of the following derivations. Now, we may differentiate (6.37) with respect to $\tilde{\theta}$, multiply the result by $m' = m_B$ and then set $\theta = \tilde{\theta}$. The general form of the additional tidal torque becomes

$$\mathcal{T}^{*B}_{lm} = -m_B\, m \sum_{h=0}^{l}\sum_{j=-\infty}^{\infty} k_l(\omega_{lmhj})\, R_A^{2l+1}\, B^*_{lm}\, C^*_{lmhj}\,\times$$

$$\times \sum_{n}\sum_{\bar{p}}\sum_{\bar{q}} C^{B}_{lmn\bar{p}\bar{q}} \sin\left[\nu_{lmhj} - \nu_{lmn\bar{p}\bar{q}} - \varepsilon_{lmhj}\right] . \qquad (6.38)$$

Equation (6.38) can be further split into a secular term, which affects the evolution of planet A's spin rate over hundreds of orbital periods, and a periodic term, responsible for the physical libration. The secular term, which would remain non–zero after averaging over the orbital periods of the two planets as well as over the period of apsidal precession, is characterised by the condition $\nu_{lmpq} = \nu_{lmn\bar{p}\bar{q}}$, that leads to four sub–conditions:

$$\begin{aligned} q_2 &= 0 \,, \\ h &= \frac{l}{2} \,, \\ j &= m - 2p_2 - 2p_3 + q_1 \,, \\ p_4 &= \frac{n+p_1}{2} - p_2 \,. \end{aligned} \qquad (6.39)$$

Focusing only on the terms with $l = 2$ and inspecting the quantity C^{*}_{lmhj} in (6.38), we see that the secular term of tidal torque contains

$$C^{*}_{2m1j} = \frac{1}{a_A^{l+1}}\, \mathcal{F}_{2m1}(0)\, \mathcal{G}_{21j}(e_A) \,, \qquad j = m - 2p_2 - 2p_3 + q_1 \,. \qquad (6.40)$$

However, according to Kaula (1964), the only nonzero functions of inclination are those with indices $\{201\}$ and $\{220\}$, where the former one, containing $m = 0$ and present in (6.40), does not contribute to the tidal torque. Similar derivation can be performed for the torque raised by the host star on the tidal bulge due to planet–planet tides. The cross components to the tidal torque are therefore only periodic, with no secular part.

The remaining, planet–planet component can be derived from the disturbing potential

$$\begin{aligned} \delta\mathcal{U}^{B}_{lm}(\mathbf{r}')\Big|_{\mathbf{r}'=\mathbf{r}} &= \sum_{n}\sum_{\bar{p}}\sum_{\bar{q}} k_l(\omega_{lmn\bar{p}\bar{q}})\, R_A^{2l+1}\, B^{B}_{lm}\, C^{B}_{lmn\bar{p}\bar{q}} \times \\ &\times \sum_{w}\sum_{\bar{h}}\sum_{\bar{j}} C^{B}_{lmw\bar{h}\bar{j}} \cos\left[(\nu_{lmn\bar{p}\bar{q}} - m\theta) - (\nu_{lmw\bar{h}\bar{j}} - m\tilde{\theta}) - \varepsilon_{lmn\bar{p}\bar{q}}\right] . \end{aligned} \qquad (6.41)$$

in the same manner. Here, the multiindices $\bar{h}$ and $\bar{j}$ are defined similarly to $\bar{p}$ and $\bar{q}$ as $\bar{h} = \{h_1, h_2, h_3, h_4\}$ and $\bar{j} = \{j_1, j_2\}$. We obtain the additional tidal torque

$$\begin{aligned} \mathcal{T}^{BB}_{lm} = -m_B\, m \sum_{n}\sum_{\bar{p}}\sum_{\bar{q}} k_l(\omega_{lmn\bar{p}\bar{q}})\, R_A^{2l+1}\, B^{B}_{lm}\, C^{B}_{lmn\bar{p}\bar{q}} \times \\ \times \sum_{w}\sum_{\bar{h}}\sum_{\bar{j}} C^{B}_{lmw\bar{h}\bar{j}} \sin\left[\nu_{lmn\bar{p}\bar{q}} - \nu_{lmw\bar{h}\bar{j}} - \varepsilon_{lmn\bar{p}\bar{q}}\right] , \end{aligned} \qquad (6.42)$$

whose secular term satisfies the following conditions

$$\begin{aligned} j_2 &= q_2 \,, \\ j_1 &= q_1 + 2(h_2 + h_3 - p_2 - p_3) \,, \\ h_4 &= p_2 + p_4 - h_2 + \frac{h_1 + w - p_1 - n}{2} \,. \end{aligned} \tag{6.43}$$

In this case, the secular term is not necessarily zero and it may contribute to the long–term evolution of planet A's rotation.

6.3 Illustration: planet–planet tidal heating in the TRAPPIST-1 system

Although it is, in principle, possible to calculate the heat rate generated by planet–planet tides analytically, from the tidal potential given in equation (6.27) and using either equation (2.43) or equation (2.44) from Chapter 2, the method is extremely computationally challenging. The importance of planet–planet tides increases greatly with decreasing relative distance between the two bodies. Unfortunately, a direct consequence of this fact is a very high ratio between the semi–major axes $(a_</a_>)$ in the relevant cases and a need for series expansion to high degrees n (see the example in Figure 6.1, calculated by the derived method). The most challenging step in this procedure is the precise evaluation of the prefactor emerging in the definition of Gegenbauer polynomials (equation (6.18)).

Given the limited applicability of the analytical formula for planet–planet tidal heating, especially in comparison with the extreme complexity of such calculation, we do not present results of the analytical method here. Nevertheless, to illustrate the effect of planet–planet heating in the TRAPPIST–1 system (also studied by Hay and Matsuyama, 2019), we implement the loading by a second planet to the numerical model presented later in Chapter 7. The illustration given in Figures 6.2 is calculated for the same[2] model parameters as considered by Hay and Matsuyama (2019) in the low–viscosity regime: the planets are considered as homogeneous spheres governed by the Maxwell rheology, with average rigidity $\mu = 50\,\mathrm{GPa}$ and average viscosity $\eta = 10^{14}\,\mathrm{Pa\,s}$. The colour scale of the graph corresponds to the logarithm of the average heat rate due to planet–planet tides, compared to the heat generated by star–planet tides. Averaging in the numerical model was performed over the last orbital period for the star–planet tides and over the last conjunction period for the planet–planet tides.

The main feature that we may notice in Figures 6.2 is the relatively higher importance of tidal heating induced by an inner perturber, than the dissipation caused by an outer perturber. The relative effect of mutual tides between pairs of neighbouring planets is comparable among the two bodies. As was also observed

[2]However, contrary to Hay and Matsuyama (2019), we also include the effect of orbital eccentricity in planet–planet tidal loading.

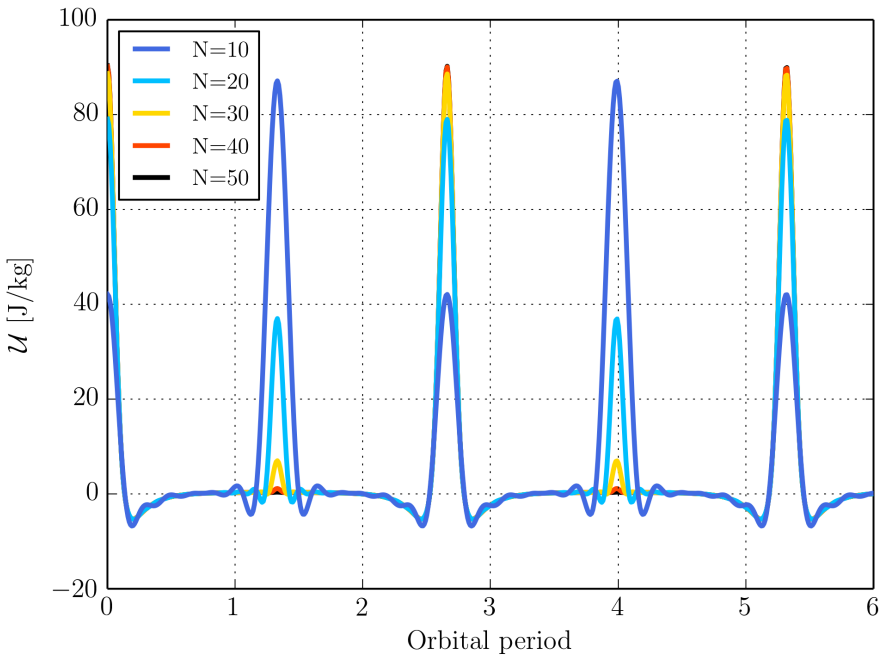

Figure 6.1: Tidal potential sensed by TRAPPIST–1 b due to the gravitational action of planet c, as calculated by the derived method. The period of mutual conjunctions is $\sim$ 2.65 orbital periods of the inner planet. Different colours correspond to different cutoff values N of the index n in the expansion (6.27). Note the artificial maxima at half the conjunction periods, emerging at lower–degree expansions.

by Hay and Matsuyama (2019) and pointed out by Wright (2018), the greatest role is played by planet–planet tides on planet g, especially due to the action of planet f. Given the relatively low orbital eccentricity $e_g = 0.002$, this result is not unexpected. In concordance with the results of Hay and Matsuyama (2019), the planet–planet tidal heating in this low–viscosity case is 19% of the heating induced by the host star, and it may present relatively important contribution to the planet's heat budget ($\sim$ 1 TW).

6.4 Concluding remarks

The tidal interaction between neighbouring planets in tightly packed systems may play an important, yet not fully understood role in the dynamics of planetary interiors and surface or subsurface oceans. Specifically, in the case of subsurface oceans, the tidal response may depend strongly on the loading frequencies (Hay et al., 2020). In this chapter, we tried to find a link between the traditional Darwin–Kaula expansion for the tidal potential (Kaula, 1961, 1964, or Section 1.3.2) and an accordingly derived expansion for the planet–planet tidal potential. On the one hand, such a derivation provides an insight into the parameter dependencies of the

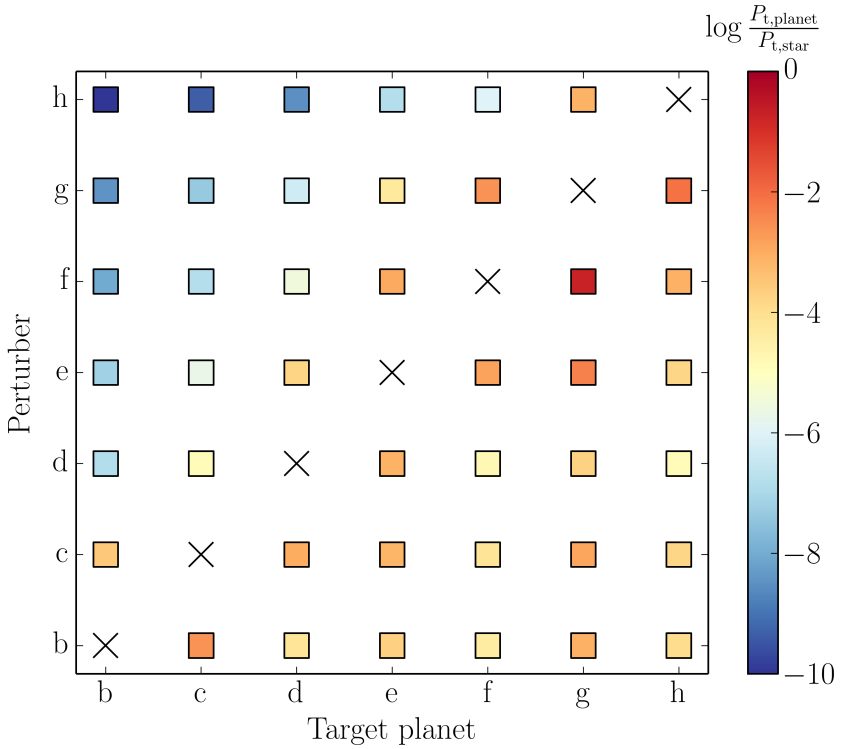

Figure 6.2: The magnitude of planet–planet tidal heating in the TRAPPIST–1 planets, compared to the tidal heating induced by the host star. Mantle viscosity of all planets was set to 10^{14} Pa s. Tidal heating was calculated by the numerical model *Andy*, assuming Maxwell rheology (see Chapter 7).

potential and provides us with the coefficients and frequencies of the Fourier modes without having to calculate the Fourier transform numerically. On the other hand, the resulting expression for the tidal potential (equation (6.27)) as well as for the algebraic prefactors $\mathcal{F}^0_{lmn\bar{p}}$ (equation (6.23)) is extremely complex—even in the simple, coplanar case considered here. The same is also true for the planet–planet tidal torque, that can potentially contribute to the planet's physical libration. Therefore, in most practical cases, it is more convenient to prefer numerical models of these phenomena.

7. Tidal effects in differentiated viscoelastic bodies: a numerical approach

The entire chapter was adapted from Walterová and Běhounková (2017). Notation introduced in the text may differ from the convention used in the rest of the work.

In the previous chapters, we have studied the thermal and orbital evolution of viscoelastic planets using analytical or semi–analytical methods. Now, in the last chapter of this work, we will discuss an alternative approach, making use of the spherical harmonic decomposition and of the finite differences for the *numerical* calculation of the deformations and tidal heating in a viscoelastic continuum. As was the case with Chapter 6, the present study also constitutes an independent piece of work and it should be understood as an alternative—rather than a complement—to the previously discussed analytical approach.

The importance of analytical models lies in their ability to effectively parameterise and explore the main features of tidal evolution. Appropriate parameterisation enables utilisation of effective and precise time schemes for the computation of long–term processes, including the secular variations in orbital parameters. Most analytical models of tides are, however, describing the planet as a homogeneous or only radially–stratified sphere. If we are interested in the effects of possibly laterally–stratified internal structure on the tidal deformation and internal heating, it is necessary to proceed to numerical simulations. As a recent example, Frouard et al. (2016) presented a general numerical model of tides on viscoelastic bodies described by the Kelvin–Voigt rheology. Their approach is based on an N–body simulation of gravitating particles connected together in a spring–dashpod network, and therefore represents an alternative to our method.

In this chapter, we introduce a numerical model enabling the computation of the tidal torque and the tidal heating inside of a possibly nonhomogeneous mantle of rocky exoplanets. The model of a viscoelastic mantle governed by either the Maxwell or the Andrade rheology is described in Section 7.1, with further details on the numerical scheme provided in Appendix D.1. Section 7.2 is dedicated to the parameter dependence of tidal torque, with qualitative comparison of our results for the Maxwell model with the work of Correia et al. (2014). In Section 7.3 we present a parameter study of tidal heating, showing a substantial difference between the predictions of both rheological models (the Maxwell and the Andrade model). Finally, the two traditional tidal parameters—the Love number k and the phase lag ε—are discussed in Section 7.4.

7.1 Model

The model planet is a spherical body composed of a solid inner core, liquid outer core and a viscoelastic mantle, described either by the Maxwell or the Andrade rheology. We compute the deformation and stress field solely inside of the mantle, which is assumed to be incompressible and hydrostatically prestressed, and neglect the deformations and dissipation in the core, as well as the core–mantle friction. For the sake of simplicity, we also neglect the tides raised by the planet on the host star.

If the deformations are small compared to the overall size of the body, we may use the linear approximation and write the Eulerian governing equations, representing the mass conservation and the linear momentum conservation (neglecting inertia), as (Tobie et al., 2008; Běhounková et al., 2015; Souček et al., 2016)

$$\nabla \cdot \mathbf{u} = 0\,, \tag{7.1}$$

$$-\nabla\pi + \nabla \cdot \mathbf{D} = -\rho_{\mathrm{M}}\,\mathbf{f}\,, \tag{7.2}$$

with a constitutive equation

$$2\varepsilon = \frac{1}{\mu}\mathbf{D} + \int_0^t \frac{1}{\eta}\mathbf{D}(t')\,\mathrm{d}t' + \int_0^t \mu^{\alpha-1}\left(\frac{t-t'}{\zeta\eta}\right)^{\alpha}\dot{\mathbf{D}}(t')\,\mathrm{d}t' \tag{7.3}$$

and linearised boundary conditions expressing the force equillibrium on the undeformed boundaries (e.g. Souček et al., 2016)

$$(-\pi\mathbf{I} + \mathbf{D}) \cdot \mathbf{e}_{\mathrm{r}} + u_{\mathrm{r}}\,\rho_{\mathrm{M}}\,g_{\mathrm{s}}\,\mathbf{e}_{\mathrm{r}} = \mathbf{0} \qquad \text{on the upper boundary} \tag{7.4}$$

and

$$(-\pi\mathbf{I} + \mathbf{D}) \cdot \mathbf{e}_{\mathrm{r}} - u_{\mathrm{r}}\,(\rho_{\mathrm{C}} - \rho_{\mathrm{M}})\,g_{\mathrm{b}}\,\mathbf{e}_{\mathrm{r}} = -\rho_{\mathrm{C}}\,\mathcal{U}\,\mathbf{e}_{\mathrm{r}} \tag{7.5}$$

on the lower boundary.

Here, $\mathbf{u}$ is the displacement vector, $\varepsilon = \frac{1}{2}(\nabla\mathbf{u} + \nabla^T\mathbf{u})$ stands for the incremental strain tensor, π and $\mathbf{D}$ are the isotropic and the deviatoric parts of the incremental Cauchy stress tensor, $\mathbf{f} = \nabla\mathcal{U}$ represents the body force per unit mass, η and μ are the viscosity and the rigidity (shear modulus) of the mantle, respectively, and α and ζ are empirically given parameters of the Andrade rheology. For the boundary conditions, ρ_{C} is the density of the liquid outer core, ρ_{M} denotes the density of the mantle, g_{s} and g_{b} are the mean gravity accelerations on the upper and the lower boundary, $\mathbf{I}$ is the identity matrix, $\mathbf{e}_{\mathrm{r}}$ is the radial unit vector and $u_{\mathrm{r}} = \mathbf{u} \cdot \mathbf{e}_{\mathrm{r}}$ represents the radial component of the displacement.

Equation (7.3) in general holds for the Andrade rheology: its first term represents the instantaneous elastic reaction, while the other two terms account for the viscous and the anelastic creep, respectively. A constitutive equation for the linear Maxwell rheology can be obtained by excluding the last term, that is

$$2\varepsilon = \frac{1}{\mu}\mathbf{D} + \int_0^t \frac{1}{\eta}\mathbf{D}(t')\,\mathrm{d}t'\,. \tag{7.6}$$

The body force $\mathbf{f}$ (and accordingly the potential $\mathcal{U}$) in our model consists of three parts: the tidal force $\mathbf{f}_{\rm t}$ due to the host star, the centrifugal force $\mathbf{f}_{\rm cf}$ due to planet rotation and the self–gravity $\mathbf{f}_{\rm self}$ induced by the tidal deformation. First, we will focus on the tidal force. The model planet with mass m orbits a star with mass m_* and its orbit is described by the semi–major axis a and the eccentricity e. The star is considered spherical and the planet's obliquity is, for the sake of simplicity, assumed to be zero. At each instant of time, the tidal force acting on a unit volume with planetocentric coordinates $\mathbf{r}' = (r', \vartheta', \varphi')$ due to a disturbing body at coordinates $\mathbf{r} = (r, \vartheta_*, \varphi_*)$ can be written as

$$\mathbf{f}_{\rm t}(r', \vartheta', \varphi') = \sum_{lm} f_{lm}^{l-1}(r') \mathbf{Y}_{lm}^{l-1}(\vartheta', \varphi') \,, \tag{7.7}$$

where $\mathbf{Y}_{lm}^{l-1}$ are vector spherical harmonics (see Appendix D.2 or e.g. Varshalovich et al., 1988) and coefficients f_{lm}^{l-1} are given by

$$f_{lm}^{l-1}(r') = \frac{\mathcal{G} m_*}{r^2} \, 4\pi \sqrt{\frac{l}{2l+1}} \left(\frac{r'}{r}\right)^{l-1} \bar{Y}_{lm}(\vartheta_*, \varphi_*) \,, \tag{7.8}$$

with $\mathcal{G}$ being Newton's gravitational constant and bar above Y_{lm} symbolising complex conjugation. The instantaneous distance of the planet from the star is $r = a(1 - e\cos E(t))$ and the eccentric anomaly $E(t)$ is obtained from the iteratively solved Kepler equation. Similarly, the tidal potential can be decomposed into spherical harmonics as

$$\mathcal{U}_{\rm t}(r', \vartheta', \varphi') = \sum_{lm} v_{lm}(r') Y_{lm}(\vartheta', \varphi') \tag{7.9}$$

with coefficients

$$v_{lm}(r') = \frac{\mathcal{G} m_*}{r} \frac{4\pi}{2l+1} \left(\frac{r'}{r}\right)^{l} \bar{Y}_{lm}(\vartheta_*, \varphi_*) \,. \tag{7.10}$$

The centrifugal force and the centrifugal potential depend on the rotational frequency of the planet $\Omega_{\rm rot}$ through

$$\mathbf{f}_{\rm cf}(r', \vartheta', \varphi') = \frac{\sqrt{16\pi}}{3} \, \Omega_{\rm rot}^2 r' \, \mathbf{Y}_{00}^1(\vartheta', \varphi') + \frac{\sqrt{8\pi}}{3} \, \Omega_{\rm rot}^2 r' \, \mathbf{Y}_{20}^1(\vartheta', \varphi') \tag{7.11}$$

and

$$\mathcal{U}_{\rm cf}(r', \vartheta', \varphi') = -\sqrt{\frac{4\pi}{9}} \, \Omega_{\rm rot}^2 (r')^2 \, Y_{00}(\vartheta', \varphi') + \sqrt{\frac{4\pi}{45}} \, \Omega_{\rm rot}^2 (r')^2 \, Y_{20}(\vartheta', \varphi'). \tag{7.12}$$

Finally, using the Helmert's method of condensation (Helmert, 1884), the effect of self–gravity inside of the homogeneous mantle is introduced by

$$\begin{aligned} \mathbf{f}_{\rm self}(r', \vartheta', \varphi') = 4\pi\mathcal{G} \, \sum_{lm} \Bigg\{ & \sqrt{\frac{l+1}{2l+1}} \left(\rho_{\rm C} - \rho_{\rm M}\right) (u_{\rm r}^{\rm b})_{lm} \left(\frac{r_{\rm b}}{r'}\right)^{l+2} \mathbf{Y}_{lm}^{l+1}(\vartheta', \varphi') + \\ & + \sqrt{\frac{l}{2l+1}} \, \rho_{\rm M} \, (u_{\rm r}^{\rm s})_{lm} \left(\frac{r'}{r_{\rm s}}\right)^{l-1} \mathbf{Y}_{lm}^{l-1}(\vartheta', \varphi') \Bigg\} \,, \end{aligned} \tag{7.13}$$

where indices "b" and "s" denote the lower and the upper boundary, respectively, and $(u_\mathrm{r})_{lm}$ are spherical harmonic coefficients of the radial component of displacement, related to the coefficients of displacement vector u^n_{lm} at any radius r' by

$$(u_\mathrm{r})_{lm} = \sqrt{\frac{l}{2l+1}}\, u^{l-1}_{lm}(r') - \sqrt{\frac{l+1}{2l+1}}\, u^{l+1}_{lm}(r')\,. \tag{7.14}$$

For the corresponding additional potential, we have

$$\begin{aligned} &\mathcal{U}_\mathrm{self}(r',\vartheta',\varphi') = \\ =&4\pi\mathcal{G}\sum_{lm}\frac{1}{2l+1}\left\{r_\mathrm{b}\big(\rho_\mathrm{C}-\rho_\mathrm{M}\big)(u^\mathrm{b}_\mathrm{r})_{lm}\left(\frac{r_\mathrm{b}}{r'}\right)^{l+1} + r_\mathrm{s}\,\rho_\mathrm{M}\,(u^\mathrm{s}_\mathrm{r})_{lm}\left(\frac{r'}{r_\mathrm{s}}\right)^{l+1}\right\}Y_{lm}(\vartheta',\varphi')\,. \end{aligned} \tag{7.15}$$

The set of partial differential equations (7.1)—(7.3) is solved directly in the time domain. We use an extension of the tool described and employed in Tobie et al. (2008) and Běhounková et al. (2015) and implemented by prof. Ondřej Čadek. For the spatial discretisation, we use a spherical harmonic decomposition in the lateral directions and a staggered finite difference scheme in the radial direction. The mantle is decomposed into 95 layers and the maximum degree of spherical harmonic decomposition is set to $l = 5$. For an evaluation of the tidal torque alone it would be sufficient to assume $l = 2$; the numerical computation of the tidal heating, however, requires higher values of l. In order to include the self–gravity term correctly, we calculate the memory terms of constitutive equation (7.3) or (7.6), and thus the coefficients of u_r as well, iteratively in each time step. The time scheme is described in Appendix D.1. Depending on the considered viscosity, we evaluate the tidal torque and the tidal dissipation hundred or thousand times per orbit. Typical timestep for the model planet described in Table 7.1 is therefore $\Delta t = 10^{-3}$ or $\Delta t = 10^{-4}$ years.

Additionally, before we start the computation itself, it is necessary to choose appropriate set of initial conditions. The time integration is then performed from these conditions until a relaxed solution is found. We consider the solution as relaxed when the changes in the average tidal dissipation or tidal torque over one orbital period become negligible (see Běhounková et al., 2010). Naturally, our desire is to choose such set of initial strains and stresses, from which the relaxed solution is found as fast as possible. We seek the suitable initial conditions by analyzing the tidal potential. Each mode of the tidal potential consists of two parts: the first, which is constant in time, and the second, with short–term or long–term variations in the orbit (compare with the Fourier series of Kaula, 1964). Under our assumption of zero obliquity, the zonal modes ($m = 0$) always involve a nonzero constant term due to the gravitational field of the host star and the centrifugal acceleration caused by the planetary rotation. The sectoral modes ($m = l$), on the other hand, are generally strictly time dependent and their constant term only becomes nonzero in the spin–orbit resonances.

For this reason and in order to improve the rate of convergence of the solution, two kinds of initial conditions were used for our computations. Outside of the

spin-orbit resonances we assume that the coefficients of sectoral modes for both the deformation and the internal stresses are initially zero. When considering a tidally locked planet or the zonal modes, however, we first precompute a fast converging "fluid limit", i.e. the relaxed shape and stresses corresponding to a low–viscosity body influenced solely by the constant part of the tidal potential. The computation for the actual viscosity then proceeds from these results, which naturally include nonspherical shape of the body—a hydrostatical shape acquired under the constant part of the potential.

With the stress and strain tensors converged and given, we may proceed to the computation of tidal heating and tidal torque. The average rate of tidal dissipation over a time interval T is computed as

$$P = \frac{1}{T} \int_V \int_t^{t+T} \dot{\varepsilon}(\tau) : \mathbf{D}(\tau) \, \mathrm{d}\tau \, \mathrm{dV} \,, \tag{7.16}$$

where V represents the volume of the planetary mantle and $\dot{\varepsilon}$ is the strain rate tensor. Only in a special case of the Maxwell rheology we may compute the dissipation rate directly as (see e.g. Hanyk et al., 2005)

$$P = \frac{1}{T} \int_V \int_t^{t+T} \frac{\mathbf{D}(\tau) : \mathbf{D}(\tau)}{2\eta} \, \mathrm{d}\tau \, \mathrm{dV} \,. \tag{7.17}$$

To compare the shape of our numerical results with a semi–analytical solution, we re–derive a formula for the tidal heating of a homogeneous spherical body based on the equations (10)—(12) of Segatz et al. (1988). Discretising the time integral and using the Parseval's theorem for the discrete Fourier transform (DFT), one gets

$$P = \frac{5}{8\pi^2} \, \frac{n_{\mathrm{orb}} \Delta t}{\mathcal{G} \, r_{\mathrm{s}} \, N} \int_S \sum_{i=0}^{N-1} \frac{\mathrm{Im}\{\bar{k}_2(\omega_i)\}}{\omega_i} \, |\xi_i|^2 \, \mathrm{d}S \,, \tag{7.18}$$

where n_{orb} is the mean motion, ω_i are tidal frequencies, $\bar{k}_2$ is a frequency–dependent complex Love number of degree 2 and ξ_i are DFT coefficients of $\frac{\partial \mathcal{U}_{\mathrm{t}}}{\partial t}$. Time derivatives of the tidal potential are computed numerically with a timestep Δt at N points in the orbit. The complex Love number is defined e.g. in Castillo-Rogez et al. (2011) in correspondence with the static Love number as

$$\bar{k}_2(\omega) = \frac{3}{2} \frac{\bar{J}(\omega)}{\bar{J}(\omega) + \frac{57}{8\pi\mathcal{G}\rho^2 r_{\mathrm{s}}^2}} \,, \tag{7.19}$$

where ρ is the mean density of the planet and $\bar{J}(\omega)$ signifies the complex compliance. Relation (7.19) is valid as long as we remain in the linear approximation. The compliance of a material described by the Andrade rheology can be expressed as (Castillo-Rogez et al., 2011)

$$\bar{J}(\omega) = \frac{1}{\mu} - \frac{\mathrm{i}}{\eta\omega} + \frac{1}{\mu(\mathrm{i}\zeta\tau_{\mathrm{M}}\omega)^{\alpha}} \, \Gamma(1+\alpha) \,, \tag{7.20}$$

with $\tau_{\rm M} = \frac{\eta}{\mu}$ representing the Maxwell time and $\Gamma(x)$ being the Gamma function. The compliance of the Maxwell model is obtained by dropping the last term in the expression.

In order to assess the tidal torque acting on the model planet, we first need to evaluate the disturbing force due to the tidal bulge, i.e. due to the deformation of both upper and lower boundary. At the position of the host star, the disturbing force is given by

$$\mathbf{f}_{\rm dist}(r, \vartheta_*, \varphi_*) = \sum_{lm} \left[\zeta^{\rm b}_{lm} \left(\frac{r_{\rm b}}{r} \right)^{l+2} + \zeta^{\rm s}_{lm} \left(\frac{r_{\rm s}}{r} \right)^{l+2} \right] \mathbf{Y}^{l+1}_{lm}(\vartheta_*, \varphi_*) \,, \tag{7.21}$$

with coefficients

$$\zeta^{\rm b}_{lm} = 4\pi \sqrt{\frac{l+1}{2l+1}}\, \mathcal{G} \left(\rho_{\rm C} - \rho_{\rm M} \right) (u^{\rm b}_{\rm r})_{lm} \qquad \text{and} \qquad \zeta^{\rm s}_{lm} = 4\pi \sqrt{\frac{l+1}{2l+1}}\, \mathcal{G}\, \rho_{\rm M}\, (u^{\rm s}_{\rm r})_{lm} \,. \tag{7.22}$$

The tidal torque acting on a unit mass of the planet due to the star at a distance $\mathbf{r}$ is then

$$\mathcal{T} = \mathbf{r} \times \mathbf{f}_{\rm dist} \,. \tag{7.23}$$

We apply the model on an Earth–size terrestrial planet orbiting a low–mass star (see Table 7.1) and study the tidal effects as a function of the eccentricity, the mantle viscosity, the spin-orbit ratio and the rheological model.

Table 7.1: Model parameters

Parameter	Definition	Value
a	Semi-major axis	0.1 AU
e	Eccentricity	0.0 to 0.5
m_*	Mass of the host star	0.1 $m_\odot$
$\rho_{\rm M}$	Density of the mantle	$5000\,\mathrm{kg \cdot m^{-3}}$
$\rho_{\rm C}$	Density of the liquid outer core	$9000\,\mathrm{kg \cdot m^{-3}}$
$\rho_{\rm I}$	Density of the inner core	$12000\,\mathrm{kg \cdot m^{-3}}$
$r_{\rm s}$	Planetary radius	6370 km
$r_{\rm b}$	Radius of the core–mantle boundary	3890 km
$r_{\rm I}$	Inner core radius	1200 km
μ	Mantle rigidity	200 GPa
η	Mantle viscosity	10^{14} to 10^{24} Pa s
α	Parameter of the Andrade model	0.3
ζ	Parameter of the Andrade model	1

7.2 Tidal torque

Evolution of the planetary spin rate is driven by the tidal torque, given by the equation (7.23). This torque causes the planet rotation to decelerate when negative and to accelerate when positive. A long–term stability of the spin state requires zero average tidal torque and a distinct shape of its dependence on the spin-orbit ratio (see Figures 7.1 and 7.2): the function is above zero to the left from the stable state and below zero to the right. We employ the numerical model to compute the secular tidal torque acting on a deformed planetary body with a highly eccentric orbit ($e = 0.4$). The choice of this particular eccentricity is motivated by a qualitative comparison of our results with the analytical study of Correia et al. (2014).

Figure 7.1 shows the frequency dependence of the average tidal torque for a body described by the Maxwell rheology, Figure 7.2 is the average torque for the Andrade rheology. Individual plots illustrate distinct rheological regimes of the planet, given by the mantle viscosity and the orbital period, which is held constant at $T_{\rm orb} = 0.1\,$yrs. The two different sets of viscosities were chosen in order to evaluate the tidal effects in a broad range of realistic terrestrial exoplanets. While the tidal viscosity in the Andrade model could be identified with the same parameter in the mantle convection problems, the viscosity in the Maxwell model should be understood rather as an effective value for the tidal deformation, which correctly predicts the tidal heating in rocky bodies, mimicking the dissipation in the Andrade model (Běhounková et al., 2010, 2013). The effective tidal viscosity is introduced as a frequency–dependent quantity and in the case of terrestrial planets loaded at high frequencies is up to few orders lower than the standard viscosity. Here, we neglect its frequency dependence and consider it a parameter.

The first picture (upper left corner on both figures) represents the low–viscosity regime ($\eta = 1.4 \times 10^{16}\,$Pa s) with only one stable spin state. Such a system would evolve toward pseudo–synchronisation, as predicted by the constant time lag theories (Darwin, 1880; Alexander, 1973; Mignard, 1979; Ferraz-Mello et al., 2008), with spin-orbit ratio given by $\Omega/n = 1 + 6e^2 + O(e^4)$. When we increase the viscosity of the mantle, the shape of the function becomes more complex and multiple stable spin states arise, associated with the spin-orbit resonances. This pattern is consistent with predictions of rheologically–motivated analytical studies, such as Ferraz-Mello (2013), Correia et al. (2014) and Ferraz-Mello (2015). Finally, in a purely elastic case, the average tidal torque would be zero for every rotational frequency.

7.3 Tidal heating

Conclusions of the previous section can be compared with the spin–orbit ratio dependence of average tidal heat rate, depicted in Figures 7.3 and 7.4. For the sake of consistency, we keep the high eccentricity of the orbit, i.e. $e = 0.4$, constant orbital period, $T_{\rm orb} = 0.1\,$yrs, and the same range of viscosities for both models. The most striking feature of the figures is a significant difference

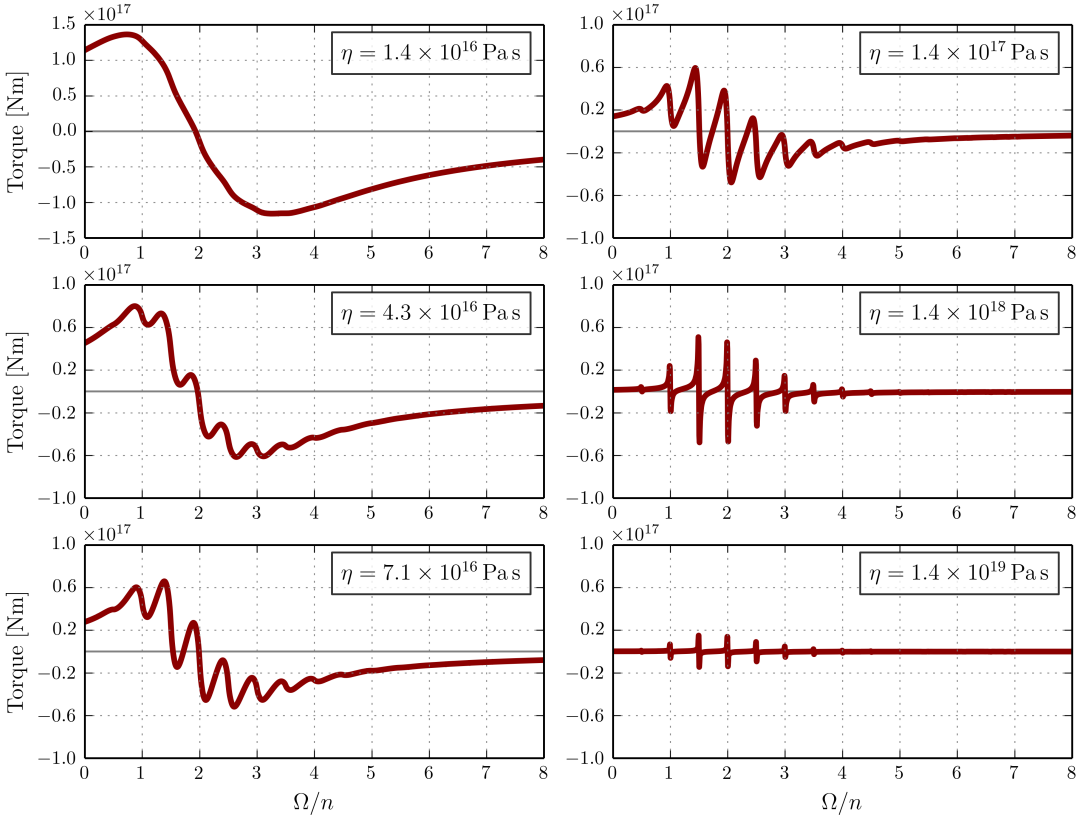

Figure 7.1: Average tidal torque as a function of the spin–orbit ratio for six different viscosities in the Maxwell rheological model. The orbital eccentricity was set to $e = 0.4$ (cf. Correia et al., 2014).

between the magnitude of tidal heating in the Maxwell and the Andrade model at high frequencies (high spin–orbit ratios). Specifically, the power produced in the Andrade model increases with higher spin–orbit ratios and acquires values much higher than observed around the synchronous rotation ($\Omega/n = 1$). The overall shape of the spin–orbit ratio dependence of tidal heating in the Andrade case remains similar for all mantle viscosities.

Another distinction between the two models lies in the shape of local minima. Similarly to the tidal torque with its sole stable spin state at low viscosity, there is only one local minimum in the viscous regime ($\eta = 1.4 \times 10^{16}$ Pa s) and multiple minima elsewhere, typically associated with low spin–orbit resonances. The local minima of the Maxwell model get gradually deeper and narrower as we increase the viscosity of the mantle and their depths differ, depending on the orbital eccentricity (Figure 7.5). In the Andrade model, on the other hand, local minima remain shallow and broad, disappearing eventually at high mantle viscosities ($\eta > 1.4 \times 10^{19}$ Pa s). Further increase in viscosity ($\eta = 1.4 \times 10^{22}$ Pa s) leads the planet close to the elastic regime with only one global minimum, similar to the global minimum in viscous regime.

At this point we should note that the planet on eccentric orbit is tidally loaded

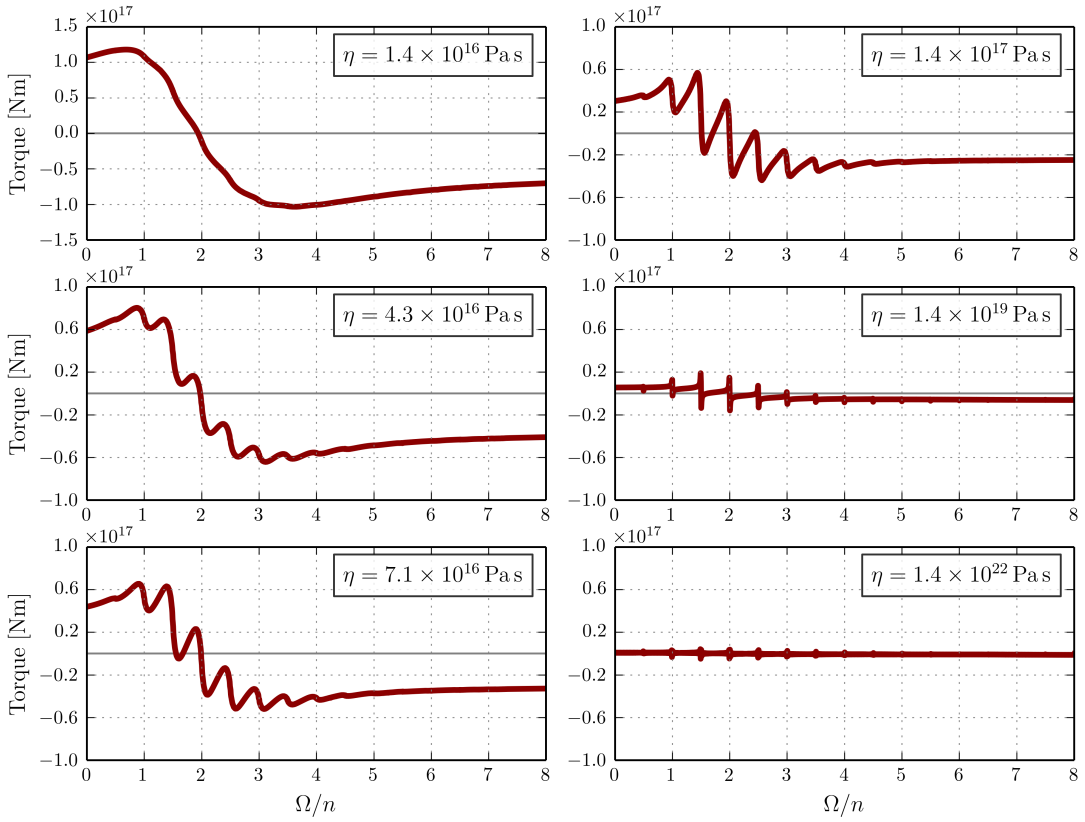

Figure 7.2: Average tidal torque in the Andrade rheological model. The orbital eccentricity was set to $e = 0.4$.

at a range of frequencies, and while it responds as an elastic body at one frequency, it can still be far from elasticity at another frequency. The terms "elastic" or "viscous" regime, which we use throughout this study, refer to the highest or the lowest value of considered mantle viscosities (see Table 7.1). A purely elastic body would, in reality, dissipate no energy, independently of the spin–orbit ratio.

A detailed picture of the tidal heating at low spin-orbit ratios (bounded by the 1:1 and the 5:2 spin-orbit resonance) is presented in Figures 7.5 and 7.6. Here, we compare the results for six orbital eccentricities ranging from $e = 0$ to $e = 0.5$ and three different viscosities in both rheological models: 10^{16}, 10^{18} and 10^{20} Pa s in the Maxwell model and 10^{16}, 10^{20} and 10^{24} Pa s in the Andrade model. In the viscous regime ($\eta = 10^{16}$ Pa s) and at low spin–orbit ratios, the Andrade rheology is well approximated by the Maxwell model and the results therefore coincide. Here, we see that the position of the sole local minimum depends on the orbital eccentricity—it tends to higher spin–orbit ratios with more eccentric orbit.

As was mentioned before, the multiple local minima of Maxwell model occur around the spin–orbit resonances. The relative depths of these minima depend on the orbital eccentricity, with the deepest minimum located at the 1:1 spin–orbit resonance of a circular orbit. It is clear that the synchronously rotating, zero

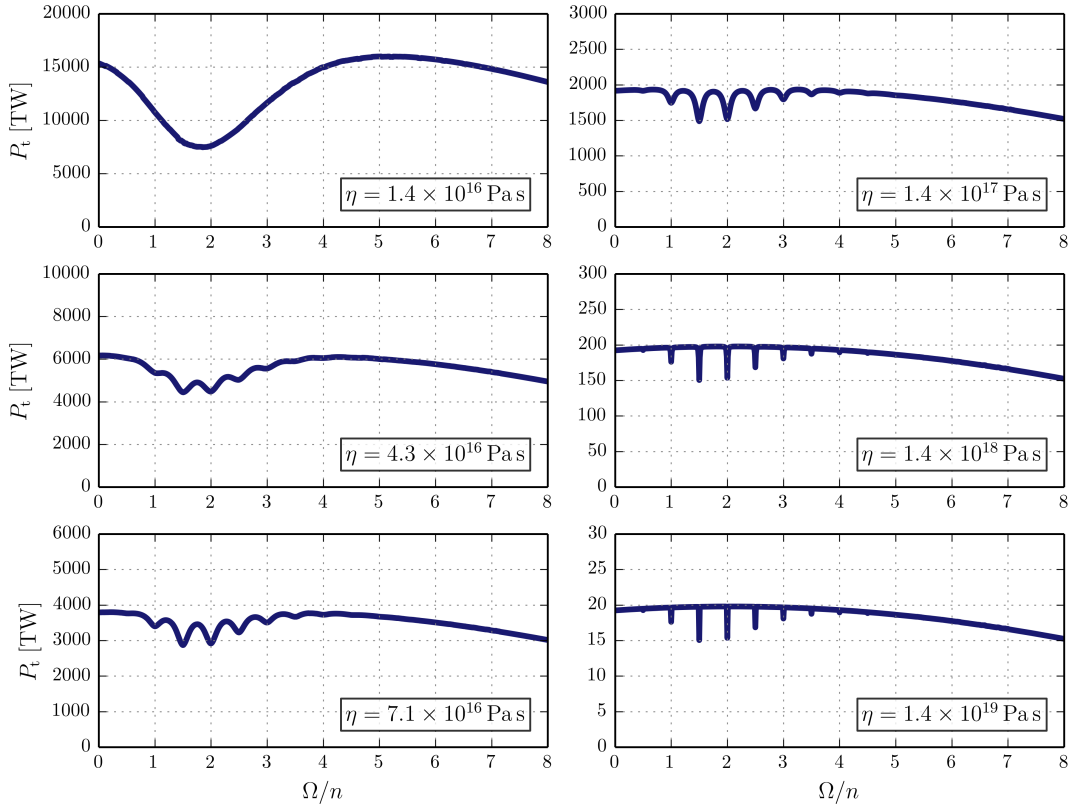

Figure 7.3: Average tidal heating of the model planet presented in Figure 7.1, Maxwell model, $e = 0.4$.

eccentricity planet exhibits no tidal heating, independently on the viscosity, as it remains locked in its sole stable spin state. Generally, the depth of the minima at higher spin–orbit resonances (2:1, 5:2) increases with increasing eccentricity, while the depth of the minima associated with lower resonances (1:1, 3:2) decreases. The tidal heating computed for the Andrade model with higher viscosities follows a functional dependence on the spin–orbit ratio that is very similar to the viscous regime, including the position of the global minimum. The local minima remain broad and shallow for each of the considered eccentricities.

7.4 Love numbers

The additional potential $\delta\mathcal{U}$ due to tidal distortions is related to the tide–raising potential $\mathcal{U}$ via Love number k. In a static case, which is treated as fiducial in the standard theories (Kaula, 1964; Mignard, 1979), the Love number of the l-th mode is a real number, defined as

$$k_l = \frac{\delta U_l}{U_l}\,, \tag{7.24}$$

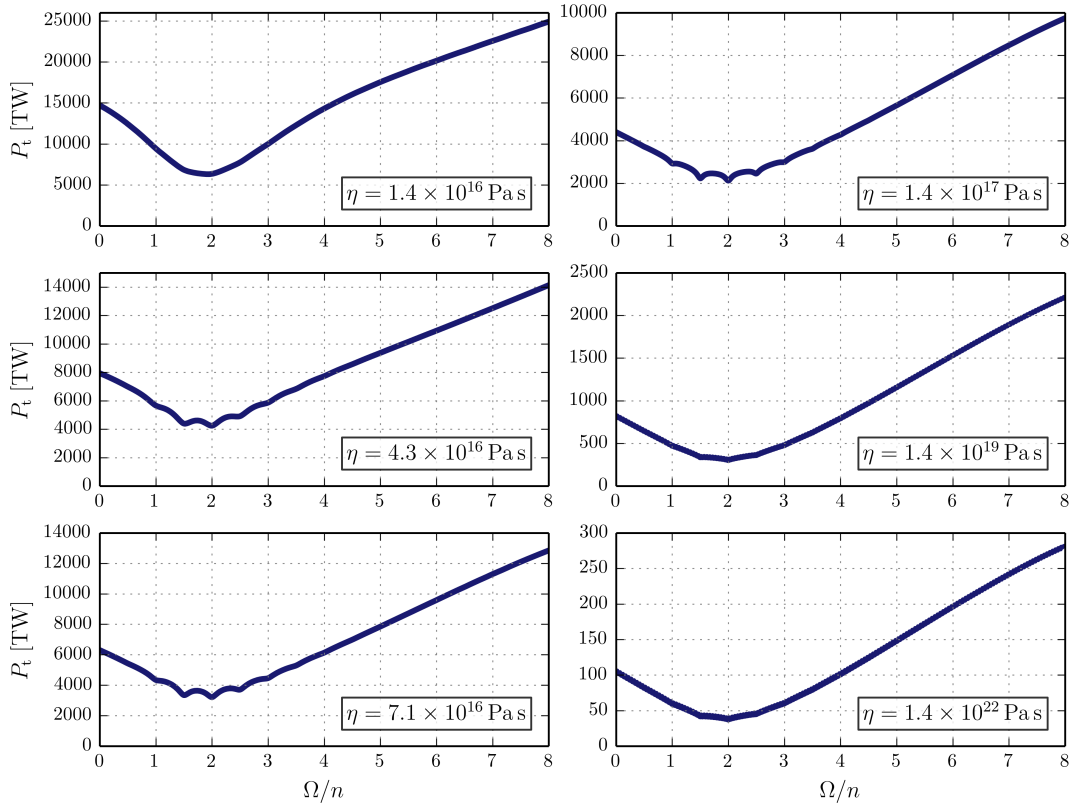

Figure 7.4: Average tidal heating of the model planet presented in Figure 7.2, Andrade model, $e = 0.4$.

where both potentials are evaluated at the surface of non–rotating planet. Each Love number could be equipped with a phase lag or a time lag, mimicking the overall lagging of the rotating physical body. Choice of a particular frequency dependence (or independence) of the phase lag determines the rheology of the planet.

Here, we compute the Love numbers in the time domain as

$$k_{lm}(t) = \frac{\delta v_{lm}(t)}{v_{lm}(t)} = |k_{lm}(t)| e^{-\mathrm{i}\varepsilon_{lm}(t)}\,, \tag{7.25}$$

with $v_{lm}(t)$ and $\delta v_{lm}(t)$ being the spherical harmonic coefficients of the overall potential $\mathcal{U}$ and of the additional potential $\mathcal{U}_{\mathrm{self}}$, respectively, both evaluated at the surface. The phase $\varepsilon_{lm}(t)$ is an angle between the symmetry axes of the two potentials in the time domain. When the order m is nonzero, the coefficients of the potentials are complex, rendering a complex–valued $k_{lm}(t)$ as well. In this special case and considering loading of the mode (l, m) only on one frequency (e.g. a nonsynchronously rotating planet on a circular orbit), the phase $\varepsilon_{lm}(t)$ coincides with the phase lag between the tidal and the additional potential, as traditionally defined in the frequency domain (e.g. Kaula, 1964). To illustrate the

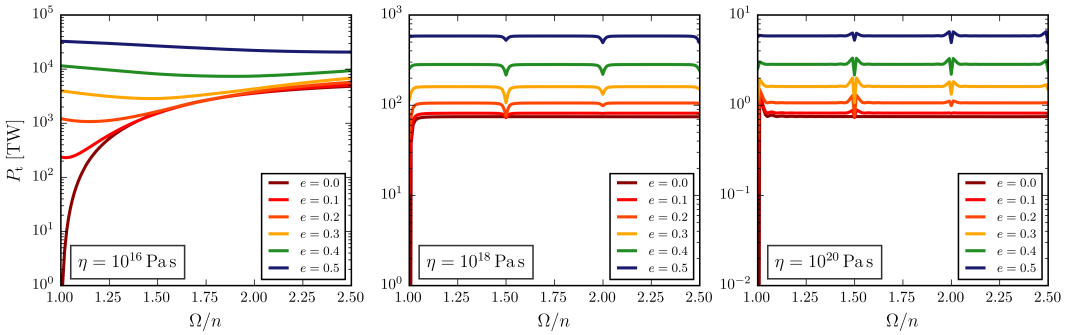

Figure 7.5: Average tidal heating as a function of the spin–orbit ratio computed for the Maxwell rheology. Comparison of tidal heat flow for three different viscosities and six eccentricities.

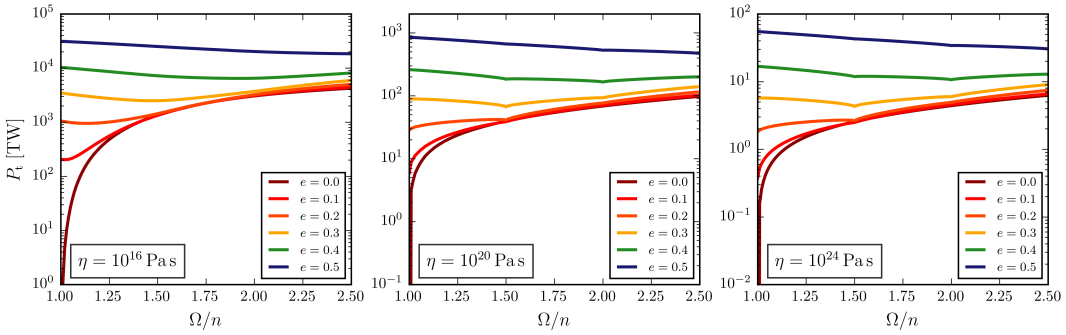

Figure 7.6: Average tidal heating as a function of the spin–orbit ratio computed for the Andrade rheology. Comparison of tidal heat flow for three different viscosities and six eccentricities.

tidal deformation in the two rheological models considered here, we plot the Love numbers $k_{22}(t)$ and $k_{20}(t)$ for two different orbital eccentricities and spin states.

Our first toy–model is a synchronously rotating planet on an eccentric orbit with $e = 0.4$. We evaluate the quantities mentioned above, assuming that the planet behaves either as a Maxwell body with effective viscosities between 10^{15} and 10^{18} Pa s or as an Andrade body with viscosities ranging from 10^{15} to 10^{24} Pa s. Other parameters, including the rigidity of the mantle, are kept constant. Figure 7.7 shows time variations of the tidal phase lag ε_{22}. The tidal deformation in a viscous regime ($\eta = 10^{15}$ Pa s) is properly described by a constant time lag model (e.g. Darwin, 1880; Mignard, 1979; Correia and Laskar, 2010), which prescribes the phase lag as a linear function of the loading frequency. The instantaneous angular velocity of the disturbing body on the planet's sky, in our case, is related to the time derivative of the true anomaly v,

$$\text{freq.} = \Omega_{\rm rot} - \frac{\mathrm{d}v}{\mathrm{d}t}\,, \tag{7.26}$$

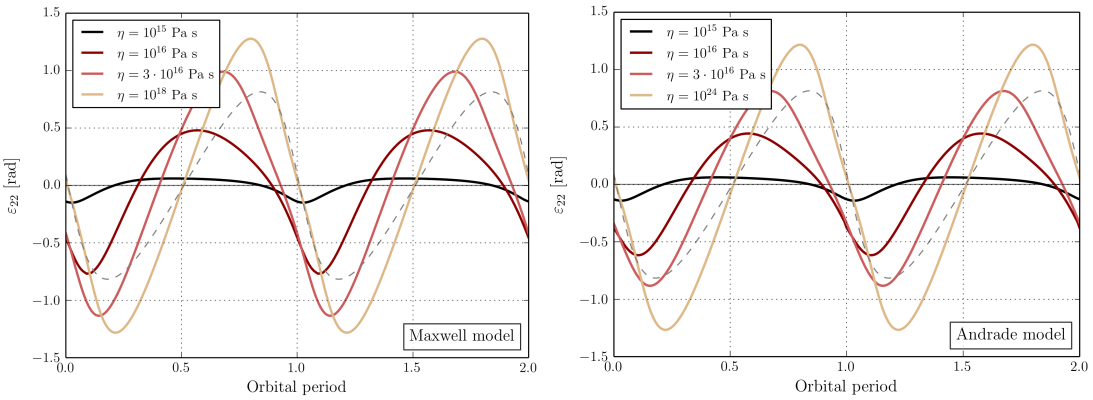

Figure 7.7: Variations of the tidal phase lag $\varepsilon_{22}(t)$ as a function of the mantle viscosity for a model with fixed orbital eccentricity $e = 0.4$. Dashed line indicates planetographic longitude of substellar point.

and this gives the low–viscosity phase lag the shape of its time dependence (black curve in Figure 7.7).

A characteristic feature also arises in the high–viscosity regime, where the relaxation time gets long compared to the orbital period. Here, we initiate the computations in a "fluid limit". The "fluid" tidal bulge, corresponding to the constant part of the tidal potential, virtually freezes at the zero longitude, resulting in a periodically changing nonzero tidal lag (and nonzero instantaneous tidal torque), which follows the geometric libration of the planet. The phase lag is therefore zero, when the planet resides in the periapsis or apoapsis, and—if there were no other components to the tidal bulge—would attain a maximum value of approximately $2 \arcsin e$ (that is ≈ 0.8 in our case, dashed line in Figure 7.7) at a planet–star distance $r = a\sqrt[4]{(1-e^2)}$ (Dobrovolskis, 2007). Another, nonconstant parts of the tidal potential excite the mantle on a variety of frequencies, resulting in an overall tidal lag which differs from the prescribed value and which is here plotted in tan colour.

Figure 7.8 presents the time variations of the magnitudes of the Love numbers $k_{20}(t)$ and $k_{22}(t)$ for the Maxwell (left column) and the Andrade (right column) rheology. Again, we may see that the time variations are small for the viscous limit, when the planet almost perfectly complies with the changing tidal potential, and are large in the high–viscosity regime, when the planet acts like a rigid body. Furthermore, we may see that the mean value of both Love numbers in the low–viscosity case is close to the fluid limit $k = 1.5$. When we increase the viscosity, the relaxation time of the mantle increases as well and it becomes longer than the loading period. The planet then keeps a permanent shape corresponding to the constant part of the potential. In the periapsis, its deformation is smaller than that of a fluid body subjected to the same tidal potential, and the value of $k_{20}(t)$ and $k_{22}(t)$ is substantially lower than 1.5. In the apoapsis, on the other side, the acquired permanent deformation is larger than would correspond to

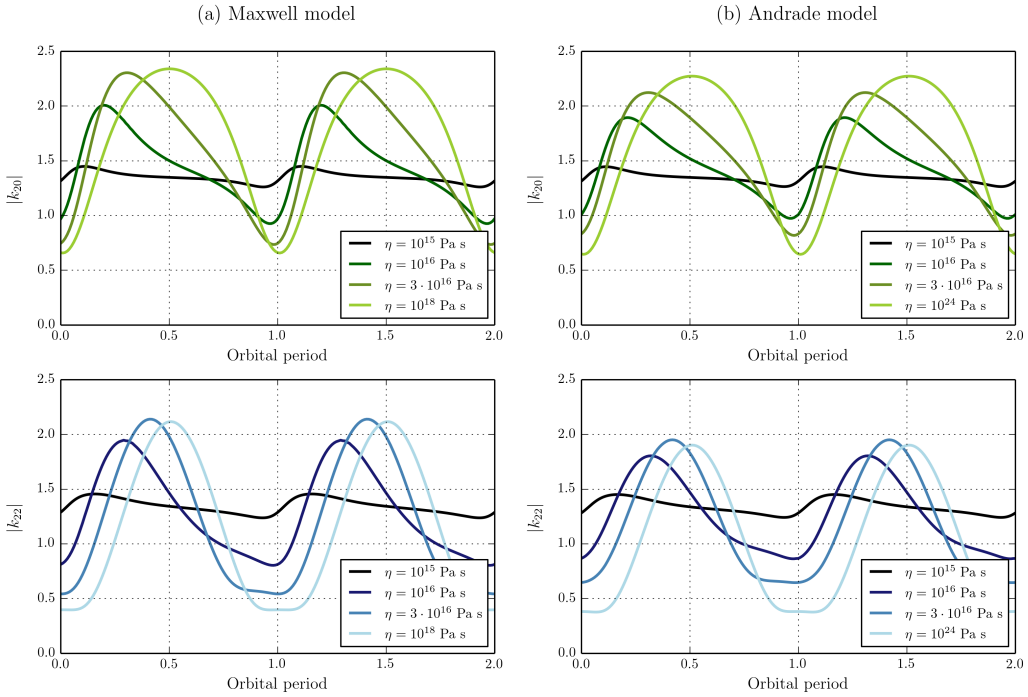

Figure 7.8: Variations of the magnitude of potential Love numbers $|k_{20}(t)|$ and $|k_{22}(t)|$ as a function of mantle viscosity.

the tidal potential, and the Love numbers exceed 1.5. The highest viscosity case ($\eta = 10^{18}$ Pa s in the Maxwell model or $\eta = 10^{24}$ Pa s in the Andrade model), plotted in light green and light blue in Figure 7.8, confronts us with a time dependence of Love numbers that is driven essentially by the variations of the denominator in (7.24).

Our second toy–model is a nonsynchronously rotating planet on a circular orbit. In this case, the magnitude of the Love numbers $k_{20}(t)$ and $k_{22}(t)$ as well as the phase lag $\varepsilon_{22}(t)$ attain a constant value, which is, among other parameters, a function of the tidal frequency and the viscosity. Here, we set the tidal frequency constant ($\Omega/n = 2.1$) and explore the viscosity dependence of the Love number k_{22}. As depicted in Figure 7.9, tidal loading may operate in two extreme regimes, characterising the elastic and the viscous limit with a negligible tidal lag, and in a transitional regime, where the tidal lag attains its maximal value (cf. Love numbers in the analytical model of Correia et al., 2014). At higher viscosities the Love numbers, and especially their phase lags, differ substantially for the two rheologies under considerations. The decrease in the phase lag toward the elastic limit is much more gradual in the case of the Andrade rheology than for the Maxwell rheology. Differences in the magnitude of the Love number are less pronounced.

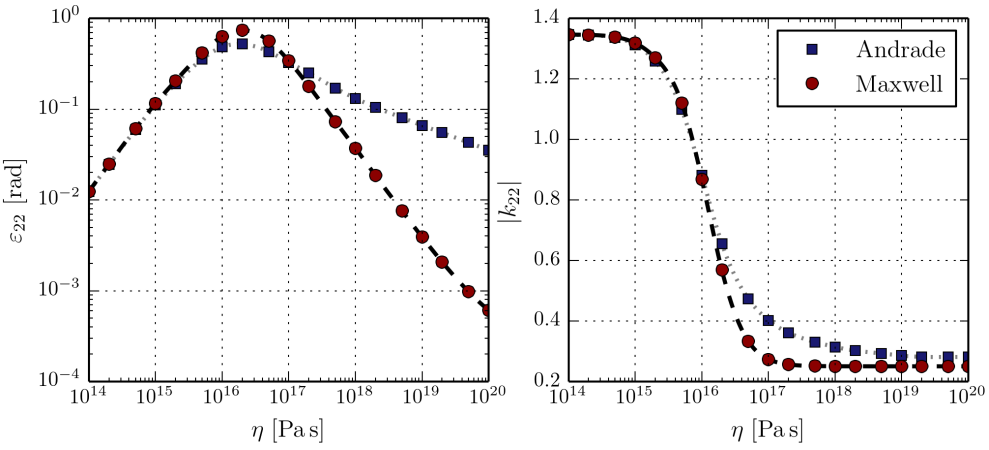

Figure 7.9: The phase lag ε_{22} and the Love number $|k_{22}|$ as a function of the mantle viscosity for a planet on circular orbit rotating nonsynchronously with spin-orbit ratio $\Omega/n = 2.1$. Red dots indicate the Maxwell rheology, blue squares stand for the Andrade rheology.

7.5 Discussion

The thermal and rotational state of close–in exoplanets subjected to significant tidal dissipation is dictated by their orbital elements and the rheological regime. Increase of the orbital eccentricity may enhance the tidal heating by an order of magnitude. Different frequency dependencies of the tidal response in both rheological models in question may lead to a completely different thermal evolution. While a planet governed by the Maxwell rheology attains deep local minima of the tidal heating, associated with the lower spin-orbit resonances, and the dissipation undergone by its interior diminishes as we proceed to higher spin rates, the heat production of a body described by the Andrade model increases with faster rotation and the local minima are observed rather at high spin–orbit resonances. We note that the location and depth of the local minima, as well as the occurence of other tidal effects (e.g. locking into stable spin states), depend not only on the mantle viscosity, but rather on a combination of the viscosity and the tidal frequency. These two parameters together determine the rheological regime of the planet.

The tidal heating depicted in Figures 7.3 to 7.6 would be, in extreme cases, able to melt the entire planetary mantle, leading eventually to a fluid–like behaviour. Furthermore, even in a less extreme scenario, the enhanced heat production combined with possible tidal locking and resulting uneven insolation may alter the planet's rheological regime (due to the temperature dependence of viscosity or due to different deformation mechanisms involved in the mantle dynamics) and lead to decrease or further increase in the tidal dissipation. The tidal evolution of a close–in rocky exoplanet, e.g. its despinning, its thermal history or the rate of orbital evolution, is therefore closely related to its rheological regime, which may, on the contrary, vary with the instantaneous orbital or rotational parameters.

As the tidal heating and the insolation pattern depend on the exact orbital parameters (e.g. Beuthe, 2013; Dobrovolskis, 2013), the rheological structure of realistic close–in exoplanets may become considerably heterogeneous. Tidal locking into a spin–orbit resonance or, specifically, into the synchronous spin state, also leads to a distinct convection pattern (Běhounková et al., 2010; Gelman et al., 2011; van Summeren et al., 2011). The numerical model described here also enables computation of tidal effects in a planet with generally 3d viscosity structure and with possibly radially dependent rigidity. However, in the present parametric studies, we held the mantle viscosity homogeneous and only studied the effects of its varying magnitude, so that the numerical model could be compared with existing analytical tidal theories. Figure 7.1, depicting the spin–orbit ratio dependence of tidal torque in the Maxwell model, was intended to be compared qualitatively with Figure 4 of Correia et al. (2014). Similarly, Figure 7.9 could be identified with Figure 2 of the same paper or with any plot of the dissipation spectrum for the Maxwell and the Andrade rheology (e.g. Castillo-Rogez et al., 2011; Efroimsky, 2012b; Běhounková et al., 2013).

The characteristic pattern of the average tidal torque and the existence of two distinct regimes—a sole pseudo–synchronous rotation of low–viscosity bodies versus multiple stable spin states of high–viscosity spheres—has already been explored and discussed by the authors of recent analytical tidal models (Correia et al., 2014; Ferraz-Mello, 2015). It is worth noting that the rheological regime of the planet is determined not only by its viscosity, but rather by a combination of the viscosity and the excitation frequency. Therefore, even a terrestrial planet may behave as a "fluid" body and a close–in gas giant (a "hot Jupiter") on eccentric orbit may become locked into a nonsynchronous spin–orbit resonance. Both Correia et al. (2014) and Ferraz-Mello (2015) take this into account by introducing a combination of the mean motion and the relaxation time or relaxation factor, which could be related to the mean viscosity of the planet.

Moreover, the number and exact positions of zero points of the average tidal torque are a function of eccentricity. We have particularly presented the case of a highly eccentric orbit with $e = 0.4$. Several other cases, however, can be found in Ferraz-Mello (2015), who studies the stationary spin states for eccentricities ranging from $e = 0$ to $e = 0.5$. The author shows that increase in the eccentricity causes shifting of the sole solution in the low–viscosity case (in concordance with constant time lag models) and increase in the number of solutions in the high–viscosity case. The relative stabilities of particular solutions are affected as well, enabling the prediction of rotation states of moons and planets on eccentric orbits. Ferraz-Mello (2015) also shows that spin-orbit resonances, in contrast to pseudo–synchronous rotation, are not stationary solutions but periodic attractors: a planet on eccentric orbit undergoes physical libration.

In order to compare the numerically obtained tidal heating with a semi–analytical solution, we evaluated the dissipation in a homogeneous sphere subjected to the same tidal potential as in the numerical model. The average heat production due to the tidal dissipation was computed in correspondence with Segatz et al. (1988), where we substituted the frequency independent static Love number k_2

with a set of frequency (and rheology) dependent complex Love numbers, described e.g. in Castillo-Rogez et al. (2011). This was done for both the Maxwell and the Andrade rheology. Resulting tidal heating of a body with $\eta = 10^{18}$ Pa s is shown in Figure 7.10. For the sake of comparison, we also replot Figure 7.9 with the addition of semi–analytically obtained Love numbers $|k_2|$ and phase lags ε_2. Here, it is necessary to point out that the planet in the semi–analytical model is considered a homogeneous sphere, dissipating the energy in the entire volume, whereas our numerical model computes the dissipation solely in the mantle. The tidal heating obtained semi–analytically is therefore several times higher than the numerical predictions. The overall shape of the spin rate dependence of tidal heating is, nevertheless, very similar in both approaches, verifying the applicability of our model.

Similarly, the semi–analytical and the numerical Love numbers (Figure 7.11) tend to different values at the limits of the viscosity scale. This is naturally caused by the presence of a planetary core. Folonier et al. (2015) and Wahl et al. (2017) predict that for a two–layer core–shell model of a fluid planet the surface flattening is always smaller than would correspond to a homogeneous body. Using the equation (41) of Folonier et al. (2015) and approximating our solid-liquid core by a single fluid sphere (as we do not consider the deformation of the inner core), we find the theoretical value of the fluid Love number to be $k_\mathrm{f} \approx 1.349$. This is close to our numerical result, giving $k_\mathrm{f} \approx 1.346$ in the lowest viscosity case ($\eta = 10^{14}$ Pa s). The slight discrepancy can be attributed to different density structure of the core in our study and to the fact that our "lowest viscosity case" is still only an approximation to the real fluid limit.

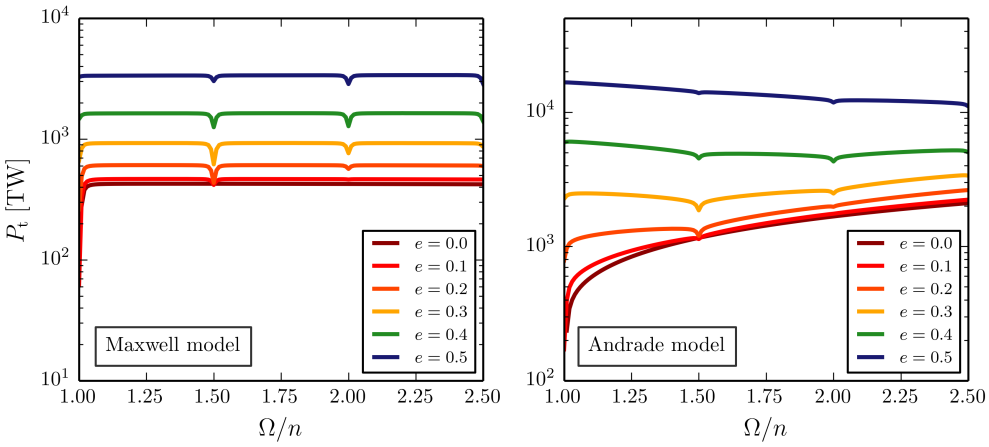

Figure 7.10: Average tidal heating computed semi–analytically for $\eta = 10^{18}$ Pa s and both rheological models.

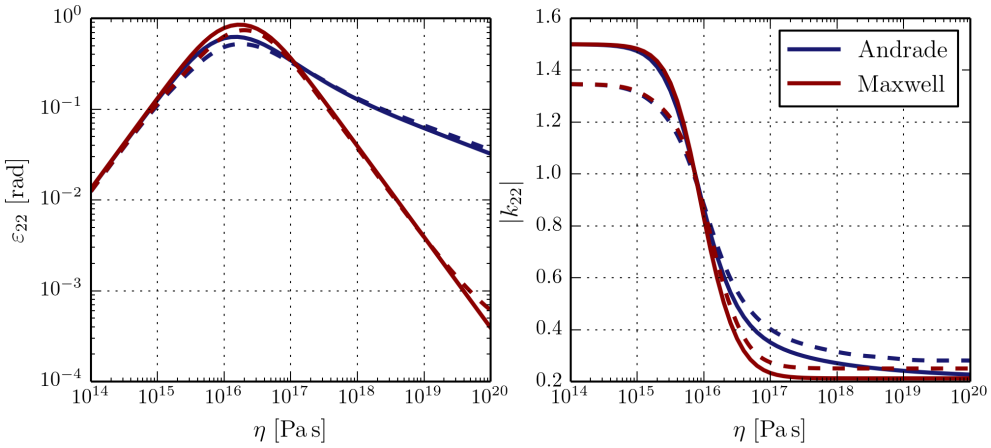

Figure 7.11: Comparison of semi–analytical (solid line) and numerical (dashed line) phase lags and Love numbers for a planet on circular orbit with spin–orbit ratio $\Omega/n = 2.1$.

7.6 Concluding remarks

In this chapter, we presented a numerical model of tides based on the direct solution of the continuum mechanics equations for a disturbed planetary mantle. The model enables computation of tidal deformation and dissipation for generally nonhomogeneous planets governed either by the Maxwell or the Andrade rheology. We then performed a series of calculations, studying the parameter dependence of the tidal heating, the tidal torque and the complex Love numbers. The results for the Maxwell rheology were qualitatively compared to the analytical model of Correia et al. (2014). We also computed the tidal heating semi–analytically, by a method based on Segatz et al. (1988) and Castillo-Rogez et al. (2011).

When describing the tidal response of terrestrial bodies, the Maxwell model is often utilised as a practical substitute for the more complex and more accurate Andrade rheology. Indeed, the two models almost coincide at low viscosities (or low frequencies) and their predictions for the tidal torque and the Love numbers are very similar also in the higher viscosity regimes, as long as we keep the notion of effective tidal viscosities, which can be up to few orders lower than the "standard" viscosities utilised e.g. in the mantle convection models. The crucial difference between the two rheological models arises in the comparison of spin–orbit ratio dependence of the tidal heating. However, even in this case the Andrade model can be approximated by the Maxwell model—the concept of frequency–dependent effective viscosity remains valid. When computing the tidal evolution or the tidal heating of terrestrial exoplanets, we must remember that only a planet on circular orbit is excited at one sole frequency. Hence, only the dissipation inside planets on circular orbits would be consistently approximated by a single–viscosity Maxwell model. For the eccentric orbits, it would be necessary to find all present frequencies and to sum the tidal heating over multiple Maxwell models, with a variety of effective viscosities. Only after this procedure, we would

be able to get Figure 7.4 or 7.6 without using the Andrade model directly.

As was already pointed out by Frouard et al. (2016), the place of numerical models among analytical theories is irreplaceable when dealing with complex rheologies, planets with nontrivial internal structure or nonspherical shape, and with analytically–challenging phenomena. While the analytical models provide us with general predictions for the tidal evolution of terrestrial bodies, semi–analytical or numerical models may help us to understand subtle details, given for example by coupling of the orbital (or rotational) and the internal dynamics or by sensitivity of the tidal heating to the chosen rheology.

Conclusion

Looking back at the seven chapters behind us, we may now summarise the main messages and conclusions of our journey. The thesis has discussed several aspects of the tidally–induced orbital evolution, from the theoretical foundations of the desired methods through semi–analytical exploration of the thermal–orbital coupling to two independent studies.

Theoretical background In Chapter 1, we introduced the Keplerian elements, presented several sets of equations governing the orbital evolution, and we also tried to explain the main aspects of the Darwin–Kaula expansion. In particular, the exposition focused on two of the mechanisms affecting the orbital dynamics of moons and planets: the tidal loading and the third–body perturbation. Chapter 2 opened several topics related to the interior properties of terrestrial worlds. We discussed the detection and characterisation techniques used in exoplanetary science, as well as the additional sources of information that may be helpful in reducing the degeneracy of interior models based on the measurements of mass and radius. With respect to the tidal models, the chapter also dealt with the mechanisms of seismic–wave attenuation in the Earth and with empirically–motivated rheological models used in modern tidal theories. The theoretical part of the work was then concluded by a brief overview of heating mechanisms and of the mantle convection.

Parametric studies The subsequent three chapters, constituting the principal part of the thesis, were dedicated to the coupled thermal and spin–orbital evolution of strongly tidally–loaded exoplanets. In Chapter 3, we first explored the tidal response of a planet described by the simplest rheological models. Specifically, the analysis focused on the parameter dependence of the tidal torque under the Maxwell or the Kelvin–Voigt rheology and only later transitioned to a semi–numerical parametric study of the tidal locking and tidal heating of a generic terrestrial exoplanet governed by the Andrade rheology. Apart from illustrating the regions of stability for the higher–order (i.e., super–synchronous) resonances, the parametric study provided us with the following observations:

- For moderate eccentricities ($e < 0.4$), the tidal heating in higher–order spin–orbit resonances only weakly depends on the orbital eccentricity and is mainly dictated by the rheological parameters and the spin rate.
- The contribution of super–synchronous resonant rotation to the tidal dissipation is most prominent at relatively low orbital eccentricities, where it may even exceed the contribution from the eccentricity tides.
- Decreasing the radius and/or the core–mass fraction (CMF) of the model planet increases the susceptibility to locking into a higher–order spin–orbit resonance. Moreover, at relatively small planetary radii ($R < 0.8R_\oplus$), the average surface tidal heat flux slowly increases with increasing CMF (i.e., with a thinner mantle). At larger radii ($R > 0.8R_\oplus$) the surface tidal heat flux decreases with increasing CMF.

Coupled thermal–orbital evolution Endowed with an intuition for the parametric dependencies of the tidal phenomena, we continued to Chapter 4, which covered a more advanced problem: the coupling between the thermal, orbital, and rotational dynamics of tidally–loaded exoplanets in single–planetary systems. This chapter also introduced a two–cycle computational scheme, required by the substantial difference between the time scales of the orbital and the rotational evolution, and a 1d parameterised model of mantle convection with a simplified treatment of mantle melting. The developed semi–analytical tool for the computation of coupled thermal–orbital evolution was applied to three low–mass exoplanets (Proxima Centauri b, GJ 625 b, and GJ 411 b) with presumably non–zero orbital eccentricities and with absent—or very weak—eccentricity forcing by other bodies in the system. Regarding the coupled thermal–orbital evolution, we may highlight the following results:

- The tidal dissipation—and subsequently the rate of orbital evolution—is mainly affected by two effects. At high orbital eccentricities, the magnitude of tidal dissipation may drop due to the formation of a magma ocean. At low orbital eccentricities, the most important mechanism, reducing the tidal dissipation considerably, is despinning into the synchronous rotation. The decrease in tidal dissipation induced by these two effects may enable the planet to maintain high orbital eccentricity for a long period of time ($> 10\,\mathrm{Gyr}$)
- The thermal evolution of planets on initially eccentric orbits proceeds as a sequence of equilibria. Depending on the rate of tidal dissipation, the planet quickly attains an equilibrium temperature profile, ensuring that the convective heat transfer fully compensates the tidal heat generation. Each drop in the tidal dissipation, e.g. due to the despinning into a lower spin–orbit resonance, is also accompanied by a transition to a new thermal equilibrium (at lower temperatures).
- Since the tidal dissipation at higher–order spin–orbit resonances only weakly depends on the orbital eccentricity, the aforementioned thermal equilibria are stable as long as the planet maintains a super–synchronous resonant rotation. Upon despinning to the synchronous rotation, the dissipation becomes clearly eccentricity–dependent and the interior temperatures gradually decrease with decaying eccentricity.

Kozai–Lidov mechanism with viscoelastic tides In Chapter 5, the coupled thermal–orbital model was further extended by adding a second planet to the system. In particular, we explored the orbital dynamics of the generic terrestrial exoplanet from Chapter 3, subjected to third–body perturbation by a giant planet on a highly–inclined outer orbit. The orbital parameters of the perturber were intentionally chosen to give rise to the Kozai–Lidov mechanism, which was then studied in combination with viscoelastic tides. Assuming three different radii of the giant planet's circular orbit, we observed two modes of orbital evolution:

- In a system with a close perturber ($a_2 = 1\,\mathrm{AU}$), the relatively slow tidal evolution of the model planet does not break the secular resonance. Tidally–induced eccentricity decay, combined with the resonant eccentricity forcing, contributes to a gradual loss of angular momentum, to a slow decrease in the mutual inclination (due to a e–i–ω coupling), and to the planet's migration towards the host star.
- In a system with a more distant perturber ($a_2 = 5\,\mathrm{AU}$ or $a_2 = 10\,\mathrm{AU}$), the tidal evolution proceeds on timescales comparable to the period of the Kozai–Lidov cycles. Therefore, the tidally–induced eccentricity decay may eventually break the secular resonance and the dynamics of the system can change considerably. The orbital evolution is then dominated by tidal circularisation.

The above–mentioned behaviour was mainly observed in model cases with constant interior properties (i.e., without the thermal evolution). In models with coupled thermal–orbital evolution, the model planet exhibited a tendency analogical to Chapter 4:

- Once the increased upper–mantle temperature triggers the formation of a magma ocean, the tidal dissipation drops substantially and the tidal evolution is effectively inhibited. In the model system with a close perturber, this phenomenon, preceded by a short period of tidally–induced eccentricity decay, may lead to locking into the secular resonance. However, the feedback between the tides, the eccentricity forcing, and the thermal evolution is, in general, extremely complex.

Additional studies Not related to the coupled models of thermal–orbital evolution, the last two chapters discussed two independent studies of tidal phenomena. Chapter 6 dealt with tidal loading between moons or planets orbiting the same primary: a mechanism that may be potentially important in tightly–packed multi-planetary systems. The tidal potential between two planets was expressed in the form of a Darwin–Kaula expansion. However, given the high complexity of such an expression, the numerical treatment of this topic is often preferable. Finally, in Chapter 7, we included a numerical approach to the analysis of tidal effects, based on the spherical harmonic decomposition of the governing equations and calculating the tidal deformation and subsequent energy dissipation in the time domain. We note that the numerical model was also used for the testing of the semi–analytical model's accuracy, and although it is only included at the end of the seven chapters, it played an irreplaceable role in our understanding of the tidal phenomena in viscoelastic bodies[1].

[1] As we saw in Chapter 6, the numerical model can also be applied to the study of planet–planet tides.

Bibliography

Y. Abe. Thermal and chemical evolution of the terrestrial magma ocean. *Phys. Earth Planet. Inter.*, 100(1):27–39, 1997. doi: 10.1016/S0031-9201(96)03229-3.

V. Adibekyan, S. G. Sousa, and N. C. Santos. Characterization of Exoplanet-Host Stars. In Tiago L. Campante, Nuno C. Santos, and Mário J. P. F. G. Monteiro, editors, *Asteroseismology and Exoplanets: Listening to the Stars and Searching for New Worlds*, volume 49, page 225, 2018. doi: 10.1007/978-3-319-59315-9_12.

C. B. Agee. Compressibility of water in magma and the prediction of density crossovers in mantle differentiation. *Philos. Trans. R. Soc. A*, 366(1883):4239–4252, 2008. doi: 10.1098/rsta.2008.0071.

C. B. Agee and D. Walker. Olivine flotation in mantle melt. *Earth Planet. Sci. Lett.*, 114(2-3):315–324, 1993. doi: 10.1016/0012-821X(93)90033-6.

E. Agol, J. Steffen, R. Sari, and W. Clarkson. On detecting terrestrial planets with timing of giant planet transits. *Mon. Not. R. Astron. Soc.*, 359(2):567–579, 2005. doi: 10.1111/j.1365-2966.2005.08922.x.

M. E. Alexander. The Weak Friction Approximation and Tidal Evolution in Close Binary Systems. *Astrophys. Space Sci.*, 23(2):459–510, 1973. doi: 10.1007/BF00645172.

R. R. Allan. On the Motion of Nearly Synchronous Satellites. *Proc. R. Soc. A*, 288(1412):60–68, 1965. doi: 10.1098/rspa.1965.0201.

D. L. Anderson and J. W. Given. Absorption band Q model for the Earth. *J. Geophys. Res.*, 87(B5):3893–3904, 1982. doi: 10.1029/JB087iB05p03893.

D. L. Anderson and J. B. Minster. The frequency dependence of Q in the Earth and implications for mantle rheology and Chandler wobble. *Geophys. J.*, 58: 431–440, 1979. doi: 10.1111/j.1365-246X.1979.tb01033.x.

H. Andoyer. Mémoires et observations. Contribution à la théorie des petites planètes dont le moyen mouvement est sensiblement double de celui de Jupiter. *Bulletin Astronomique, Serie I*, 20:321–356, 1903.

E. N. Da C. Andrade. On the Viscous Flow in Metals, and Allied Phenomena. *Proc. R. Soc. A*, 84(567):1–12, 1910.

D. Andrault, N. Bolfan-Casanova, G. L. Nigro, M. A. Bouhifd, G. Garbarino, et al. Solidus and liquidus profiles of chondritic mantle: Implication for melting of the Earth across its history. *Earth Planet. Sci. Lett.*, 304(1-2):251–259, 2011. doi: 10.1016/j.epsl.2011.02.006.

G. Anglada-Escudé, P. J. Amado, J. Barnes, Z. M. Berdinas, R. P. Butler, et al. A terrestrial planet candidate in a temperate orbit around Proxima Centauri. *Nature*, 536(7617):437–440, 2016. doi: 10.1038/nature19106.

P. Auclair-Desrotour, J. Leconte, and C. Mergny. Generic frequency dependence for the atmospheric tidal torque of terrestrial planets. *Astron. Astrophys.*, 624

(A17):22, 2019. doi: 10.1051/0004-6361/201834685.

A. Baglin. COROT: A minisat for pionnier science, asteroseismology and planets finding. *Adv. Space Res.*, 31(2):345–349, 2003. doi: 10.1016/S0273-1177(02)00624-5.

S. Ballard, D. Fabrycky, F. Fressin, D. Charbonneau, J.-M. Desert, et al. The Kepler-19 System: A Transiting 2.2 $R_\oplus$ Planet and a Second Planet Detected via Transit Timing Variations. *Astrophys. J.*, 743(2):200, 2011. doi: 10.1088/0004-637X/743/2/200.

R. Barnes, B. Jackson, R. Greenberg, and S. N. Raymond. Tidal Limits to Planetary Habitability. *Astrophys. J. Lett.*, 700(1):L30–L33, 2009. doi: 10.1088/0004-637X/700/1/L30.

R. Barnes, K. Mullins, C. Goldblatt, V. S. Meadows, J. F. Kasting, et al. Tidal Venuses: Triggering a Climate Catastrophe via Tidal Heating. *Astrobiology*, 13(3):225–250, 2013. doi: 10.1089/ast.2012.0851.

A. C. Barr, V. Dobos, and L. L. Kiss. Interior structures and tidal heating in the TRAPPIST-1 planets. *Astron. Astrophys.*, 613(A37):13, 2018. doi: 10.1051/0004-6361/201731992.

D. Bashi, R. Helled, S. Zucker, and Ch. Mordasini. Two empirical regimes of the planetary mass-radius relation. *Astron. Astrophys.*, 604:A83, 2017. doi: 10.1051/0004-6361/201629922.

G. Basri, W. J. Borucki, and D. Koch. The Kepler Mission: A wide-field transit search for terrestrial planets [review article]. *New Astron. Rev.*, 49:478–485, 2005. doi: 10.1016/j.newar.2005.08.026.

M. Bataille, A.-S. Libert, and A. C. M. Correia. Dynamical evolution of triple-star systems by Lidov-Kozai cycles and tidal friction. *Mon. Not. R. Astron. Soc.*, 479(4):4749–4759, 2018. doi: 10.1093/mnras/sty1758.

K. Batygin and G. Laughlin. On the Dynamical Stability of the Solar System. *Astrophys. J.*, 683(2):1207–1216, 2008. doi: 10.1086/589232.

D. Bercovici, Y. Ricard, and G. Schubert. A two-phase model for compaction and damage: 1. General Theory. *J. Geophys. Res. Solid Earth*, 106(B5):8887–8906, 2001. doi: 10.1029/2000JB900430.

M. Beuthe. Spatial patterns of tidal heating. *Icarus*, 223(1):308–329, 2013. doi: 10.1016/j.icarus.2012.11.020.

M. Beuthe. Crustal control of dissipative ocean tides in Enceladus and other icy moons. *Icarus*, 280:278–299, 2016. doi: 10.1016/j.icarus.2016.08.009.

S. Blunt, M. Endl, L. M. Weiss, W. D. Cochran, A. W. Howard, et al. Radial Velocity Discovery of an Eccentric Jovian World Orbiting at 18 au. *Astron. J.*, 158(5):181, 2019. doi: 10.3847/1538-3881/ab3e63.

P. Bodenheimer, D. N. C. Lin, and R. A. Mardling. On the Tidal Inflation of Short-Period Extrasolar Planets. *Astrophys. J.*, 548(1):466–472, 2001. doi:

10.1086/318667.

E. Bolmont and S. Mathis. Effect of the rotation and tidal dissipation history of stars on the evolution of close-in planets. *Celest. Mech. Dyn. Astron.*, 126(1-3): 275–296, 2016. doi: 10.1007/s10569-016-9690-3.

E. Bolmont, B.-O. Demory, S. Blanco-Cuaresma, E. Agol, S. L. Grimm, et al. Impact of tides on the transit-timing fits to the TRAPPIST-1 system. *Astron. Astrophys.*, 635:A117, 2020. doi: 10.1051/0004-6361/202037546.

X. Bonfils, M. Gillon, T. Forveille, X. Delfosse, D. Deming, et al. A short-period super-Earth orbiting the M2.5 dwarf GJ 3634. Detection with HARPS velocimetry and transit search with Spitzer photometry. *Astron. Astrophys.*, 528:A111, 2011. doi: 10.1051/0004-6361/201015981.

G. Boué. Cassini states of a rigid body with a liquid core. *Celest. Mech. Dyn. Astron.*, 132(3):21, 2020. doi: 10.1007/s10569-020-09961-9.

G. Boué and M. Efroimsky. Tidal evolution of the Keplerian elements. *Celest. Mech. Dyn. Astron.*, 131(7):30, 2019. doi: 10.1007/s10569-019-9908-2.

G. Boué, A. C. M. Correia, and J. Laskar. Complete spin and orbital evolution of close-in bodies using a Maxwell viscoelastic rheology. *Celest. Mech. Dyn. Astron.*, 126(1-3):31–60, 2016. doi: 10.1007/s10569-016-9708-x.

G. Boué, J. Laskar, and F. Farago. A simple model of the chaotic eccentricity of Mercury. *Astron. Astrophys.*, 548:A43, 2012. doi: 10.1051/0004-6361/201219991.

D. Breuer and T. Spohn. Viscosity of the Martian mantle and its initial temperature: Constraints from crust formation history and the evolution of the magnetic field. *Planet. Space Sci.*, 54(2):153–169, 2006. doi: 10.1016/j.pss.2005.08.008.

M. Brogi, I. A. G. Snellen, R. J. de Kok, S. Albrecht, J. Birkby, et al. The signature of orbital motion from the dayside of the planet τ Boötis b. *Nature*, 486(7404):502–504, 2012. doi: 10.1038/nature11161.

M. Brogi, R. J. de Kok, S. Albrecht, I. A. G. Snellen, J. L. Birkby, et al. Rotation and Winds of Exoplanet HD 189733 b Measured with High-dispersion Transmission Spectroscopy. *Astrophys. J.*, 817(2):106, 2016. doi: 10.3847/0004-637X/817/2/106.

D. Brouwer and G. M. Clemence. *Methods of celestial mechanics*. First edition. Academic Press, New York, 1961. ISBN 978-1-4832-0075-0.

M. Běhounková, G. Tobie, G. Choblet, and O. Čadek. Coupling mantle convection and tidal dissipation: applications to Enceladus and Earth-like planets. *J. Geophys. Res.*, 115(E09011), 2010. doi: 10.1029/2009JE003564.

M. Běhounková, G. Tobie, G. Choblet, and O. Čadek. Tidally Induced Thermal Runaways on Extrasolar Earths: Impact on Habitability. *Astrophys. J.*, 728(2): 7, 2011. doi: 10.1088/0004-637X/728/2/89.

M. Běhounková, G. Tobie, G. Choblet, and O. Čadek. Impact of tidal heating on the onset of convection in Enceladus's ice shell. *Icarus*, 226(1):898–904, 2013.

doi: 10.1016/j.icarus.2013.06.033.

M. Běhounková, G. Tobie, O. Čadek, G. Choblet, C. Porco, et al. Timing of water plume eruptions on Enceladus explained by interior viscosity structure. *Nat. Geosci.*, 8:601–604, 2015. doi: 10.1038/ngeo2475.

H. S. Carslaw and J. C. Jaeger. *Conduction of heat in solids*. Oxford Science Publications. Oxford University Press, 1959. ISBN 978-0198533689. Second Edition.

J. A. Carter, J. C. Yee, J. Eastman, B. S. Gaudi, and J. N. Winn. Analytic Approximations for Transit Light-Curve Observables, Uncertainties, and Covariances. *Astrophys. J.*, 689(1):499–512, 2008. doi: 10.1086/592321.

P. Cassen, R. T. Reynolds, and S. J. Peale. Is there liquid water on Europa? *Geophys. Res. Lett.*, 6(9):731–734, 1979. doi: 10.1029/GL006i009p00731.

M. Castillo-Rodríguez, M. L. Nó, J. A. Jiménez, O. A. Ruano, and J. San Juan. High temperature internal friction in a Ti-46Al-1Mo-0.2Si intermetallic, comparison with creep behaviour. *Acta Mater.*, 103:46–56, 2016. doi: 10.1016/j.actamat.2015.09.052.

J. C. Castillo-Rogez, M. Efroimsky, and V. Lainey. The tidal history of Iapetus: Spin dynamics in the light of a refined dissipation model. *J. Geophys. Res. Planets*, 116(E9):E09008, 2011. doi: 10.1029/2010JE003664.

A. Cayley. Tables of the developments of functions in the theory of elliptic motion. *Mem. R. Astron. Soc.*, 29:191–306, 1861.

A. Celletti, C. Galeş, G. Pucacco, and A. J. Rosengren. Analytical development of the lunisolar disturbing function and the critical inclination secular resonance. *Celest. Mech. Dyn. Astron.*, 127(3):259–283, 2017. doi: 10.1007/s10569-016-9726-8.

J. H. Checlair, S. L. Olson, M. F. Jansen, and D. S. Abbot. No Snowball on Habitable Tidally Locked Planets with a Dynamic Ocean. *Astrophys. J. Lett.*, 884:L46, 2019. doi: 10.3847/2041-8213/ab487d.

E. M. A. Chen, F. Nimmo, and G. A. Glatzmaier. Tidal heating in icy satellite oceans. *Icarus*, 229:11–30, 2014. doi: 10.1016/j.icarus.2013.10.024.

J. Chen and D. Kipping. Probabilistic Forecasting of the Masses and Radii of Other Worlds. *Astrophys. J.*, 834(1):17, 2017. doi: 10.3847/1538-4357/834/1/17.

J. R. Cherniack. Computation of Hansen Coefficients. *SAO Special Report*, 346, 1972.

S. V. Chernov, P. B. Ivanov, and J. C. B. Papaloizou. Dynamical tides in exoplanetary systems containing hot Jupiters: confronting theory and observations. *Mon. Not. R. Astron. Soc.*, 470(2):2054–2068, 2017. doi: 10.1093/mnras/stx1234.

U. R. Christensen. Thermal evolution models for the earth. *J. Geophys. Res.*, 90: 2995–3007, 1985. doi: 10.1029/JB090iB04p02995.

J. W. Christy and R. S. Harrington. The satellite of Pluto. *Astron. J.*, 83:1005,

1978. doi: 10.1086/112284.

C. F. Chyba, D. G. Jankowski, and P. D. Nicholson. Tidal evolution in the Neptune-Triton system. *Astron. Astrophys.*, 219(1-2):L23–L26, 1989.

H. Čížková, A. van den Berg, and M. Jacobs. Impact of compressibility on heat transport characteristics of large terrestrial planets. *Phys. Earth Planet. Inter.*, 268:65–77, 2017. doi: 10.1016/j.pepi.2017.04.007.

W. D. Cochran and A. P. Hatzes. Radial Velocity Searches for Other Planetary Systems: Current Status and Future Prospects. *Astrophys. Space Sci.*, 241(1): 43–60, 1996. doi: 10.1007/BF00644214.

D. M. Cole. On the physical basis for the creep of ice: the high temperature regime. *J. Glaciol.*, 66(257):401–414, 2020. doi: 10.1017/jog.2020.15.

G. Colombo. Cassini's second and third laws. *Astron. J.*, 71:891, 1966. doi: 10.1086/109983.

A. C. M. Correia. Stellar and planetary Cassini states. *Astron. Astrophys.*, 582: A69, 2015. doi: 10.1051/0004-6361/201525939.

A. C. M. Correia and J. Laskar. Long-term evolution of the spin of Venus. II. numerical simulations. *Icarus*, 163(1):24–45, 2003. doi: 10.1016/S0019-1035(03)00043-5.

A. C. M. Correia and J. Laskar. Mercury's capture into the 3/2 spin-orbit resonance including the effect of core-mantle friction. *Icarus*, 201(1):1–11, 2009. doi: 10.1016/j.icarus.2008.12.034.

A. C. M. Correia and J. Laskar. Tidal Evolution of Exoplanets. In S. Seager, editor, *Exoplanets*, pages 239–266. University of Arizona Press, Tucson, AZ, 2010. ISBN 978-0-8165-2945-2.

A. C. M. Correia, G. Boué, J. Laskar, and M. H. M. Morais. Tidal damping of the mutual inclination in hierarchical systems. *Astron. Astrophys.*, 553:A39, 2013. doi: 10.1051/0004-6361/201220482.

A. C. M. Correia, G. Boué, J. Laskar, and A. Rodríguez. Deformation and tidal evolution of close-in planets and satellites using a Maxwell viscoelastic rheology. *Astron. Astrophys.*, 571:A50, 2014. doi: 10.1051/0004-6361/201424211.

Sz. Csizmadia, H. Hellard, and A. M. S. Smith. An estimate of the k_2 Love number of WASP-18Ab from its radial velocity measurements. *Astron. Astrophys.*, 623: A45, 2019. doi: 10.1051/0004-6361/201834376.

M. Ćuk and S. T. Stewart. Making the Moon from a Fast-Spinning Earth: A Giant Impact Followed by Resonant Despinning. *Science*, 338(6110):1047, 2012. doi: 10.1126/science.1225542.

M. Damasso, F. Del Sordo, and G. Anglada-Escudé. A low-mass planet candidate orbiting Proxima Centauri at a distance of 1.5 AU. *Solid Earth*, 6(3):eaax7467, 2020. doi: 10.1126/sciadv.aax7467.

G. H. Darwin. On the bodily tides of viscous and semi-elastic spheroids and on

the ocean tides upon a yielding nucleus. *Philos. Trans. R. Soc.*, 170:1–35, 1879. (repr. in Scientific Papers, Cambridge, Vol. II, 1908).

G. H. Darwin. On the secular change in the elements of the orbit of a satellite revolving about a tidally distorted planet. *Philos. Trans. R. Soc.*, 171:713–891, 1880. (repr. in Scientific Papers, Cambridge, Vol. II, 1908).

J. H. Davies and D. R. Davies. Earth's surface heat flux. *Solid Earth*, 1(1):5–24, 2010. doi: 10.5194/se-1-5-2010.

R. De Batist. Internal friction of iron-chromium alloys in the temperature range between 20 and 800 °C. *J. Nucl. Mater.*, 31(3):307–315, 1969. doi: 10.1016/0022-3115(69)90227-X.

J. de Wit and S. Seager. Constraining Exoplanet Mass from Transmission Spectroscopy. *Science*, 342(6165):1473–1477, 2013. doi: 10.1126/science.1245450.

R. Deienno, D. Nesvorný, D. Vokrouhlický, and T. Yokoyama. Orbital Perturbations of the Galilean Satellites during Planetary Encounters. *Astron. J.*, 148(2):25, 2014. doi: 10.1088/0004-6256/148/2/25.

A. D. Del Genio, N. Y. Kiang, M. J. Way, D. S. Amundsen, L. E. Sohl, et al. Albedos, Equilibrium Temperatures, and Surface Temperatures of Habitable Planets. *Astrophys. J.*, 884(1):75, 2019. doi: 10.3847/1538-4357/ab3be8.

J.-B. Delisle and J. Laskar. Tidal dissipation and the formation of Kepler near-resonant planets. *Astron. Astrophys.*, 570:L7, 2014. doi: 10.1051/0004-6361/201424227.

B.-O. Demory, M. Gillon, S. Seager, B. Benneke, D. Deming, et al. Detection of Thermal Emission from a Super-Earth. *Astrophys. J. Lett.*, 751(2):L28, 2012. doi: 10.1088/2041-8205/751/2/L28.

S. F. Dermott, R. Malhotra, and C. D. Murray. Dynamics of the Uranian and Saturnian satelite systems: A chaotic route to melting Miranda? *Icarus*, 76(2):295–334, 1988. doi: 10.1016/0019-1035(88)90074-7.

R. F. Díaz, X. Delfosse, M. J. Hobson, I. Boisse, N. Astudillo-Defru, et al. The SOPHIE search for northern extrasolar planets. XIV. A temperate (T_{eq} 300 K) super-earth around the nearby star Gliese 411. *Astron. Astrophys.*, 625:A17, 2019. doi: 10.1051/0004-6361/201935019.

V. Dobos, R. Heller, and E. L. Turner. The effect of multiple heat sources on exomoon habitable zones. *Astron. Astrophys.*, 601(A91):7, 2017. doi: 10.1051/0004-6361/201730541.

A. R. Dobrovolskis. Spin states and climates of eccentric exoplanets. *Icarus*, 192(1):1–23, 2007. doi: 10.1016/j.icarus.2007.07.005.

A. R. Dobrovolskis. Insolation patterns on synchronous exoplanets with obliquity. *Icarus*, 204(1):1–10, 2009. doi: 10.1016/j.icarus.2009.06.007.

A. R. Dobrovolskis. Insolation on exoplanets with eccentricity and obliquity. *Icarus*, 226(1):760–776, 2013. doi: 10.1016/j.icarus.2013.06.026.

A. R. Dobrovolskis. Insolation patterns on eccentric exoplanets. *Icarus*, 250: 395–399, 2015. doi: 10.1016/j.icarus.2014.12.017.

C. Dorn, A. Khan, K. Heng, J. A. D. Connolly, Y. Alibert, et al. Can we constrain the interior structure of rocky exoplanets from mass and radius measurements? *Astron. Astrophys.*, 577:A83, 2015. doi: 10.1051/0004-6361/201424915.

C. Dorn, L. Noack, and A. B. Rozel. Outgassing on stagnant-lid super-Earths. *Astron. Astrophys.*, 614:A18, 2018. doi: 10.1051/0004-6361/201731513.

P. E. Driscoll and R. Barnes. Tidal Heating of Earth-like Exoplanets around M Stars: Thermal, Magnetic, and Orbital Evolutions. *Astrobiology*, 15(9):739–760, 2015. doi: 10.1089/ast.2015.1325.

A. M. Dziewonski and D. L. Anderson. Preliminary reference Earth model. *Phys. Earth Planet. Inter.*, 25(4):297–356, 1981. doi: 10.1016/0031-9201(81)90046-7.

M. Efroimsky. Bodily tides near spin-orbit resonances. *Celest. Mech. Dyn. Astron.*, 112(3):283–330, 2012a. doi: 10.1007/s10569-011-9397-4.

M. Efroimsky. Tidal Dissipation Compared to Seismic Dissipation: In Small Bodies, Earths and Super-Earths. *Astrophys. J.*, 746(2):150, 2012b. doi: 10.1088/0004-637X/746/2/150.

M. Efroimsky. Tidal Evolution of Asteroidal Binaries. Ruled by Viscosity. Ignorant of Rigidity. *Astron. J.*, 150(4):98, 2015. doi: 10.1088/0004-6256/150/4/98.

M. Efroimsky and V. Lainey. Physics of bodily tides in terrestrial planets and the appropriate scales of dynamical evolution. *J. Geophys. Res. Planets*, 112 (E12):E12003, 2007. doi: 10.1029/2007JE002908.

M. Efroimsky and V. V. Makarov. Tidal Dissipation in a Homogeneous Spherical Body. I. Methods. *Astrophys. J.*, 795(1):19, 2014. doi: 10.1088/0004-637X/795/1/6.

M. Efroimsky and J. G. Williams. Tidal torques. A critical review of some techniques. *Celest. Mech. Dyn. Astron.*, 104(3):257–289, 2009. doi: 10.1007/s10569-009-9204-7.

P. P. Eggleton and L. Kiseleva-Eggleton. Orbital Evolution in Binary and Triple Stars, with an Application to SS Lacertae. *Astrophys. J.*, 562(2):1012–1030, 2001. doi: 10.1086/323843.

D. C. Fabrycky and S. Tremaine. Shrinking Binary and Planetary Orbits by Kozai Cycles with Tidal Friction. *Astrophys. J.*, 669(2):1298–1315, 2007. doi: 10.1086/521702.

D. C. Fabrycky, E. T. Johnson, and J. Goodman. Cassini States with Dissipation: Why Obliquity Tides Cannot Inflate Hot Jupiters. *Astrophys. J.*, 665(1):754–766, 2007. doi: 10.1086/519075.

D. C. Fabrycky, J. J. Lissauer, D. Ragozzine, J. F. Rowe, J. H. Steffen, et al. Architecture of Kepler's Multi-transiting Systems. II. New Investigations with Twice as Many Candidates. *Astrophys. J.*, 790(2):146, 2014. doi: 10.1088/

0004-637X/790/2/146.

R. J. M. Farla, I. Jackson, J. D. Fitz Gerald, U. H. Faul, and M. E. Zimmerman. Dislocation Damping and Anisotropic Seismic Wave Attenuation in Earth's Upper Mantle. *Science*, 336(6079):332, 2012. doi: 10.1126/science.1218318.

U. H. Faul and I. Jackson. The seismological signature of temperature and grain size variations in the upper mantle. *Earth Planet. Sci. Lett.*, 234(1-2):119–134, 2005. doi: 10.1016/j.epsl.2005.02.008.

S. Ferraz-Mello. Tidal synchronization of close-in satellites and exoplanets. A rheophysical approach. *Celest. Mech. Dyn. Astron.*, 116(2):109–140, 2013. doi: 10.1007/s10569-013-9482-y.

S. Ferraz-Mello. Earth tides in MacDonald's model. *arXiv e-prints*, art. arXiv:1301.5617, 2013.

S. Ferraz-Mello. Tidal synchronization of close-in satellites and exoplanets: II. Spin dynamics and extension to Mercury and exoplanet host stars. *Celest. Mech. Dyn. Astron.*, 122(4):359–389, 2015. doi: 10.1007/s10569-015-9624-5.

S. Ferraz-Mello, A. Rodríguez, and H. Hussmann. Tidal friction in close-in satellites and exoplanets: The Darwin theory re-visited. *Celest. Mech. Dyn. Astron.*, 101(1-2):171 – 201, 2008. doi: 10.1007/s10569-008-9133-x.

S. Ferraz-Mello, C. Beaugé, H. A. Folonier, and G. O. Gomes. Tidal friction in satellites and planets. The new version of the creep tide theory. *Eur. Phys. J. Spec. Top.*, 229(8):1441–1462, 2020. doi: 10.1140/epjst/e2020-900184-5.

H.-J. Fischer and T. Spohn. Thermal-orbital histories of viscoelastic models of Io (J1). *Icarus*, 83(1):39–65, 1990. doi: 10.1016/0019-1035(90)90005-T.

B. J. Foley and A. J. Smye. Carbon Cycling and Habitability of Earth-Sized Stagnant Lid Planets. *Astrobiology*, 18(7):873–896, 2018. doi: 10.1089/ast.2017.1695.

B. J. Foley, D. Bercovici, and W. Landuyt. The conditions for plate tectonics on super-Earths: Inferences from convection models with damage. *Earth Planet. Sci. Lett.*, 331-332:281 – 290, 2012. doi: 10.1016/j.epsl.2012.03.028.

H. A. Folonier, S. Ferraz-Mello, and K. V. Kholshevnikov. The flattenings of the layers of rotating planets and satellites deformed by a tidal potential. *Celest. Mech. Dyn. Astron.*, 122(2):183–198, 2015. doi: 10.1007/s10569-015-9615-6.

J. J. Fortney. The effect of condensates on the characterization of transiting planet atmospheres with transmission spectroscopy. *Mon. Not. R. Astron. Soc.*, 364(2):649–653, 2005. doi: 10.1111/j.1365-2966.2005.09587.x.

E. A. Frank, B. S. Meyer, and S. J. Mojzsis. A radiogenic heating evolution model for cosmochemically Earth-like exoplanets. *Icarus*, 243:274–286, 2014. doi: 10.1016/j.icarus.2014.08.031.

J. Friedel. *Dislocations*. International Series of Monographs on Solid State Physics. Elsevier Science, 2013. ISBN 9781483135922.

Ch. Froeschle and A. Morbidelli. The Secular Resonances in the Solar System. In A. Milani, M. di Martino, and A. Cellino, editors, *Asteroids, Comets, Meteors 1993*, volume 160 of *IAU Symposium*, page 189, 1994.

J. Frouard, A. C. Quillen, M. Efroimsky, and D. Giannella. Numerical Simulation of Tidal Evolution of a Viscoelastic Body Modeled with a Mass-Spring Network. *Mon. Not. R. Astron. Soc.*, 458(3):2890–2901, 2016. doi: 10.1093/mnras/stw491.

B. J. Fulton and E. A. Petigura. The California-Kepler Survey. VII. Precise Planet Radii Leveraging Gaia DR2 Reveal the Stellar Mass Dependence of the Planet Radius Gap. *Astron. J.*, 156(6):264, 2018. doi: 10.3847/1538-3881/aae828.

B. J. Fulton, E. A. Petigura, A. W. Howard, H. Isaacson, G. W. Marcy, et al. The California-Kepler Survey. III. A Gap in the Radius Distribution of Small Planets. *Astron. J.*, 154(3):109, 2017. doi: 10.3847/1538-3881/aa80eb.

B. Funk, A.-S. Libert, Á. Süli, and E. Pilat-Lohinger. On the influence of the Kozai mechanism in habitable zones of extrasolar planetary systems. *Astron. Astrophys.*, 526:A98, 2011. doi: 10.1051/0004-6361/201015218.

S. E. Gelman, L. T. Elkins-Tanton, and S. Seager. Effects of Stellar Flux on Tidally Locked Terrestrial Planets: Degree-1 Mantle Convection and Local Magma Ponds. *Astrophys. J.*, 735(2):72, 2011. doi: 10.1088/0004-637X/735/2/72.

H. Gerstenkorn. Über Gezeitenreibung beim Zweikörperproblem. *Zeitschrift für Astrophysik*, 36:245–275, 1955.

G. E. O. Giacaglia. A Note on Hansen's Coefficients in Satellite Theory. *Celestial Mechanics*, 14(4):515–523, 1976. doi: 10.1007/BF01229062.

G. E. O. Giacaglia. The Equations of Motion of an Artificial Satellite in Nonsingular Variables. *Celestial Mechanics*, 15(2):191–215, 1977. doi: 10.1007/BF01228462.

M. Gillon, A. A. Lanotte, T. Barman, N. Miller, B.-O. Demory, et al. The thermal emission of the young and massive planet CoRoT-2b at 4.5 and 8 μm. *Astron. Astrophys.*, 511:A3, 2010. doi: 10.1051/0004-6361/200913507.

M. Gillon, A. H. M. J. Triaud, B.-O. Demory, E. Jehin, E. Agol, et al. Seven temperate terrestrial planets around the nearby ultracool dwarf star TRAPPIST-1. *Nature*, 542(7642):456–460, 2017. doi: 10.1038/nature21360.

H. Gleiter. The migration of small angle boundaries. *Philos. Mag.*, 20(166): 821–830, 1969. doi: 10.1080/14786436908228047.

M. Godolt, N. Tosi, B. Stracke, J. L. Grenfell, T. Ruedas, et al. The habitability of stagnant-lid Earths around dwarf stars. *Astron. Astrophys.*, 625(A12):15, 2019. doi: 10.1051/0004-6361/201834658.

T. Gold and S. Soter. Atmospheric Tides and the Resonant Rotation of Venus. *Icarus*, 11(3):356–366, 1969. doi: 10.1016/0019-1035(69)90068-2.

P. Goldreich. On the eccentricity of satellite orbits in the solar system. *Mon. Not. R. Astron. Soc.*, 126:257, 1963. doi: 10.1093/mnras/126.3.257.

P. Goldreich. An explanation of the frequent occurrence of commensurable mean

motions in the solar system. *Mon. Not. R. Astron. Soc.*, 130:159, 1965. doi: 10.1093/mnras/130.3.159.

P. Goldreich. Final spin states of planets and satellites. *Astron. J.*, 71:1, 1966. doi: 10.1086/109844.

P. Goldreich and S. Peale. Spin-orbit coupling in the solar system. *Astron. J.*, 71: 425, 1966. doi: 10.1086/109947.

P. Goldreich and S. Soter. Q in the Solar System. *Icarus*, 5(1):375–389, 1966. doi: 10.1016/0019-1035(66)90051-0.

R. H. Gooding. A recurrence relation for inclination functions. *Celestial Mechanics*, 4(1):91–98, 1971. doi: 10.1007/BF01230324.

M. Grott and D. Breuer. The evolution of the martian elastic lithosphere and implications for crustal and mantle rheology. *Icarus*, 193(2):503–515, 2008. doi: 10.1016/j.icarus.2007.08.015.

B. M. S. Hansen. Calibration of Equilibrium Tide Theory for Extrasolar Planet Systems. *Astrophys. J.*, 723(1):285–299, 2010. doi: 10.1088/0004-637X/723/1/285.

L. Hanyk, C. Matyska, and D. A. Yuen. Short time-scale heating of the Earth's mantle by ice-sheet dynamics. *Earth Planets Space*, 57(9):895–902, 2005.

N. C. Hara, F. Bouchy, M. Stalport, I. Boisse, J. Rodrigues, et al. The SOPHIE search for northern extrasolar planets. XVI. HD 158259: A compact planetary system in a near-3:2 mean motion resonance chain. *Astron. Astrophys.*, 636:L6, 2020. doi: 10.1051/0004-6361/201937254.

H. C. F. C. Hay and I. Matsuyama. Tides Between the TRAPPIST-1 Planets. *Astrophys. J.*, 875(1):22, 2019. doi: 10.3847/1538-4357/ab0c21.

H. C. F. C. Hay, A. Trinh, and I. Matsuyama. Powering the Galilean Satellites with Moon-Moon Tides. *Geophys. Res. Lett.*, 47(15):e88317, 2020. doi: 10.1029/2020GL088317.

H. Hellard, Sz. Csizmadia, S. Padovan, H. Rauer, J. Cabrera, et al. Retrieval of the Fluid Love Number k_2 in Exoplanetary Transit Curves. *Astrophys. J.*, 878 (2):119, 2019. doi: 10.3847/1538-4357/ab2048.

H. Hellard, Sz. Csizmadia, S. Padovan, F. Sohl, and H. Rauer. HST/STIS Capability for Love Number Measurement of WASP-121b. *Astrophys. J.*, 889 (1):66, 2020. doi: 10.3847/1538-4357/ab616e.

R. Heller and R. Barnes. Exomoon Habitability Constrained by Illumination and Tidal Heating. *Astrobiology*, 13(1):18–46, 2013. doi: 10.1089/ast.2012.0859.

R. Heller, J. Leconte, and R. Barnes. Tidal obliquity evolution of potentially habitable planets. *Astron. Astrophys.*, 528:16, 2011. doi: 10.1051/0004-6361/201015809.

F. R. Helmert. *Die mathematischen und physikalischen Theorieen der Höheren Geodäsie. II. Teil: Die physikalischen Theorieen.* B. G. Teubner, Leipzig, 1884.

W. G. Henning and T. Hurford. Tidal heating in multilayered terrestrial exoplanets. *Astrophys. J.*, 789(1):30, 2014. doi: 10.1088/0004-637X/789/1/30.

W. G. Henning, R. J. O'Connell, and D. D. Sasselov. Tidally Heated Terrestrial Exoplanets: Viscoelastic Response Models. *Astrophys. J.*, 707(2):1000–1015, 2009. doi: 10.1088/0004-637X/707/2/1000.

W. G. Henning, J. P. Renaud, P. W. L. Saxena, A. M. Mandell, S. Matsumura, et al. Highly Volcanic Exoplanets, Lava Worlds, and Magma Ocean Worlds: An Emerging Class of Dynamic Exoplanets of Significant Scientific Priority. *arXiv e-prints*, art. arXiv:1804.05110, 2018.

C. Herzberg and J. Zhang. Melting experiments on anhydrous peridotite KLB-1: Compositions of magmas in the upper mantle and transition zone. *J. Geophys. Res. Solid Earth*, 101(B4):8271–8295, 1996. doi: 10.1029/96JB00170.

P. B. Hirsch, R. W. Horne, and M. J. Whelan. LXVIII. Direct observations of the arrangement and motion of dislocations in aluminium. *Philos. Mag.*, 1(7): 677–684, 1956. doi: 10.1080/14786435608244003.

J. P. Hirth and J. Lothe. *Theory of Dislocations*. Krieger Publishing Company, 1992. ISBN 9780894646171.

M. J. Holman and N. W. Murray. The Use of Transit Timing to Detect Terrestrial-Mass Extrasolar Planets. *Science*, 307(5713):1288–1291, 2005. doi: 10.1126/science.1107822.

M. J. Holman, D. C. Fabrycky, D. Ragozzine, E. B. Ford, J. H. Steffen, et al. Kepler-9: A System of Multiple Planets Transiting a Sun-Like Star, Confirmed by Timing Variations. *Science*, 330(6000):51, 2010. doi: 10.1126/science.1195778.

R. Hu, B. L. Ehlmann, and S. Seager. Theoretical Spectra of Terrestrial Exoplanet Surfaces. *Astrophys. J.*, 752(1):7, 2012. doi: 10.1088/0004-637X/752/1/7.

C. X. Huang, C. Petrovich, and E. Deibert. Dynamically Hot Super-Earths from Outer Giant Planet Scattering. *Astrophys. J.*, 153(5):210, 2017. doi: 10.3847/1538-3881/aa67fb.

D. Hull and D. J. Bacon. *Introduction to Dislocations*. Materials science and technology. Elsevier Science, 2011. ISBN 9780080966731.

H. Hussmann and T. Spohn. Thermal-orbital evolution of Io and Europa. *Icarus*, 171(2):391–410, 2004. doi: 10.1016/j.icarus.2004.05.020.

H. Hussmann, G. Choblet, V. Lainey, D. L. Matson, C. Sotin, et al. Implications of Rotation, Orbital States, Energy Sources, and Heat Transport for Internal Processes in Icy Satellites. *Space Sci. Rev.*, 153(1-4):317–348, 2010. doi: 10.1007/s11214-010-9636-0.

P. Hut. Tidal evolution in close binary systems. *Astron. Astrophys.*, 99:126–140, 1981.

J. Irwin, Z. K. Berta, Ch. J. Burke, D. Charbonneau, P. Nutzman, et al. On the Angular Momentum Evolution of Fully Convective Stars: Rotation Periods for

Field M-dwarfs from the MEarth Transit Survey. *Astrophys. J.*, 727(1):56, 2011. doi: 10.1088/0004-637X/727/1/56.

T. Ito and K. Ohtsuka. The Lidov-Kozai Oscillation and Hugo von Zeipel. *Monographs on Environment, Earth and Planets*, 7(1):1–113, 2019. doi: 10.5047/meep.2019.00701.0001.

I. G. Izsak, J. M. Gerard, R. Efimba, and M. P. Barnett. Construction of Newcomb Operators on a Digital Computer. *SAO Special Report*, 140, 1964.

B. Jackson, R. Barnes, and R. Greenberg. Tidal heating of terrestrial extrasolar planets and implications for their habitability. *Mon. Not. R. Astron. Soc.*, 391 (1):237–245, 2008. doi: 10.1111/j.1365-2966.2008.13868.x.

I. Jackson. 2.21 - properties of rocks and minerals: Physical origins of anelasticity and attenuation in rock. In G. Schubert, editor, *Treatise on Geophysics (Second Edition)*, pages 539 – 571. Elsevier, Oxford, second edition edition, 2015. ISBN 978-0-444-53803-1. doi: https://doi.org/10.1016/B978-0-444-53802-4.00045-2.

C. Jaupart, S. Labrosse, and J.-C. Mareschal. Temperatures, heat and energy in the mantle of the earth. In G. Schubert, editor, *Treatise on Geophysics*, pages 253 – 303. Elsevier, Amsterdam, 2007. ISBN 978-0-444-52748-6. doi: https://doi.org/10.1016/B978-044452748-6.00114-0.

H. Jeffreys. Creep in the earth and planets. *Tectonophysics*, 13:569–582, 1972. doi: 10.1016/0040-1951(72)90038-8.

H. Jeffreys. Developments in Geophysics. *Annu. Rev. Earth Planet. Sci.*, 1:1, 1973. doi: 10.1146/annurev.ea.01.050173.000245.

J. S. Jenkins, J. Harrington, R. C. Challener, N. T. Kurtovic, R. Ramirez, et al. Proxima Centauri b is not a transiting exoplanet. *Mon. Not. R. Astron. Soc.*, 487(1):268–274, 2019. doi: 10.1093/mnras/stz1268.

A. S. Jermyn, C. A. Tout, and G. I. Ogilvie. Tidal heating and stellar irradiation of hot Jupiters. *Mon. Not. R. Astron. Soc.*, 469(2):1768–1782, 2017. doi: 10.1093/mnras/stx831.

L. Kaltenegger, W. G. Henning, and D. D. Sasselov. Detecting Volcanism on Extrasolar Planets. *Astron. J.*, 140(5):1370–1380, 2010. doi: 10.1088/0004-6256/140/5/1370.

S. R. Kane and S. M. Torres. Obliquity and Eccentricity Constraints for Terrestrial Exoplanets. *Astrophys. J.*, 154(5):204, 2017. doi: 10.3847/1538-3881/aa8fce.

S. R. Kane, D. M. Gelino, and M. C. Turnbull. On the Orbital Inclination of Proxima Centauri b. *Astrophys. J.*, 153(2):52, 2017. doi: 10.3847/1538-3881/153/2/52.

S. Karato. A Dislocation Model of Seismic Wave Attenuation and Micro-creep in the Earth: Harold Jeffreys and the Rheology of the Solid Earth. *Pure Appl. Geophys.*, 153(2-4):239–256, 1998. doi: 10.1007/s000240050195.

S. Karato. Rheological structure of the mantle of a super-Earth: Some insights from

mineral physics. *Icarus*, 212(1):14–23, 2011. doi: 10.1016/j.icarus.2010.12.005.

S. Karato and H. A. Spetzler. Defect microdynamics in minerals and solid state mechanisms of seismic wave attenuation and velocity dispersion in the mantle. *Rev. Geophys.*, 28(4):399–421, 1990. doi: 10.1029/RG028i004p00399.

S. Karato and H. R. Wenk. *Plastic Deformation of Minerals and Rocks*. Reviews in Mineralogy & Geochemistry. De Gruyter, 2018. ISBN 9781501509285.

J. F. Kasting, D. P. Whitmire, and R. T. Reynolds. Habitable Zones around Main Sequence Stars. *Icarus*, 101(1):108–128, 1993. doi: 10.1006/icar.1993.1010.

W. M. Kaula. Analysis of Gravitational and Geometric Aspects of Geodetic Utilization of Satellites. *Geophys. J. R. Astron. Soc.*, 5(2):104–133, 1961. doi: 10.1111/j.1365-246X.1961.tb00417.x.

W. M. Kaula. Development of the lunar and solar disturbing functions for a close satellite. *Astron. J.*, 67(5):300–303, 1962. doi: 10.1086/108729.

W. M. Kaula. Tidal dissipation by solid friction and the resulting orbital evolution. *Rev. Geophys.*, 2(4):661–685, 1964. doi: 10.1029/RG002i004p00661.

E. S. Kite, E. Gaidos, and M. Manga. Climate instability on tidally locked exoplanets. *Astrophys. J.*, 743(1):41, 2011. doi: 10.1088/0004-637X/743/1/41.

W. Kley and R. P. Nelson. Planet-Disk Interaction and Orbital Evolution. *Annu. Rev. Astron. Astrophys.*, 50:211–249, 2012. doi: 10.1146/annurev-astro-081811-125523.

Z. Kopal. Some remarks on the interpretation of apsidal-motion constants in close binary systems. *Mon. Not. R. Astron. Soc.*, 113:769, 1953. doi: 10.1093/mnras/113.6.769.

R. K. Kopparapu, R. Ramirez, J. F. Kasting, J. F. Kasting, V. Eymet, et al. Habitable Zones around Main-sequence Stars: New Estimates. *Astrophys. J.*, 765(2):131, 2013. doi: 10.1088/0004-637X/765/2/131.

R. K. Kopparapu, R. Ramirez, J. SchottelKotte, J. F. Kasting, S. Domagal-Goldman, et al. Habitable Zones around Main-sequence Stars: Dependence on Planetary Mass. *Astrophys. J. Lett.*, 787(2):L29, 2014. doi: 10.1088/2041-8205/787/2/L29.

J. Korenaga. Urey ratio and the structure and evolution of Earth's mantle. *Rev. Geophys.*, 46(2):RG2007, 2008. doi: 10.1029/2007RG000241.

J. Kovalevsky. *Introduction to celestial mechanics*. Astrophysics and space science library. Springer, New York, 1967. ISBN 978-9401175500.

Y. Kozai. Secular perturbations of asteroids with high inclination and eccentricity. *Astron. J.*, 67:591–598, 1962. doi: 10.1086/108790.

L. Kreidberg. Exoplanet atmosphere measurements from transmission spectroscopy and other planet star combined light observations. In H. J. Deeg and J. A. Belmonte, editors, *Handbook of Exoplanets*, pages 2083–2105. Springer International Publishing, Cham, 2018. ISBN 978-3-319-55333-7. doi:

10.1007/978-3-319-55333-7_100.

L. Kreidberg, J. L. Bean, J.-M. Désert, B. Benneke, D. Deming, et al. Clouds in the atmosphere of the super-Earth exoplanet GJ1214b. *Nature*, 505(7481): 69–72, 2014. doi: 10.1038/nature12888.

A. Lakki and R. Schaller. High Temperature Microplasticity of Fine-Grained Ceramics. *Journal de Physique IV Colloque*, 06(C8):C8–331–C8–340, 1996. doi: 10.1051/jp4:1996872.

L. D. Landau, E. M. Lifshitz, A. M. Kosevich, J. B. Sykes, L. P. Pitaevskii, et al. *Theory of Elasticity: Volume 7*. Course of theoretical physics. Elsevier Science, 1986. ISBN 9780750626330.

J. Laskar. Large-scale chaos in the solar system. *Astron. Astrophys.*, 287:L9–L12, 1994.

J. Laskar. Chaotic diffusion in the Solar System. *Icarus*, 196(1):1–15, 2008. doi: 10.1016/j.icarus.2008.02.017.

J. Laskar and M. Gastineau. Existence of collisional trajectories of Mercury, Mars and Venus with the Earth. *Nature*, 459(7248):817–819, 2009. doi: 10.1038/nature08096.

H. C. P. Lau and U. H. Faul. Anelasticity from seismic to tidal timescales: Theory and observations. *Earth Planet. Sci. Lett.*, 508:18–29, 2019. doi: 10.1016/j.epsl.2018.12.009.

J. Leconte, F. Forget, B. Charnay, R. Wordsworth, and A. Pottier. Increased insolation threshold for runaway greenhouse processes on Earth-like planets. *Nature*, 504(7479):268–271, 2013. doi: 10.1038/nature12827.

J. Leconte, H. Wu, K. Menou, and N. Murray. Asynchronous rotation of Earth-mass planets in the habitable zone of lower-mass stars. *Science*, 347(6222): 632–635, 2015. doi: 10.1126/science.1258686.

S. Lépine and E. Gaidos. An All-sky Catalog of Bright M Dwarfs. *Astron. J.*, 142 (4):138, 2011. doi: 10.1088/0004-6256/142/4/138.

A.-S. Libert and N. Delsate. Interesting dynamics at high mutual inclination in the framework of the Kozai problem with an eccentric perturber. *Mon. Not. R. Astron. Soc.*, 422(3):2725–2736, 2012. doi: 10.1111/j.1365-2966.2012.20855.x.

A.-S. Libert and K. Tsiganis. Kozai resonance in extrasolar systems. *Astron. Astrophys.*, 493(2):677–686, 2009. doi: 10.1051/0004-6361:200810843.

M. L. Lidov. The evolution of orbits of artificial satellites of planets under the action of gravitational perturbations of external bodies. *Planet. Space Sci.*, 9 (10):719–759, 1962. doi: 10.1016/0032-0633(62)90129-0.

M. Lingam and A. Loeb. Implications of Tides for Life on Exoplanets. *Astrobiology*, 18(7):967–982, 2018. doi: 10.1089/ast.2017.1718.

J. J. Lissauer, D. Ragozzine, D. C. Fabrycky, J. H. Steffen, E. B. Ford, et al. Architecture and Dynamics of Kepler's Candidate Multiple Transiting Planet

Systems. *Astrophys. J., Suppl. Ser.*, 197(1):8, 2011. doi: 10.1088/0067-0049/197/1/8.

Y. Lithwick and Y. Wu. Theory of Secular Chaos and Mercury's Orbit. *Astrophys. J.*, 739(1):17, 2011. doi: 10.1088/0004-637X/739/1/31.

H.-P. Liu, D. L. Anderson, and H. Kanamori. Velocity dispersion due to anelasticity; implications for seismology and mantle composition. *Geophys. J.*, 47(1):41–58, 1976. doi: 10.1111/j.1365-246X.1976.tb01261.x.

K. Lodders. Solar System Abundances and Condensation Temperatures of the Elements. *Astrophys. J.*, 591(2):1220–1247, 2003. doi: 10.1086/375492.

R. O. P. Loyd, E. L. Shkolnik, A. C. Schneider, T. S. Barman, V. S. Meadows, et al. HAZMAT. IV. Flares and Superflares on Young M Stars in the Far Ultraviolet. *Astrophys. J.*, 867(1):13, 2018. doi: 10.3847/1538-4357/aae2ae.

M. Lugaro, U. Ott, and Á. Kereszturi. Radioactive nuclei from cosmochronology to habitability. *Prog. Part. Nucl. Phys.*, 102:1–47, 2018. doi: 10.1016/j.ppnp.2018.05.002.

R. Luger, M. Sestovic, E. Kruse, S. L. Grimm, B.-O. Demory, et al. A seven-planet resonant chain in TRAPPIST-1. *Nat. Astron.*, 1:0129, 2017. doi: 10.1038/s41550-017-0129.

G. J. F. MacDonald. The Earth's Free Oscillations. *Science*, 134(3491):1663–1668, 1961. doi: 10.1126/science.134.3491.1663.

G. J. F. MacDonald. Tidal Friction. *Rev. Geophys. Space Phys.*, 2:467–541, 1964. doi: 10.1029/RG002i003p00467.

G. Maciejewski. Planet-star tidal interactions with precise transit timing. *Contrib. Astron. Obs. Skaln. Pleso*, 49(2):334–340, 2019.

V. V. Makarov. Conditions of Passage and Entrapment of Terrestrial Planets in Spin-orbit Resonances. *Astrophys. J.*, 752(1):73, 2012. doi: 10.1088/0004-637X/752/1/73.

V. V. Makarov. Equilibrium Rotation of Semiliquid Exoplanets and Satellites. *Astrophys. J.*, 810(1):12, 2015. doi: 10.1088/0004-637X/810/1/12.

V. V. Makarov and M. Efroimsky. No Pseudosynchronous Rotation for Terrestrial Planets and Moons. *Astrophys. J.*, 764(1):27, 2013. doi: 10.1088/0004-637X/764/1/27.

V. V. Makarov, J. Frouard, and B. Dorland. Forced libration of tidally synchronized planets and moons. *Mon. Not. R. Astron. Soc.*, 456(1):665–671, 2016. doi: 10.1093/mnras/stv2735.

V. V. Makarov, C. T. Berghea, and M. Efroimsky. Spin-orbital Tidal Dynamics and Tidal Heating in the TRAPPIST-1 Multiplanet System. *Astrophys. J.*, 857(2):14, 2018. doi: 10.3847/1538-4357/aab845.

N. Makris. The frequency response function of the creep compliance. *Meccanica*, 54:19–31, 2019. doi: 10.1007/s11012-018-00929-6.

R. A. Marcus, D. Sasselov, L. Hernquist, and S. T. Stewart. Minimum Radii of Super-Earths: Constraints from Giant Impacts. *Astrophys. J. Lett.*, 712(1): L73–L76, 2010. doi: 10.1088/2041-8205/712/1/L73.

Z. Martinec. *Principles of Continuum Mechanics: A Basic Course for Physicists*. Nečas Center Series. Springer International Publishing, 2019. ISBN 9783030053901.

I. Matsuyama and F. Nimmo. Tectonic patterns on reoriented and despun planetary bodies. *Icarus*, 195(1):459–473, 2008. doi: 10.1016/j.icarus.2007.12.003.

I. Matsuyama, M. Beuthe, H. C. F. C. Hay, F. Nimmo, and S. Kamata. Ocean tidal heating in icy satellites with solid shells. *Icarus*, 312:208–230, 2018. doi: 10.1016/j.icarus.2018.04.013.

C. Matyska and D. A. Yuen. The importance of radiative heat transfer on superplumes in the lower mantle with the new post-perovskite phase change [rapid communication]. *Earth Planet. Sci. Lett.*, 234(1-2):71–81, 2005. doi: 10.1016/j.epsl.2004.10.040.

M. Mayor and D. Queloz. A Jupiter-mass companion to a solar-type star. *Nature*, 378(6555):355–359, 1995. doi: 10.1038/378355a0.

M. Mayor and D. Queloz. A search for substellar companions to solar-type stars via precise Doppler measurements: a first Jupiter mass companion detected. In R. Pallavicini and A. K. Dupree, editors, *Cool Stars, Stellar Systems, and the Sun*, volume 109 of *Astronomical Society of the Pacific Conference Series*, page 35, 1996.

W. F. McDonough. Compositional Model for the Earth's Core. *Treatise on Geochemistry*, 2:568, 2003. doi: 10.1016/B0-08-043751-6/02015-6.

V. S. Meadows, G. N. Arney, E. W. Schwieterman, J. Lustig-Yaeger, A. P. Lincowski, et al. The Habitability of Proxima Centauri b: Environmental States and Observational Discriminants. *Astrobiology*, 18(2):133–189, 2018. doi: 10.1089/ast.2016.1589.

F. Mignard. The Evolution of the Lunar Orbit Revisited. I. *Moon and Planets*, 20(3):301–315, 1979. doi: 10.1007/BF00907581.

J. B. Minster and D. L. Anderson. Dislocations and nonelastic processes in the mantle. *J. Geophys. Res.*, 85(B11):6347–6352, 1980. doi: 10.1029/JB085iB11p06347.

J. B. Minster and D. L. Anderson. A Model of Dislocation-Controlled Rheology for the Mantle. *Philos. Trans. R. Soc. A*, 299(1449):319–356, 1981. doi: 10.1098/rsta.1981.0025.

A. Mocquet, O. Grasset, and C. Sotin. Very high-density planets: a possible remnant of gas giants. *Philos. Trans. R. Soc. A*, 372(2014):20130164–20130164, 2014. doi: 10.1098/rsta.2013.0164.

J. Monteux, D. Andrault, and H. Samuel. On the cooling of a deep terrestrial magma ocean. *Earth Planet. Sci. Lett.*, 448:140–149, 2016. doi: 10.1016/j.epsl.2016.05.010.

W. B. Moore. Tidal heating and convection in Io. *J. Geophys. Res.*, 108(E8), 2003. doi: 10.1029/2002JE001943.

W. B. Moore, J. I. Simon, and A. A. G. Webb. Heat-pipe planets. *Earth Planet. Sci. Lett.*, 474:13–19, 2017. doi: 10.1016/j.epsl.2017.06.015.

L. Moresi and V. Solomatov. Mantle convection with a brittle lithosphere: thoughts on the global tectonic styles of the Earth and Venus. *Geophys. J. Int.*, 133(3): 669–682, 1998. doi: 10.1046/j.1365-246X.1998.00521.x.

W. H. Munk and G. J. MacDonald. *The Rotation of the Earth: A Geophysical Discussion*. Cambridge Monographs on Mechanics and Applied Mathematics. Cambridge University Press, 1960. ISBN 9780521207782.

C. D. Murray and S. F. Dermott. *Solar system dynamics*. Cambridge University Press, Cambridge, 1999. ISBN 0-521-57597-4.

P. E. Nacozy and S. S. Dallas. The geopotential in nonsingular orbital elements. *Celestial Mechanics*, 15:453–466, 1977. doi: 10.1007/BF01228611.

F. Namouni. Origin Theories for the Eccentricities of Extrasolar Planets. In Benest D., Froeschle C., and Lega E., editors, *Topics in Gravitational Dynamics. Lecture Notes in Physics, vol 729*, pages 233–256. Springer, Berlin, Heidelberg, 2007.

S. Naoz. The Eccentric Kozai-Lidov Effect and Its Applications. *Annu. Rev. Astron. Astrophys.*, 54:441–489, 2016. doi: 10.1146/annurev-astro-081915-023315.

S. Naoz and D. C. Fabrycky. Mergers and Obliquities in Stellar Triples. *Astrophys. J.*, 793(2):137, 2014. doi: 10.1088/0004-637X/793/2/137.

S. Naoz, B. Kocsis, A. Loeb, and N. Yunes. Resonant Post-Newtonian Eccentricity Excitation in Hierarchical Three-body Systems. *Astrophys. J.*, 773(2):187, 2013. doi: 10.1088/0004-637X/773/2/187.

D. Nesvorný, D. M. Kipping, L. A. Buchhave, G. Á. Bakos, J. Hartman, et al. The Detection and Characterization of a Nontransiting Planet by Transit Timing Variations. *Science*, 336(6085):1133, 2012. doi: 10.1126/science.1221141.

M. Neveu and A. R. Rhoden. Evolution of Saturn's mid-sized moons. *Nat. Astron.*, 3:543–552, 2019. doi: 10.1038/s41550-019-0726-y.

S. Newcomb. A development of the perturbative function in cosines of multiples of the mean anomalies and of angles of multiples of the mean anomalies and of angles between the perihelia and common node and in powers of the eccentricities and mutual inclination. *United States. Nautical Almanac Office. Astronomical paper ; v.5*, 5:1–48, 1895.

L. Noack and D. Breuer. Plate tectonics on rocky exoplanets: Influence of initial conditions and mantle rheology. *Planet. Space Sci.*, 98:41 – 49, 2014. doi: 10.1016/j.pss.2013.06.020.

L. Noack, M. Godolt, P. von Paris, A.-C. Plesa, B. Stracke, et al. Can the interior structure influence the habitability of a rocky planet? *Planet. Space Sci.*, 98:

14–29, 2014. doi: 10.1016/j.pss.2014.01.003.

L. Noack, A. Rivoldini, and T. Van Hoolst. Volcanism and outgassing of stagnant-lid planets: Implications for the habitable zone. *Phys. Earth Planet. Inter.*, 269: 40–57, 2017. doi: 10.1016/j.pepi.2017.05.010.

O. Novotný. *Motions, gravity field and figure of the Earth: lecture notes for post-graduate studies*. Bahia: Instituto de Física, Salvador, 1998.

A. S. Nowick and B. S. Berry. *Anelastic relaxation in crystalline solids*. Academic Press, New York, 1972. ISBN 0125226500.

B. Noyelles, J. Frouard, V. V. Makarov, and M. Efroimsky. Spin-orbit evolution of Mercury revisited. *Icarus*, 241:26–44, 2014. doi: 10.1016/j.icarus.2014.05.045.

G. I. Ogilvie and D. N. C. Lin. Tidal Dissipation in Rotating Giant Planets. *Astrophys. J.*, 610(1):477–509, 2004. doi: 10.1086/421454.

E. Ohtani, Y. Nagata, A. Suzuki, and T. Kato. Melting relations of peridotite and the density crossover in planetary mantles. *Chem. Geol.*, 120(3-4):207–221, 1995. doi: 10.1016/0009-2541(94)00139-Y.

G. W. Ojakangas and D. J. Stevenson. Episodic volcanism of tidally heated satellites with application to Io. *Icarus*, 66(2):341–358, 1986. doi: 10.1016/0019-1035(86)90163-6.

C. O'Neill and A. Lenardic. Geological consequences of super-sized Earths. *Geophys. Res. Lett.*, 34(19):L19204, 2007. doi: 10.1029/2007GL030598.

C. O'Neill, A. Lenardic, A. M. Jellinek, and W. S. Kiefer. Melt propagation and volcanism in mantle convection simulations, with applications for Martian volcanic and atmospheric evolution. *J. Geophys. Res.*, 112(E7):E07003, 2007. doi: 10.1029/2006JE002799.

C. O'Neill, J. Lowman, and J. Wasiliev. The effect of galactic chemical evolution on terrestrial exoplanet composition and tectonics. *Icarus*, 352:114025, 2020. doi: 10.1016/j.icarus.2020.114025.

E. Orowan. Zur Kristallplastizität. III. *Z. Phys.*, 89(9-10):634–659, 1934. doi: 10.1007/BF01341480.

I. Z. Palubski, A. L. Shields, and R. Deitrick. Habitability and Water Loss Limits on Eccentric Planets Orbiting Main-sequence Stars. *Astrophys. J.*, 890(1):30, 2020. doi: 10.3847/1538-4357/ab66b2.

J. C. B. Papaloizou, E. Szuszkiewicz, and C. Terquem. The TRAPPIST-1 system: orbital evolution, tidal dissipation, formation and habitability. *Mon. Not. R. Astron. Soc.*, 476(4):5032–5056, 2018. doi: 10.1093/mnras/stx2980.

S. J. Peale. Generalized Cassini's Laws. *Astron. J.*, 74(3):483–489, 1969. doi: 10.1086/110825.

S. J. Peale. Orbital resonance in the solar system. *Annu. Rev. Astron. Astrophys.*, 14:215–246, 1976. doi: 10.1146/annurev.aa.14.090176.001243.

S. J. Peale and P. Cassen. Contribution of tidal dissipation to lunar thermal

history. *Icarus*, 36(2):245–269, 1978. doi: 10.1016/0019-1035(78)90109-4.

S. J. Peale and T. Gold. Rotation of the Planet Mercury. *Nature*, 206(4990): 1240–1241, 1965. doi: 10.1038/2061240b0.

S. J. Peale, P. Cassen, and R. T. Reynolds. Melting of Io by Tidal Dissipation. *Science*, 203(4383):892–894, 1979. doi: 10.1126/science.203.4383.892.

W. R. Peltier. The impulse response of a Maxwell earth. *Rev. Geophys.*, 12: 649–669, 1974. doi: 10.1029/RG012i004p00649.

W. R. Peltier, D. A. Yuen, and P. Wu. Postglacial rebound and transient rheology. *Geophys. Res. Lett.*, 7(10):733–736, 1980. doi: 10.1029/GL007i010p00733.

W. R. Peltier, P. Wu, and D. A. Yuen. The viscosities of the earth's mantle. In F. D. Stacey, M. S. Paterson, and A. Nicholas, editors, *Anelasticity in the Earth*, pages 59–77. American Geophysical Union (AGU), Washington, DC, 1981. ISBN 9781118669945. doi: https://doi.org/10.1029/GD004p0059.

G. Petit and B. Luzum. IERS Conventions (2010). *IERS Technical Note*, 36:1, 2010.

C. Petrovich. Steady-state Planet Migration by the Kozai-Lidov Mechanism in Stellar Binaries. *Astrophys. J.*, 799(1):27, 2015. doi: 10.1088/0004-637X/799/1/27.

C. Petrovich, S. Tremaine, and R. Rafikov. Scattering outcomes of close-in planets: constraints on planet migration. *Astrophys. J.*, 786(2):101, 2014. doi: 10.1088/0004-637x/786/2/101.

G. H. Pettengill and R. B. Dyce. A Radar Determination of the Rotation of the Planet Mercury. *Nature*, 206(4990):1240, 1965. doi: 10.1038/2061240a0.

A.-C. Plesa and T. Spohn. The Influence of Partial Melt on Mantle Convection. In W. Nagel, D. Kröner, and M. Resch, editors, *High Performance Computing in Science and Engineering '11*. Springer, 2012.

J. P. Poirier, L. Boloh, and P. Chambon. Tidal dissipation in small viscoelastic ice moons: The case of Enceladus. *Icarus*, 55(2):218–230, 1983. doi: 10.1016/0019-1035(83)90076-3.

W. H. Press, S. A. Teukolsky, W. T. Vetterling, and B. P. Flannery. *Numerical recipes in FORTRAN: the art of scientific computing*. Cambridge University Press, second edition, 1992.

B. Pu and D. Lai. Eccentricities and inclinations of multiplanet systems with external perturbers. *Mon. Not. R. Astron. Soc.*, 478(1):197–217, 2018. doi: 10.1093/mnras/sty1098.

E. Ragusa, G. Rosotti, J. Teyssandier, R. Booth, Cathie J. Clarke, et al. Eccentricity evolution during planet-disc interaction. *Mon. Not. R. Astron. Soc.*, 474 (4):4460–4476, 2018. doi: 10.1093/mnras/stx3094.

R. Raj and M. F. Ashby. On grain boundary sliding and diffusional creep. *Metallurgical Transactions*, 2:1113–1127, 1971. doi: 10.1007/BF02664244.

A. Ralston. *A First Course in Numerical Analysis*. McGraw-Hill, New York, 1965. ISBN 978-0-0705-1157-6.

M. Reimer. *Gegenbauer Polynomials*, pages 19–38. Birkhäuser Basel, Basel, 2003. ISBN 978-3-0348-8095-4. doi: 10.1007/978-3-0348-8095-4_2.

H. Rein and S.-F. Liu. REBOUND: an open-source multi-purpose N-body code for collisional dynamics. *Astron. Astrophys.*, 537:A128, 2012. doi: 10.1051/0004-6361/201118085.

F. Remus, S. Mathis, J.-P. Zahn, and V. Lainey. Anelastic tidal dissipation in multi-layer planets. *Astron. Astrophys.*, 541:A165, 2012. doi: 10.1051/0004-6361/201118595.

J. P. Renaud and W. G. Henning. Increased Tidal Dissipation Using Advanced Rheological Models: Implications for Io and Tidally Active Exoplanets. *Astrophys. J.*, 857(2):29, 2018. doi: 10.3847/1538-4357/aab784.

A. R. Rhoden, G. Wurman, E. M. Huff, M. Manga, and T. A. Hurford. Shell tectonics: A mechanical model for strike-slip displacement on Europa. *Icarus*, 218(1):297–307, 2012. doi: 10.1016/j.icarus.2011.12.015.

I. Ribas, E. Bolmont, F. Selsis, A. Reiners, J. Leconte, et al. The habitability of Proxima Centauri b. I. Irradiation, rotation and volatile inventory from formation to the present. *Astron. Astrophys.*, 596:A111, 2016. doi: 10.1051/0004-6361/201629576.

K. Rice. The Detection and Characterization of Extrasolar Planets. *Challenges*, 5:296–323, 2014. doi: 10.3390/challe5020296.

G. R. Ricker, J. N. Winn, R. Vanderspek, David W. Latham, Gáspár Á. Bakos, et al. Transiting Exoplanet Survey Satellite (TESS). *J. Astron. Telesc. Instrum. Syst.*, 1:014003, 2015. doi: 10.1117/1.JATIS.1.1.014003.

L. A. Rogers. Most 1.6 Earth-radius Planets are Not Rocky. *Astrophys. J.*, 801 (1):41, 2015. doi: 10.1088/0004-637X/801/1/41.

M. Rovira-Navarro, M. Rieutord, T. Gerkema, L. R. M. Maas, W. der Wal, et al. Do tidally-generated inertial waves heat the subsurface oceans of Europa and Enceladus? *Icarus*, 321:126–140, 2019. doi: 10.1016/j.icarus.2018.11.010.

D. P. Rubincam. General relativity and satellite orbits: the motion of a test particle in the Schwarzschild metric. *Celestial mechanics*, 15(1):21–33, 1977. doi: 10.1007/BF01229045.

H. N. Russell. On the advance of periastron in eclipsing binaries. *Mon. Not. R. Astron. Soc.*, 88:641–643, 1928. doi: 10.1093/mnras/88.8.641.

R. Sabadini and B. Vermeersen. *Global Dynamics of the Earth: Applications of Normal Mode Relaxation Theory to Solid-Earth Geophysics*. Kluwer Academic Publishers, Dodrech, the Netherlands, 2004. ISBN 1-4020-2135-6.

N. C. Santos. Extra-solar planets: Detection methods and results. *New Astron. Rev.*, 52(2-5):154–166, 2008. doi: 10.1016/j.newar.2008.04.011.

N. C. Santos and J. P. Faria. Exoplanetary Science: An Overview. In Tiago L. Campante, Nuno C. Santos, and Mário J. P. F. G. Monteiro, editors, *Asteroseismology and Exoplanets: Listening to the Stars and Searching for New Worlds*, volume 49, page 165, 2018. doi: 10.1007/978-3-319-59315-9_9.

G. Schoeck, E. Bisogni, and J. Shyne. The activation energy of high temperature internal friction. *Acta Metallurgica*, 12(12):1466 – 1468, 1964. ISSN 0001-6160. doi: https://doi.org/10.1016/0001-6160(64)90141-5.

G. Schubert, D. L. Turcotte, and P. Olson. *Mantle Convection in the Earth and Planets*. Cambridge University Press, Cambridge, 2004. ISBN 0-521-79836-1.

G. Schubert, H. Hussmann, V. Lainey, D. L. Matson, W. B. McKinnon, et al. Evolution of Icy Satellites. *Space Sci. Rev.*, 153(1-4):447–484, 2010. doi: 10.1007/s11214-010-9635-1.

E. W. Schwieterman, C. T. Reinhard, S. L. Olson, C. E. Herman, and T. W. Lyons. A Limited Habitable Zone for Complex Life. *Astrophys. J.*, 878(1):9, 2019. doi: 10.3847/1538-4357/ab1d52.

S. Seager. Exoplanet Habitability. *Science*, 340(6132):577–581, 2013. doi: 10.1126/science.1232226.

S. Seager and Lam Hui. Constraining the Rotation Rate of Transiting Extrasolar Planets by Oblateness Measurements. *Astrophys. J.*, 574(2):1004–1010, 2002. doi: 10.1086/340994.

M. Segatz, T. Spohn, M. N. Ross, and G. Schubert. Tidal Dissipation, Surface Heat Flow, and Figure of Viscoelastic Models of Io. *Icarus*, 75(2):187–206, 1988. doi: 10.1016/0019-1035(88)90001-2.

F. Selsis, A. S. Maurin, F. Hersant, J. Leconte, E. Bolmont, et al. The effect of rotation and tidal heating on the thermal lightcurves of super Mercuries. *Astron. Astrophys.*, 555:A51, 2013. doi: 10.1051/0004-6361/201321661.

C. J. Shallue and A. Vanderburg. Identifying Exoplanets with Deep Learning: A Five-planet Resonant Chain around Kepler-80 and an Eighth Planet around Kepler-90. *Astron. J.*, 155(2):94, 2018. doi: 10.3847/1538-3881/aa9e09.

D. Shoji and K. Kurita. Thermal-Orbital Coupled Tidal Heating and Habitability of Martian-sized Extrasolar Planets around M Stars. *Astrophys. J.*, 789(1):12, 2014. doi: 10.1088/0004-637X/789/1/3.

A. Socrates, B. Katz, S. Dong, and S. Tremaine. Super-eccentric Migrating Jupiters. *Astrophys. J.*, 750(2):106, 2012. doi: 10.1088/0004-637X/750/2/106.

I. S. Sokolnikoff. *Mathematical theory of elasticity*. Second edition. McGraw-Hill„ New York, 1956. ISBN 978-0070596290.

V. S. Solomatov. Scaling of temperature- and stress-dependent viscosity convection. *Phys. Fluids.*, 7(2):266–274, 1995. doi: 10.1063/1.868624.

C. Sotin, G. Tobie, J. Wahr, and W. B. McKinnon. Tides and tidal heating on Europa. In R T Pappalardo, W B McKinnon, and K. Khurana, editors, *Europa*,

pages 85–117. University of Arizona Press Tuscon, 2009.

O. Souček, J. Hron, M. Běhounková, and O. Čadek. Effect of the tiger stripes on the deformation of Saturn's moon Enceladus. *Geophys. Res. Lett.*, 43(14): 7417–7423, 2016. doi: 10.1002/2016GL069415.

Ch. Spalding and S. C. Millholland. Stellar Oblateness versus Distant Giants in Exciting Kepler Planet Mutual Inclinations. *Astron. J.*, 160(3):105, 2020. doi: 10.3847/1538-3881/aba629.

M. Spiegelman. Physics of Melt Extraction: Theory, Implications and Applications. *Philos. Trans. R. Soc. A*, 342(1663):23–41, 1993. doi: 10.1098/rsta.1993.0002.

T. Spohn. Mantle differentiation and thermal evolution of Mars, Mercury, and Venus. *Icarus*, 90(2):222–236, 1991. doi: 10.1016/0019-1035(91)90103-Z.

F. D. Stacey. The theory of creep in rocks and the problem of convection in the Earth's mantle. *Icarus*, 1(1-6):304–312, 1963. doi: 10.1016/0019-1035(62)90028-3.

V. Stamenković, L. Noack, D. Breuer, and T. Spohn. The Influence of Pressure-dependent Viscosity on the Thermal Evolution of Super-Earths. *Astrophys. J.*, 748(1):41, 2012. doi: 10.1088/0004-637X/748/1/41.

K. G. Stassun, K. A. Collins, and B. S. Gaudi. Accurate Empirical Radii and Masses of Planets and Their Host Stars with Gaia Parallaxes. *Astron. J.*, 153 (3):136, 2017. doi: 10.3847/1538-3881/aa5df3.

T. Steinke, H. Hu, D. Höning, W. van der Wal, and B. Vermeersen. Tidally induced lateral variations of Io's interior. *Icarus*, 335:113299, 2020. doi: 10.1016/j.icarus.2019.05.001.

T. E. Sterne. Apsidal motion in binary stars. *Mon. Not. R. Astron. Soc.*, 99: 451–462, 1939. doi: 10.1093/mnras/99.5.451.

N. I. Storch and D. Lai. Viscoelastic tidal dissipation in giant planets and formation of hot Jupiters through high-eccentricity migration. *Mon. Not. R. Astron. Soc.*, 438(2):1526–1534, 2014. doi: 10.1093/mnras/stt2292.

N. I. Storch and D. Lai. Analytical model of tidal distortion and dissipation for a giant planet with a viscoelastic core. *Mon. Not. R. Astron. Soc.*, 450(4): 3952–3957, 2015. doi: 10.1093/mnras/stv904.

K. G. Strassmeier, T. A. Carroll, M. Weber, T. Granzer, J. Bartus, et al. Binary-induced magnetic activity?. Time-series echelle spectroscopy and photometry of HD 123351 = CZ CVn. *Astron. Astrophys.*, 535:A98, 2011. doi: 10.1051/0004-6361/201117167.

A. Suárez Mascareño, J. I. González Hernández, R. Rebolo, S. Velasco, B. Toledo-Padrón, et al. HADES RV Programme with HARPS-N at TNG. V. A super-Earth on the inner edge of the habitable zone of the nearby M dwarf GJ 625. *Astron. Astrophys.*, 605(A92):15, 2017. doi: 10.1051/0004-6361/201730957.

G. Suissa, J. Chen, and D. Kipping. A HARDCORE model for constraining an

exoplanet's core size. *Mon. Not. R. Astron. Soc.*, 476(2):2613–2620, 2018. doi: 10.1093/mnras/sty381.

M. Sundberg and R. F. Cooper. A composite viscoelastic model for incorporating grain boundary sliding and transient diffusion creep; correlating creep and attenuation responses for materials with a fine grain size. *Philos. Mag.*, 90(20): 2817–2840, 2010. doi: 10.1080/14786431003746656.

M R. Swain, R. Estrela, Ch. Sotin, G M. Roudier, and R T. Zellem. Two Terrestrial Planet Families with Different Origins. *Astrophys. J.*, 881(2):117, 2019. doi: 10.3847/1538-4357/ab2714.

A. Szeto and K. Lambeck. On Eccentricity Functions for Eccentric Orbits. *Celestial Mechanics*, 27(4):325–337, 1982. doi: 10.1007/BF01228558.

G. Takeda and F. A. Rasio. High Orbital Eccentricities of Extrasolar Planets Induced by the Kozai Mechanism. *Astrophys. J.*, 627(2):1001–1010, 2005. doi: 10.1086/430467.

H. Takeuchi and M. Saito. Seismic Surface Waves. *Methods in Computational Physics: Advances in Research and Applications*, 11:217–295, 1972. doi: 10.1016/B978-0-12-460811-5.50010-6.

H. Takeuchi, M. Saito, and N. Kobayashi. Statical Deformations and Free Oscillations of a Model Earth. *J. Geophys. Res.*, 67(3):1141–1154, 1962. doi: 10.1029/JZ067i003p01141.

O. Tamuz, D. Ségransan, S. Udry, M. Mayor, A. Eggenberger, et al. The CORALIE survey for southern extra-solar planets. XV. Discovery of two eccentric planets orbiting HD 4113 and HD 156846. *Astron. Astrophys.*, 480(3):L33–L36, 2008. doi: 10.1051/0004-6361:20078737.

G. I. Taylor. The Mechanism of Plastic Deformation of Crystals. Part I. Theoretical. *Proc. R. Soc. A*, 145(855):362–387, 1934. doi: 10.1098/rspa.1934.0106.

F. Thévenin, J. Provost, P. Morel, G. Berthomieu, F. Bouchy, et al. Asteroseismology and calibration of alpha Cen binary system. *Astron. Astrophys.*, 392: L9–L12, 2002. doi: 10.1051/0004-6361:20021074.

A. Thiabaud, U. Marboeuf, Y. Alibert, N. Cabral, I. Leya, et al. From stellar nebula to planets: The refractory components. *Astron. Astrophys.*, 562:A27, 2014. doi: 10.1051/0004-6361/201322208.

F. Thomas and A. Morbidelli. The Kozai Resonance in the Outer Solar System and the Dynamics of Long-Period Comets. *Celest. Mech. Dyn. Astron.*, 64(3): 209–229, 1996. doi: 10.1007/BF00728348.

W. Thomson and P. G. Tait. *Treatise on Natural Philosophy*. Number Part II in Treatise on Natural Philosophy. Cambridge University Press, Cambridge, 1895.

F. Tisserand. *Traité de Mécanique Céleste*. Tome I. Gauthier-Villars et fils, Paris, 1889.

G. Tobie, O. Grasset, J. I. Lunine, A. Mocquet, and S. Sotin. Tidal dissipation

within large icy satellites: Applications to Europa and Titan. *Icarus*, 175(2): 496–502, 2005a. doi: 10.1016/j.icarus.2004.12.007.

G. Tobie, A. Mocquet, and C. Sotin. Titan's internal structure inferred from a coupled thermal-orbital model. *Icarus*, 177(2):534 – 549, 2005b. doi: 10.1016/j.icarus.2005.04.006.

G. Tobie, O. Čadek, and C. Sotin. Solid tidal friction above a liquid water reservoir as the origin of the South Pole Hotspot on Enceladus. *Icarus*, 196(2):642–652, 2008. doi: 10.1016/j.icarus.2008.03.008.

G. Tobie, O. Grasset, C. Dumoulin, and A. Mocquet. Tidal response of rocky and ice-rich exoplanets. *Astron. Astrophys.*, 630:A70, 2019. doi: 10.1051/0004-6361/201935297.

N. Tosi, M. Godolt, B. Stracke, T. Ruedas, J. L. Grenfell, et al. The habitability of a stagnant-lid Earth. *Astron. Astrophys.*, 605(A71):21, 2017. doi: 10.1051/0004-6361/201730728.

Y. Tsapras. Microlensing Searches for Exoplanets. *Geosciences*, 8(10):365, 2018. doi: 10.3390/geosciences8100365.

A. Tsiaras, I. P. Waldmann, G. Tinetti, J. Tennyson, and S. N. Yurchenko. Water vapour in the atmosphere of the habitable-zone eight-Earth-mass planet K2-18 b. *Nat. Astron.*, 3:1086–1091, 2019. doi: 10.1038/s41550-019-0878-9.

M. Turbet, J. Leconte, F. Selsis, E. Bolmont, F. Forget, et al. The habitability of Proxima Centauri b. II. Possible climates and observability. *Astron. Astrophys.*, 596(A112):29, 2016. doi: 10.1051/0004-6361/201629577.

R. H. Tyler, W. G. Henning, and C. W. Hamilton. Tidal Heating in a Magma Ocean within Jupiter's Moon Io. *Astrophys. J., Suppl. Ser.*, 218(2):22, 2015. doi: 10.1088/0067-0049/218/2/22.

S. Udry, X. Dumusque, C. Lovis, D. Ségransan, R. F. Diaz, et al. The HARPS search for southern extra-solar planets. XLIV. Eight HARPS multi-planet systems hosting 20 super-Earth and Neptune-mass companions. *Astron. Astrophys.*, 622:A37, 2019. doi: 10.1051/0004-6361/201731173.

A. A. Vakhidov. Some Recurrence Relations Between Hansen Coefficients. *Celest. Mech. Dyn. Astron.*, 81(3):177–190, 2001.

D. Valencia and R. J. O'Connell. Convection scaling and subduction on Earth and super-Earths. *Earth Planet. Sci. Lett.*, 286(3-4):492–502, 2009. doi: 10.1016/j.epsl.2009.07.015.

D. Valencia, R. J. O'Connell, and D. Sasselov. Internal structure of massive terrestrial planets. *Icarus*, 181(2):545–554, 2006. doi: 10.1016/j.icarus.2005.11.021.

D. Valencia, R. J. O'Connell, and D. D. Sasselov. Inevitability of Plate Tectonics on Super-Earths. *Astrophys. J. Lett.*, 670(1):L45–L48, 2007. doi: 10.1086/524012.

D. Valencia, V. Y. Y. Tan, and Z. Zajac. Habitability from Tidally Induced

Tectonics. *Astrophys. J.*, 857(2):13, 2018. doi: 10.3847/1538-4357/aab767.

A. P. van den Berg, D. A. Yuen, G. L. Beebe, and M. D. Christiansen. The dynamical impact of electronic thermal conductivity on deep mantle convection of exosolar planets. *Phys. Earth Planet. Inter.*, 178(3-4):136–154, 2010. doi: 10.1016/j.pepi.2009.11.001.

V. Van Eylen and S. Albrecht. Eccentricity from Transit Photometry: Small Planets in Kepler Multi-planet Systems Have Low Eccentricities. *Astrophys. J.*, 808(2):126, 2015. doi: 10.1088/0004-637X/808/2/126.

V. Van Eylen, S. Albrecht, and X. Huang. The Orbital Eccentricity of Small Planet Systems. *Astron. J.*, 157(2):16, 2019. doi: 10.3847/1538-3881/aaf22f.

H. J. van Heck and P. J. Tackley. Plate tectonics on super-Earths: Equally or more likely than on Earth. *Earth Planet. Sci. Lett.*, 310(3):252–261, 2011. doi: 10.1016/j.epsl.2011.07.029.

J. van Summeren, C. P. Conrad, and E. Gaidos. Mantle convection, plate tectonics, and volcanism on hot exo-Earths. *Astrophys. J. Lett.*, 736(L15), 2011. doi: 10.1088/2041-8205/736/L15.

F. Varadi. Periodic Orbits in the 3:2 Orbital Resonance and Their Stability. *Astron. J.*, 118(5):2526–2531, 1999. doi: 10.1086/301088.

D. A. Varshalovich, A. N. Moskalev, and V. K. Khersonskii. *Quantum theory of angular momentum: irreducible tensors, spherical harmonics, vector coupling coefficients, 3nj symbols*. World Scientific, Singapore, 1988. ISBN 9971-50-996-2.

G. J. Veeder, D. L. Matson, and T. V. Johnson. Io's heat flow from infrared radiometry: 1983-1993. *J. Geophys. Res.*, 99(E8):17095–17162, 1994. doi: 10.1029/94JE00637.

D. Veras, M. Efroimsky, V. V. Makarov, G. Boué, V. Wolthoff, et al. Orbital relaxation and excitation of planets tidally interacting with white dwarfs. *Mon. Not. R. Astron. Soc.*, 486(3):3831–3848, 2019. doi: 10.1093/mnras/stz965.

K. Vilella and E. Kaminski. Fully determined scaling laws for volumetrically heated convective systems, a tool for assessing habitability of exoplanets. *Phys. Earth Planet. Inter.*, 266:18 – 28, 2017. doi: 10.1016/j.pepi.2017.02.001.

H. von Zeipel. Sur l'application des séries de M. Lindstedt à l'étude du mouvement des comètes périodiques. *Astron. Nachr.*, 183(22):345, 1910. doi: 10.1002/asna.19091832202.

H. Von Zeipel. Sur le calcul des opérateurs de Newcomb. *Ark. Mat. Astro. Fys.*, 8 (19):9, 1912.

S. M. Wahl, W. B. Hubbard, and B. Militzer. The Concentric Maclaurin Spheroid method with tides and a rotational enhancement of Saturn's tidal response. *Icarus*, 282:183–194, 2017. doi: 10.1016/j.icarus.2016.09.011.

J. C. G. Walker, P. B. Hays, and J. F. Kasting. Carbon Cycling and Habitability of Earth-Sized Stagnant Lid Planets. *J. Geophys. Res.*, 86(C10):9776–9782,

1981. doi: 10.1029/JC086iC10p09776.

M. Walterová and M. Běhounková. Thermal and orbital evolution of low-mass exoplanets. *Astrophys. J.*, 900(1):24, 2020. doi: 10.3847/1538-4357/aba8a5.

M. Walterová and M. Běhounková. Tidal effects in differentiated viscoelastic bodies: a numerical approach. *Celest. Mech. Dyn. Astron.*, 129(1-2):235–256, 2017. doi: 10.1007/s10569-017-9772-x.

A. Wandel. On the Biohabitability of M-dwarf Planets. *Astrophys. J.*, 856(2):13, 2018. doi: 10.3847/1538-4357/aaae6e.

A. Wandel and J. Gale. The bio-habitable zone and atmospheric properties for planets of red dwarfs. *Int. J. Astrobiol.*, 19(2):126–135, 2020. doi: 10.1017/S1473550419000235.

W.-L. Wang, X.-Q. Xu, and X.-H. Liao. Orbital evolution of a planet with tidal dissipation in a restricted three-body system. *Res. Astron. Astrophys.*, 19(9): 130, 2019. doi: 10.1088/1674-4527/19/9/130.

Y. Wang, J.-L. Zhou, L. Hui-Gen, and Z. Meng. Forming Different Planetary Architectures. I. The Formation Efficiency of Hot Jupiters from High-eccentricity Mechanisms. *Astrophys. J.*, 848(1):20, 2017. doi: 10.3847/1538-4357/aa8868.

W. R. Ward. Tidal friction and generalized Cassini's laws in the solar system. *Astron. J.*, 80:64–70, 1975. doi: 10.1086/111714.

W. R. Ward, R. M. Canup, and R. Rufu. Analytical Model for the Tidal Evolution of the Evection Resonance and the Timing of Resonance Escape. *J. Geophys. Res. Planets*, 125(6):e06266, 2020. doi: 10.1029/2019JE006266.

L. M. Weiss and G. W. Marcy. The Mass-Radius Relation for 65 Exoplanets Smaller than 4 Earth Radii. *Astrophys. J. Lett.*, 783(1):L6, 2014. doi: 10.1088/2041-8205/783/1/L6.

M. B. Weller, A. Lenardic, and C. O'Neill. The effects of internal heating and large scale climate variations on tectonic bi-stability in terrestrial planets. *Earth Planet. Sci. Lett.*, 420:85–94, 2015. doi: 10.1016/j.epsl.2015.03.021.

P. T. Williams. Turbulent magnetohydrodynamic elasticity: Boussinesq-like approximations for steady shear. *New Astron.*, 10(2):133–144, 2004. doi: 10.1016/j.newast.2004.03.006.

J. N. Winn and M. J. Holman. Obliquity Tides on Hot Jupiters. *Astrophys. J. Lett.*, 628(2):L159–L162, 2005. doi: 10.1086/432834.

O. C. Winter and C. D. Murray. Resonance and chaos. I. First-order interior resonances. *Astron. Astrophys.*, 319:290–304, 1997.

J. Wisdom and Z. L. Tian. Early evolution of the Earth-Moon system with a fast-spinning Earth. *Icarus*, 256:138–146, 2015. doi: 10.1016/j.icarus.2015.02.025.

E. Wnuk. The inclination function for high values of indices. *Acta Astron.*, 38(2): 127–140, 1988.

E. Wnuk. Highly eccentric satellite orbits. *Adv. Space Res.*, 19(11):1735–1740,

1997. doi: 10.1016/S0273-1177(97)00336-0.

A. Wolfgang, L. A. Rogers, and E. B. Ford. Probabilistic Mass-Radius Relationship for Sub-Neptune-Sized Planets. *Astrophys. J.*, 825(1):19, 2016. doi: 10.3847/0004-637X/825/1/19.

J. T. Wright. Radial velocities as an exoplanet discovery method. In H. J. Deeg and J. A. Belmonte, editors, *Handbook of Exoplanets*, pages 619–631. Springer International Publishing, Cham, 2018. ISBN 978-3-319-55333-7. doi: 10.1007/978-3-319-55333-7_4.

J. T. Wright and G. B. Scott. Exoplanet detection methods. In T. D. Oswalt, L. M. French, and P. Kalas, editors, *Planets, Stars and Stellar Systems: Volume 3: Solar and Stellar Planetary Systems*, pages 489–540. Springer Netherlands, Dordrecht, 2013. ISBN 978-94-007-5606-9. doi: 10.1007/978-94-007-5606-9_10.

P. Wu and W. R. Peltier. Viscous gravitational relaxation. *Geophys. J.*, 70(2): 435–485, 1982. doi: 10.1111/j.1365-246X.1982.tb04976.x.

Y. Wu and N. Murray. Planet Migration and Binary Companions: The Case of HD 80606b. *Astrophys. J.*, 589(1):605–614, 2003. doi: 10.1086/374598.

C. F. Yoder. Tidal rigidity of phobos. *Icarus*, 49(3):327–346, 1982. doi: 10.1016/0019-1035(82)90040-9.

D. A. Yuen and W. R. Peltier. Normal modes of the viscoelastic earth. *Geophys. J.*, 69:495–526, 1982. doi: 10.1111/j.1365-246X.1982.tb04962.x.

J. J. Zanazzi and D. Lai. Triaxial deformation and asynchronous rotation of rocky planets in the habitable zone of low-mass stars. *Mon. Not. R. Astron. Soc.*, 469 (3):2879–2885, 2017. doi: 10.1093/mnras/stx1076.

J. J. Zanazzi and A. H. M. J. Triaud. The ability of significant tidal stress to initiate plate tectonics. *Icarus*, 325:55–66, 2019. doi: 10.1016/j.icarus.2019.01.029.

C. Zener. *Elasticity and Anelasticity of Metals*. University of Chicago Press, Chicago, 1948.

L. Zeng and D. Sasselov. A Detailed Model Grid for Solid Planets from 0.1 through 100 Earth Masses. *Publ. Astron. Soc. Pac*, 125(925):227, 2013. doi: 10.1086/669163.

L. Zeng, D. D. Sasselov, and S. B. Jacobsen. Mass-Radius Relation for Rocky Planets Based on PREM. *Astrophys. J.*, 819(2), 2016. doi: 10.3847/0004-637X/819/2/127.

L. Zeng, S. B. Jacobsen, D. D. Sasselov, M. I. Petaev, A. Vanderburg, et al. Growth model interpretation of planet size distribution. *Proc. Natl. Acad. Sci. U.S.A.*, 116(20):9723–9728, 2019. doi: 10.1073/pnas.1812905116.

W. Zhu, C. X. Huang, G. Zhou, and D. N. C. Lin. Constraining the Oblateness of Kepler Planets. *Astrophys. J.*, 796(1):67, 2014. doi: 10.1088/0004-637X/796/1/67.

List of Abbreviations

CMB	core–mantle boundary
CMF	core mass fraction
h.t.b.	high temperature background
PSR	pseudo–synchronous rotation
RV	radial velocity
SAS	standard anelastic solid
SLS	standard linear solid
TBL	thermal boundary layer
TTV	transit–timing variation

List of Symbols

Listed are only symbols relevant to the discussed models and derivations. Auxiliary symbols introduced in the text (e.g., the total mass $\mathcal{M}$ in the two–body problem) are not included.

Universal constants and variables

Orbital elements are often used with subscripts.

c	speed of light
$\mathcal{G}$	universal gravitational constant
$m_\oplus$	Earth mass
$m_\odot$	solar mass
R_{gas}	universal gas constant
$\mathcal{F}_{lmp}(i)$	Kaula's inclination functions
$\mathcal{G}_{lpq}(e)$	eccentricity functions for an inner perturber
$\Gamma(x)$	gamma function
$\mathcal{H}_{lpq}(e)$	eccentricity functions for an outer perturber
$\mathcal{P}_{lm}(x)$	associated Legendre polynomials
$X_j^{n,k}(e)$	Hansen's coefficients
a	semi–major axis
e	orbital eccentricity
$\mathcal{E}$	energy
$\mathcal{E}^*$	activation energy
g	gravitational acceleration (typically on the surface)
i	orbital inclination
k_l	tidal Love number (real)
$\bar{k}_l(\omega)$	tidal Love number (complex)
m_*	stellar mass
n	mean motion axis
Q	quality factor
R	planetary radius
v	true anomaly

Chapter 1: Secular orbital evolution

C	principal moment of inertia
ϵ	mean longitude at epoch

ε_{lmpq}, ε_{c}	phase lag (mode–dependent or constant)
Φ	potential
$J^{n,k}_{\rho,\sigma}$	integer–valued polynomials
λ	mean longitude
M	mean anomaly
m_1	mass of the inner planet
m_2	mass of the outer planet
μ	reduced mass
ω	argument of periapsis
ω_{lmpq}	loading frequency (signed)
Ω	longitude of the ascending node
ϖ	longitude of periapsis
r	instantaneous star–planet distance
$\mathcal{R}$	disturbing function
$\varrho, \vartheta, \varphi$	planetocentric equatorial spherical coordinates (radius, colatitude, longitude)
σ	mean anomaly at epoch
t_0	time of periapsis passage
Δt	time lag
T	orbital period
$\mathcal{T}$	secular tidal torque
θ	sidereal time
$X^{n,k}_{\rho,\sigma}$	Newcomb's operators
ξ, η, ζ, ν	nonsingular elements

Chapter 2: Interior structure and dynamics

Δ	relaxation strength
E	Young modulus
$\epsilon, \bar{\epsilon}$	strain (1d, time domain or frequency domain)
$\boldsymbol{\epsilon}$	Eulerian strain tensor
$\boldsymbol{\epsilon}^{\mathrm{D}}$	deviatoric part of $\boldsymbol{\epsilon}$
ε	phase lag (loss angle)
η	dynamic viscosity (3d)
F	Newtonian viscosity (1d)
h	volumetric heat rate
$J(t)$	creep function
J_{R}	relaxed compliance
J_{U}	unrelaxed compliance
$\bar{J}(\omega)$	dynamic compliance
$\bar{J}_1(\omega)$	storage compliance
$\bar{J}_2(\omega)$	loss compliance

$\lvert\bar{J}(\omega)\rvert$	absolute dynamic compliance
δJ	relaxation of the compliance
μ	rigidity (shear modulus)
ω	angular frequency
p	mechanical pressure
$\sigma, \bar{\sigma}$	stress (1d, time domain or frequency domain)
$\boldsymbol{\sigma}$	incremental Cauchy stress tensor
$\boldsymbol{\sigma}^{\mathrm{D}}$	deviatoric part of $\boldsymbol{\sigma}$
T	temperature
τ_{M}	relaxation time of Maxwell model
τ_{KV}	retardation time of Kelvin–Voigt model
τ	characteristic time in general
$\mathbf{u}$	infinitesimal deformation

Chapter 3: Tidal torque and tidal heat rate

A	coefficient in the Maxwell model
α	parameter of the Andrade model
B	coefficient in the Kelvin–Voigt model
η	dynamic viscosity
Φ_{tide}	average surface tidal heat flux
g	surface gravity
μ	rigidity (shear modulus)
ω	angular frequency
$\bar{P}^{\mathrm{tide}}$	orbit–averaged tidal heat rate (summed over the entire volume of the planet)
ρ	average density
$\mathcal{T}_2$	degree–2 secular tidal torque
τ_{M}	Maxwell (relaxation) time
τ_{KV}	Kelvin–Voigt (retardation) time
$\dot{\theta}$	spin rate
ζ	parameter of the Andrade model

Chapter 4: Coupled thermal and orbital evolution of low–mass exoplanets

A_{m}, A_{c}	surface area of the mantle and of the core
α	parameter of the Andrade model

α_m	thermal expansivity of the mantle
β	planet's obliquity
C	principal moment of inertia with respect to the rotational axis
c_m, c_c	specific heat capacity of the mantle and of the core
D_l	thickness of the stagnant lid
δ_S	upper limit on $\ddot{\theta}/\dot{\theta}$ in the short cycle
δ_c,δ_u	thicknesses of the lower and upper thermal boundary layers
Δ_μ, Δ_η	disaggregation widths
Δt_S	step size in the short cycle
Δt_L	step size in the long cycle
ε_{lmpq}	phase lag at mode $\{lmpq\}$
$\boldsymbol{\epsilon}^\mathrm{D}$	deviatoric part of the Eulerian strain tensor
ϵ_S	maximum local error of the short cycle
ϵ_L	maximum local error of the long cycle
η	dynamic viscosity
η_m	(average) mantle viscosity
η_0	reference viscosity
$\eta(T)$	viscosity at temperature T
η_max, η_min	parameters of the melting model
ϕ_m	total melt fraction in the mantle
$\phi(r)$	melt fraction at radius r
ϕ_D	disaggregation point
$\bar{J}(\omega)$	dynamic compliance
k_m, k_l	thermal conductivity of the mantle and of the lithosphere
L_m	latent heat
m_p	mass of the model planet
μ	rigidity (shear modulus)
μ_m	(average) mantle rigidity
μ_max, μ_min	parameters of the melting model
ω_{lmpq}	loading frequency at mode $\{lmpq\}$ (signed)
P	pressure
$\bar{P}^\mathrm{tide}$	orbit–averaged tidal heat rate (summed over the entire volume of the planet)
q_c	heat flux from the core to the mantle
q_m	heat flux from the mantle to the lithosphere
R_l	outer radius of the mantle (lithosphere base)
ρ_m,ρ_c	mean density of the mantle and of the core
St	Stefan number
$\boldsymbol{\sigma}^\mathrm{D}$	deviatoric part of the incremental Cauchy stress tensor
T_0	reference temperature
$T(r)$	local temperature at radius r
T_b	temperature on the bottom of the convecting mantle
T_c	temperature at the core–mantle boundary

T_l	temperature at the base of the lithosphere
T_m	temperature at the top of the convecting mantle
T_s	surface temperature
T_sol, T_liq	solidus and liquidus temperature
$\dot{\theta}$	spin rate
$\mathbf{u}$	infinitesimal deformation
V_m, V_c	volume of the mantle and of the core
ζ	parameter of the Andrade model

Chapter 5: Effect of an inclined outer perturber

η_0	reference viscosity
J_2	the second gravitational moment
λ_1, λ_2	mean longitudes
m_1	mass of the model (inner) planet
m_2	mass of the outer perturber
ω_1	inner orbit's argument of periapsis
Ω_1, Ω_2	arguments of the ascending nodes
ϖ_1, ϖ_2	longitudes of periapses
ψ	argument of the disturbing function
$\mathcal{R}_1$	disturbing function for the inner planet due to third–body perturbation
$\bar{\rho}$	mean density of the planet
Θ	Kozai's parameter
Θ_0	limit value of Kozai's parameter

Chapter 6: Planet–planet tides in tightly packed systems

α	right ascension of planet B, as observed from planet A
α_0	initial rotation of planet A
$\varepsilon_{lmn\bar{p}\bar{q}}$	tidal phase lag
$\mathcal{F}^0_{lmn\bar{p}}$	algebraic prefactor
m_A, m_B	masses
M_A, M_B	mean anomalies
ϖ	relative longitude of the perturber's pericentre
r, ϑ, φ	planetocentric equatorial coordinates of the disturber
r', ϑ', φ'	planetocentric equatorial coordinates of the disturbed unit volume

r_A, r_B	instantaneous distances
$r_<$, $r_>$	instantaneous distances of the inner and the outer planet from the host star
σ_A, σ_B	mean anomalies at epoch
θ	sidereal time
$\mathcal{U}$	tidal potential

Chapter 7: Tidal effects in differentiated viscoelastic bodies, a numerical approach

α	parameter of the Andrade model
$\mathbf{D}$	deviatoric part of the incremental Cauchy stress tensor
$E(t)$	eccentric anomaly
$\mathbf{e}_\mathrm{r}$	radial unit vector
$\varepsilon_{lm}(t)$	phase lag between $v_{lm}(t)$ and $\delta v_{lm}(t)$
ε	incremental strain tensor
$\dot{\varepsilon}$	strain rate tensor
η	mantle viscosity
$\mathbf{f}$	body force per unit mass
$\mathbf{f}_\mathrm{t}$	tidal force
$\mathbf{f}_\mathrm{cf}$	centrifugal force
$\mathbf{f}_\mathrm{self}$	self–gravity
f_{lm}^k	SH coefficients of the force
g_s, g_b	mean gravity accelerations on the upper and the lower boundary of the mantle
$\mathbf{I}$	identity matrix
$\bar{J}(\omega)$	dynamic compliance
$k_{lm}(t)$	ratio of $\delta v_{lm}(t)$ and $v_{lm}(t)$ (Love number)
k_f	fluid Love number
m	mass of the model planet
μ	mantle rigidity (shear modulus)
Ω_rot	planet's spin rate
π	isotropic part of the incremental Cauchy stress tensor
r', ϑ', φ'	planetocentric coordinates of a disturbed volume
r, ϑ_*, φ_*	planetocentric coordinates of the host star
r_s	planetary radius
r_b	radius of the core–mantle boundary
r_I	inner core radius
ρ	mean density of the planet
ρ_C	density of the (liquid) outer core
ρ_I	density of the inner core
ρ_M	density of the mantle

Δt	timestep
T	period for the heat rate averaging
$\mathcal{T}$	tidal torque
τ_{M}	Maxwell time
$\mathbf{u}$	displacement vector
u_{r}	radial component of displacement
$(u_{\mathrm{r}})_{lm}$	SH coefficients of the radial component of displacement
$\mathcal{U}$	potential
$\mathcal{U}_{\mathrm{t}}$	tidal potential
$\mathcal{U}_{\mathrm{cf}}$	centrifugal potential
$\mathcal{U}_{\mathrm{self}}$	self–gravitational potential
$v_{lm}(t)$	SH coefficients of $\mathcal{U}$
$\delta v_{lm}(t)$	SH coefficients of $\mathcal{U}_{\mathrm{self}}$
V	volume of the planetary mantle
ζ	parameters of the Andrade model

List of publications

1. Walterová, M. and Běhounková, M., (2020). **Thermal and orbital evolution of low-mass exoplanets**, *The Astrophysical Journal*, 900, No. 24, doi: 10.3847/1538-4357/aba8a5.

2. Walterová, M. and Běhounková, M. (2017). **Tidal effects in differentiated viscoelastic bodies: a numerical approach**, *Celestial Mechanics and Dynamical Astronomy*, 129(1-2), pages 235–256, doi:10.1007/s10569-017-9772-x.

3. Tosi, N., Čadek, O., Běhounková, M., Káňová, M., Plesa A.-C., Grott, M., Breuer, D., Padovan, S. and Wieczorek, M.A. (2015). **Mercury's low-degree geoid and topography controlled by insolation-driven elastic deformation,** *Geophysical Research Letters*, 42, pages 7327–7335, doi:10.1002/2015GL065314.

A. Outline of the normal mode theory

This appendix is almost identical[1] to Appendix A of Walterová and Běhounková (2020).

Assuming an incompressible, elastic and layered spherical planet subjected to external body force, the incremental deformation can be expressed as a sum of radial and lateral terms,

$$\mathbf{u} = \sum_{n=0}^{\infty} \left[U_n(r)\, \mathcal{P}_n(\cos\theta)\, \mathbf{e}_r + V_n(r)\, \frac{\partial}{\partial\theta} \mathcal{P}_n(\cos\theta)\, \mathbf{e}_\theta \right], \tag{A.1}$$

the additional potential induced by the deformation can be decomposed into

$$\delta\phi = \sum_{n=0}^{\infty} \Phi_n(r)\, \mathcal{P}_n(\cos\theta) \tag{A.2}$$

and the incremental pressure is

$$\delta p = \sum_{n=0}^{\infty} \Pi_n(r)\, \mathcal{P}_n(\cos\theta)\ . \tag{A.3}$$

In the above expressions, $\mathcal{P}_n(\cos\theta)$ are Legendre polynomials and $\mathbf{e}_r$, $\mathbf{e}_\theta$ are unit vectors in the radial and lateral (eastward) directions, respectively. As a consequence of the spherical harmonic decomposition, the set of governing equations (e.g., Sabadini and Vermeersen, 2004), which ensures the conservation of mass and momentum in the continuum, as well as the constitutive equation for an elastic material, can be rewritten into a set of ordinary differential equations of the form

$$\dot{\mathbf{Y}} = \mathbb{A}\mathbf{Y}, \tag{A.4}$$

where

$$\mathbf{Y} = \Big(U_n, V_n, T_{rn}, T_{\theta n}, \Phi_n, Q_n \Big)^t \tag{A.5}$$

with U_n, V_n and Φ_n introduced above and the other variables defined as

$$T_{rn}(r) = -\Pi_n + 2\mu \dot{U}_n\ , \tag{A.6}$$

$$T_{\theta n}(r) = \mu \left(\dot{V}_n - \frac{1}{r} V_n + \frac{1}{r} U_n \right)\ , \tag{A.7}$$

[1]Here, we have corrected a mistake in equation (A10) of the cited paper. Equation (A.10) now correctly represents the interior boundary conditions used in the semi–analytical model.

$$Q_n(r) = \dot{\Phi}_n + \frac{n+1}{r}\Phi_n + 4\pi\mathcal{G}\rho U_n \,. \tag{A.8}$$

Here, ρ is the mean density at radius r and symbol μ stands for static rigidity. The set of governing equations is constrained by boundary conditions prescribed at each interior interface, at the surface, and in the centre. Specifically, in the case of tidal loading, the boundary conditions at the surface are (Takeuchi et al., 1962; Sabadini and Vermeersen, 2004)

$$\begin{aligned} T_{rn}(R) &= 0 \,, \\ T_{\theta n}(R) &= 0 \,, \\ Q_n(R) &= -\frac{2n+1}{R} \,. \end{aligned} \tag{A.9}$$

In the centre, we only require regularity of the solution. The interior boundary conditions depend on the type of interfaces between the layers. Here, we consider each transition between layers as a solid-solid interface, which yields continuity of all components of the vector (A.5), i.e.,

$$\left[U_n\right]^+_- = \left[V_n\right]^+_- = \left[T_{rn}\right]^+_- = \left[T_{\theta n}\right]^+_- = \left[\Phi_n\right]^+_- = \left[Q_n\right]^+_- = 0 \,. \tag{A.10}$$

When applying the correspondence principle and shifting from the elastic to the viscoelastic problem, this choice of boundary conditions also means that each liquid layer needs to be considered as viscous. The incorporation of inviscid layers is, however, straightforward (Wu and Peltier, 1982).

The general solution to the set of ordinary differential equations (A.4) in layer $j \in [1, N]$ is a superposition of six linearly independent solutions,

$$\mathbf{Y}(r) = \sum_{i=1}^{6} C_i^{(j)} \mathbf{y}_i(r) \,, \tag{A.11}$$

where $C_i^{(j)}$ are layer-dependent constants given by the boundary conditions. Both the constants $C_i^{(j)}$ and the individual solutions $\mathbf{y}_i(r)$ of the viscoelastic problem attain complex values, which contain the information on the amplitude of deformations, stresses and potential, alike with the physical lagging caused by attenuation in the medium. While the phase lag between the strain and stress enables us to enumerate the energy dissipation anywhere inside the planet, the lagging between the external and additional gravitational potential presents a key parameter entering the spin and orbital evolution equations. Specifically, the complex tidal Love number $\bar{k}_l(\omega)$ is related to the constants $C_i^{(j)}$ by

$$\bar{k}_n(\omega) = -C_3^{(N)} R^n - C_6^{(N)} R^{-n-1} - 1 \,. \tag{A.12}$$

B. Darwin-Kaula expansion of the tidal heat rate for a stratified body

B.1 Global tidal heat rate

In the derivation of the global tidal heat rate, we restrict ourselves to the case of $l = 2$, which is used in this work. A detailed derivation of the expression for the tidal heating, based on continuum mechanics and paying special attention to the degeneracy of tidal modes, is presented in Efroimsky and Makarov (2014). The average heat rate produced by the dissipation in the entire volume of the planet over one orbital period can be written as (Segatz et al., 1988)

$$\bar{P}^{\rm tide} = -\frac{5\,n}{8\pi^2 \mathcal{G} R} \int_0^{T_{\rm orb}} \int_S \delta\Phi_2(R,\vartheta,\varphi,t)\, \frac{\partial \Phi_2(R,\vartheta,\varphi,t)}{\partial t}\, {\rm d}S\, {\rm d}t\,, \tag{B.1}$$

where Φ_2 and $\delta\Phi_2 = |\bar{k}_2(\omega)|\, \Phi_{2,\rm lag}$ are the degree–2 tidal and additional potential evaluated at the planet's surface. The subscript "lag" indicates that the argument of the disturbing potential should be complemented with the tidal phase lag. Using the traditional notation of Kaula (1964), the $\{2, m, p, q\}$ mode of the disturbing potential at the planet's surface can be expressed as

$$\begin{aligned}\delta\Phi_{2mpq}(R,\vartheta,\varphi,t) = k_2(\omega_{2mpq})\, R^2\, B_{2m}\, C_{2mpq}\, \mathcal{P}_{2m}(\cos\vartheta)\, \times \\ \times \begin{Bmatrix}\cos\\ \sin\end{Bmatrix}_{2-m\ \rm odd}^{2-m\ \rm even} \Big[\nu_{2mpq} - \varepsilon_{2mpq} - m(\varphi+\theta)\Big]\end{aligned} \tag{B.2}$$

with

$$\nu_{2mpq} = m\alpha + (2-2p+q)\, M + (2-2p)\, \gamma\ , \tag{B.3}$$

$$B_{2m} = \mathcal{G} m_* \frac{(2-m)!}{(2+m)!}\, (2-\delta_{m0}) \tag{B.4}$$

and

$$C_{2mpq} = \frac{1}{a^3}\, \mathcal{F}_{2mp}(\beta)\, \mathcal{G}_{2pq}(e)\ . \tag{B.5}$$

Similarly, we may write the time derivative of the tidal potential experienced at the planet's surface as

$$\left(\frac{\partial\Phi}{\partial t}\right)_{2mpq} = \omega_{2mpq}\, R^2\, B_{2m}\, C_{2mpq}\, \mathcal{P}_{2m}(\cos\vartheta) \begin{Bmatrix}-\sin\\ \cos\end{Bmatrix}_{2-m\ \rm odd}^{2-m\ \rm even} \Big[\nu_{2mpq} - m(\varphi+\theta)\Big]\ . \tag{B.6}$$

In both of the above expressions, ω_{2mpq} symbolises the tidal frequency, namely

$$\omega_{2mpq} = m\dot{\alpha} + (2-2p+q)\,n + (2-2p)\,\dot{\gamma} - m\dot{\theta} \approx (2-2p+q)\,n - m\dot{\theta}\,, \tag{B.7}$$

where the approximate value corresponds to a planet whose orbital and axial precession timescales are much longer than the orbital period.

To express the average tidal heat rate generated by the entire planet in the form of a sum, we need to substitute equations (B.2) and (B.6) to definition (B.1). When evaluating the integrals, we make use of the orthogonality of associated Legendre polynomials

$$\int_0^{\pi} \mathcal{P}_{lm}(\cos\vartheta)\mathcal{P}_{l'm}(\cos\vartheta)\sin\vartheta \mathrm{d}\vartheta = \frac{2(l+m)!}{(2l+1)(l-m)!}\,\delta_{ll'} \tag{B.8}$$

and of the following identities

$$\int_0^{2\pi} \left\{ \begin{matrix} -\cos\left(\psi_1 - m\varphi\right)\sin\left(\psi_2 - m\varphi\right) \\ \sin\left(\psi_1 - m\varphi\right)\cos\left(\psi_2 - m\varphi\right) \end{matrix} \right\} \mathrm{d}\varphi = -2\pi\cos\psi_1\sin\psi_2 \tag{B.9}$$

for $m = 0$ and

$$\int_0^{2\pi} \left\{ \begin{matrix} -\cos\left(\psi_1 - m\varphi\right)\sin\left(\psi_2 - m'\varphi\right) \\ \sin\left(\psi_1 - m\varphi\right)\cos\left(\psi_2 - m'\varphi\right) \end{matrix} \right\} \mathrm{d}\varphi = \pi\sin\left(\psi_1 - \psi_2\right)\delta_{mm'} \tag{B.10}$$

for $m \neq 0$. For the sake of clarity, we substituted ψ_1 and ψ_2 for the parts of the respective arguments that do not depend on the longitude φ, i.e.,

$$\begin{aligned} \psi_1 &= m\alpha + (2-2p+q)\,M + (2-2p)\,\gamma - m\theta - \varepsilon_{2mpq}\,, \\ \psi_2 &= m'\alpha + (2-2p'+q')\,M + (2-2p')\,\gamma - m'\theta\,. \end{aligned}$$

Specifically, for $m = m'$, we have

$$\psi_1 - \psi_2 = [2(p'-p) - (q'-q)]M + 2(p'-p)\gamma - \varepsilon_{2mpq}\,. \tag{B.11}$$

At this step, we may rewrite the definition (B.1) with evaluated integrals over ϑ and φ as

$$\bar{P}^{\mathrm{tide}} = \frac{R}{2\pi\mathcal{G}} \sum_{pqp'q'} \int_0^{2\pi} k_2(\omega_{20pq})\,\omega_{20p'q'} R^4 \mathcal{B}_{20}^2 C_{20pq} C_{20p'q'}\,\cos\psi_1 \sin\psi_2\,\mathrm{d}M \tag{B.12}$$

for $m = 0$ and

$$\bar{P}^{\mathrm{tide}} = -\frac{R}{4\pi\mathcal{G}} \sum_{mpqp'q'} \int_0^{2\pi} k_2(\omega_{2mpq})\,\omega_{2mp'q'} R^4 \mathcal{B}_{2m}^2 C_{2mpq} C_{2mp'q'} \frac{(2+m)!}{(2-m)!}\,\sin\left(\psi_1 - \psi_2\right)\mathrm{d}M \tag{B.13}$$

for $m \neq 0$. The remaining integral over the mean anomaly M can be evaluated similarly. If we substitute

$$b = 2 - 2p + q$$

and

$$b' = 2 - 2p' + q' \ ,$$

we may write the integral of expression (B.9), which holds for $m = 0$, as

$$\int_0^{2\pi} \cos\psi_1 \sin\psi_2 \, \mathrm{d}M = -\,\pi \sin\left[2(p'-p)\gamma - \varepsilon_{2mpq}\right] \delta_{bb'} + \\ + \pi \sin\left[2(2-p'-p)\gamma - \varepsilon_{2mpq}\right] \delta_{b,-b'} \tag{B.14}$$

for $b \neq 0 \vee b' \neq 0$ and

$$\int_0^{2\pi} \cos\psi_1 \sin\psi_2 \, \mathrm{d}M = -2\pi \cos\left(q\gamma + \varepsilon_{2mpq}\right) \sin q'\gamma \tag{B.15}$$

for $b = b' = 0$. Note, however, that the expression evaluated in equation (B.15) corresponds to zero frequency and does not contribute to the total tidal heat rate. Finally, the integral of expression (B.10), which holds for $m \neq 0$, is

$$\int_0^{2\pi} \sin\left(\psi_1 - \psi_2\right) \mathrm{d}M = 2\pi \sin\left[2(p'-p)\gamma - \varepsilon_{2mpq}\right] \delta_{bb'} \ . \tag{B.16}$$

In the next step, we are going to contemplate the terms with $m = 0$. Substituting expression (B.14) into the equation (B.12) and retaining only the non–zero terms, we obtain

$$\begin{aligned} \bar{P}^{\mathrm{tide}} = &-\frac{R^5}{2\mathcal{G}a^6} \sum_{pqp'} \omega_{20pq} \; k_2(\omega_{20pq}) \, \mathcal{B}_{20}^2 \mathcal{F}_{20p}(\beta) \, \mathcal{G}_{2pq}(e) \times \\ &\times \Big\{ \mathcal{F}_{20p'}(\beta) \, \mathcal{G}_{2,p',q+2(p'-p)}(e) \; \sin\left[2(p'-p)\gamma - \varepsilon_{20pq}\right] + \\ &+ \mathcal{F}_{20p'}(\beta) \, \mathcal{G}_{2,p',-q-2(2-p'-p)}(e) \; \sin\left[2(2-p'-p)\gamma - \varepsilon_{20pq}\right] \Big\} \end{aligned} \tag{B.17}$$

where we used the identities (see equation (B.7))

$$\omega_{2,0,p',q+2(p'-p)} = \omega_{2,0,p,q} \ ,$$

$$\omega_{2,0,p',-q-2(l-p'-p)} = -\omega_{2,0,p,q} \ .$$

The curly brackets in equation (B.17) contain two terms that can be rewritten

to the same form. Following Efroimsky and Makarov (2014), we reformulate the second term by performing the reindexing

$$\bar{p} = 2 - p' \qquad \text{and} \qquad \bar{q} = -q'$$

and immediately changing the notation, so that $\bar{p} \to p'$ and $\bar{q} \to q'$. Since the values attained by $\bar{p}$ and $\bar{q}$ are identical to the values attained by the former p' and q', this reindexing and renaming presents only a cosmetic change, which has no effect on the actual terms entering the summation. Now, the second term in the curly brackets of equation (B.17) reads as

$$\mathcal{F}_{2,0,2-p'}(\beta)\, \mathcal{G}_{2,2-p',-q'}(e)\, \sin\left[2(p'-p)\gamma - \varepsilon_{20pq}\right] , \tag{B.18}$$

where $q' = q + 2(p' - p)$. Therefore, in the last step, we apply the symmetries (Giacaglia, 1976; Wnuk, 1988)

$$\mathcal{G}_{lpq} = \mathcal{G}_{l,l-p,-q}$$

and

$$\mathcal{F}_{l,-m,p}(i) = (-1)^l \frac{(l-m)!}{(l+m)!} \mathcal{F}_{l,m,l-p}(i) ,$$

which, in our case of $l = 2$ and $m = 0$, enable us to rewrite the term (B.18) as

$$\begin{aligned} \mathcal{F}_{2,0,2-p'}(\beta)\, \mathcal{G}_{2,2-p',-q'}(e)\, \sin\left[2(p'-p)\gamma - \varepsilon_{20pq}\right] = \\ = \mathcal{F}_{2,0,p'}(\beta)\, \mathcal{G}_{2,p',q'}(e)\, \sin\left[2(p'-p)\gamma - \varepsilon_{20pq}\right] . \end{aligned} \tag{B.19}$$

After this reformulation, both terms in the curly brackets of equation (B.17) are the same.

Putting together equations (B.12) and (B.13) with the substitutions (B.14) and (B.16), and making use of the reformulation from the previous paragraph, we may write

$$\begin{aligned} \bar{P}^{\text{tide}} = -\frac{\mathcal{G}m_*^2}{a}\left(\frac{R}{a}\right)^5 \sum_{mpqp'} (2-\delta_{m0})\, \frac{(2-m)!}{(2+m)!}\, \mathcal{F}_{2mp}(\beta)\, \mathcal{F}_{2mp'}(\beta)\, \mathcal{G}_{2pq}(e)\, \mathcal{G}_{2p'q'}(e) \times \\ \times\, \omega_{2mpq}\Big[\mathrm{Re}\big\{\bar{k}_2(\omega_{2mpq})\big\} \sin 2(p'-p)\gamma + \mathrm{Im}\big\{\bar{k}_2(\omega_{2mpq})\big\} \cos 2(p'-p)\gamma\Big] , \end{aligned} \tag{B.20}$$

where $q' = q + 2(p' - p)$. Additionally, averaging expression (B.20) over the period of axial precession, and thus eliminating terms with γ, results in even more compact formula,

$$\bar{P}^{\text{tide}} = -\frac{\mathcal{G}m_*^2}{a}\left(\frac{R}{a}\right)^5 \sum_{mpq} (2-\delta_{m0})\, \frac{(2-m)!}{(2+m)!}\, \big[\mathcal{G}_{2pq}(e)\big]^2\, \big[\mathcal{F}_{2mp}(\beta)\big]^2\, \omega_{2mpq}\, \mathrm{Im}\big\{\bar{k}_2(\omega_{2mpq})\big\} . \tag{B.21}$$

B.2 Tidal dissipation in a unit volume

The volumetric energy dissipation in an incompressible viscoelastic continuum can be expressed as

$$h^{\mathrm{tide}}(r,\vartheta,\varphi,\omega) = \mathrm{Re}\Big\{\bar{\boldsymbol{\sigma}}(r,\vartheta,\varphi,\omega) : \dot{\bar{\boldsymbol{\epsilon}}}(r,\vartheta,\varphi,\omega)\Big\}\,, \tag{B.22}$$

with $\bar{\boldsymbol{\sigma}}$ being the incremental Cauchy stress tensor and $\dot{\boldsymbol{\epsilon}}$ symbolising the incremental strain rate tensor. At an arbitrary time and in an arbitrary point of the layered planet, the components of the displacement are related to the tidal potential $\Phi_{lm} = \sum_{pq} \Phi_{lmpq}$ by (e.g., Tobie et al., 2005a)

$$u_r(r,\vartheta,\varphi) = \sum_{lm} U_l(r)\Phi_{lm}(\vartheta,\varphi)\,, \tag{B.23a}$$

$$u_\vartheta(r,\vartheta,\varphi) = \sum_{lm} V_l(r)\frac{\partial\Phi_{lm}(\vartheta,\varphi)}{\partial\vartheta}\,, \tag{B.23b}$$

$$u_\varphi(r,\vartheta,\varphi) = \sum_{lm} \frac{V_l(r)}{\sin\vartheta}\frac{\partial\Phi_{lm}(\vartheta,\varphi)}{\partial\varphi}\,, \tag{B.23c}$$

where U_l and V_l are complex–valued coefficients of the spherical harmonic (SH) decomposition carried out in the overview of the normal mode theory (Appendix A). Since the incremental strain tensor is defined as

$$\bar{\boldsymbol{\epsilon}} = \frac{1}{2}\left(\nabla\mathbf{u} + \nabla^{\mathrm{T}}\mathbf{u}\right)\,, \tag{B.24}$$

we may write down its components as (e.g., Sokolnikoff, 1956)

$$\bar{\epsilon}_{rr} = \sum_{lmpq} \frac{\partial U_n(\omega_{lmpq})}{\partial r}\,\Phi_{lmpq}\,, \tag{B.25a}$$

$$\bar{\epsilon}_{\vartheta\vartheta} = \frac{1}{r}\sum_{lmpq}\left[V_n(\omega_{lmpq})\,\frac{\partial^2\Phi_{lmpq}}{\partial\vartheta^2} + U_n(\omega_{lmpq})\Phi_{lmpq}\right]\,, \tag{B.25b}$$

$$\bar{\epsilon}_{\varphi\varphi} = \frac{1}{r}\sum_{lmpq}\left[V_n(\omega_{lmpq})\frac{1}{\sin^2\vartheta}\frac{\partial^2\Phi_{lmpq}}{\partial\varphi^2} + V_n(\omega_{lmpq})\cot\vartheta\frac{\partial\Phi_{lmpq}}{\partial\vartheta} + U_n(\omega_{lmpq})\Phi_{lmpq}\right]\,, \tag{B.25c}$$

$$\bar{\epsilon}_{r\vartheta} = \bar{\epsilon}_{\vartheta r} = \sum_{lmpq}\frac{T_{\vartheta n}(\omega_{lmpq})}{2\bar{\mu}(\omega_{lmpq})}\,\frac{\partial\Phi_{lmpq}}{\partial\vartheta}\,, \tag{B.25d}$$

$$\bar{\epsilon}_{r\varphi} = \bar{\epsilon}_{\varphi r} = \sum_{lmpq}\frac{T_{\vartheta n}(\omega_{lmpq})}{2\bar{\mu}(\omega_{lmpq})}\,\frac{1}{\sin\vartheta}\,\frac{\partial\Phi_{lmpq}}{\partial\varphi}\,, \tag{B.25e}$$

$$\bar{\epsilon}_{\vartheta\varphi} = \bar{\epsilon}_{\varphi\vartheta} = \frac{1}{r}\sum_{lmpq} V_n(\omega_{lmpq})\left[\frac{1}{\sin\vartheta}\frac{\partial^2\Phi_{lm}}{\partial\vartheta\partial\varphi} - \frac{\cos\vartheta}{\sin^2\vartheta}\frac{\partial\Phi_{lmpq}}{\partial\varphi}\right]\,. \tag{B.25f}$$

where $\bar{\mu}$ is complex rigidity and $T_{\vartheta n}$ are the complex–valued coefficients of the SH decomposition of normal traction. The corresponding components of the incremental stress tensor are expressed accordingly, following the constitutive relation

$$\bar{\boldsymbol{\sigma}} = -p\,\mathbf{I} + 2\bar{\mu}(\omega)\,\bar{\boldsymbol{\epsilon}}\,. \tag{B.26}$$

Since we are assuming an incompressible medium, the incremental pressure is identically zero. The energy stored or dissipated per unit volume, averaged over one orbital period, is then evaluated for each component as

$$\langle \bar{h}_{ij} \rangle = \frac{1}{2\pi} \int_0^{2\pi} \bar{\sigma}_{ij}\, \dot{\bar{\epsilon}}_{ij}\, \mathrm{d}M\,, \tag{B.27}$$

where M stands for the mean anomaly. Finally, the average rate of energy dissipation in a unit volume is obtained from

$$\langle h^{\mathrm{tide}} \rangle (r, \vartheta, \varphi) = \mathrm{Re} \left\{ \sum_{ij} \langle \bar{h}_{ij} \rangle \right\}\,. \tag{B.28}$$

In this work, we only calculate degree–2 tidal dissipation. To ensure the correctness of the calculation at this degree, the implementations of the two analytical methods described in the present appendix were tested against each other, as well as against the numerical model of Chapter 7.

C. Partial derivatives of the disturbing function

The partial derivatives listed in this appendix are provided in the same functional form as in the implemented model, the results of which are presented in Chapters 3 to 5. Specifically, the partial derivatives from Section C.1 are inserted into the set of tidal evolution equations (1.40), while the partial derivatives from Section C.2 are used with the second set of Lagrange's planetary equations (1.10). The time derivatives of Keplerian elements, obtained from the mentioned sets, enable us to calculate the time derivatives of the nonsingular elements (1.58).

C.1 Tidal loading

Using the notation

$$\mathcal{A}_{lm} = \frac{(l-m)!}{(l+m)!}\,\kappa_m\ ,$$

and

$$\omega_{lmpq} = (l-2p)\dot{\gamma} + (l-2p+q)(n+\dot{\sigma}) + m(\dot{\alpha}-\dot{\theta}) \approx (l-2p+q)n - m\dot{\theta}\ ,$$

and defining the disturbing function as (Boué and Efroimsky, 2019, with different signing convention and in neglection of the dissipation in the host star)

$$\mathcal{R} = \frac{m_1+m_*}{m_1}\,\Phi^{\mathrm{tide}}$$

the partial derivatives of the disturbing function used in the equations for the secular orbital evolution can be written as (see also Boué and Efroimsky, 2019)

$$\left(\frac{\partial\mathcal{R}}{\partial\sigma}\right)_{lmpq} = (l-2p+q)\,\mathcal{A}_{lm}\,n^2a^2\,\frac{m_*}{m_1}\left(\frac{R}{a}\right)^{2l+1}\left[\mathcal{F}_{lmp}(\beta)\right]^2\left[\mathcal{G}_{lpq}(e)\right]^2\mathrm{Im}\{\bar{k}_l(\omega_{lmpq})\} \tag{C.1a}$$

$$\left(\frac{\partial\mathcal{R}}{\partial\gamma}\right)_{lmpq} = (l-2p)\,\mathcal{A}_{lm}\,n^2a^2\,\frac{m_*}{m_1}\left(\frac{R}{a}\right)^{2l+1}\left[\mathcal{F}_{lmp}(\beta)\right]^2\left[\mathcal{G}_{lpq}(e)\right]^2\mathrm{Im}\{\bar{k}_l(\omega_{lmpq})\} \tag{C.1b}$$

$$\left(\frac{\partial\mathcal{R}}{\partial\alpha}\right)_{lmpq} = m\,\mathcal{A}_{lm}\,n^2a^2\,\frac{m_*}{m_1}\left(\frac{R}{a}\right)^{2l+1}\left[\mathcal{F}_{lmp}(\beta)\right]^2\left[\mathcal{G}_{lpq}(e)\right]^2\mathrm{Im}\{\bar{k}_l(\omega_{lmpq})\} \tag{C.1c}$$

$$\left(\frac{\partial\mathcal{R}}{\partial\beta}\right)_{lmpq} = \mathcal{A}_{lm}\,n^2a^2\,\frac{m_*}{m_1}\left(\frac{R}{a}\right)^{2l+1}\mathcal{F}_{lmp}(\beta)\,\frac{\mathrm{d}\mathcal{F}_{lmp}(\beta)}{\mathrm{d}\beta}\left[\mathcal{G}_{lpq}(e)\right]^2\mathrm{Re}\{\bar{k}_l(\omega_{lmpq})\} \tag{C.1d}$$

$$\left(\frac{\partial\mathcal{R}}{\partial e}\right)_{lmpq} = \mathcal{A}_{lm}\,n^2a^2\,\frac{m_*}{m_1}\left(\frac{R}{a}\right)^{2l+1}\left[\mathcal{F}_{lmp}(\beta)\right]^2\mathcal{G}_{lpq}(e)\,\frac{\mathrm{d}\mathcal{G}_{lpq}(e)}{\mathrm{d}e}\,\mathrm{Re}\{\bar{k}_l(\omega_{lmpq})\} \tag{C.1e}$$

$$\left(\frac{\partial \mathcal{R}}{\partial a}\right)_{lmpq} = -(l+1)\,\mathcal{A}_{lm}\,n^2 a\,\frac{m_*}{m_1}\left(\frac{R}{a}\right)^{2l+1}\,\left[\mathcal{F}_{lmp}(\beta)\right]^2\left[\mathcal{G}_{lpq}(e)\right]^2\,\mathrm{Re}\{\bar{k}_l(\omega_{lmpq})\} \tag{C.1f}$$

C.2 Third–body perturbation

In this subsection, we are going to use the following notation:

$$\mathcal{B}^{\mathrm{i}}_{lm} = \mathcal{G}m_2\frac{(l-m)!}{(l+m)!}(2-\delta_{m0}) \tag{C.2}$$

$$\mathcal{B}^{\mathrm{o}}_{lm} = \mathcal{G}m_1\frac{(l-m)!}{(l+m)!}(2-\delta_{m0}) \tag{C.3}$$

$$\psi = (l-2p'+q')\lambda' - (l-2p+q)\lambda - q'\varpi' + q\varpi + (m-l+2p')\Omega' - (m-l+2p)\Omega \tag{C.4}$$

Substituting the multiindex of each mode by $\alpha = \{lmpp'qq'\}$, where $l \geq 2$, the derivatives of the disturbing function for the inner planet can be written as

$$\left(\frac{\partial \mathcal{R}_1}{\partial \epsilon_1}\right)_\alpha = -(l-2p+q)\,\frac{a_1^l}{a_2^{l+1}}\,\mathcal{B}^{\mathrm{i}}_{lm}\,\mathcal{F}_{lmp}(i_1)\,\mathcal{F}_{lmp'}(i_2)\,\mathcal{H}_{lpq}(e_1)\,\mathcal{G}_{lp'q'}(e_2)\,\sin\psi \tag{C.5a}$$

$$\left(\frac{\partial \mathcal{R}_1}{\partial \varpi_1}\right)_\alpha = q\,\frac{a_1^l}{a_2^{l+1}}\,\mathcal{B}^{\mathrm{i}}_{lm}\,\mathcal{F}_{lmp}(i_1)\,\mathcal{F}_{lmp'}(i_2)\,\mathcal{H}_{lpq}(e_1)\,\mathcal{G}_{lp'q'}(e_2)\,\sin\psi \tag{C.5b}$$

$$\left(\frac{\partial \mathcal{R}_1}{\partial \Omega_1}\right)_\alpha = -(m-l+2p)\,\frac{a_1^l}{a_2^{l+1}}\,\mathcal{B}^{\mathrm{i}}_{lm}\,\mathcal{F}_{lmp}(i_1)\,\mathcal{F}_{lmp'}(i_2)\,\mathcal{H}_{lpq}(e_1)\,\mathcal{G}_{lp'q'}(e_2)\,\sin\psi \tag{C.5c}$$

$$\left(\frac{\partial \mathcal{R}_1}{\partial i_1}\right)_\alpha = \frac{a_1^l}{a_2^{l+1}}\,\mathcal{B}^{\mathrm{i}}_{lm}\,\frac{\mathrm{d}\mathcal{F}_{lmp}(i_1)}{\mathrm{d}i_1}\,\mathcal{F}_{lmp'}(i_2)\,\mathcal{H}_{lpq}(e_1)\,\mathcal{G}_{lp'q'}(e_2)\,\cos\psi \tag{C.5d}$$

$$\left(\frac{\partial \mathcal{R}_1}{\partial e_1}\right)_\alpha = \frac{a_1^l}{a_2^{l+1}}\,\mathcal{B}^{\mathrm{i}}_{lm}\,\mathcal{F}_{lmp}(i_1)\,\mathcal{F}_{lmp'}(i_2)\,\frac{\mathrm{d}\mathcal{H}_{lpq}(e_1)}{\mathrm{d}e_1}\,\mathcal{G}_{lp'q'}(e_2)\,\cos\psi \tag{C.5e}$$

$$\left(\frac{\partial \mathcal{R}_1}{\partial a_1}\right)_\alpha = l\frac{a_1^{l-1}}{a_2^{l+1}}\,\mathcal{B}^{\mathrm{i}}_{lm}\,\mathcal{F}_{lmp}(i_1)\,\mathcal{F}_{lmp'}(i_2)\,\mathcal{H}_{lpq}(e_1)\,\mathcal{G}_{lp'q'}(e_2)\,\cos\psi \tag{C.5f}$$

and for the outer planet as

$$\left(\frac{\partial \mathcal{R}_2}{\partial \epsilon_2}\right)_\alpha = (l-2p'+q')\,\frac{a_1^l}{a_2^{l+1}}\,\mathcal{B}^{\mathrm{o}}_{lm}\,\mathcal{F}_{lmp}(i_1)\,\mathcal{F}_{lmp'}(i_2)\,\mathcal{H}_{lpq}(e_1)\,\mathcal{G}_{lp'q'}(e_2)\,\sin\psi \tag{C.6a}$$

$$\left(\frac{\partial \mathcal{R}_2}{\partial \varpi_2}\right)_\alpha = -q'\,\frac{a_1^l}{a_2^{l+1}}\,\mathcal{B}^{\mathrm{o}}_{lm}\,\mathcal{F}_{lmp}(i_1)\,\mathcal{F}_{lmp'}(i_2)\,\mathcal{H}_{lpq}(e_1)\,\mathcal{G}_{lp'q'}(e_2)\,\sin\psi \tag{C.6b}$$

$$\left(\frac{\partial \mathcal{R}_2}{\partial \Omega_2}\right)_\alpha = (m-l+2p')\,\frac{a_1^l}{a_2^{l+1}}\,\mathcal{B}^{\mathrm{o}}_{lm}\,\mathcal{F}_{lmp}(i_1)\,\mathcal{F}_{lmp'}(i_2)\,\mathcal{H}_{lpq}(e_1)\,\mathcal{G}_{lp'q'}(e_2)\,\sin\psi \tag{C.6c}$$

$$\left(\frac{\partial \mathcal{R}_2}{\partial i_2}\right)_\alpha = \frac{a_1^l}{a_2^{l+1}}\, \mathcal{B}^{\circ}_{lm}\, \mathcal{F}_{lmp}(i_1)\, \frac{\mathrm{d}\mathcal{F}_{lmp'}(i_2)}{\mathrm{d}i_2}\, \mathcal{H}_{lpq}(e_1)\, \mathcal{G}_{lp'q'}(e_2)\, \cos\psi \tag{C.6d}$$

$$\left(\frac{\partial \mathcal{R}_2}{\partial e_2}\right)_\alpha = \frac{a_1^l}{a_2^{l+1}}\, \mathcal{B}^{\circ}_{lm}\, \mathcal{F}_{lmp}(i_1)\, \mathcal{F}_{lmp'}(i_2)\, \mathcal{H}_{lpq}(e_1)\, \frac{\mathrm{d}\mathcal{G}_{lp'q'}(e_2)}{\mathrm{d}e_1}\, \cos\psi \tag{C.6e}$$

$$\left(\frac{\partial \mathcal{R}_2}{\partial a_2}\right)_\alpha = -(l+1)\frac{a_1^l}{a_2^{l+2}}\, \mathcal{B}^{\circ}_{lm}\, \mathcal{F}_{lmp}(i_1)\, \mathcal{F}_{lmp'}(i_2)\, \mathcal{H}_{lpq}(e_1)\, \mathcal{G}_{lp'q'}(e_2)\, \cos\psi \tag{C.6f}$$

Furthermore, the partial derivatives of the degree-1 terms ($\alpha = \{1mpp'qq'\}$) with the asterocentric correction (1.20), specific for the outer planet, are

$$\left(\frac{\partial \mathcal{R}_2}{\partial \epsilon_2}\right)_\alpha = (1 - 2p' + q')\, \mathcal{B}^{\circ}_{1m} \times \\ \times \left[\frac{a_1}{a_2^2}\mathcal{H}_{1pq}(e_1)\mathcal{G}_{1p'q'}(e_2) - \frac{a_2}{a_1^2}\mathcal{G}_{1pq}(e_1)\mathcal{H}_{1p'q'}(e_2)\right]\mathcal{F}_{1mp}(i_1)\mathcal{F}_{1mp'}(i_2)\sin\psi \tag{C.7a}$$

$$\left(\frac{\partial \mathcal{R}_2}{\partial \varpi_2}\right)_\alpha = -q'\, \mathcal{B}^{\circ}_{1m}\left[\frac{a_1}{a_2^2}\mathcal{H}_{1pq}(e_1)\mathcal{G}_{1p'q'}(e_2) - \frac{a_2}{a_1^2}\mathcal{G}_{1pq}(e_1)\mathcal{H}_{1p'q'}(e_2)\right]\mathcal{F}_{1mp}(i_1)\mathcal{F}_{1mp'}(i_2)\sin\psi \tag{C.7b}$$

$$\left(\frac{\partial \mathcal{R}_2}{\partial \Omega_2}\right)_\alpha = (m - 1 + 2p')\, \mathcal{B}^{\circ}_{1m} \times \\ \times \left[\frac{a_1}{a_2^2}\mathcal{H}_{1pq}(e_1)\mathcal{G}_{1p'q'}(e_2) - \frac{a_2}{a_1^2}\mathcal{G}_{1pq}(e_1)\mathcal{H}_{1p'q'}(e_2)\right]\mathcal{F}_{1mp}(i_1)\mathcal{F}_{1mp'}(i_2)\sin\psi \tag{C.7c}$$

$$\left(\frac{\partial \mathcal{R}_2}{\partial i_2}\right)_\alpha = \mathcal{B}^{\circ}_{1m}\left[\frac{a_1}{a_2^2}\mathcal{H}_{1pq}(e_1)\mathcal{G}_{1p'q'}(e_2) - \frac{a_2}{a_1^2}\mathcal{G}_{1pq}(e_1)\mathcal{H}_{1p'q'}(e_2)\right]\mathcal{F}_{1mp}(i_1)\frac{\mathrm{d}\mathcal{F}_{lmp'}(i_2)}{\mathrm{d}i_2}\cos\psi \tag{C.7d}$$

$$\left(\frac{\partial \mathcal{R}_2}{\partial e_2}\right)_\alpha = \mathcal{B}^{\circ}_{1m}\left[\frac{a_1}{a_2^2}\mathcal{H}_{1pq}(e_1)\frac{\mathrm{d}\mathcal{G}_{1p'q'}(e_2)}{\mathrm{d}e_2} - \frac{a_2}{a_1^2}\mathcal{G}_{1pq}(e_1)\frac{\mathrm{d}\mathcal{H}_{1p'q'}(e_2)}{\mathrm{d}e_2}\right]\mathcal{F}_{1mp}(i_1)\mathcal{F}_{lmp'}(i_2)\cos\psi \tag{C.7e}$$

$$\left(\frac{\partial \mathcal{R}_2}{\partial a_2}\right)_\alpha = \mathcal{B}^{\circ}_{1m}\left[-2\frac{a_1}{a_2^3}\mathcal{H}_{1pq}(e_1)\mathcal{G}_{1p'q'}(e_2) - \frac{1}{a_1^2}\mathcal{G}_{1pq}(e_1)\mathcal{H}_{1p'q'}(e_2)\right]\mathcal{F}_{1mp}(i_1)\mathcal{F}_{1mp'}(i_2)\cos\psi \tag{C.7f}$$

D. Details of the numerical approach

D.1 Iterative time scheme

To find the numerical solution of the governing equations, we use and further develop a tool employed in Tobie et al. (2008) and Běhounková et al. (2015), implemented by Ondřej Čadek. We have extended this code to account for a general tidal potential, rotational deformation and self-gravity. In order to evaluate the tidal torque correctly, we have updated originally explicit time scheme to include the self-gravity and the memory term implicitly.

For the $(i+1)$-th time step and the explicit time scheme, considering constant time step Δt, the equations (7.1) – (7.5) are discretised as follows (Běhounková et al., 2015):

Governing equations:

$$\nabla \cdot \mathbf{u}_{i+1} = 0 \tag{D.1}$$

$$-\nabla \pi_{i+1} + \nabla \cdot \mathbf{D}_{i+1} = \rho_{\mathrm{M}} \left[(\mathbf{f}_{\mathrm{t}})_{i+1} + (\mathbf{f}_{\mathrm{cf}})_{i+1} + (\mathbf{f}_{\mathrm{self}})_i \right]. \tag{D.2}$$

Constitutive equation:

$$2\varepsilon_{i+1} - \frac{\mathbf{D}_{i+1}}{\mu} = \overbrace{\frac{1}{2}\frac{\mathbf{D}_0}{\eta}\Delta t + \sum_{j=1}^{j=i} \frac{\mathbf{D}_j}{\eta}\Delta t}^{M_i} + \underbrace{\frac{1}{2} w_{(i+1)0} \left(\frac{\mathbf{D}_1}{(\zeta\eta)^\alpha} - \frac{\mathbf{D}_0}{(\zeta\eta)^\alpha} \right) + \sum_{j=1}^{j=i-1} \frac{1}{2} w_{(i+1)j} \left(\frac{\mathbf{D}_{j+1}}{(\zeta\eta)^\alpha} - \frac{\mathbf{D}_{j-1}}{(\zeta\eta)^\alpha} \right)}_{A_i}, \tag{D.3}$$

where w_{ij} are weights,

$$w_{(i+1)j} = (i+1-j)^\alpha \Delta t^\alpha \mu^{\alpha-1}, \tag{D.4}$$

M_i is the explicit memory term for the Maxwell rheology and A_i is the additional explicit memory term describing the Andrade rheology.

Boundary conditions:

$$(-\pi_{i+1}\mathbf{I} + \mathbf{D}_{i+1}) \cdot \mathbf{e}_{\mathrm{r}} - (u_{\mathrm{r}}^{\mathrm{s}})_{i+1}\, \rho_{\mathrm{M}}\, \mathbf{g}_{\mathrm{s}} = 0, \tag{D.5}$$

$$(-\pi_{i+1}\mathbf{I} + \mathbf{D}_{i+1}) \cdot \mathbf{e}_{\mathrm{r}} + \left(u_{\mathrm{r}}^{\mathrm{b}}\right)_{i+1} (\rho_{\mathrm{C}} - \rho_{\mathrm{M}})\, \mathbf{g}_{\mathrm{b}} = -\rho_{\mathrm{C}} \left[(\mathcal{U}_{\mathrm{t}})_{i+1} + (\mathcal{U}_{\mathrm{cf}})_{i+1} + (\mathcal{U}_{\mathrm{self}})_i \right] \mathbf{e}_{\mathrm{r}}. \tag{D.6}$$

The initial step ($l = 0$) in the iterative scheme is determined explicitly. For the

lth ($l \geq 1$) iteration, we then have

Governing equations:

$$\nabla \cdot \mathbf{u}_{i+1} = 0 \tag{D.7}$$

$$-\nabla \pi_{i+1} + \nabla \cdot \mathbf{D}_{i+1} = \rho_{\mathrm{M}} \left[(\mathbf{f}_{\mathrm{t}})_{i+1} + (\mathbf{f}_{\mathrm{cf}})_{i+1} + (\mathbf{f}_{\mathrm{self}})_{i+1}^{l-1} \right]. \tag{D.8}$$

Constitutive equation:

$$2\varepsilon_{i+1} - \frac{\mathbf{D}_{i+1}}{\mu} = M_i + \frac{1}{2}\frac{\mathbf{D}_{i+1}^{l-1}}{\eta}\Delta t + A_i + \frac{1}{4} w_{(i+1)i} \left(\frac{\mathbf{D}_{i+1}^{l-1}}{(\zeta\eta)^{\alpha}} - \frac{\mathbf{D}_{i-1}}{(\zeta\eta)^{\alpha}} \right). \tag{D.9}$$

Boundary conditions:

$$(-\pi_{i+1}\mathbf{I} + \mathbf{D}_{i+1}) \cdot \mathbf{e}_{\mathrm{r}} - (u_{\mathrm{r}}^{\mathrm{s}})_{i+1}\, \rho_{\mathrm{M}}\, \mathbf{g}_{\mathrm{s}} = 0, \tag{D.10}$$

$$(-\pi_{i+1}\mathbf{I} + \mathbf{D}_{i+1}) \cdot \mathbf{e}_{\mathrm{r}} + \left(u_{\mathrm{r}}^{\mathrm{b}}\right)_{i+1} (\rho_{\mathrm{C}} - \rho_{\mathrm{M}})\, \mathbf{g}_{\mathrm{b}} = -\rho_{\mathrm{C}} \left[(\mathcal{U}_{\mathrm{t}})_{i+1} + (\mathcal{U}_{\mathrm{cf}})_{i+1} + (\mathcal{U}_{\mathrm{self}})_{i+1}^{l-1} \right] \mathbf{e}_{\mathrm{r}}. \tag{D.11}$$

The iteration is repeated until $\frac{|\mathbf{D}_{\mathrm{II}}^{l} - \mathbf{D}_{\mathrm{II}}^{l-1}|}{\mathbf{D}_{\mathrm{II}}^{l}} < \epsilon$, where we usually assume $\epsilon = 10^{-4}$.

D.2 Spherical harmonics

Any quadratically integrable scalar function f of spherical coordinates ϑ and φ can be expressed as a linear combination of surface spherical harmonics Y_{lm} (see e.g. Varshalovich et al., 1988)

$$f(\vartheta, \varphi) = \sum_{l=0}^{\infty} \sum_{m=-l}^{l} f_{lm} Y_{lm}(\vartheta, \varphi) \tag{D.12}$$

with coefficients

$$f_{lm} = \int_0^{2\pi} \int_0^{\pi} f(\vartheta, \varphi) \bar{Y}_{lm}(\vartheta, \varphi)\, \sin\vartheta \, \mathrm{d}\vartheta \, \mathrm{d}\varphi \,. \tag{D.13}$$

We introduce the spherical harmonics as

$$Y_{lm}(\vartheta, \varphi) = (-1)^m \mathcal{N}_{lm} \mathcal{P}_{lm}(\cos\vartheta) e^{im\varphi} \,, \tag{D.14}$$

where $\mathcal{N}_{lm}$ is the normalisation factor

$$\mathcal{N}_{lm} = \sqrt{\frac{(2l+1)(l-m)!}{4\pi(l+m)!}} \,, \tag{D.15}$$

and $\mathcal{P}_{lm}(\cos\vartheta)$ are fully normalised associated Legendre polynomials of degree l and order m. Spherical harmonics represent a complete set of orthonormal functions on the surface of a sphere, with the orthonormality relation given by

$$\int_0^{2\pi}\int_0^{\pi} Y_{l_1 m_1}(\vartheta,\varphi)\bar{Y}_{l_2 m_2}(\vartheta,\varphi)\,\sin\vartheta\,\mathrm{d}\vartheta\,\mathrm{d}\varphi = \delta_{l_1 l_2}\delta_{m_1 m_2}\,. \tag{D.16}$$

The notion of spherical harmonic decomposition can be generalised to account for the vector and tensor functions as well. Vector spherical harmonics are introduced as

$$\mathbf{Y}^k_{lm}(\vartheta,\varphi) = \sum_{\mu=-1}^{+1}\sum_{\nu=-k}^{k} \mathcal{C}^{lm}_{k\nu 1\mu} Y_{k\nu}\,\mathbf{e}_\mu\,, \tag{D.17}$$

with $\mathcal{C}^{lm}_{k\nu 1\mu}$ being the Clebsch-Gordan coefficients and $\mathbf{e}_\mu$ being the components of a basis which appropriately follows the pattern of Y_{lm} under rotations. They are related to the cartesian basis vectors $\{\mathbf{e}_x,\mathbf{e}_y,\mathbf{e}_z\}$ by

$$\begin{aligned}
\mathbf{e}_{-1} &= \frac{1}{\sqrt{2}}\big(\mathbf{e}_x - i\mathbf{e}_y\big)\,,\\
\mathbf{e}_0 &= \mathbf{e}_z\,,\\
\mathbf{e}_1 &= -\frac{1}{\sqrt{2}}\big(\mathbf{e}_x + i\mathbf{e}_y\big)\,.
\end{aligned} \tag{D.18}$$

Finally, we define the tensor spherical harmonics

$$\mathbf{Y}^{kn}_{lm}(\vartheta,\varphi) = \sum_{\mu=-1}^{+1}\sum_{\nu=-k}^{k} \mathcal{C}^{lm}_{k\nu n\mu} Y_{k\nu}\,\mathbf{e}_{n\mu}\,, \tag{D.19}$$

with a basis

$$\mathbf{e}_{j\lambda} = \sum_{\nu,\mu} \mathcal{C}^{j\lambda}_{1\nu 1\mu}\,\mathbf{e}_\nu \otimes \mathbf{e}_\mu\,, \tag{D.20}$$

where $\otimes$ symbolises a dyadic product.